

Design of CO₂ Electrolysers and Electrocatalyst Integration



Swansea University
Prifysgol Abertawe

*A Doctoral thesis submitted in fulfilment of the requirements
for the degree of Doctor of Philosophy*

SUBMITTED BY

Odin J E Bain

SUPERVISED BY

ACADEMIC SUPERVISOR

Dr. Enrico Andreoli

Prof.

SECONDARY SUPERVISOR

Dr. Alvin White

Honorary Assoc. Prof.

ENERGY SAFETY RESEARCH INSTITUTE

FACULTY OF SCIENCE & ENGINEERING

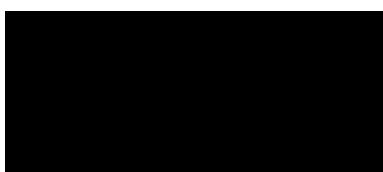
SWANSEA UNIVERSITY, UK

September, 2023

Declaration of Authorship

I, Odin J E Bain, declare that this thesis titled, “Design of CO₂ Electrolysers and Electrocatalyst Integration” and the work presented in it are my own. I confirm that:

- This work was done wholly or mainly while in candidature for a research degree at Swansea University.
- No part of this thesis has previously been submitted for a degree or any other qualification at this University or any other institution.
- Where I have consulted the published work of others, this is always clearly attributed.
- Where I have quoted from the work of others, the source is always given. With the exception of such quotations, this thesis is entirely my own work.
- Where the thesis is based on work done by myself jointly with others, I have made clear exactly what was done by others and what I have contributed myself.
- Where necessary, I have followed the ethical procedures and guidelines of the University.
- I hereby give my consent for my work, if relevant and accepted, to be available for photocopying and for inter-library loans after expiry of a bar on access approved by the University.



Odin J E Bain

September, 2023

“A pessimist sees the difficulty in every opportunity; an optimist sees the opportunity in every difficulty.”

“Success consists of going from failure to failure without loss of enthusiasm.”

Sir Winston Churchill



Swansea University
Prifysgol Abertawe

Abstract

Doctor of Philosophy

Design of CO₂ Electrolysers and Electrocatalyst Integration

by Odin J E Bain

The advancement of CO₂ catalysis has progressed significantly in the last two decades owing in part to the increased awareness of climate change. CO₂ capture and utilisation has become a major area of research for reducing atmospheric CO₂ levels. The initial part of this thesis approaches the development of CO₂ electrolyzers from a design perspective whereby the cell was optimised for current density through modelling and experimental techniques. Cell parameters such as electrode separation, electrolyte concentration, flow rate and buffering effect, and electrolyte circulation system configuration were examined alongside the effect of increased cathode electrochemical surface area. The results showed that proton transport limitation due to the Nafion membrane was a limiting factor but only at high applied voltages. Next the effect of additive-modified copper foams was explored to optimise the faradaic efficiency for C₂ products. With the inclusion of a gas diffusion electrode a considerable faradaic efficiency for ethanol was observed, whilst the lysine-modified copper foams showed a hydrogen quenching effect.

Acknowledgements

I would like to thank both Dr Enrico Andreoli and Dr Alvin White for giving me the opportunity to conduct this work and for their support, guidance, and patience throughout.

Thanks to all my friends and colleagues at the Energy Safety Research Institute (ESRI), past and present, your support has been greatly appreciated over the years. A particular thank you to Dr Stephen Shearan, Dr Kat Glover, Dr James Courtney, Dr Craig Armstrong, Dr Dan Jones, Dr Donald Hill, Dr Wafaa Al-Shatty, Henry Apsey, Max Newberry, Jen Seats.... apologies to the names I have missed. My time in ESRI with you all will be remembered fondly and I hope to work with you again in the future.

Additional thanks are due to Dr Dan Jones for his guidance with MatLab coding. I am also very grateful to Dr Stephen Shearan and Dr James Courtney for making sure I got some fresh air from time to time, and kept my sanity.

I also wish to thank Andrew Crossley, for his perseverance in making sure I understood and valued chemistry, despite me not seeing its importance at the time.

Last, but certainly not least, I would like to thank my family. Without whose support and encouragement over the last few years this would not have been possible.

Dedication

To all those that reads this... Thank you, I hope it's useful.

For all those that have doubted I could do this, including myself ... Here it is.

*In memory of my grandfather, a greater inspiration and role model a person could not
have asked for.*

*Oh and to James, Steve and Henry; If you've made it to the meatball bit, you really are
alright.*

Contents

Declaration of Authorship	iii
Abstract	v
Acknowledgements	vii
1 Introduction	1
1.1 Past and Current Carbon Emissions	2
1.2 Basics of Carbon Capture and Utilisation	5
1.3 Thesis Structure	9
1.4 Thesis Aims	12
2 Literature review	15
2.1 Cell Classification	15
2.1.1 H-Cells	16
2.1.2 Flow Cells	16
2.2 Electrodes	19
2.3 Electrolyte Transport	21
2.3.1 Effect of Gas Bubbles	23
2.4 Technology Gaps	23
3 Methods & Materials	25
3.1 Materials	25
3.2 Chronoamperometry	28
3.3 Electrode Characterisation	29

3.4	Product Analysis	30
3.5	Data Analysis and Processing	31
3.6	CAD CAM	31
3.7	High Speed Imagery	32
3.8	Flow Rate Calibration	33
3.9	Construction Techniques and Best Practices	34
4	Cell Design and Component Optimisation	37
4.1	Evaluation of Current Designs	37
4.1.1	Cells Examined in Practice	38
4.1.2	Cells Examined in the Literature	46
4.1.3	Cells Commercially Available	52
4.1.4	Analysis of Reviewed Cells and Design Limitations	55
4.2	Design Parameters and Specification	57
4.3	Custom System Design	59
4.3.1	Electrolyte Circulation	59
4.3.2	CO ₂ Supply	61
4.3.3	Product Separation	62
4.3.4	Power Supply	63
4.4	Cell Design Iterations	64
4.4.1	Designed Cell: MK 1	64
4.4.2	Designed Cell: MK 2	68
4.4.3	Designed Cell: MK 3	73
4.5	Flow Modelling	76
4.5.1	Mesh Refinement	76
4.5.2	Bubble dispersion	79
4.5.3	Flow Path	80
4.5.4	High Speed Imagery	84
4.5.5	Proposed Cell Design	87

4.5.6	Conclusion	89
4.6	Chapter Summary	90
4.6.1	Cell and System Evaluation and Limitations	91
4.6.2	Future Design Outlook	91
5	Cell Characterisation and Performance Optimisation	93
5.1	Introduction	93
5.1.1	Testing Profile	94
5.2	Results and Discussion	95
5.2.1	Effect of Flow Rate	95
5.2.2	Effect of Electrode Separation	98
5.2.3	Effect of Electrolyte Concentration	102
5.2.4	Effect of Supplied Gas	105
5.2.5	Effect of System Configuration	110
5.2.6	Effect of Electrode Surface Morphology	116
5.2.7	Foam Scaling	116
5.3	Chapter Summary	119
5.4	Outlook and Future Work	120
6	Testing Optimisation and Machine Learning	123
6.1	Introduction	123
6.2	Method	124
6.3	Results and Discussion	128
6.4	Conclusion	134
6.5	Contributions	135
7	Cell and CO₂ Electrocatalysts Integration	137
7.1	Introduction	137
7.2	Material Characterisation	143
7.2.1	SEM	143

7.2.2	EDX	146
7.2.3	Discussion	146
7.3	Affect of Applied Voltage on CO ₂ Electrolysis using Organic Modified Cu Foams	148
7.3.1	Results	149
7.3.2	Discussion	160
7.3.3	Summary	162
7.4	Affect of Time on CO ₂ Electrolysis using Organic Modified Cu Foams	163
7.4.1	Results	163
7.4.2	Discussion	168
7.4.3	Summary	170
7.5	Affect of GDE Inclusion on CO ₂ Electrolysis using Organic Modified Cu Foams	171
7.5.1	Results	172
7.5.2	Discussion	174
7.5.3	Summary	174
7.6	<i>In Situ</i> Surface Study on the Interface of Cu-foam Electrodes using EXAFS	175
7.6.1	Experimental	176
7.6.2	Results and Discussion	177
7.6.3	Conclusion	181
7.6.4	Acknowledgments	181
7.7	Conclusion and Outlook	182
8	Conclusions	183
8.1	Future works	186
	Bibliography	189
A	Supplementary Information 1	223

A.1	Deatiled graphs	223
A.2	Matlab code for J/V curve	240
B	Supplementary Information 2	243
B.1	Matlab code for Q calculation	243
B.2	Additional Results	246
B.2.1	EDX	246
B.2.2	Time plots	249
C	Background Theory	253
C.1	Cell Components	253
C.1.1	Electrodes	253
C.1.2	Membranes	255
C.1.3	Electrolyte	256
C.2	Electrochemical Concepts	258
C.2.1	Carbon Dioxide Reduction Reaction	261
C.2.2	Hydrogen Evolution Reaction	263
C.2.3	Oxygen Evolution Reaction	264
C.2.4	Efficiencies	265
C.2.5	Over-potential	267
C.3	Carbon Dioxide - Water System	270
C.3.1	Buffers	272
C.3.2	Henry's Law	274
C.3.3	Diffusion	275
C.3.4	Flow Characterisation	276

List of Figures

1.1	CCU paths	7
2.1	H-Cell Schematic	15
2.2	Flow Cell concept image	16
2.3	Flow Cell variations 1	17
2.4	Flow Cell variations 2	18
2.5	Electrode material classification grouping	20
2.6	Pump Classification	21
3.1	Flow Calibration	33
4.1	Syringe cell	38
4.2	Pine Research cell	41
4.3	Exploded view of Passas' design	44
4.4	Exploded view of Rearden's 2 mm cell	45
4.5	Comparison of Rearden's six cell stack design	46
4.6	Billy's cell schematic	47
4.7	Jeanty's flow by cell schematic	48
4.8	Jeanty's cell, system schematic	49
4.9	Jeanty's electrolyte flow plates	50
4.10	Wu's cell schematic	51
4.11	FM01-Cell schematic	53
4.12	The C-Flow Lab 5x5 laboratory-scale flow cell	54
4.13	Final System Design Schematic	59

4.14 System Gas Trap Schematic	63
4.15 Drawings of the 1, 2 and 4 electrode plates	66
4.16 MK 1 cell design exploded schematic	67
4.17 Photo of the MK 2 cell showing anodic bubble build up	70
4.18 Photo of the MK 2 cell showing the 3 electrode set up	70
4.19 MK 2 cell design exploded schematic	72
4.20 MK 3 cell design exploded schematic	75
4.21 Schematic of cell sections	76
4.22 Simulated mesh flow traces.	78
4.23 Simulated mesh flow nodes	78
4.24 Anodic flow plate designs	79
4.25 Simulated flow paths for the anodic chamber	80
4.26 Flow plate designs used in simulations	82
4.27 Simulated flow paths	82
4.28 High Speed Imagery for different flow plates	85
4.29 Proposed cell design exploded schematic	88
5.1 Pump flow rate plot	97
5.2 Total electrode separation plot 1: 3, 6, 9, 13mm	99
5.3 Total electrode separation plot 2: 3, 4, 5, 6 mm	101
5.4 Total electrode separation plot 3: 3, 4, 5, 6 mm, between 2.5 V and 12.5 V	102
5.5 Electrolyte Concentration Plot	104
5.6 J-V plot; CO ₂ and N ₂ in 0.1M	106
5.7 pH Plot 1; CO ₂ in 0.1M	107
5.8 pH Plot 2; N ₂ in 0.1M	107
5.9 J-V plot; CO ₂ and N ₂ in 1M	108
5.10 pH Plot 3; CO ₂ in 1M	109
5.11 pH Plot 4; N ₂ in 1M	109

5.12	Modified basic system design schematic	111
5.13	Dual vs Single reservoirs at 0.1 M	113
5.14	pH Plot 5; Single Reservoir at 0.1M	113
5.15	Dual vs Single reservoirs at 1 M	114
5.16	pH Plot 6; Single Reservoir at 0.1M	114
5.17	Plain foam SEM at 15s, 30s and 45s of deposition	117
5.18	Foam vs Plate current density plot	118
6.1	Fuzzy System Validation Plot	130
6.2	Membership Function Plot	130
6.3	Machine Learning: 3D plot of ML model for Electrode Separation .	131
6.4	Machine Learning cost estimate and particle convergence curves .	132
6.5	Machine Learning results	133
7.1	Foam growth mechanism	138
7.2	Dendritic PDL structure	141
7.3	SEM images of copper foams at 120x	144
7.4	SEM images of copper foams at 500x	145
7.5	EDX map images for Cu foams	147
7.6	Gaseous products at various applied voltages for copper plate elec- trode	149
7.7	Gaseous products at various applied voltages for Plain foam elec- trode	150
7.8	Gaseous products at various applied voltages for Poly Acrylamide modified foam electrode	151
7.9	Gaseous products at various applied voltages for Sodium Acrylate (Poly) modified foam electrode	152
7.10	Gaseous products at various Applied voltages for D-Lysine modi- fied foam electrode	153

7.11 Gaseous products at various applied voltages for L-Lysine modified foam electrode	154
7.12 Gaseous products at various applied voltages for Pollyallyamine modified foam electrode	155
7.13 Gaseous products at various applied voltages for Poly-D-Lysine modified foam electrode	156
7.14 Bar chart of ethylene, ethane and hydrogen FE at 3 V	157
7.15 Bar chart of ethylene, ethane and hydrogen FE at 4 V	158
7.16 Bar chart of ethylene, ethane and hydrogen FE at 5 V	159
7.17 Modified Foams Time Plots	165
7.18 Possible mechanistic pathways of CO ₂ reduction to C ₁ and C ₂ products	170
7.19 FE for Modified Foams on GDE at 4 V	172
7.20 FE for Modified Foams on GDE at 5 V	173
7.21 Instrumental set-up used for the EXAFS study.	177
7.22 EXAFS spectra for reference standards	178
7.23 EXAFS spectra standards	178
7.24 Averaged EXAFS spectra for various times for Cu foam at -1 V in Ar saturated 1 M NaOH	179
7.25 Averaged EXAFS spectra for various times for Cu foam at -1 V in CO ₂ saturated 1 M NaOH	180
7.26 Selected EXAFS spectra from Figure 7.25	180
A.1 Detailed: Pump flow rate plot	224
A.2 Detailed: Total electrode separation plot 1: 3, 6, 9, 13mm	225
A.3 Detailed: Total electrode separation plot 2: 3, 4, 5, 6 mm	226
A.4 Detailed: Total electrode separation plot 3: 3, 4, 5, 6 mm, between 2.5 V and 12.5 V	227
A.5 Detailed: Electrolyte Concentration Plot	228

A.6 Detailed: J-V plot; CO ₂ and N ₂ in 0.1M	229
A.7 Detailed: J-V plot; CO ₂ and N ₂ in 1M	230
A.8 Detailed: pH Plot 1; CO ₂ in 0.1M	231
A.9 Detailed: pH Plot 2; N ₂ in 0.1M	232
A.10 Detailed: pH Plot 3; CO ₂ in 1M	233
A.11 Detailed: pH Plot 4; N ₂ in 1M	234
A.12 Detailed: Dual vs Single reservoirs at 0.1 M	235
A.13 Detailed: Dual vs Single reservoirs at 1 M	236
A.14 Detailed: pH Plot 5; Single Reservoir at 0.1M	237
A.15 Detailed: pH Plot 6; Single Reservoir at 0.1M	238
A.16 Detailed: Foam vs Plate current density plot	239
 B.1 EDX spectra for Plain Cu foam	 246
B.2 EDX spectra for PA Cu foam	246
B.3 EDX spectra for PSA Cu foam	247
B.4 EDX spectra for DL Cu foam	247
B.5 EDX spectra for LL Cu foam	247
B.6 EDX spectra for PAA Cu foam	248
B.7 EDX spectra for PDL Cu foam	248
B.8 Plots for Plain foam over 3 hours of CO ₂ RR at 4 V	249
B.9 Plots for DL foam over 3 hours of CO ₂ RR at 4 V	250
B.10 Plots for LL foam over 3 hours of CO ₂ RR at 4 V	251
B.11 Plots for PDL foam over 3 hours of CO ₂ RR at 4 V	252
 C.1 Possible mechanistic pathways of CO ₂ reduction to C ₁ and C ₂ prod- ucts	 262
C.2 Breakdown of overall cell voltage	268
C.3 Bicarb pH	274
C.4 Flow Classification diagram	277

List of Tables

4.1	Parts table for MK 1 design.	67
4.2	Parts table for MK 2 design.	72
4.3	Parts table for MK 3 design.	75
4.4	Mesh resolution factor and resulting number of nodes / elements. .	77
4.5	Internal Volume, Volumetric refresh rates and the Number of Cell Volumes required for examined flow plates.	87
4.6	Parts table for the proposed cell design.	89
5.1	Electrode separations and resulting cathodic volumes.	99
5.2	revised electrode separations and resulting cathodic volumes. . . .	102
6.1	Statistical evaluation of the fuzzy-based model	129
6.2	Machine Learning results for electrode separation.	133
6.3	Machine Learning results.	134
7.1	Selected foam modifiers.	142
7.2	Average pore diameter and wall thickness for each Cu foam in μm . .	143
7.3	Atomic % of Cu, O, S and Cl for each of the foams.	146
C.1	CO ₂ Reduction Potentials for Various CO ₂ Reduction Reactions Products	263

Abbreviations

AEM	Anion Exchange Membrane
ANFIS	Adaptive Network-based Fuzzy Inference System
CCS	Carbon Capture and Sequestration
CCU	Carbon Capture and Utilisation
CFD	Computational Fluid Dynamics
CO₂RR	Carbon Dioxide Reduction Reaction
DL	D-Lysine
DR	Dual Reservoir system
EDX	Energy-dispersive X-ray spectroscopy
EIS	Electrochemical Impedance Spectroscopy
EXAFS	Extended X-Ray Absorption Fine Structure
FE	Faradaic Efficiency
FL	Fuzzy Logic
FM	Fuzzy Modelling
gbest	Group best
GC	Gas Chromatography
GDE	Gas Diffusion Electrode

GDL	Gas Diffusion Layer
HER	Hydrogen Evolution Reaction
HSI	High Speed Imagery
ID	Internal Diameter
j	Current Density
LL	L-Lysine
LSV	Linear Sweep Voltammetry
MEA	Membrane Electrode Assembly
MF	Membership Function
ML	Machine Learning
MRF	Mesh Resolution Factor
MSE	Mean Square Error
NMR	Nuclear Magnetic Resonance spectroscopy
OD	Outer Diameter
PAA	Pollyallyamine
PA	Poly Acrylamide
pbest	Personal best
PDL	Poly-D-Lysine
PEM	Proton Exchange Membrane
PSA	(Poly) Sodium Acrylate
PSO	Particle Swarm Optimisation
PSU	Power Suply Unit

PSU	Power Supply Unit
PTFE	Polytetrafluoroethylene
RSME	Root Mean Square Error
SA_g	Geometric Surface Area
SA	Surface Area
SEM	Scanning Electron Microscopy
SR	Single Reservoir system
UHMW	Ultra-High molecular weight
XAS	X-Ray Absorption Spectroscopy

Physical Constants

Avogadro's Number	$N_A = 6.022\,140\,86 \times 10^{23} \text{ mol}^{-1}$
Boltzmann Constant	$k_B = 1.380\,649 \times 10^{-23} \text{ J mol}^{-1}$
Faraday Constant	$F = 96\,485.33 \text{ C mol}^{-1}$
Ideal Gas Constant	$R = 8.314\,462\,618\,153\,24 \text{ J mol}^{-1} \text{ K}^{-1}$
Standard Atmosphere	$atm = 101.325 \text{ kPa}$
Amp-Hour	$A_{Hour} = 3600 \text{ C}$
Kilowatt-hour	$kWh = 3600 \text{ kJ}$

List of Symbols

A	Area	m^2
A_{cs}	Cross sectional area	m^2
E	Potential measured against the reference electrode	V
E_{Rev}	Reversible potential versus a reference electrode	V
L	Length	m
W	Watts	W
G_e	Electrical Conductance	$\text{S}(\Omega^{-1})$
C	Capital investment	£
C_F	Fixed Capital	£
C_L	Land Capital	£
C_W	Working Capital	£
ne	Number of electrons	
σ	Conductivity	Sm^{-1}
σ_e	Electrical Conductivity	Sm^{-1}
Ω	Resistance	$\text{kgm}^2\text{s}^{-3}\text{A}^{-2}$
ρ	Resistivity	Ω

Chapter 1

Introduction

In 1882 Thomas Edison opened his first power plant at Pearl Street Station in Manhattan. His design for the electrical system was to have lots of small local power stations, providing energy to the surrounding area, however this was costly and the fossil fuel burning power plants of the time were noisy, dirty and inefficient. With Nikola Tesla opening his Niagara Falls hydro power plant, in 1895, using AC generators to transport power hundreds of miles to Chicago and New York the system evolved, utilising fewer, large scale power plants far away from the consumer [1].

Today, we are starting to re-examine Edison's distribution philosophy. With fossil fuels in limited supply, carbon emissions forming a major contributor to global warming, and continually increasing demand for energy, researchers are looking to smaller local power generation across the globe [2, 3]. This reflects the increasing number of worldwide Governments creating policies to encourage distributed generation, such as the United Kingdom's Feed-In Tariff scheme[4]. Similarly a desire from companies for smaller scale power generation with localised distribution systems is evident; Examples include SPECIFIC with their Active Office and active Classroom projects [5], the Pricewaterhouse-Coopers (PwC) London headquarters at One Embankment Place and the Co-Operative Group's One Angel Square Manchester headquarters.

More and more the global community is looking for cleaner, small-scale distributed power generation. Large numbers of renewable energy sources are being connected to distribution grids which are posing considerable impacts on the operation and protection of these networks [6–8]. Small scale power systems require an effective energy storage method [9] that can provide energy when other sources are unavailable. Carbon Capture and Utilisation (CCU) could offer this if the scale up barriers can be overcome [10, 11]. Additionally CCU can further reduce humanities' emissions causing climate change by reducing the contribution made by the chemical industry where instead of making carbon-based chemicals from fossil carbon they can be produced from CO₂ [12].

1.1 Past and Current Carbon Emissions

In the last two centuries, the primary sources of the global energy supply have changed. Prior to the Industrial Revolution, base bio-fuels (wood) were used and this developed into an energy supply dominated by fossil fuels (coal, oil and natural gas) as demand rapidly increased [13]. This key change occurred due to the requirement of the industrialised world for more reliable fuels with a higher combustion temperature and energy density to drive steam engines and later, generate electricity [14]. The mid 1900s saw the transition to oil, with the development of the combustion engine replacing the steam engine's heavier and bulkier design, leading to the development of many of the technologies we use today. However, this resulted in the global energy use in 1970 becoming 38 Gboe (Giga-barrels of oil equivalent) per year, a figure that has continued to rise, with 85% of the 13.5TW consumed globally in 2001, coming from fossil fuels [15].

Continued Fossil Fuel Usage

Industrialisation of nations across the globe can be attributed to the discovery and adoption of fossil fuels which provided a relatively cheap, plentiful and accessible energy source enabling widespread use of personal transport, heating and electric generation. Since 1970 the global energy demand has more than doubled (as of 2010) to 86 Gboe per year, driven by increasing populations and rising global standard of living with more people having access to domestic power and personal transport plus expecting their governments to provide easy, economical access to reliable energy. Worldwide energy consumption is predicted to rise by another 48% by 2040, driven by the rapid development of the highly populated B.R.I.C. (Brazil, Russia, India, China) countries which are currently undergoing fast economic growth [16, 17].

Since the mid 2000s, there has been an increase in the low carbon energy sources used globally, with a major shift expected to have occurred as soon as 2050. Those same communities wanting cheap, available energy are increasing concurrently concerned about global warming and sustainability. The research required for the invention of new technologies and the development of existing ones is vital for this energy transition to take place. In the UK during 2018, 33.4% of electricity was generated from renewable sources, with 17.4% coming from wind, 3.9% from solar, and 10.7% from bio-energy. The unprecedented roll out of renewable generation has driven down costs; an electricity comparison showed that onshore wind was the cheapest form of electricity generation at \$ 40 per MWh, and solar was comparable to natural gas at \$51 and \$48 per MWh respectively [18]. Off-shore wind technology shows promise to realise further cost savings in the near future as recent price auctions in the UK showed that the cost of the technology dropped by over 50% in the last 5 years [19].

Fossil Fuel Issues

As the use of fossil fuels increased globally, the issues caused by their utilisation have become more prominent. Large mining operations have created significant negative local environmental and ecological effects, locations such as the Tagebau Garzweiler mine have dramatically changed the local ecology and biosphere as well as creating large amounts of pollutants from the mining and transportation of lignite (brown coal). It is now widely accepted that the combustion of these fossil fuels is a prominent factor in the current changes seen in the global climate, also causing higher levels of several toxins which are detrimental to human health. Some gases produced from the combustion of the fossil fuels have contributed to substantial destruction of the natural environment and degradation of man-made structures. These gases dissolve in water forming acids affecting the pH of the environment both locally and globally, and heavily trafficked shipping routes are a particular concern [20].

The emissions from the combustion of these fossil fuels causes harmful air pollution, with particular issues associated with nitrogen dioxide, sulphur dioxide and carbon monoxide; all causing significant harm to life. This pollution is particularly severe within densely populated areas and has been linked to over 40,000 deaths per year in the EU [21, 22].

The combustion of fossil fuels releases carbon previously stored as geological deposits and this has caused an increase in the level of carbon dioxide in the atmosphere from 280 ppm in 1850 to 404 ppm in 2017 [23] and has reached over 423 ppm as of September 2024 [24]. Carbon dioxide acts as a greenhouse gas, trapping solar radiation that would have otherwise been reflected back out of the atmosphere, causing an increase to the temperature of the earth and its lower atmosphere [25]. If CO₂ levels increase further, considerable irreversible damage may be done to the climate and global eco-structure [26–30].

Fossil Fuel Alternatives

With global energy consumption continuing to increase due to population and economic growth, providing the required energy without fossil energy resources, particularly coal, will be difficult. Solar energy is by far the largest exploitable green resource, with more energy reaching the surface of the earth in 1 hour than is consumed globally in a year [31]. The indeterminacy and localisation of solar energy means that if it is to become a primary energy source it must be stored in a way that can be supplied on demand to the consumer. One approach has been to store solar-converted energy in the form of chemical bonds, through enhanced photosynthesis reactions in plant and algae. More recently electrocatalysis is being explored with schemes aiming to capture and convert solar energy, then storing that energy in the form of chemical bonds by producing oxygen, from water, and a reduced fuel such as hydrogen or methane, creating an artificial carbon neutral cycle [32, 33].

1.2 Basics of Carbon Capture and Utilisation

Carbon capture is expected to play a key role in meeting the global temperature targets set by the IPCC [34] and at COP21 [35]. Several advancements for CO₂ capture have been recently reported including enhanced chemical absorption techniques to remove CO₂ from combustion waste streams at commercial-scale capture facilities such as the SaskPower's Boundary Dam 3 CCS Facility (Canada) and Shells' CANSOLV facilities [36, 37]. The Boundary Dam facility is reported to be able to capture 90% carbon dioxide, 100% sulphur dioxide and 50% of the Nox produced by the Coal power plant, a reported reduction of up to one million tonnes of carbon dioxide each year. Such progress in CO₂ capture techniques highlights the need to determine what to do with the captured CO₂.

Carbon capture and storage (CCS) has two possible roots; artificial storage and

natural storage. Global CCS plans and infrastructure are evident and include reforestation schemes where the CO₂ is captured by the vegetation and stored as solid carbon. In time it will be released again to the atmosphere either through combustion or decomposition, forming a natural carbon cycle. Natural storage is already a considerable factor with Zhu *et al.* [38] reporting a persistent and widespread increase of greening over 25% to 50% of the global vegetated area, whereas less than 4% of the globe shows browning. CO₂ fertilisation effects were suggested to explain 70% of the observed greening trend. Alternatively the carbon can be stored in large deposits such as depleted oil fields as is currently seen in the North Sea [39, 40], where the CO₂ can be used for enhanced oil recovery from the deposits [41] with Burrows *et al.* showing that CO₂ can recover 90-100% of the oil deposit [42].

A further option is to use carbon capture and utilisation to create an artificial carbon cycle through conversion of the captured CO₂ to fuels, or they can be sequestered through use as chemical feedstocks before being eventually released back into natural carbon cycle [43, 44]. The added advantage is that the sale of these products can be used to offset the cost of CO₂ capture which is a key disincentive of adopting current capture techniques.

Figure 1.1 shows the ways that CO₂ can be utilised once captured from waste streams.

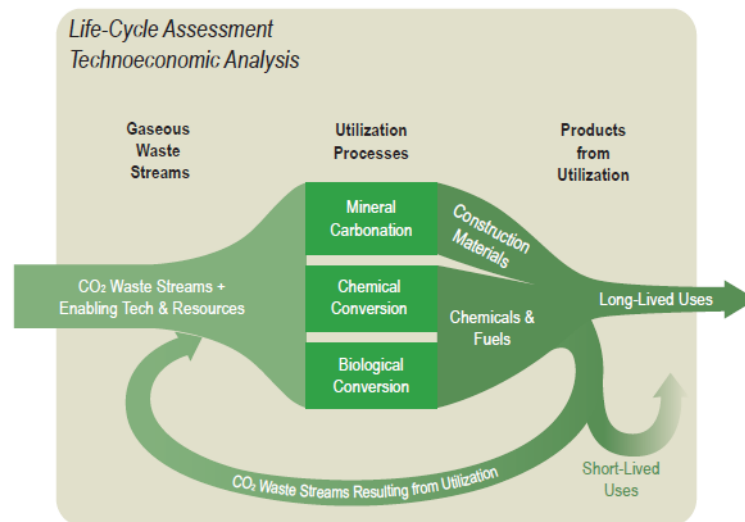


FIGURE 1.1: Reproduced from the National Academies of Science Engineering and Medicine publication [43]: Possible carbon utilisation paths.

CO₂ is already used in some commercial processes, both in its pure form and as a feedstock in the synthesis of bulk chemicals such as urea.

Direct Use

CO₂ is used directly in several forms, often offering temporary storage, before being released into the atmosphere. In the pure form, CO₂ is used in the food industry for a wide variety of applications ranging from carbonation of drinks to accelerated production of greenhouse grown fruit crops [45]. Likewise, bulk CO₂ is used as solvents in processes such as dry cleaning of fabric and decaffeination [46]. as well as other practical direct uses such as fire extinguishers, refrigerants (such as dry ice).

Mineral Carbonation

The process of mineral carbonisation converts CO₂ into a more stable form of carbon, typically a carbonate, which can be used in construction materials such as concrete. Mineralization involves reaction of minerals usually calcium or magnesium silicates. The reaction to form carbonates is exothermic and does not require

energy input to sustain the reaction (though cooling may be required to control it), although significant energy is typically required to generate the requisite feed minerals. The current bottleneck for viable mineral carbonation processes on an industrial scale is the reaction rate of carbonation. Additionally, new formulations will require structural testing and material characterisation before being accepted by users and regulators.

Bio Conversion

Biological conversion of CO₂ involves using photosynthetic and other metabolic processes inherent to plants, algae, bacteria and fungi to produce higher value chemicals. Several factors have expanded the repertoire of biobased products that can be synthesised directly from CO₂, including the large number of CO₂-utilising microorganisms, genetic modification of microorganisms and tailoring enzymatic/protein properties through protein engineering. Biological utilisation has a large range of potential uses in the development of commercial products including various biofuels, chemicals, and fertilisers. However, biological utilisation rates and scalability remain challenges.

Chemical Conversion

It is possible to use CO₂ for the production of fuels and chemicals by reacting it with other molecules and/or providing electrochemical, photochemical or thermal energy, with a catalyst required to overcome kinetic barriers. Because the carbon in CO₂ is in its most highly oxidized form, many of the resulting reactions are reductions, either through the addition of hydrogen or electrons. Catalysts are critical not only for making the transformation possible, but also for reducing the energy inputs to (ideally) the minimum amount dictated by the thermodynamics of the transformation. Discovery of appropriate catalysts and development of energy-efficient processes are the current barriers to rapid expansion and greater utilisation.

In modern life, as damaging as they can be to the environment, plastics have become an irreplaceable material. The ability to replace costly and environmentally damaging fossil fuel base plastics with captured carbon base products would greatly reduce the global impact, as well as acting as a form of CCS by storing the carbon in long life plastics. Alternatively there is the ability to create a carbon neutral fuel source by converting CO₂ into fuel sources such as methane [47].

As of 2021, pilot-scale carbon dioxide electrochemical reduction is being developed by several companies including Siemens [48, 49], Dioxide Materials [50, 51], Twelve and GIGKarasek. The process of CO₂ chemical conversion through electrocatalysis will be examined in more detail in Chapter 2.

Summary

In terms of scale, building materials and fuels are produced and consumed on a much larger scale than chemicals [52]. With annual CO₂ emissions from anthropogenic activity in 2017 at around 40 gigatons [53], only approximately 0.35 billion tonnes of plastics are made each year [54, 55]. Addressing fuels is a much more promising solution for reducing emissions, with over two thirds of the UK's CO₂ emissions coming from fossil fuel consumption [56].

1.3 Thesis Structure

Chapter 1: Introduction

The opening chapter sets the foundation for this thesis by providing a comprehensive introduction to the topic of CO₂ utilisation. It outlines the background and motivation behind the study, emphasising the need to address CO₂ emissions and explore sustainable approaches for CO₂ utilisation. The objectives of

the study are stated, highlighting the specific areas of investigation. It also outlines the organisation and structure of the thesis, giving an overview of the subsequent chapters and their respective contributions to the field.

Chapter 2: Literature Review

The literature review chapter provides a comprehensive overview of the existing body of knowledge and research related to CO₂ electrocatalysis. It serves as a critical analysis of the current state of the field, highlighting the key findings, advancements and gaps in the literature.

Chapter 3: Experimental Techniques

Chapter 3 describes the various techniques used in the thesis and details the equipment and materials. It explains why they were selected and provides additional information such as the supplier and purity.

Chapter 4: Cell Design and Optimisation

Detailed case studies of existing electrolyser designs and analyses trends in the designs are presented in Chapter 4. These trends are combined with a design specification in order to inform cell design and development. It explains how the chosen design was selected and further developed to create a design optimised to better suit the needs of later work. Computational fluid dynamics (CFD) modelling is conducted to better understand and optimise flow within the cell.

Chapter 5: Cell Characterisation and Resistance Optimisation

In Chapter 5, the optimisation of cell for electrical conductivity is explained. This includes characterisation of key parameters; electrolyte flow rate, electrode separation and electrolyte concentration. It examines the limiting factors for the designed cell, with the cell supporting system redesigned and saturation gas varied to examine the cause of pH build up within the cell. The chapter is concluded by examination of enhancing the electrochemical surface area of the cell.

Chapter 6: Testing Optimisation and Machine Learning

This chapter consists of Adaptive Network-based Fuzzy Inference System (ANFIS) and Particle Swarm Optimisation (PSO) machine learning techniques, and how they can be used to supplement the experientially obtained data thus enhancing the accuracy of the optimisation.

Chapter 7: Application of Electrolysers in CO₂ Conversion using Additive-Modified Copper Electrocatalysts

Chapter 7 presents the work conducted to improve the selectivity of the CO₂ products. Options for enhancing metal foams for CO₂RR are examined in the literature with several organic modifiers selected for analysis. The organic modified foams are examined for product selectivity at different voltages, before long duration testing is conducted to fully characterise their product selectivity through Nuclear Magnetic Resonance (NMR) analysis. The cell design is adapted for the inclusion of a gas diffusion electrode on which a selection of the organic modifiers are examined. The chapter concludes with Extended X-Ray Absorption Fine Structure (EXAFS) analysis of the copper foams.

Chapter 8: Conclusion

The final chapter provides the conclusions for the work conducted in the thesis. It also recommends future works that could be taken forward based on the findings of this research.

Appendix A: Supplementary Information 1

Additional graphs and program code for Chapter 5 are presented

Appendix B: Supplementary Information 2

Additional graphs, EDX spectra and program code for Chapter 7 are presented

Appendix C: Theory

The fundamental principles of CO₂ electrochemical reduction are explored in this Appendix with an overview of the underlying mechanisms and key concepts involved in the electrochemical conversion of CO₂ into value-added products. The discussion explores the various pathways and intermediates involved in CO₂ reduction, highlighting the importance of catalyst materials in controlling reaction selectivity and efficiency. It considers the role of electrode materials, electrolytes, and reaction conditions in influencing the performance of CO₂ electrochemical systems.

1.4 Thesis Aims

The overall objective of this thesis is to develop the designs of CO₂ electrolyzers and examine ways of integrating electrocatalyst. This objective was divided into three main aims:

Firstly to design, develop, and characterise an electrochemical cell which can be operated for CO₂ conversion over a range of applied potentials and operating parameters.

Secondly to characterise the designed cell, minimising the electrical losses.

Finally, to integrate novel additive-modified copper foams as CO₂ electrocatalysts to enhance C₂ product selectivity.

Chapter 2

Literature review

2.1 Cell Classification

There are two cell main cell design styles, static (or contained) cells and flow cells. Static cells have all the electrolyte and system components contained within the reaction chamber as seen in Figure 2.1 from Billy *et al.* [57].

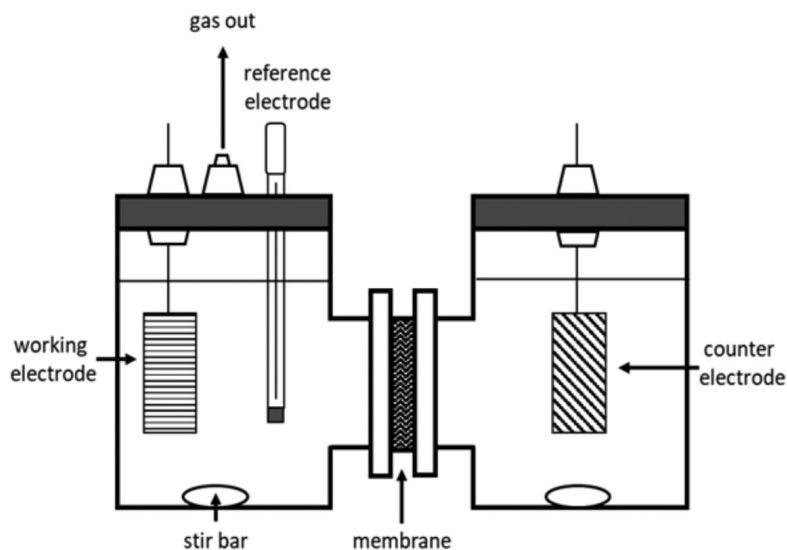


FIGURE 2.1: Reproduced with permission from Billy *et al.* [57]: Schematic drawing of a typical H-cell.

Conversely the flow cell designs require a supporting system of pumps and reservoirs to allow the cell to function, an example of which is shown in Figure 2.2.

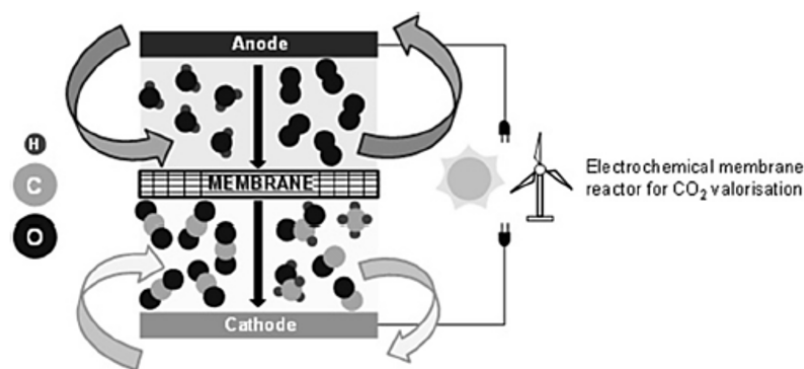


FIGURE 2.2: Reproduced with permission from Garcia *et al.* [58]: Schematic drawing of a typical generalised flow cell.

2.1.1 H-Cells

H - Cells have a much simpler design style than flow cells; all of the electrolyte is contained within the anodic and cathodic compartments, there can be movement of the electrolyte through mixing, and gas is usually bubbled directly into the cathodic compartment of the cell. This makes the cells often cheaper to construct (or purchase) than flow cells, for the same capacity, although the streamlined design often makes them un-modifiable.

2.1.2 Flow Cells

Garcia *et al.* [58] presented comprehensive analysis of electrocatalysis cell, and their configurations, that have been published in recent literature. Figure 2.2 shows the operating principles of flow cells, with electrolyte circulating through the anodic and cathodic chambers, regulating the electrolyte as well as maintaining a constant supply of reactants and efficient removal of products.

The main limiting factor in electrocatalytic cells is the mass transport across the membrane and the reaction medium [59]. In order to improve the mass transport in the cell, the membrane can be mounted to one or both electrodes forming a

'coupled electrode' and a Membrane Electrode Assembly (MEA) respectively, as seen in Figure 2.3.

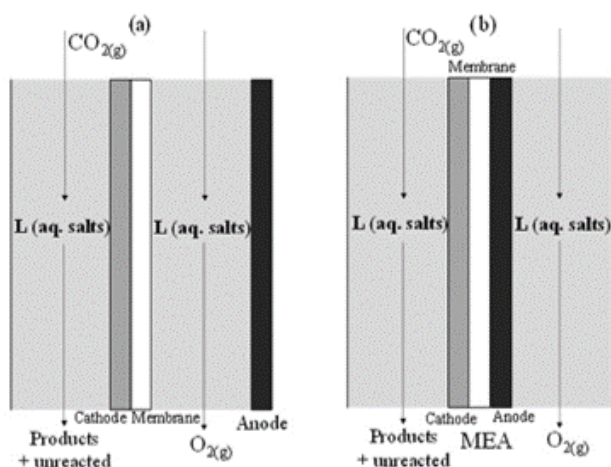


FIGURE 2.3: Reproduced with permission from Garcia *et al.* [58]: Schematic drawing of a coupled electrode (a) and a MEA (b) flow cell.

Garcia *et al.* [58] reported two different porous electrode configurations (Figure 2.3), classified by the location of the ion exchange membrane, relative to the porous electrode. Figure 2.3(a) shows a cathodic coupled membrane configuration, whilst (b) shows a MEA, where both electrodes are coupled to the membrane, minimising the electrode separation. This configuration enhances the transport of species between the electrodes

However, the electrodes required for these cells are more complex and expensive to produce, as they need to be porous, allowing reactants through the electrodes, from the bulk electrolyte to reaction site, and the products to pass through in the other direction. These porous electrodes have been developed further into 3 phase cells, where the issues of low CO_2 solubility in water can be avoided and the effects of the HER can be greatly reduced. Work into GDEs development converting CO_2 directly in the gas phase has become much more active recently.

These GDEs can also be configured in different ways within the cell, as seen in Figure 2.4.

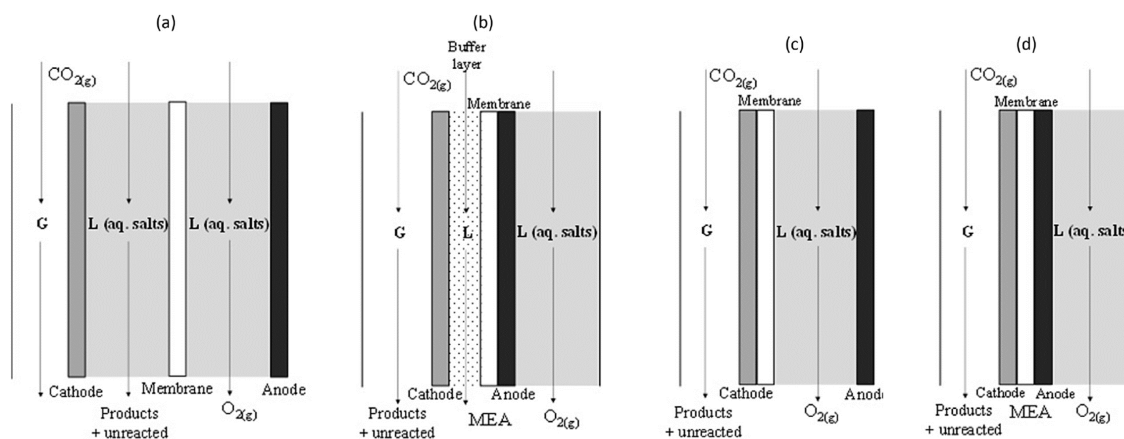


FIGURE 2.4: Reproduced with permission from Garcia *et al.* [58]: Schematic drawing of flow cell configurations with GDEs.

Figure 2.4 a, shows the most basic form of a GDE cell. The GDE is between the gas stream and the catholyte, separating both phases. Alternatively, the catholyte can be replaced by a pH-buffer layer (aqueous salt solution), most commonly between the cathode and the membrane (Figure 2.4 b). This configuration permits the transport of ionic species (e.g. H^+) by using different aqueous salts such as KHCO_3 .

Figure 2.4 c and d present cell configurations for the reduction of CO_2 in gas phase; c contains a porous cathode coupled to the membrane, with the anolyte solution between the anode and membrane.

In the second configuration 2.4d, the electrodes are sandwiched together with the membrane (MEA) facilitating the transport of ionic species, which may be beneficial for an effective valorisation of CO_2 into more reduced products such as CH_4 and C_2H_4 .

2.2 Electrodes

CO₂ is a stable molecule, meaning that the oxygen atoms require a comparatively large amount of energy to overcome the bond with the carbon atom. As such catalysts are required to reduce activation energy for the majority of reactions to occur. Nitopi *et al.* [60] reported on works for the selectivity of CO₂ products on different metal electrodes with only Cu showing selectivity for C₂ products. Due to this unique property, Cu is an important CO₂ reduction catalyst, with its utilisation being the only way to reduce CO₂ for appreciable quantities of carbon monoxide (CO) and formate [61–63].

Bagger *et al.* [64] grouped the metals electrodes according to their major product of CO₂ electrolysis: H₂, CO, formic acid and beyond CO* (hydrocarbons or alcohols). Figure 2.5 shows the different metals and Bagger's grouping as a plot of hydrogen binding energy (ΔE_{co^*}) versus carbon monoxide binding energy (ΔE_{H^*}). For the red group CO* is absorbed on the electrodes surface so strongly that it is unable to react and poisons the electrode for CO₂ catalysis, however this also makes these metals highly selective for hydrogen evolution at the electrodes surface, hence the H₂ classification. Conversely for the Yellow group of metals so little H* is bonded to the electrode surface that only formate production is possible, as there is insufficient H* to form a water molecule. The Blue group of metals a small amount of H* available and as such CO can be produced at the electrode surface. Copper sits in its own group, where there is sufficient H* and CO* bonded to the electrode surface at the right bond strength meaning products that use CO as a intermediate, such as ethylene, can be generated (as discussed in section C.2.1).

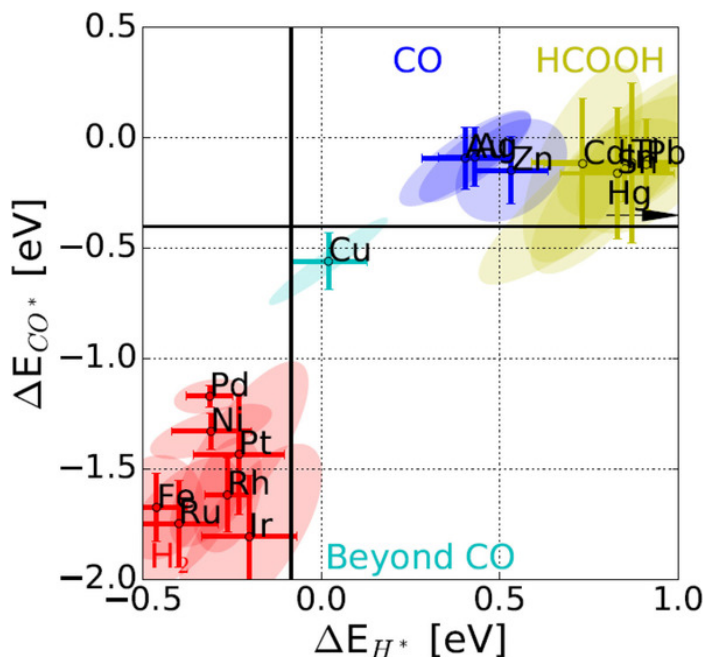


FIGURE 2.5: Reproduced with permission from Bagger *et al.*[64]: CO₂ reduction classification for metals by primary product group.

Therefore, the use of Cu as an electrocatalyst for CO₂ electrocatalysis has been widely reported on several different electrode surfaces / structures: solid copper surfaced electrodes [65–67], copper foils [60, 68–70], copper nanoparticles [71–73], copper nanocrystals [74–77], copper nanowires[78–80], and copper metal–organic framework (MOF) [81–83]. These copper electrodes are known to be sensitive to contaminants in the electrolyte, and Nitopi *et al.* [60] discussed how this ‘deactivation’ of the copper electrode can be attributed to three factors; “poisoning by impurities from the experimental setup, poisoning of the surface with reaction intermediates, and/or restructuring of the surface under reaction conditions.” The electrodes often show decay in their selectivity over time, which is attributed to deposition of metal contaminants from the electrolyte [84–87]. In order to prevent this, extensive purification of both the electrode surface and electrolyte is required before electrocatalysis can be conducted, greatly increasing the cost and time required for preparation.

Notably copper foams have shown resistance to contaminants, remaining active

without electropolishing or scavenging the electrolyte [87, 88]. The deposition of metal foams has been previously reported and is discussed further in Chapter 7.

2.3 Electrolyte Transport

In order for a fluid to move against gravity a force must be applied to it. Pipes or tubing is the most effective way of directing the flow of a fluid with pumps moving fluids from an area of low pressure to an area of high pressure, where the effect of gravity can be overcome.

Pumps can be classified into two different categories, Dynamic (Centrifugal) and Displacement as seen in Figure 2.6.

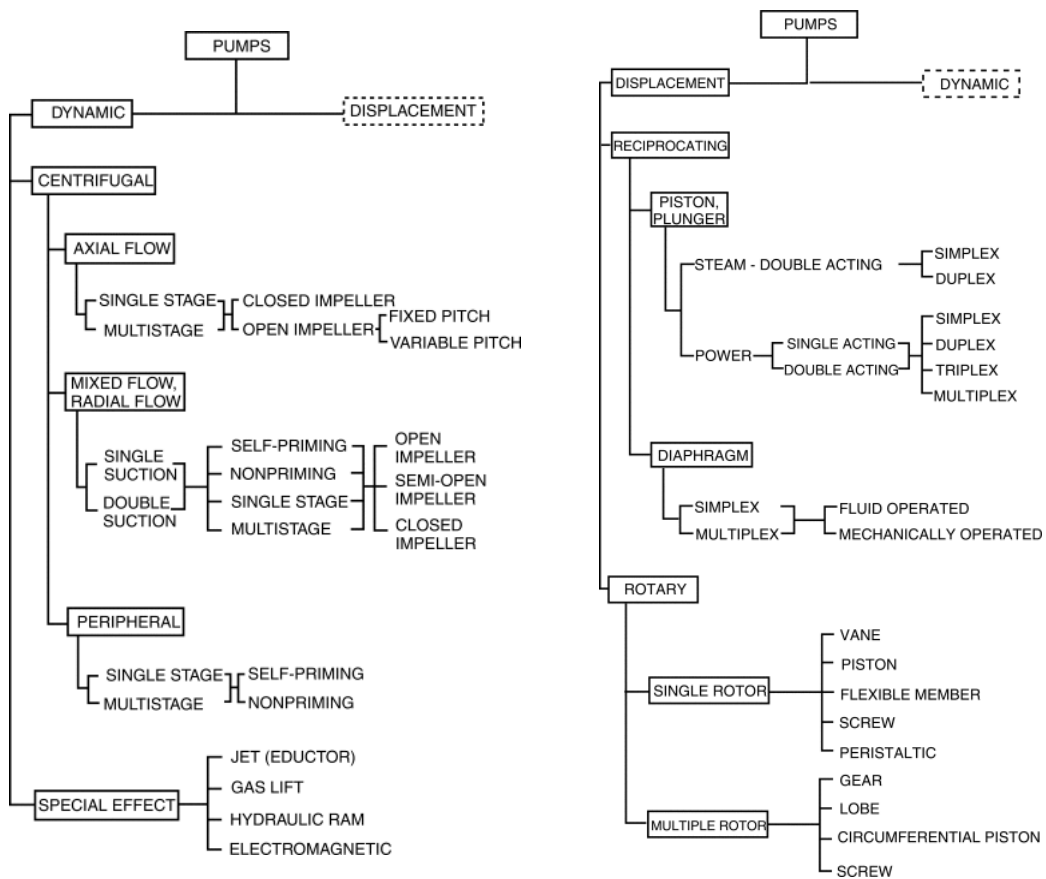


FIGURE 2.6: Reproduced from Krutzsch *et al.* [89]: The classification of pumps, Dynamic and Displacement.

Dynamic pumps use centrifugal force to generate velocity in the liquid, this is then converted to pressure. As the kinetic energy decreases the pressure increases. This difference in pressure drives the fluid through the system. A dynamic pump contains a rotating impeller which generates a vacuum that moves the fluid. The impeller's housing is designed to reduce pressure at the inlet, with the created velocity driving the fluid to the outside of the pump's housing, where the pressure increases generating an output. These are the most common type of pump that can transfer fluid of low viscosity at a high flow rate. Also, they are low-pressure installations making them perfect for applications that require pumps to deal with large volumes. Overall, dynamic pumps have a simple design and fewer moving parts, which result in lower maintenance requirements and costs, making them best suited for continuous operation.

In contrast, a positive displacement pump moves a set volume of liquid at a time. Pressure is created as the fluid is forced through the pump and then discharged, with displacement pumps converting energy directly into pressure. A volume within the pump is opened to the low pressure side and fluid flows in, the chamber is then sealed, and then opened to the high pressure side where the fluid is mechanically forced from the chamber into the high pressure side, completing the cycle. Positive displacement pumps use various mechanisms such as; the reciprocating motion of pistons, plungers, or diaphragms to move the fluid, but are all based on the same basic principle and suffer from the same drawback of producing a pulsated flow.

Positive displacement pumps have a complex design and are often selected for their ability to handle high viscosity fluid at high pressure. They can also handle relatively low flow rates as their efficiency is not affected by inlet or output pressure. They can therefore operate in conditions or ranges where dynamic pumps may fail. They can run at any point on their curve and can be used in suction mode, whilst handling variations in pressure, flow, and viscosity.

2.3.1 Effect of Gas Bubbles

The effect of electrolytic gas bubbles on the cell performance was investigated by Zeng and Zhang who modelled the bubble formation on a metal electrode in a stagnant electrolyte, showing the critical diameter of bubble detachment to be a function of buoyancy, expansion force and interfacial tension force, and electrolyte concentration to have a key effect [90]. With electrolyte circulation, the additional forces on the gas bubble cause early detachment of the bubbles, and Zeng and Zhang demonstrate a small reduction in the cell voltage when flowing electrolyte is used; attributed to early detachment of the bubbles. The bulk of the resistance was still present and was attributed to the bubble curtain between the two electrodes [90].

Bongenaar-Schlenter *et al.* showed that the electrolyte flow rate reduces the cell resistance in a finite gap cell, with large reductions in cell voltage reported at high current densities ($> 500 \text{ mA} \cdot \text{cm}^{-2}$), suggesting that the void fraction in the inter-electrode gap was the key factor, and that the effects from the bubble curtain suggested by Zhang could be mitigated [91].

2.4 Technology Gaps

Pletcher *et al.* [92] shows that the "impact that the change from beaker cells to flow electrolysis cells could have on the reputation of organic electrosynthesis in the laboratory." suggesting that flow cells are the future of electro-chemistry. They also highlighted several key parameters to be examined on each flow cell; "Operated with suitable control parameters (cell current, flow rate, reactant concentration, medium), all flow electrolysis offers the possibility of higher selectivity and productivity than can be achieved with beaker cells." [92] These will need to be examined on any cell constructed.

This thesis aims to design a cell that can be utilised to examine the effect of the control parameters highlighted by Pletcher *et al.* and refined into a optimised design which can be used to integrate novel electro-catalysts for C₂ products. This will act an initial stepping stone, moving from lab based research towards a practical commercial scale operation, buy examining the difficulties of CO₂ electrolyser scale-up, not only in electrode size but also in transition form short life H-Cells to longer duration capable Flow cells.

Chapter 3

Methods & Materials

3.1 Materials

Cell Construction

Clear acrylic (Polymer Plastics Company LC) in 2 mm, 3 mm and 5 mm thicknesses, was used for the construction of the cell. It was chosen as it was transparent and chemically inert to the potassium bicarbonate electrolyte. The sheets were cut to the required shape, specified by the cell design, by using the techniques listed in section 3.6.

6mm OD Acrylic tubes (The Plastic Shop, UK) were mounted to the acrylic end-plates using Tensol 12, (Sheet Plastics, UK) to chemically bind the two acrylic parts, to create the flow port in and out of the cell.

Silicone rubber sheets, 30 Shore, 1 mm thickness (Seals & gaskets LTD), were used as gaskets between the acrylic sheets in order to prevent leaks.

M6 threaded stainless steel rods were inserted through holes in the plates and used to align the cell plates and hold them together using washers and wing-nuts. Wing-nuts were used in regular nut to form a locking nut on one end of the threaded rods, this made handling during assembly of the cell easier as it only required one spanner to tighten.

Electrode Preparation

A 20mm x 10mm rectangle was cut from 2mm Natural Copper Sheet, grade C101 (99.90%, Metaloffcuts, UK) and embedded into the acrylic sheet 'holder' from the relevant design, with Araldite epoxy resin (Huntsman Advanced Materials, Switzerland). A 3mm diameter wire was soldered on using lead-free solder with flux to ensure a clean and conductive connection to the copper plate. The electrode was then mechanically polished utilising alumina slurry up to 0.3 μm , followed by rinsing and ultra-sonicating in deionized water for 1 min.

Copper Foam Preparation

The preparation was adapted from previously published work [93]. A copper foam was electro-deposited onto the copper plate by submerging in 0.2 M of CuSO_4 , 1.5 M of $\text{H}_2\text{SO}_{4(aq)}$ and 0.01 M of applicable modifier (See table 7.1), then a fixed cathodic current of 3 A/cm^2 was applied for 45 seconds. The electro deposited foams were submerged in deionized water for 5 mins to remove traces of electrodeposition solution before being assembled into the cell.

The rinsed foams were then assembled into the MK3 cell without the GDE modification (Section 4.4.3). The electrolyte solution was prepared by saturating a 0.1 M KHCO_3 solution with CO_2 , bubbling at 40 mL/min for 20 mins prior to use with the pH of the solution measured at 6.8. 150 ml of 0.1 M KHCO_3 was added to the cathodic and anodic side of the system. The gaseous product were measured in the syringe and gas trap 1 minute after the end of the electrolysis.

System Assembly

4mm internal-diameter polyurethane piping (item CPUM600251, Air Controls and Compressors Ltd, UK) was used to connect the pumps and reservoirs to the cell to the cell. Pipe segments were joined using John Guest Metric Plastic Push-In Fittings (Air Controls and Compressors Ltd).

The pump used for this experiment was a purpose-built peristaltic pump supplied by Welco, Model WP10-P1/8JD4-WM4-CP. A peristaltic pump was chosen, as no parts can contaminate the electrolyte.

The electrolyte reservoirs were constructed from 40 mm OD acrylic tubes (The Plastic Shop, UK), with a disc laser cut from the 5 mm acrylic sheet, chemically bonded (Tensol 12) to one end. A hole was drilled into the wall and base of the reservoir through which John Guest Metric Plastic Push-In Fittings were mounted using Araldite epoxy to create connectors for the tubing.

Chemicals

The chemicals used in the experiments are listed below and all reagents were used without further purification.

- Potassium bicarbonate (99.5%, Sigma Aldrich).
- Sodium hydroxide (99.5%, Sigma Aldrich).
- Copper sulphate pentahydrate (99.9%, Sigma Aldrich)
- Sulphuric acid (95–98%, Sigma Aldrich).
- Argon gas (99.998%, BOC, Industrial Gases, UK).
- Carbon dioxide gas (99.995%, BOC).
- L-Lysine Hydrate (Merck Life Science UK Limited(282677-25G)).
- D-Lysine (Merck Life Science UK Limited (L8021-1G)).
- Poly(acrylic acid sodium salt) (Merck Life Science UK Limited (477013-100G)).
- Poly(allylamine) solution (Merck Life Science UK Limited (479136-1G)).
- Poly(acrylamide) (Fisher Scientific Ltd (10675432)).
- Poly-D-Lysine (Fisher Scientific Ltd (16021412)).

- Deionized water with 15 MΩ.cm resistance from Merck Elix type 2 water purification system.

Membranes

10 micron UHMW Polyethylene porous sheet (Scientific Commodities inc, USA), 50 micron UHMW Polyethylene porous sheet (Scientific Commodities inc, USA), 90 Micron Polypropylene/ UHMW Polyethylene blend porous sheet (Scientific Commodities inc, USA), were prepared as directed.

Nafion 212 (Sigma Aldrich) was prepared by soaking in Di water for 24 hours, and then KHCO₃ for 24h before usage.

3.2 Chronoamperometry

Ivium

Ivium-n-stat was used in a three-electrode setup with a leak-free reference electrode based on Ag/AgCl in 3.4 M KCl (+0.210 V vs SHE; Innovative Instruments Inc., USA), the counter electrode was a platinum mesh electrode (99.9% Goodfellow, UK). Potentials are converted to the reversible hydrogen electrode (RHE) scale using Equation 3.1.

$$E_{RHE}(V) = E_{Ag/AgCl(3.4M)}(V) + 0.210V + (0.059V \times pH) + iR_u \quad (3.1)$$

The pH of the catholyte was measured after pre electrolysis bubbling CO₂ but before starting electrocatalysis, and was found to be 6.8. For three electrode electrolysis experiments, the cell was filled with potassium bicarbonate electrolyte then CO₂ was flowed through the catholyte in the bubbling chamber at a constant rate of 40 mL/min during electrolysis using a mass flow controller GFCS-010058

(Cole-Parmer, USA). Gases were collected in the gas trap and injected in to the GC, (see section 3.4) of which 0.5 mL was analysed.

Tenma

Tenma 72-2930 single channel programmable DC power supply (Farnell, UK) was used for electrochemical measurements and electrolysis. This digital control programmable power supply has low noise and ripple with a load regulation of $\leq 0.01\% + 2\text{mV}$ (voltage), $\leq 0.1\% + 5\text{mA}$ (current) and line regulation of $\leq 0.01\% + 3\text{mV}$ (voltage), $\leq 0.1\% + 3\text{mA}$ (current). The setting accuracy ($25^{\circ}\text{C} \pm 5^{\circ}\text{C}$) is $\leq 0.5\% + 20\text{mV}$ (voltage), $\leq 0.5\% + 10\text{mA}$ (current). A two-electrode setup was used with a platinum mesh counter electrode.

The pH of the catholyte was measured after pre electrolysis bubbling CO_2 but before starting electrocatalysis, and was found to be 6.8 . For two electrode electrolysis experiments, the cell was filled with potassium bicarbonate electrolyte, CO_2 was bubbled through the catholyte in the bubbling chamber at a constant rate of 40 mL/min during electrolysis using a mass flow controller GFCS-010058 (Cole-Parmer, USA). Cathodic product gases were collected in the gas trap and injected into the GC (see section 3.4), of which 0.25 mL was analysed.

3.3 Electrode Characterisation

SEM Imaging and EDX

A Hitachi TM3030 Plus scanning electron microscope was used to image the materials with a standard setting of accelerating voltage of 15 kV.

Energy Dispersive X-ray Spectroscopy (EDX) was used for elemental analysis of samples using an Aztec EDX extension to the Hitachi SEM described above, with AztecOne software allowing for automatic peak detection.

3.4 Product Analysis

Gas Chromatography

Gaseous products were quantified using Agilent 7820A gas chromatograph (GC) (Agilent Technologies, UK) equipped with a thermal conductivity detector (TCD) and flame ionization detector (FID) coupled to a methanizer, with argon used as the carrier gas. The following gaseous products of CO₂ electrolysis were quantified: hydrogen, carbon monoxide, methane, ethylene and ethane as well as oxygen, nitrogen and carbon dioxide. The method was also able to quantify propane, butane, pentane and hexane but these peaks were not present or near the limits of detection. The GC had two columns; HP-PLOT Q which separates hydrocarbons and CO₂, followed by a HP-PLOT 5A (molecular sieve) column which separates other permanent gases. The columns were connected by valves which could be programmed to be run in series or bypass mode.

The sample peak areas were compared to lone pure gases (BOC, UK) for peak identification. Multiple point calibration was used to quantify product concentration, where the calibration gas (Calgaz, USA) was diluted into nitrogen at known ratios providing different known product gas concentrations, which were used to produce a calibration curve. The results were reported in parts per million (ppm).

It is important to consider the amount of product produced to the amount of charge used by the system, so as to make the data comparable to that reported in the literature. As discussed in section C.2.4, FE is the efficiency with which charge (electrons) is transferred into a given product, as such it is used to compare CO₂ electrocatalysis performance. Using the Ideal Gas Law, Equation C.36, the number of moles of product can be obtained from the ppm (from the GC), the total volume of product collected (experimental obtained), the temperature of the collected sample and the ideal gas constant. From the number of moles, FE can be calculated using Equation C.34.

NMR Analysis

^1H NMR spectra was recorded on a Bruker Avance III 500 MHz instrument, with water suppression. All chemical shifts are reported in ppm and coupling constants are reported in Hz. A DMSO standard was added to the NMR tube to make a 0.2 mM concentration. Peak areas of the liquid products were then integrated and compared to the standard to obtain concentrations.

pH Determination

A Lab pH Electrode LE438 was used with a Mettler-Toledo Five Go F2 portable meter to determine the pH of the electrolyte in the reservoirs. The probe was calibrated using three standard solutions: 1.68 pH, 7 pH, 10.01 pH (Methler-Toledo) under standard conditions. For data collection the probe was placed in the centre of the electrode reservoir, for at least 30 seconds, until the pH reading stabilised.

3.5 Data Analysis and Processing

Matlab

Matlab 2007 was used to write two programs for interpreting collected data:

- Code presented in Appendix [A](#) used to find average point of J/V curves.
- Code presented in Appendix [B](#) used to find total charged passed during electrolysis.

3.6 CAD CAM

Autodesk fusion 360 student was utilised for all cell designs, iterations and modifications. Autodesk CFD package was used for flow modelling.

Laser Cutting

Both the acrylic and silicone rubber were cut with a Trotec Speedy 3000 laser cutter, using 2D files created from the Autodesk models.

3.7 High Speed Imagery

A Photron Fastcam 1024-PCI was used to capture high speed imagery of the flow of the electrolyte in a simulated cathodic compartment. The cathodic plate was replaced with an end plate to make observation possible. The Nafion membrane (and supporting plate) was used, with the cathodic plate replacing the anodic side of the cell, to act as a positional reference for the camera. The anodic side was filled and then sealed to prevent any flow on the anodic side, and reduce membrane pulsation. This cell was illuminated by two PhotoSEL LES600 60 watt spotlights to ensure enough light for the high speed camera which operated with a 1024 x 1024 pixels resolution at 1000 fps.

The peristaltic pump drew the KHCO_3 electrolyte from a beaker and pushed it through the cell into a waste beaker, through the previously described 4 mm tubing. The cell configuration was an iteration of the MK 2 cell design 4.4.2, with the Nafion support plate included to prevent damage due to the lack of anodic circulation. It also provided the additional advantage of visually dividing the cell into even sections, enhancing the data that could be collected.

Black water-based ink was used to dye the electrolyte. The ink was slowly injected into the tubing between the pump and the cell, just before the cell inlet. Each of the flow plates was examined at a flow rate of 60mL/min, using distilled water as the circulated liquid. The recording was started as the pump was activated with the end point being when the cell was observed to be fully filled with ink. The pump was activated again, until all the ink in the tube had entered the cell. At this point the recording and the pump were started and stopped when

all the ink had left the cell. The footage was analysed frame by frame with the difference in time calculated from the number of frames in between the start and end point of each run.

3.8 Flow Rate Calibration

The rate at which the pumps rotate, and therefore pump the electrolyte, is determined by the voltage supplied to the pump's motor. In order to obtain a specific flow rate the pumps needed to be calibrated against applied voltage.

The pump was fed from a large beaker. The temperature of water supplied to the pump was recorded prior to each test. A short length of polyurethane piping fed the pump from the large beaker and drained it into a small beaker. The mass of the small beaker was recorded prior to the test.

A range of voltages were applied as shown in the graph below. At each voltage, the pump drained into the small beaker until the power supply was stopped. The duration of drainage and the mass of the filled beaker were recorded. The beaker was emptied, dried and mass recorded before the test was repeated. Figure 3.1 shows the calibrated values for flow rate for each potential applied to the pump.

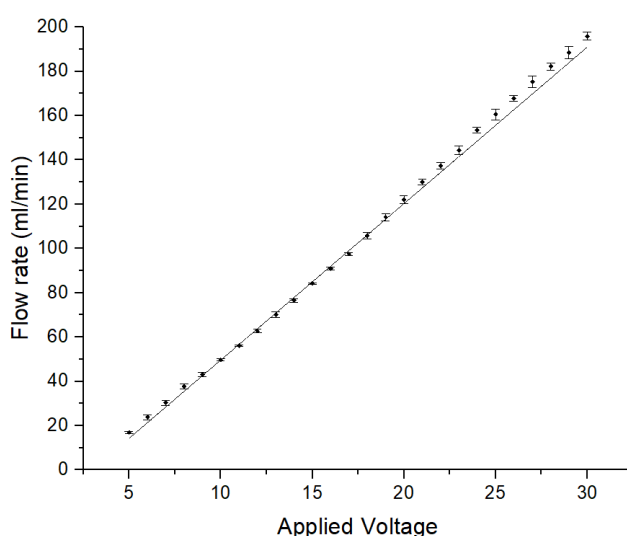


FIGURE 3.1: Flow calibrating graph for the Welco Peristaltic pumps at a given applied voltage.

3.9 Construction Techniques and Best Practices

From detailed analysis whilst in operation, several manufacturing techniques were developed to improve the cell design.

- Nafion sheets expand after being hydrated, however they cannot be bonded to another structure whilst wet. This meant that the Nafion bonded to the support plate was not stretched tight, but sagged due to expansion during hydration. To rectify this the Nafion was sandwiched between two gaskets rather than chemically bonded to a surface. This required an increased amount of Nafion, as well as the requirement for bolt holes to be cut into the Nafion after it had been hydrated.
- Laser cutting the acrylic sheets left fine ridges where the melted plastic had re-solidified on the flat surfaces of the plate. This affected the seal on the gaskets causing leaks. To solve this, all plates had to be washed in soapy water and trimmed with a scalpel or a file to produce a chamfered edge which reduced leaking. Multiple faster passes on the laser cutter, especially on the thicker 5mm acrylic sheets, was beneficial as it produced perpendicular edges and reduced burning/scorch marks on the surface of the acrylic.
- Use of a threaded bar enables undoing the bolt from either end making cell modification and disassembly easier. By counter tightening the two nuts, they act as stopper to each other, which can be easily removed and reused, unlike other products such as Nyloc nuts or welding a nut to the threading.
- Perry [94] stated that thumb screws and bolts fixed to the end plate were the best method of cell compression, with 'tools' rarely found in labs. Using a Torque wrench, despite the relatively low pressure applications, ensures even force distribution across all bolts, so that the gasket compression is equal reducing leaks. This force distribution increases the life of the bolts as

they are evenly loaded and deform equally over time, improving the life of the cell. These tools are relatively cheap and easy to procure.

- Removing corners and replacing with profiled edges, one curved the other chamfered, improved the ergonomics of the cell. It was much easier to manipulate by hand and prevents the cell being assembled in the wrong orientation when using directional components.

Chapter 4

Cell Design and Component Optimisation

4.1 Evaluation of Current Designs

To successfully design a working electrochemical cell, the cells reported in the literature need to be examined to evaluate their strengths and weaknesses informing the final design choices. This section considers several different cell designs progressing from a series of CO₂ electrolysis and water splitting cells that were physically available in the laboratory. This was accompanied by a review of the literature to establish the current state of the field of CO₂ electrocatalysis to further inform design and optimisation decisions and provide a point of comparison. A summary of all the cells is presented with the identified benefits and limitations of each. Where possible each cell is referred to by its commercial name and where this is not possible, the cell is named according to the lead author reporting its design.

4.1.1 Cells Examined in Practice

The best way to evaluate the strengths and weaknesses of a design is by physically working with it, allowing identification of which characteristics and limitations are more significant and which features are most needed. The cells listed in this section, are those that were physically available and in development within the laboratory, on which physical examination was feasible to undertake.

Syringe Cell (H-Cell)

The cells used by Ahn *et al.* [95] and Rudd *et al.* [93] were custom made H-cells, produced from medical 10 ml syringes with a 1 cm² Nafion window affixed with epoxy resin and 4 mL of 0.1 M KHCO₃ solution was used as the catholyte. The polypropylene body with a 1.6 cm diameter was cut to a 7 cm length, resulting in an internal cell volume of 10.2 cm³ with a 6.2 mL headspace. A schematic drawing of which is seen in Figure 4.1 (WE; Working electrode, RE; Reference electrode, CE; Counter electrode).

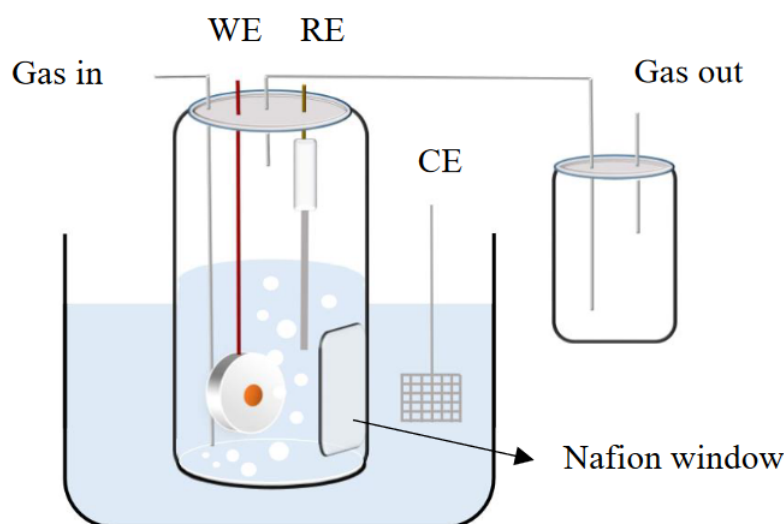


FIGURE 4.1: Schematic drawing of the custom built cell used Ahn *et al.* [95].

The top of the cell was sealed using a suba seal, through which the CO₂ was supplied by a needle positioned to bubble the CO₂ over the surface of the electrode.

The gas collection needle and the electrodes were also passed through this seal. This resulted in a crowded suba seal that was subject to increased gas leakage and occasional short circuits. The syringe was placed in a beaker containing 40 ml of anolyte where the counter electrode was positioned inline with the Nafion window. A silver/silver chloride reference electrode was used with a platinum mesh counter electrode and copper disk working electrode. This cell was relatively easy to set up and the inexpensive components used meant that it was cost effective to produce. As a consequence even though the cell's life was not very long, it could be easily repaired or replaced.

This benefit has to be balanced by four main challenges. Firstly, the electrode geometric surface area to catholyte solution volume ratio is comparatively high at $1.77 \text{ cm}^2/\text{mL}$, especially when considering that this is not a flow cell design and so the catholyte is not being replenished or circulated. This high value means that the liquid products are concentrated more easily, but the catholyte is depleted much faster. These factors meant that the cell life was approximately 2 hours which is insufficient for practical applications outside of finite lab testing. This time could be extended slightly by introducing stirring into the cell via a magnetic stirrer. Stirring the electrolyte means the bulk concentration is more evenly distributed throughout the cell, reducing the diffusion distance to the electrode surface. However, such stirring proved difficult to achieve due to the geometry of the bottom of the syringe causing the stirrer to often become dislodged. Additionally it also caused components such as the carefully positioned needle and electrode to move within the cell affecting its performance, as the CO_2 would no longer bubble consistently onto the electrode.

A further challenge was that the position and orientation of the electrodes were not fixed, meaning Electrochemical Impedance Spectroscopy (EIS) had to be conducted to compensate for the variation in electrode separation for each individual run of the experiment to produce comparable data. Whilst the EIS can effectively

measure the electrical resistance within the cell at a given point in time, the electrode was able to move during the experiments, especially when stirring was used. Both these factors meant that experimental preparation took much longer than anticipated and created experimental error.

The third issue was that the Nafion window often allowed the electrolyte to flow from one side to the other, after a couple of uses. Medical syringes are most commonly made from polypropylene, which is not recommended to be bonded by Araldite due to its inability to effectively bond with the surface of the polymer. The production of organic solvents within the catholyte during electrocatalysis, further reduces the strength of the Araldite's bond.

Finally this design suffers from dilution of the gaseous products produced during CO₂ reduction reactions. As the CO₂ was bubbled directly into the cathodic chamber, any gaseous products produced were greatly diluted in the flow of unreacted CO₂ collected by the exhaust needle within the cell. In a lab environment this dilution meant any product was harder to detect impacting the accuracy of results. The considerable air head, both in the syringe cell and the gaseous sample collection equipment, required large amounts of CO₂ to pure the system before each experimental run, further impacting product analysis. Overall, this cell was cost effective and easy to construct, but had several drawbacks as a result of the relative size of the components, poor product purity and instability rendering it less feasible for larger scale use.

Pine Research Cell (H-Cell)

Another H-cell that was physically examined for its ability to be utilised for CO₂ electrocatalysis is Pine Research's Low Volume Separated Cell. Esrafilzadeh *et al.* [96] used this cell to investigate the onset potential of the CO₂RR on a liquid metal electrocatalyst containing cerium nanoparticles. It is based on the classical H - Cell design with two glass cylinders connected through a horizontal tube

containing a salt bridge. The key variation in their design was the removal of the salt bridge leaving two separate L shaped cylinders, which were combined by sandwiching a membrane using a pinch clamp to hold the two halves together as shown in Figure 4.2.



FIGURE 4.2: Photograph of the Pine Research Low Volume Separated Cell [97].

The use of the mechanical bonding method (the metal clamp, seen in Figure 4.2) to hold the cell together, and hold the membrane in place, avoids the problem of chemical bond degradation and allows for components to be adjusted or replaced more easily. Ceramics, such as glass, are known for their high chemical resistance, low thermal and electrical conductivity, and high durability, making them an excellent material choice for electrocatalytic cells. Additionally the increase in neck width and increased half cell volume, up to 50 mL, allows for a larger electrode to be used of 6 mm diameter. This increased electrode size and electrolyte volume changes the geometric surface area to electrolyte volume ratio to $0.9 \text{ cm}^2/\text{mL}$, with much more electrolyte per cm^2 than the syringe cell. Experimentation again highlighted a number of challenges with this cell. Similar

to the Syringe cell, there is no electrolyte mixing mechanism or replenishment, however there is a much larger volume of electrolyte in the cell. The supporting feet on the bottom of the cell made magnetic stirring of the electrolyte difficult; stirring from the top was feasible but would result in losing a large amount of space in the already crowded gas tight seal and probably increase gas leaks.

Secondly, whilst glass is a strong durable material, it is not easily modifiable without specialist training and tools. The large electrode separation (6 cm) which increases the electrical resistance of the cell is difficult to adjust with limited options. It is also challenging to consistently position the plate electrodes, as they are suspended by their connecting wire from the seal. This cell is designed for cylinder electrodes that snugly fit through the supplied Low Volume Cap as seen in Figure 4.2.

The seal around the Nafion membrane is another weakness of this design as it often leaks because the electrolyte can be transported perpendicular to the main axis of the cell, through the membrane. Additionally the supplied clamp does not apply an evenly distributed force, allowing traditional leaks to also occur, on the open side of the clamp. This is due to the design of the clamp. Using a pinching mechanism to apply the force, means that it is applied in a 'V' Shape, where the clamp makes contact with the glass in an off centre position, tightly sealing the side at the point of the 'V', but applying much less force to the open side, where small leaks can occur, due to the decreased compression force.

Common with the syringe cell, an air head is formed when the cell is sealed. Whilst this can be removed through the Low Volume Cap using the supplied Purge Kit, it is difficult to do without changing the set electrolyte volume in each of the compartments. The sealing has to be done to one half of the cell and then the other, causing a pressure differential across the Nafion membrane, often deforming it and moving the electrodes. Also similar to the syringe cell, CO₂ has to be bubbled directly into the cathodic half cell, once again diluting the gaseous

products of the CO₂RR.

Whilst this cell improves on some aspects of the syringe cell discussed in section 4.1.1 such as the reliability and durability of the cell, there are several considerable negatives including the large electrode separation and limited variability.

Water Splitting Cells

Although water splitting cells are not specifically designed for CO₂ reduction, the practical analysis and examination of their development and refinement of the design over time is valuable, as well as begin the only flow cells that could be physically examined. The cells used by Phillips *et al.* [98] and Rearden *et al.* [99] are both developed from that used by Passas [100], so Passas's cell will be discussed in detail and the key modifications made in each subsequent stage are explored.

Passas' Flow Cell

The cell used by Passas [100] was made from acrylic sheets with outer dimensions of 100 mm x 100 mm and interior dimensions of 60 mm x 60 mm, or a 3600 mm² active electrode surface area (assuming perfectly smooth electrodes). A gas trap plate reduced the active surface area within the cell to 3300 mm². The electrodes were made from 0.9 mm thick medical grade stainless steel sheets, cut to the outer dimensions of the cell, with an additional 40 mm² square for connecting the electrode wires on the outside of the plate. Passas' cell can be seen in Figure 4.3.

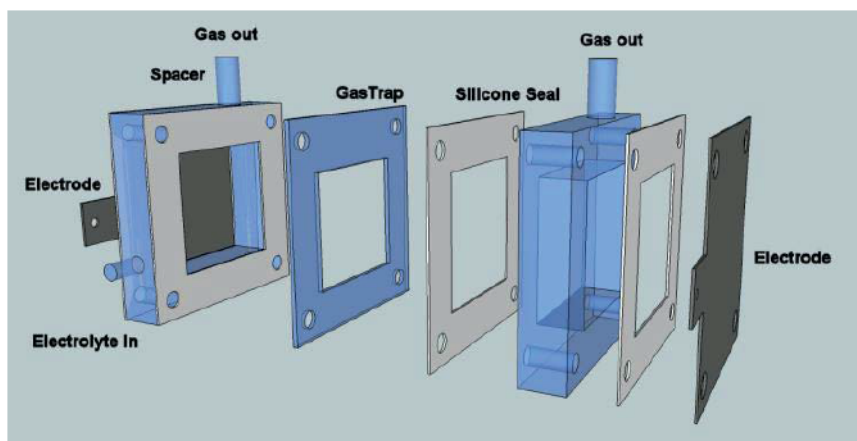


FIGURE 4.3: Reproduced from Passas *et al.* [100]: Components of the Passas cell design.

This design utilises multiple acrylic plates to vary the inside geometry of the cell, with 0.75 mm thick silicone rubber sheets used as gaskets to prevent leaks. Similar to the Pine Research cell, Passas' cell uses mechanical fastening to hold the cell together. These bolts are fastened through the outer walls of the cell, instead of a spherical clamp, providing a more evenly distributed clamping force.

Passas discussed the issue of a gas head building up within the cell which was released when it reached a critical mass. This created pressure differentials, reducing the cell's efficiency. Redesign of the plate in that particular section with a slope, effectively channelled the gas out of the cell.

Another feature of this design is the incorporation of expansion tanks outside of the cell. This removes the requirement to purge any gas head, forming in the cell, as they are displaced by the electrolyte held above the cell in the expansion tanks.

Phillips' Flow Cell

Phillips *et al.* [98] developed upon the cell used in Passas' work, reducing the resistance across the cell to the lowest possible value. The key design change was the conversion to a zero gap design, which reduced the electrode spacing

to the smallest distance possible, with only the membrane separating the electrodes. The electrodes were changed from metal plates to meshes inside the cell. These meshes allowed the produced bubbles to move through the electrode into the flow field plates, then flow out of the cell, whilst being replaced with fresh electrolyte. Additionally the Nylon bolts were replaced with steel, as they were unable to maintain the pressure required to seal the cell, causing leaks. Due to the electrodes and flow field plates being metal and electrically connected, the bolts had to be insulated to avoid shorting the cell.

Rearden's Flow Cell

Rearden *et al.* [99] investigated the cell's scalability towards a commercial product, also reducing the electrode spacing. Through modification of the electrolyte and bubble flow paths, cells could be stacked much closer together. As seen in Figure 4.5 the removal of the radial ports, in favour of axial ports, removes the minimum width restriction on the anodic and cathode chambers, maintaining as much of Phillips' zero gap work as possible. Figure 4.4 shows how multiple channels can be offset to prevent contamination whilst maintaining flow to all sections of the stack, and reducing leaks as much as possible.

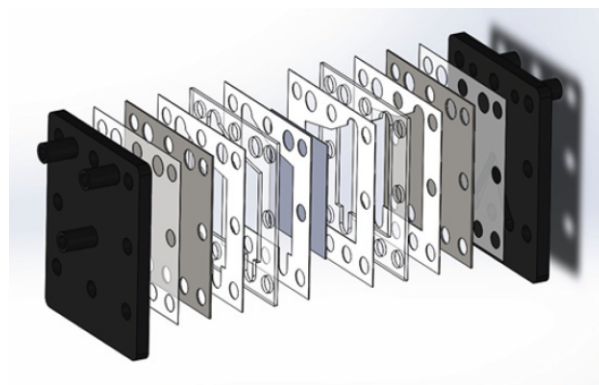


FIGURE 4.4: Reproduced from Rearden *et al.* [99](CC BY 4.0): Exploded view of Rearden's 2 mm cell.

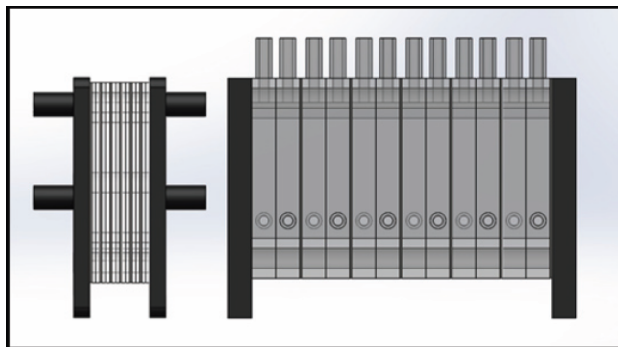


FIGURE 4.5: Reproduced from Rearden *et al.* [99](CC BY 4.0): Comparison of Rearden's six cell stacks (Right), with a 2 mm cells (left).

These water splitting cells are more modular than the cells previously used, utilising laser cut acrylic plates which are easy, quick and cheap to manufacture, making design refinement more cost effective. Additionally the redesigns result in alternate ways of supplying reactants and removing products, without issues such as creation of a gas head within the cell.

4.1.2 Cells Examined in the Literature

Although the best way to examine the functionality of a cell is through physical use of the cell, design considerations can be identified by examining the cells used in published works. Cell design choices detailed in papers by different authors from a range of institutes, show successful features that can be utilised as detailed below.

Billy's Flow Cell

Billy *et al.* [57] designed a cell to examine the effect of CO_2 supply into the cell. This varied the flow rate and concentration of the saturated electrolyte as well as varying the amount and size of the CO_2 bubbled into the cell. Similarly to the cells examined in section 4.1.1, they used an acrylic plate flow cell design, with

a Selemion anion exchange membrane and KHCO_3 electrolyte as represented in Figure 4.6.

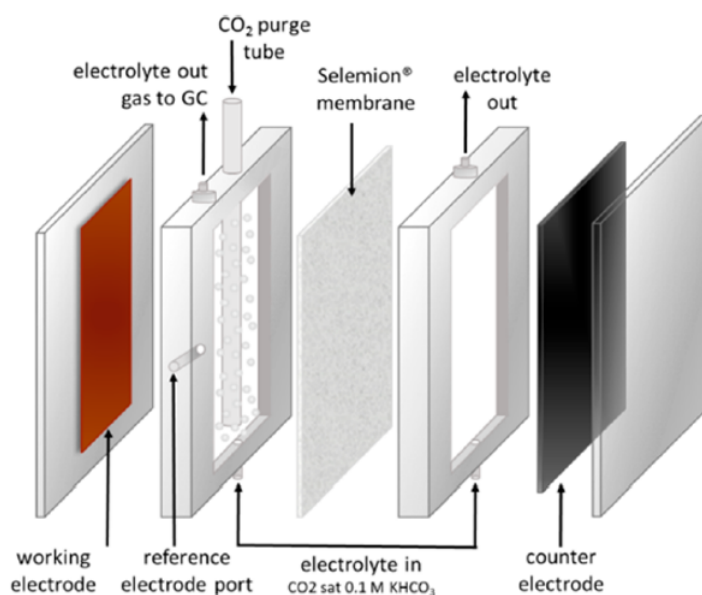


FIGURE 4.6: Reproduced with permission from Billy *et al.* [57]: Schematic of the electrochemical flow cell used by Billy in their CO_2 electroreduction experiments.

The electrode geometric surface area is reported as 26 cm^2 , with the cathodic compartment containing either 27.9 ml or 48.7 ml, depending on the flow plate used (either 1 cm or 1.75 cm) giving an electrode separation of either 2.4 cm or 3.2 cm. A 7 mm diameter glass gas-dispersion tube is used inside the cathodic compartment which limits the minimum electrode separation, however it does provide sufficient room for a reference electrode port in the plate.

Billy *et al.* [57] uses Viton rubber gaskets, which is a fluoroelastomer. This material is not suited for use with organic acids, as the reduction of CO_2 can produce carboxylic acid meaning these gaskets will perish with prolonged usage.

Jeanty's Flow Cell

Jeanty *et al.* [101] work explored the conversion of CO_2 to CO on silver gas diffusion electrode (GDE) as shown in Figure 4.7. This image demonstrates the Flow

By GDE cell design, where the CO_2 is introduced into the cell in gaseous form contra flowing with the electrolyte on the opposite side of the GDE.

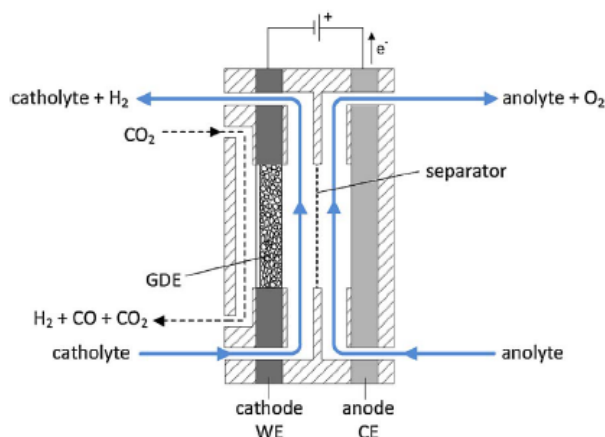


FIGURE 4.7: Reproduced with permission from Jeanty *et al.* [101]: Cross-sectional drawing of the cell used by Jeanty, Highlighting the 'Flow By' design.

This design is much larger than the previously examined CO_2 catalysis cells, with the active electrode surface area being 7.67 cm^2 . It has two membrane pumps to circulate the electrolyte through the cell and supporting containment. A gas separation tank is utilised on the output from the cathodic compartment to collect the gaseous products.

A key difference to other designs is that the anolyte and catholyte are not held separately, as seen in Figure 4.8. CO_2 is bubbled through the combined electrolyte reservoir to saturate both the catholyte and the anolyte before it is pumped back into the cell. The anodic product gases are also separated from the anolyte at this stage and removed from the system along with the excess CO_2 . This design is orientated towards commercial continuous operation, where the focus is achieving a stable galvanostatic operation, preferred by industrial applications, rather than focusing on the potential at the working electrode, as such there is no reference electrode in this design, which reduces set up and operating costs. Continuous

galvanostatic operation is preferred at the commercial scale as it greatly simplifies the system, which reduces down time and maintenance costs along with and overall improvement in efficiency.

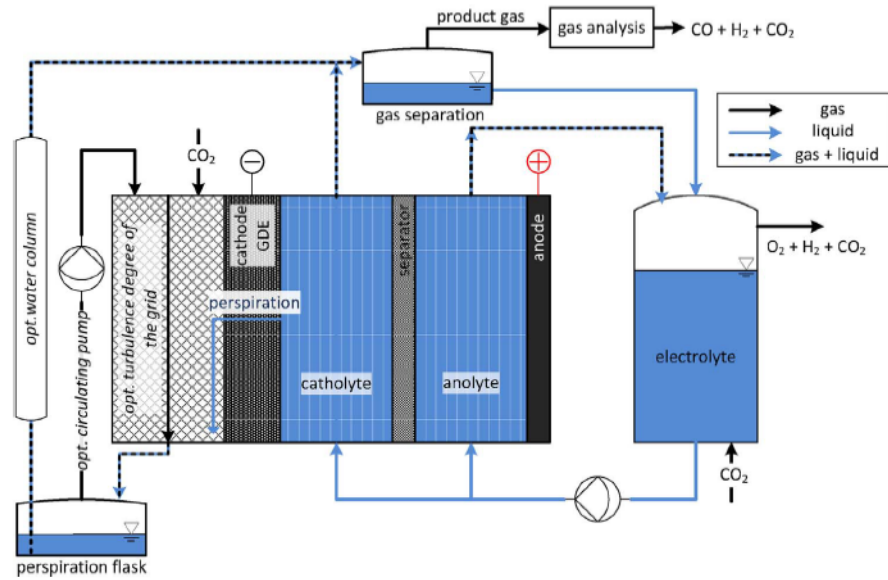


FIGURE 4.8: Reproduced with permission from Jeanty *et al.* [101]: Schematic of the flow cell and external system used by Jeanty, highlighting the combined reservoir design.

Jeanty *et al.* [101] also investigated the effects of turbulent and laminar flow by varying the geometry of the flow plate. The turbulent flow improved circulation and mixing in the cell whilst the laminar flow more efficiently removed bubbles from the cell, as shown in Figure 4.9. They developed several different flow field designs to change the turbulence in the flowing electrolyte: a promotes turbulent flow whilst b and c show various levels of lamella flow.

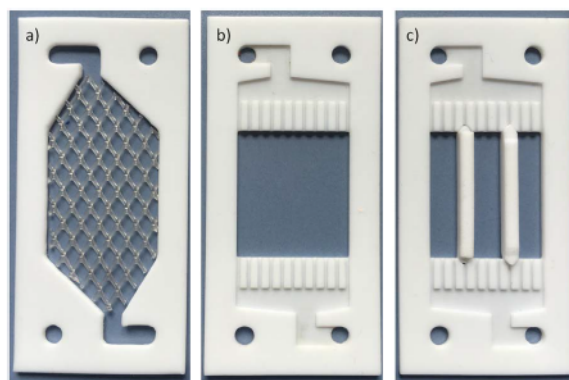


FIGURE 4.9: Reproduced with permission from Jeanty *et al.* [101]: Compartments of the cell used by Jeanty *et al.* showing the three flow plates: standard (a), modified (b) and modified with additional structures(c).

They identified a key issue with utilising GDEs was that droplets of electrolyte form on the gas side of the GDE, reducing the areas of the GDE that is exposed to the CO_2 , decreasing cell efficiency. Eventually these droplets collect and can flood the gas compartment of the cell so sufficient drainage needs to be considered with currently available GDEs or development of a GDE that is not susceptible to wetting.

Wu's Flow Cell

The third cell presented in this section, is the one utilised by Wu *et al.* [102] for CO production as outlined in Figure 4.10. This design utilises a gas diffusion layer (GDL) and a half catalyst-coated membrane (CCM), Pt/C spray coated Nafion, which were hot pressed together forming the anode with tin sprayed onto the outside of the GDL.

The use of the Sn GDL as the cathode in this cell removes the need for the aqueous catholyte to transport the CO_2 into the cell, greatly increasing the amount of CO_2 available at the electrode surface. As such, their design uses a very small amount of catholyte, 10 ml (circulated at 5ml/min), relative to the 4 cm² active surface

area of the cathode, with the cell run for 30 mins at a time. This circulating liquid-phase electrolyte buffer layer, between the Nafion membrane and Sn GDE, was found to significantly shift the selectivity toward formate formation. The low over-potentials reported were attributed to this feature of the cell, as the GDEs has a large number of triple-phase boundaries where CO_2 reduction can occur at lower over-potentials.

Wu *et al.*'s work shows that the continuous circulation of the electrolyte provided convective mixing which maintained adequate pH near the cathode surface, whilst the recirculation of the electrolyte was shown to be "a cost-effective method for the accumulation of liquid products" [102].

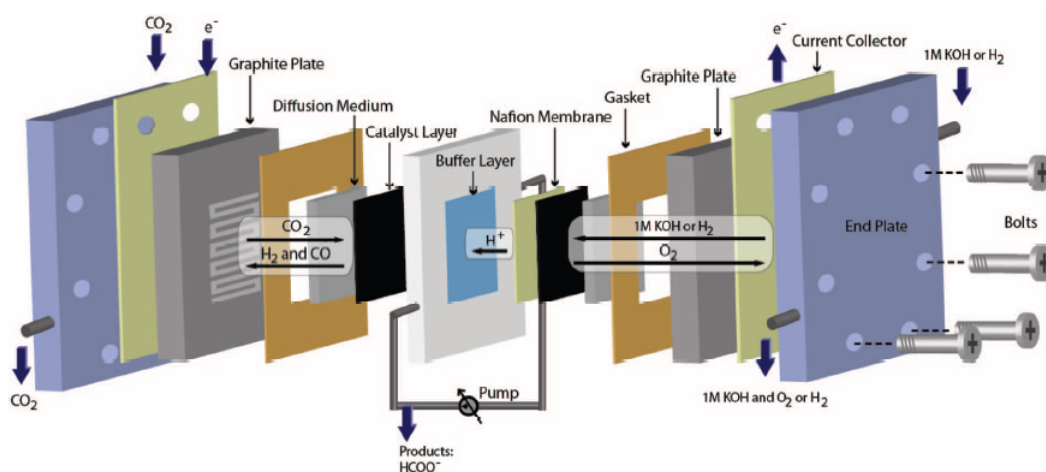


FIGURE 4.10: Reproduced with permission from Wu *et al.* [102]: An exploded drawing of the Wu electrochemical cell featuring a buffer layer of circulating liquid-phase electrolyte.

Figure 4.10 shows a schematic of the cell used in their works. It has a similar design to that seen in section 4.1.1, with the cell consisting of multiple plates, sandwiched between two thick end plates held together through the use of bolts. They also use graphite plates with serpentine channels to direct the flow of the CO_2 through the cathodic chamber of the cell, behind which gold-plated metal sheets acted as current collectors.

4.1.3 Cells Commercially Available

In this section two of the most reported commercially available cells are examined.

ICI FM01-LC (Flow Cell)

In the 1980s, a number of commercially available flow cells, using rectangular flow channels, were introduced for laboratory use. The most widely used cell was the FM01-LC electrolyser (FM01) [103] shown in Figure 4.11. The ICI (ICI-Chemicals and Polymers Ltd (now INEOS Chlor-Chemicals)) FM01 cell has been examined and utilised in several academic studies [92, 104–110]. Its 64 cm² electrode area cell is based on the FM 21-SP (21 dm²), a 2100 cm² cell used in the chlor-alkali industry, also developed by ICI.

Rivera *et al.* [105, 106] conducted detailed reviews of the flow cell and its versatility for multiple different usage scenarios including organic and inorganic electrosynthesis, metal ion removal, energy storage, environmental remediation and drinking water treatment. They highlight the avoidance of O ring seals, and the cell's ability to utilise different electrodes, separators (or ion exchange membranes) and turbulence electrodes in a chemically resistant package suitable for a wide range of electrolyte compositions and a wide temperature range.

Griffiths *et al.* [107] showed how the increase in electrolyte flow rate affected the current density in the FM01-LC cell. They examined the effect of the turbulence promoters in the cell on the pressure drop across the cell. Brown *et al.* [111] also investigated the effect of the turbulence promoters, but explored its effect on the current distribution across the electrode surface. More recently, computational flow modelling was used to rationalise this behaviour by Vazquez *et al.* [112].

Vazquez *et al.* [109, 113], as well as several others [114, 115], conducted CFD modelling on the FM01 cell. Analysis of the flow dispersion in the channel was

conducted through a mass transport study [109], with [113] including the effect of the manifolds.

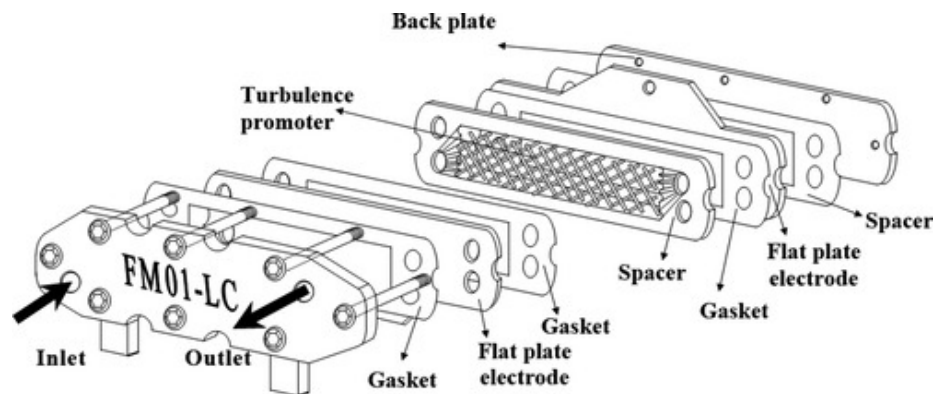


FIGURE 4.11: Reproduced with permission from Griffiths *et al.* [107]: Schematic drawing of the FM01-LC cell.

Figure 4.11 shows a schematic diagram of the FM01-LC cell [107]. The design is similar to those seen earlier with several plates and gaskets sandwiched between two end plates utilising bolts to apply an even compressive force. A key difference in this design is the turbulence promoting meshes in the flow plates. Once again the sandwiched plate design is shown to be highly modular and easy to modify, with the FM01-LC cell allowing for multiple electrode stacks to be utilised within the cell. One key consideration is the long rectangular profile of the cell; whilst this provides an even flow distribution, the electrolyte has a relatively large distance between entering and leaving the cell, meaning a high flow rate is required to maintain a low cell refresh time.

C-Flow Cell

A more recently developed cell is the C-Flow Lab 5x5 laboratory-scale flow cell (C-Flow cell) lab which has been analysed in several works [94, 116–119]. Perry *et al.* [94] highlighted the practical features of the cell; the thumb screws were found to be convenient and easy to use, along with the threaded section attached to one of the end plates as highlighted in Figure 4.12.

The cell is relatively heavy at 5.5 Kg [119] as a result of the 304 Stainless steel End plates, rather than the acrylic ones previously used. The cell has a projected electrode area of 25 cm², using a 62 mm x 62 mm electrode for an active geometric area of 50 mm x 50 mm, with the outer 6 mm being used to mount the electrode into the cell through compressive force applied to the electrodes through the brass current collectors by the end plates. Unlike the FM01-LC cell, the electrolyte ports are mounted radially to the flow distributions frames (see 5 in Figure 4.12), rather than axially through the end plates.

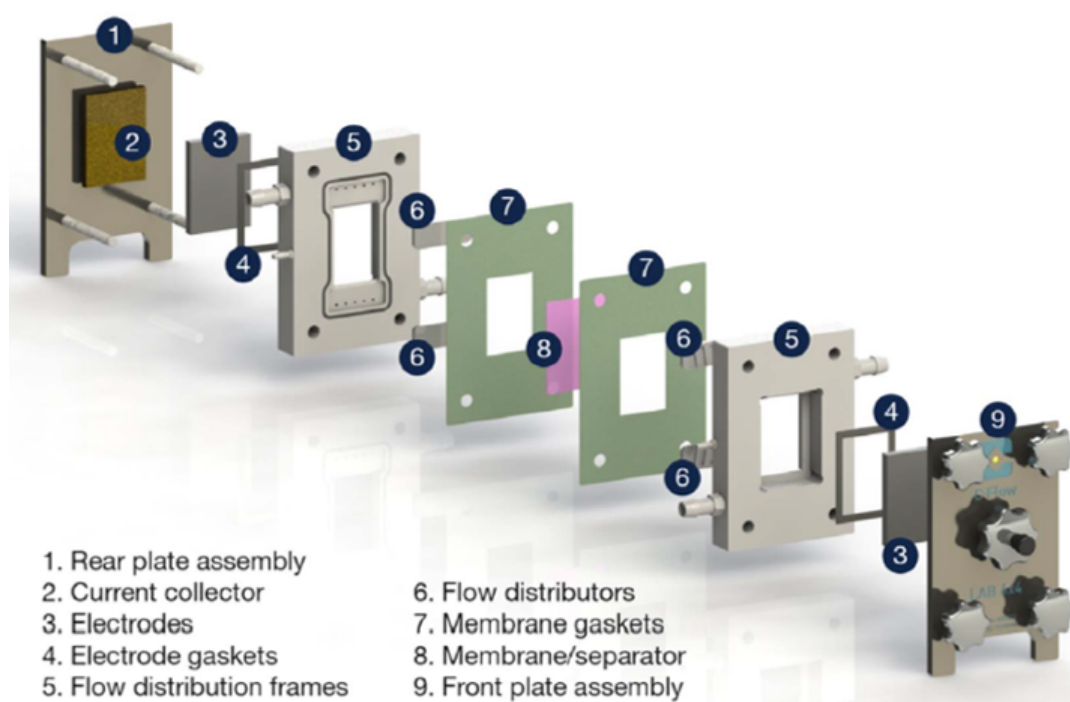


FIGURE 4.12: The C-Flow Lab 5x5 laboratory-scale flow cell [117].

In this cell the electrode separation is fixed due to the thickness of the flow distribution frames, along with the electrode geometry as it has to fill the 62 mm x 62 mm in the flow distribution frames.

4.1.4 Analysis of Reviewed Cells and Design Limitations

The cells examined vary in multiple ways, with each one designed for a specific task or factor. In all cases, the working electrode remains constant (copper), as well as the counter electrode (platinum). Copper has been shown to be the optimum material for C₂ products and allows further utilisation of the previously investigated copper foams.

Variation in the type of electrolyte used would make the cell difficult to compare with previous designs, however different concentrations should be explored with the Nafion membrane retained.

A key limitation on the size of the cell is the j requirements for copper foam deposition, which requires 3 A/cm². This limits the maximum possible size of the electrode to 1 cm² with the available equipment (Ivium and CHI used by Rudd *et al.* [93]). Multiple electrodes could be utilised as long as an area less than 13 cm² can be grown at a given time. Additionally the copper foams' growth means complex surfaces for flow paths, such as those seen in Figure 8 of Perry *et al.* [94] and Figures 3 and 4 of Jeanty *et al.* [101], are not possible as the foams would either block the paths, or be broken off from the electrode surface, by the concentrated electrolyte flow.

Several of the cells examined used ceramic materials such as glass. Whilst this is a durable material with great chemical resistance, it is not easily manufactured or modified, without specialist training and tools. As a result, the changes required to optimise the electrode would be difficult and expensive to conduct, making ceramics an unsuitable material to use during development though conversely, the high chemical and electrical resistance may make it an effective material for a fully developed end product.

The most common form of cell analysed in the literature for intermediate scale usage is flow style designs. They can be relatively easily scaled to work with any

size electrode and electrolyte volume. Additionally, the sections of the cell can be easily split into individual plates, which are comparatively easy and cheap to make. A further advantage is that this design has been shown to effectively regulate temperature, pH and mass transport inside the cell.

The syringe cell (4.1.1) and the pine research cell (4.1.1) were both H-cells, which both had significant limitations on the operating conditions, mainly their limited operating life time due fixed to the volume of static electrolyte. However the physically examined water splitting cells (section 4.1.1) could potentially operate indefinitely.

From the reviewed literature, the best design style is a zero gap cell configuration, as it reduces the electrode separation in the cell, therefore reducing the ohmic resistance within the cell. Unfortunately, zero gap cells are not suitable for use with the examined metal foams, as they are relatively unstable and would deform under hot pressing, although a partial zero gap cell or a half catalyst-coated membrane (CCM) could be used as an anode, as seen in Wu *et al.* [102].

Radially mounted electrolyte ports are quite common in the examined cells, however this dictates the minimum width a plate can be due to port sizing and required support. This means that their large plates form large compartments or complex plate interiors that are slower, more complex and expensive to manufacture, making them inappropriate for this stage in the design, despite their advantage of a simplified flow path. Additionally, as highlighted by Wu *et al.* [116] radial ports, especially those with manifolds, do not provide an even flow as the pressure gradient of the electrolyte changes across the linear manifold.

Product purity is also a key issue as many of the examined cells bubble CO₂ directly into the cell, which dilutes the concentration of the gaseous products in the cathodic compartment. Some designs have adapted GDEs in order to create a plentiful supply of CO₂ at the electrode surface whilst maintaining product purity.

Summary

In summary the best design style for further development is the Flow cell design, due to its longer operating lifetime. There is a clear trend in Flow cell design, where multiple plates are used to build up the relatively complex internal geometry required for cell operation.

The most practical design would use the acrylic plates from the examined water splitting cells (4.1.1) along with the end mounted electrolyte ports, seen in the designs used by Jeanty (4.1.2), Wu (4.1.2) and the FM01-LC (4.1.3). The C-Flow lab (4.1.3) cell presents a relatively simple starting configuration and geometry with which to start the design iterations.

4.2 Design Parameters and Specification

As observed by other researchers [120, 121], a wide range of conditions have an impact on the electrochemical reduction of CO₂, making it difficult to compare data and determine the most practical cell design for each application. In order to develop an effective cell it is necessary to identify the key functionality and parameters for the operation of the cell.

This project is based on work of Sunyik and Rudd [95] [93], with the aim of developing a higher capacity electrolysis cell. Therefore, there is a need to keep certain conditions constant; electrode materials and electrolyte used, which results in limitations in the cell and systems' design. Additionally, Walsh *et al.* [110] discuss several criteria for cell design:

- Cost effective capital and running costs - utilise components, applied cell potential difference and cell resistance in a manner that make running the cell financially viable.

- Convenience and reliability of design - making installation, operation and maintenance as simple as possible.
- Supporting equipment for controlling and monitoring of the cell - such as power supply, electrolyte refreshment and storage.
- Simple but versatile design - applicable to, and usable by, multiple users on multiple projects.
- Modular design - can be easily scaled up, in either size or number of cells, in the reactor.

There are seven parameters that need to be examined in the cell and considered during the design phase to ensure the cell is suitable for the desired testing. The cell should:

- Be easily modifiable, so that components can be modified easily and cost effectively.
- Maintain a constant volume of unreacted electrolyte.
- Be easy to install.
- Be suitable for 'foams' to be used, limited at 3 A/cm².
- Produce as pure product as possible, minimising CO₂ in the product stream.
- Have a high electrical conductivity.
- Allow an electrode size between 2 cm² and 16 cm²

As well as considering the cell requirements, a supporting system is required to contain the products and reactants, as well as transporting them to and from the cell. This system needs to be able to:

- Hold up 150 mL of electrolyte per half cell.
- Provide uncontaminated gaseous product collection.

- Circulate the electrolyte, enabling the cell to operate for long durations.

4.3 Custom System Design

As identified above, a flow cell requires an external system to operate. This section highlights the design and components used for that system. Several minor changes were made to the supporting system over the course of cell design iterations. The final custom designed support system used for all experiments, unless specified otherwise, is presented in Figure 4.13.

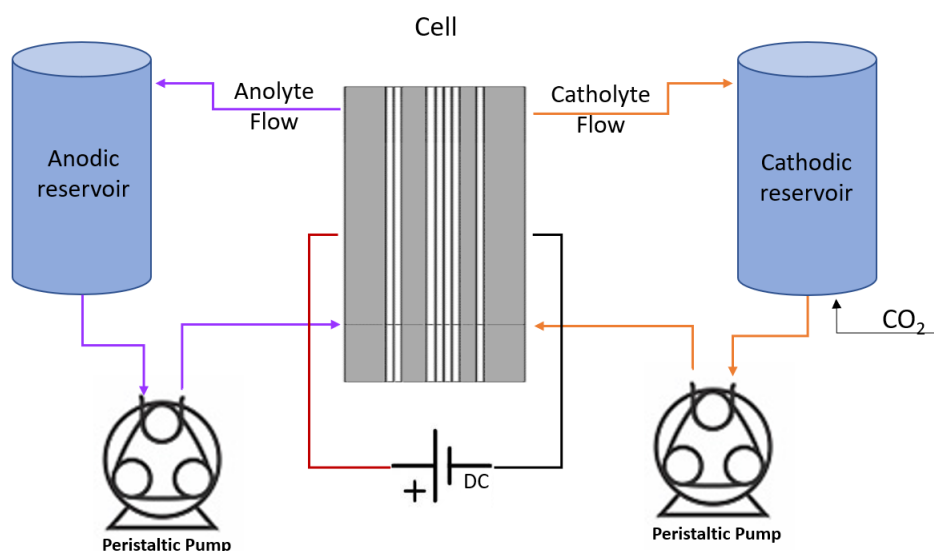


FIGURE 4.13: Schematic drawing of the custom designed system, not including gas capture.

4.3.1 Electrolyte Circulation

To keep the prevent reactants entering the product stream CO₂ is not introduced directly into the cell. Therefore the electrolyte needs to be saturated outside of the cell then circulated into the cell. Additionally the depleted electrolyte inside the cell and the CO₂RR products needs to be removed. The justification for the selection of a CO₂ supply is discussed in the next section.

To allow the CO₂ to interact with as much electrolyte as possible, the bubbler (cathodic reservoir with CO₂ bubbles) should be as narrow and as tall as possible, whilst maintaining an even electrolyte flow. This also minimises the amount of electrolyte exposed to the atmosphere, reducing off gassing. It was therefore decided to use 36 mm inner diameter (ID) acrylic tubing, cut to 20 cm to allow for up to 180 mL to be stored in the reservoirs. For the base of the reservoir a 5 mm acrylic disk was chemically bonded to the tube, with an outlet fitting in the centre. All components were connected using 4 mm ID tubing as shown in Figure 4.13, with push fittings used to make the components easily interchangeable.

To circulate the potassium bicarbonate electrolyte through this system it is necessary to use pumps. The works of Wu *et al.* [102], previously examined in section 4.1, identified the benefits of electrolyte circulation, however the optimum rate varies with cell design.

As previously discussed, in section 2.3, there are two classifications of pump; Dynamic and Displacement pumps. Jeanty *et al.* [101] used membrane pumps at 500mL/min; these displacement pumps are effective and consistent at various flow rates, but cause significant pulsation in the electrolyte which is a known issue for GDEs.

The physically examined water splitting cells, examined in section 4.1.1, used submersion pumps to circulate their electrolyte, which are dynamic pumps. A key issue with dynamic pumps is that they cause cavitation in the electrolyte. This means that CO₂ bubbles could form in the pump under high loads reducing the amount that reaches the electrode and would also pollute the product stream. An additional requirement is that immersion pumps have to be water tight including their electrical components, all of which are submerged.

After taking advice from an industry specialist, (Welco) WP10-P1/8IF4-WM6-CP peristaltic pumps were selected with a brush-less DC motor which enables a wide variety of flow rates over a long duration (up to 6 hours). These displacement

pumps produce as little pulsation as possible, whilst maintaining a consistent flow rate irrespective of pressure differential, with a minimal ramp up to or down from a given flow rate. A separate pump was used to circulate the catholyte and the anolyte. These pumps were powered by a Tenma 72-10495, dual output DC Power Supply(Farnell), with a voltage range of 0 V to 30V, at 5A, resulting in flow rates up to 200 mL/min, with individual control over each pump.

4.3.2 CO₂ Supply

Many of the cells in the literature bubble CO₂ directly into the cell, however this dilutes the gaseous product in the cathodic compartment. The most common way to overcome this issue is through the use of a GDE, however this difficult to implement. The main challenge with GDE implementation is the pressure imbalance between the liquid and gaseous phases on either side of the GDE [122]. If the gas pressure become sufficient to overcome the surface tension of the liquid phase, then the gas phase enters the liquid phase diluting gaseous products. Conversely if the gas pressure is too low, then electrode wetting occurs, as highlighted by Jeanty *et al.* [101]; the electrolyte enters the gaseous side of the electrode, flooding the gas chamber and reducing the area of the electrode that is in contact with the CO₂.

A more simplistic way to prevent the product dilution is to saturate the electrolyte with CO₂ outside of the cell, and then circulate the electrolyte into the cell. The main drawback is that the amount of CO₂ is then limited to how much can be dissolved in the electrolyte (as detailed in section C.3.1).

For this work, the initial decision was made to saturate the electrolyte with CO₂ outside of the cell, before it became necessary to implement a GDE to improve FE as detailed in Chapter 7.

Several of the examined cells used a needle to introduce the CO₂ into the electrolyte. Billy *et al.* [57] showed the importance of using small bubbles to saturate

the CO₂ quickly, as well as the effect of flow rate on the electrolyte saturation speed. Needles tend to produce a single large bubble, whereas fritted glass produces many more, smaller bubbles over a larger area. It was decided to modify the cathodic reservoir to have a fritted glass bottom, connected to a CO₂ supply. With the outlet to the pump moved to the side wall 10 mm above the frit, this outlet was also profiled to prevent CO₂ bubbles from entering, instead of deflecting them around, the outlet.

4.3.3 Product Separation

The membrane that divides the cell is a crucial part that prevents anodic and cathodic products mixing inside the cell, especially hydrogen and oxygen. The oxyhydrogen mixture is known to ignite with sparks of 20 microjoules, at standard temperature and pressure, when it is between about 4% and 95% hydrogen by volume [123]. The oxygen, from the anode, can also combust with some of the CO₂RR making it essential to keep the gaseous product separated. Therefore separate cathodic and anodic reservoirs were used to keep the electrolytes and products distinct.

For the anodic side the output from the cell flows directly into the anodic reservoir, where it enters above the waterline allowing for the evolved oxygen to be easily vented into the atmosphere.

For the cathodic side it was necessary to collect the gaseous products for analysis, so this outlet could not be vented like the anodic side. Several techniques were trialled to remove as much of the gaseous products from the cathodic outflow as possible, however the limitations explained in Chapter 7 meant that the only effective choice was a liquid displacement gas trap design as shown in Figure 4.14. The electrolyte and gases from the cathodic compartment of the cell enter through a fitting in the bottom of an acrylic container (acrylic sheet chemically bonded to a reservoir cylinder off-cut). The gases are then trapped, in the gas

head, by an inverted disposable syringe, however the electrolyte can freely flow around the gas trap and be returned to the electrolyte reservoir. The top of the syringe was sealed with epoxy resin, with two needles inside the syringe; the first allows for gas collection, whilst the second is used to flood the head space at the start of each experiment, preventing contamination.

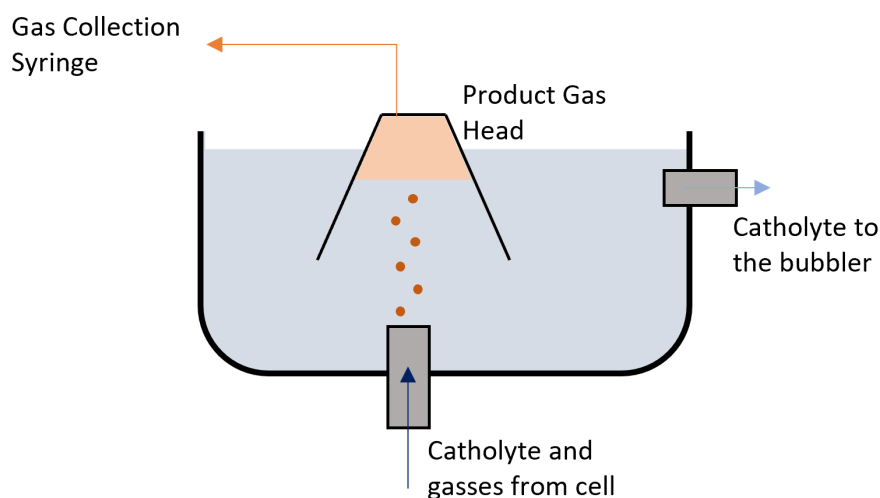


FIGURE 4.14: Schematic drawing of the gas trap used in the designed system.

4.3.4 Power Supply

Would *et al.* found that "two electrode cell systems are desirable for the real applications not only for the enhanced performance but also for the simplified systems and reduced cost" [124]. Additionally they found that solar cells could easily replace the DC power supplies in the two electrode cell system, as they provide almost the same performance. However they only use a single compartment cell and expected some difference in two-compartment reactors.

With limited available funds and the current equipment limited to 5 V and 3 A, a Tenma 72-2930 single channel programmable DC power supply was selected for this study. The 10 A capacity, allows for growth of copper foams on electrode

up to 3 cm², whilst also being able to be utilised for CO₂ electrocatalysis. Importantly its digital output enables real-time monitoring, programmable output (testing profiles) and data logging software, whilst remaining within an affordable price. Jeanty *et al.* [101] also do not use a reference electrode, highlighting that focus is on stable galvanostatic operation for long-term electrolysis, rather than examining the exact process on the working electrode surface.

4.4 Cell Design Iterations

Several initial designs were produced and compared to the design specification, the most promising of which was taken forward. In this section the cell design was developed further, using the design specification to further refine and improve the cell.

4.4.1 Designed Cell: MK 1

The initial cell design was heavily influenced by the cells examined, summarised in section 4.1.4. The designed cell is rectangular, measured 80 mm in length, 50 mm in width and was approximately 35 mm in thickness when assembled. The cell can support electrodes up to 16 cm², with a 2 cm² electrode plate and flow plates dictate the flow of the electrolyte through the cell from left to right as shown in Figure 4.16. The cell had four bolt holes, one in each corner, through which a M6 stainless steel threaded bar was used to compress the cell. Silicone rubber sheets were used as gaskets in the design due to their relatively low cost whilst having suitable resistance to all compounds in the system. The horizontal operating profile came from the FM01-LC cell (4.1.3), utilising the assembly configuration of the four bolts, one in each corner seen in the designs of the C-Flow Cell (4.1.3) and Passas' (4.1.1), and the acrylic plates from the physically examined water splitting cells (4.1.1). The C-Flow Cell (4.1.3) also influenced the anodic mounting method, as can be seen in Figure 4.16 component 5 (Anode

Holder), where the platinum mesh was held within a recess in the plate, with another small recess for electrical connection.

Whilst this cell met the design specification there were several issues. The bolt holes proved too loose for the threaded bar that passed through them. Whilst making assembly easier, quickly aligning the cell, the thin walls of the cell are not aligned well causing leaks. Only having bolts at the ends seals the cell effectively, however under electrolyte flow, pressure is applied to the cell, causing leaks to occur in the centre section where the compression is weakest. Wu et al [102] used an 8 bolt octagonal distribution which would mean substantial geometric change to the cell and was utilised in the MK 2 iteration to combat this issue. Another difficulty was that the cell would drop rapidly in current density, with the end gaskets obstructing the view of the cell; it was difficult to identify the cause of this drop, which is further discussed in Chapter 5.

Multiple Electrode Plates

A key limitation on the cell is the restriction on the size of the electrode on which a foam can be grown. As the foam deposition requires 3 A/cm^2 , the 10 A limitation in the available equipment means that the maximum electrode size is 3 cm^2 . A way to combat this is to use multiple electrode plates, where the foams can be grown on each plate individually before conducting CO_2RR on all the plates simultaneously. Using 3 cm^2 electrodes it is not possible to fill a $4 \times 4 \text{ cm}$ square; the simplest plates that could be used, are $10 \text{ mm} \times 30 \text{ mm}$ or $17.3 \text{ mm} \times 17.3 \text{ mm}$. However a 2 cm^2 electrode is much easier to incorporate into the $40 \text{ mm} \times 40 \text{ mm}$ space. Multiple cathodic holder plates were designed using 2 cm^2 electrodes, with up to 8 electrodes being able to be theoretically fit into the $40 \text{ mm} \times 40 \text{ mm}$ area. Due to the cell being transport limited (Chapter 7), the multiple electrode plates were never used, as they were superseded by the development of a GDE.

Figure 4.15 shows the CAD drawings for the 1, 2 and 4 cathode plates. In these designs various numbers of 2 cm² electrode plates are mounted in the 40 mm x 40 mm electrochemical area, with the anodic and membrane geometric surface areas being the same size and position in the cell.

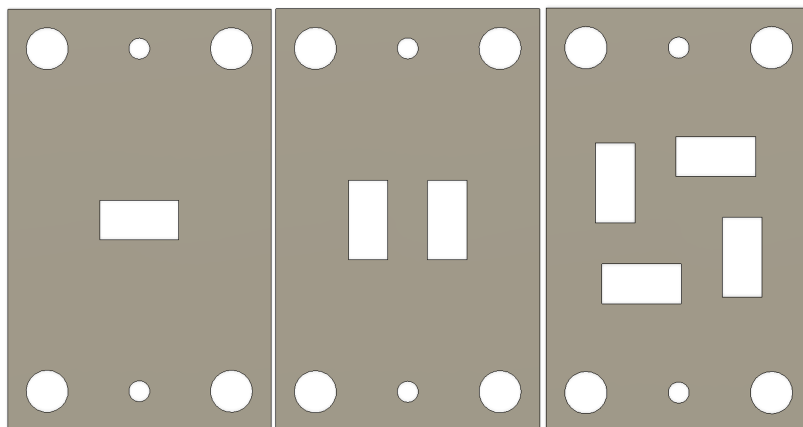


FIGURE 4.15: Top down drawing of 1, 2 and 4 cathode plates for the MK 1 cell design.

MK 1 Iteration (Design)

Figure 4.16 shows an exploded view of the MK1 design, with Table 4.1 being the associated table of parts.

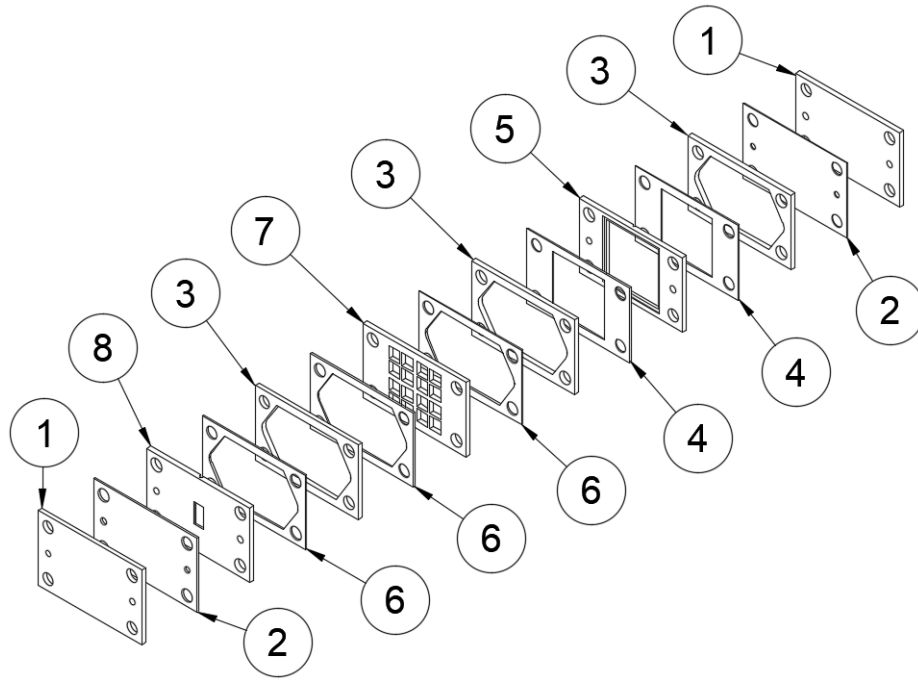


FIGURE 4.16: Exploded, Schematic Drawing of the MK 1 cell design.

Item	Part	Thickness	Material
1	End Plate	5 mm	Acrylic
2	End Gasket	1 mm	Silicone Rubber
3	Flow Plate	3 mm	Acrylic
4	Square gasket	1 mm	Silicone Rubber
5	Anode Holder	3mm	Acrylic
6	Flow Gasket	1 mm	Silicone Rubber
7	Membrane Support Plate	3mm	Acrylic
8	Cathode Holder	3 mm	Acrylic

TABLE 4.1: Parts table for MK 1 design.

4.4.2 Designed Cell: MK 2

Having conducted initial testing on the MK 1 cell, the limitations of the design prevented evaluative testing for cell properties. As such, the cell underwent substantial redesign, generating a second iteration of the cell design.

Key Changes from MK 1 cell

The key changes made between the MK 1 and MK 2 cell are:

- The centre section (where it was only in contact with the acrylic end plate) of the end gaskets were removed to allow visual observation of the cell inside of the cell during testing, making it much easier to detect gas build up in the cell.
- Cathodic end plate was removed as it was made redundant by increasing the thickness of the cathode holder to 5 mm to act as end plate, no need for cable routing channel that caused leaks.
- The cell orientation changed from a horizontal to a vertical design to improve flow in the cell by preventing gas heads from building up in the cell during set up and testing, which reduced the active surface area of the electrodes.
- The exterior profile was changed to an octagonal geometry to accommodate the additional bolts and to have them more evenly distributed for better compression, reducing the number of leaks in the cell. This also resulted in less stress on the cell especially around the bolt holes, so that the cell no longer showed stress marks and fractures from tightening of the bolts.
- Washers were added to both ends of the bolts, distributing the compressive force more evenly to the acrylic End Plates. This reduced wear to the end plates, prevented cracking, and provided more evenly distributed compressive force, reducing leaks.

- The bolt hole diameter was reduced, which improved the cell alignment during assembly, although it was harder to hold the cell together and insert the bolts.
- The flow profile was updated as per the flow modelling, discussed in section 4.5, which refined the geometry of the flow plate and gaskets.
- The anodic holder plate was removed as it did not consistently support the platinum mesh. Instead the mesh was sandwiched between two square gaskets with the compressive force, from the bolts, holding it in place.

Preventing Gas Build-up

By removing the cathodic end plate and end gasket, from the MK 1 design, as well as changing the anodic end gasket to a square gasket, the interior of the cell could be observed during CO₂ electrocatalysis. This showed that the rapid drop in current density seen in the MK 1 design was due to the build up of gases in the cell. The first change made in the MK 2 design was to rotate the flow direction of from horizontal to vertical. This modification meant that the bubbles that would produce an airhead in the top of the cell and instead naturally move towards the cell output rather than collect within the cell.

The second discovered reason for bubble build up (after the cell orientation was changed) was attributed to gas pockets forming in the membrane support plate, reducing the active surface area of the Nafion membrane. The decision was made to remove the support plate even though there would be increased pulsation within the cell.

The final source of bubble build up was found to be on the anode, as can be seen in Figure 4.17, which shows a later version of the MK 2 cell during CO₂ electrocatalysis. The anodic square gasket has been replaced with a flow gasket

to better examine the issue of gas build up behind the anode. This issue was addressed through flow modelling as discussed in detail in section 4.5.



FIGURE 4.17: Photo of the MK 2 cell showing the visibility inside the cell and anodic gas build up.



FIGURE 4.18: Photo showing the inclusion of a reference electrode on the MK 2 cell.

Reference Electrode Inclusion

During initial testing it was necessary to be able to compare the cell to that of a 3 electrode variant. With the cathodic compartment being too thin for a radial

mounting method and the cathodic plate now exposed and increased to 5mm thickness, it was possible to mount a reference electrode. By chemically bonding an acrylic inlet tube to a 6mm hole cut into the cathodic holder plate, 5mm above the single cathode holder in the centre of the cell, a reference electrode could be inserted and sealed with PTFE tape, as shown in Figure 4.18. The requirement for a GDE prevented this modification being taken further, due to the requirements for a 3 phase boundary, with a liquid phase on one side and a gas phase on the other. It was not possible to effectively seal the reference electrode access tube inside the gas chamber for the GDE.

A potentiostat can be used as a two electrode setup by combining the reference electrode and working electrode, making the reference electrode circuit measure no different to the potential of the working electrode. This combined with the knowledge that the current is measured between the working and counter electrodes [125], meant that a rough comparison could be obtained to guide the range of potential as examined in Chapter 7. By applying the optimum potential for the FE of ethylene at the working electrode as reported by Rudd *et al.* [93] as 1.4 V, the charge across the cell could be recorded. Then a potential across the cell is applied, in a two electrode configuration, and slowly increased until the same current across the cell is seen, with that applied potential being 3.98 V across the cell.

Nafion Membrane Alternatives

Several membrane alternatives were examined: 10 micron UHMW polyethylene porous sheet, 50 micron UHMW polyethylene porous sheet plus 90 Micron polypropylene/ UHMW polyethylene blend porous sheet trialled in Chapter 5. A pressure imbalance was caused by being unable to perfectly synchronise the pumps so that the pressure waves and the gravitational potential energy on each side of the membrane was equal. This meant that electrolyte flowed between the

cathodic and anodic chambers, so that one of the reservoirs would be severely depleted whilst the other was overflowing, after a short period of time.

MK 2 Iteration (Design)

The resultant MK 2 cell is shown in Figure 4.19, with Table 4.2 detailing the associated parts.

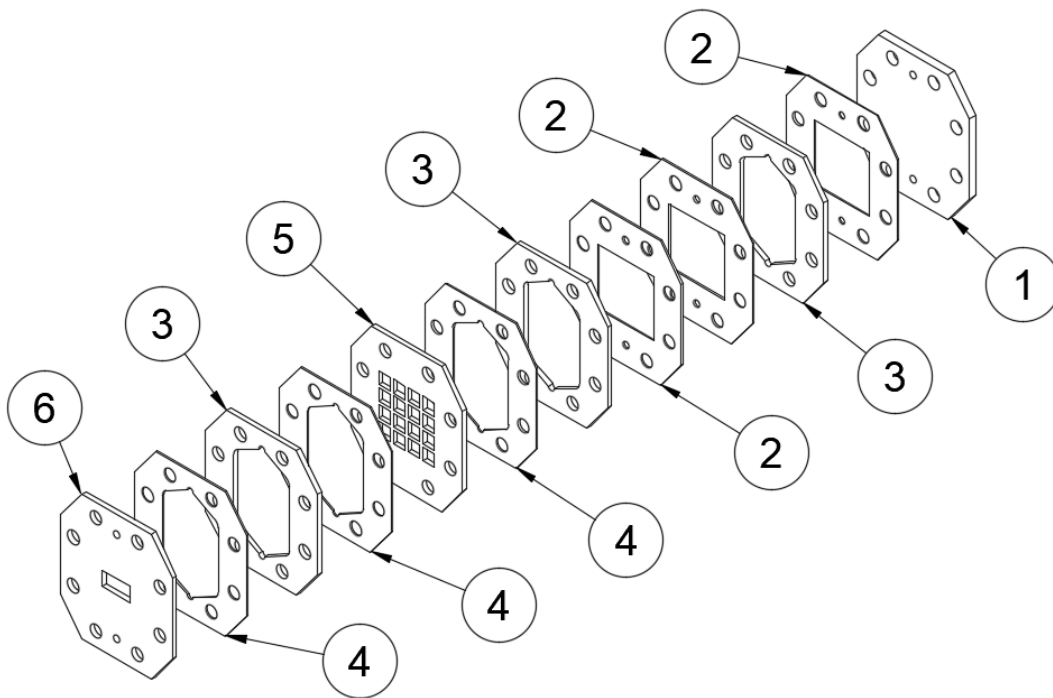


FIGURE 4.19: Exploded, Schematic Drawing of the MK 2 cell design.

Number	Part	Thickness	Material
1	End Plate	5 mm	Acrylic
2	square gasket	1 mm	Silicone
3	Flow plate	3 mm	Acrylic
4	Flow gasket	1 mm	Silicone
5	Membrane support	3 mm	Acrylic
6	Cathode Holder	5 mm	Acrylic

TABLE 4.2: Parts table for MK 2 design.

4.4.3 Designed Cell: MK 3

A third iteration of the cell was finalised after completion of the work discussed in Chapter 5, when the focus moved from the physical features of the cell to the properties of the cathode. The results of these experiments highlighted several changes were required to further improve the functionality of the cell.

Key Changes

As discovered in testing of the MK 2 design, the membrane support plate, which could now be observed through the window cut into the anodic rear gasket, caused significant bubble build up as the produced oxygen became trapped. This 'air gap' restricts the overall conductive area of the membrane, reducing cell electrical conductivity. Additionally the testing reported in Chapter 5 showed the importance of electrode spacing; the support plate was too thick to remain in the design and instead the membrane size was increased from 50 mm x 50 mm to the full cell geometry, and sandwiched between the two silicone flow gaskets (see item 4 in Table 4.3 and Figure 4.20). This ensured a tight seal between the anodic and cathodic compartment. Several other plates were removed to facilitate optimum electrode separation and flow rate.

With the addition of the anodic blocked flow plate, discussed further in section 4.5.2, the plates of the cell had to be assembled in a certain orientation (the cell was not mirrored). Filleting the external geometry at the top of the cell, whilst leaving the bottom of the cell chamfered, ensured that the cell was assembled with each plate in the incorrect orientation. With this change in external geometry, a further reduction in the diameter of the bolt holes was made, further improving the alignment of the cell. Along with this reduction in size, the bolt holes were moved further away from the internal geometry of the cell, increasing the sealing area of the gaskets, preventing leaks from occurring through the bolt holes. This

was most noticeable in the results of the high speed imagery work, where black ink was found in the bolt holes when the highly obstructed plates were examined.

The diameter of the holes for the electrode ports was increased, which meant that the connector tubes could be axially bonded to the plate, rather than surface mounted. This greatly improved the strength of the part and reduced the instances of them being snapped off.

The later iterations of the cell versions utilise fewer individual parts. The MK 2 cell had 6 different components and a total of 12 parts. In the MK 3 version there are 5 components and 7 parts (not including GDE adaption). This made assembly simpler, quicker and easier.

GDE Inclusion

Throughout Chapter 7 it became clear that the key factor limiting the product distribution was the amount of CO₂ reaching the electrode surface. The cell needed to be optimised for conductivity (in Chapter 5) and mass transport (flow modelling). The best way to improve the amount of CO₂ reaching the cathode was by converting the cell to a GDE configuration. The addition of two more connection points, to the cathodic end plate, provided a gas supply into the cell. These ports were placed between the side bolt holes, with the gas flow horizontal across the cell.

MK 3 Iteration (Design)

The resultant MK 3 cell is shown in Figure 4.20, with Table 4.3 detailing the associated parts.

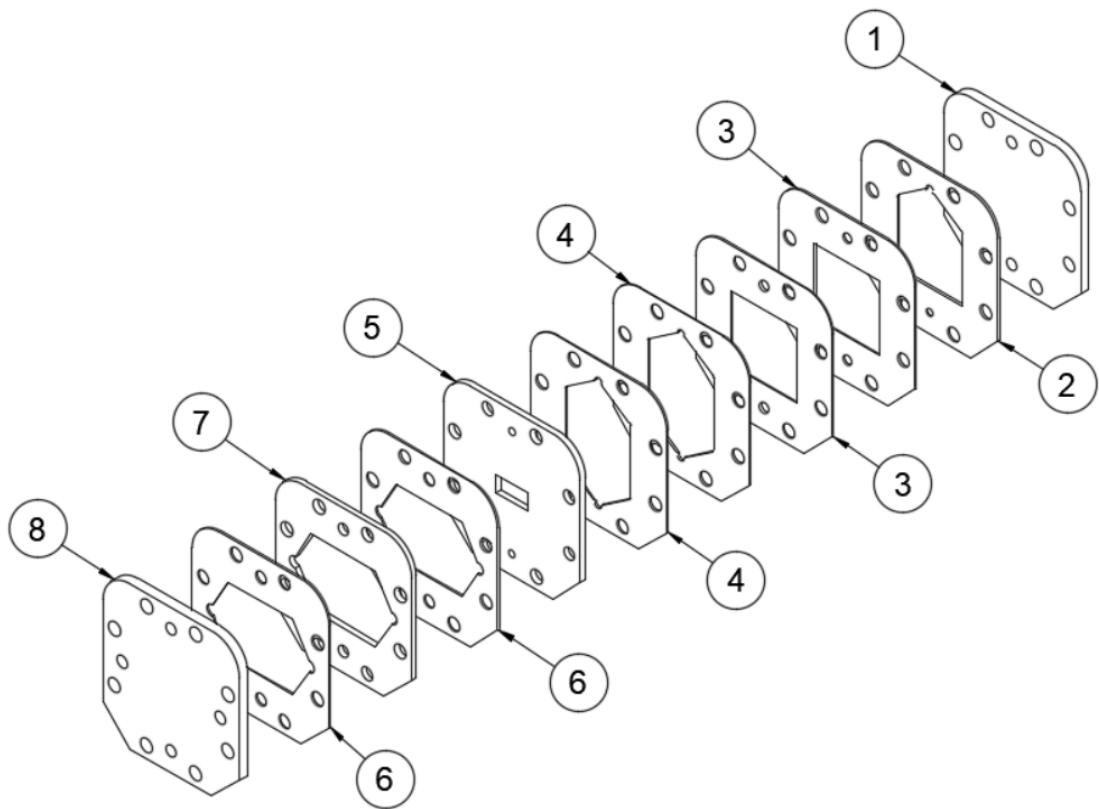


FIGURE 4.20: Exploded schematic drawing of the MK 3 cell design with GDE adaptation.

Item	Part	Thickness	Material
1	End plate	5mm	Acrylic
2	Anodic half-flow plate	2mm	Acrylic
3	Square gasket	1 mm	Silicon rubber
4	Membrane flow gaskets	1 mm	Silicon rubber
5	Cathode Holder	3 mm	Acrylic
6	Gas phase gasket	1 mm	Silicon rubber
7	Gas phase plate	3mm	Acrylic
8	3 phase end Plate	5mm	Acrylic

TABLE 4.3: Parts table for MK 3 design.

4.5 Flow Modelling

Computer modelling was conducted to examine the flow path of the electrolyte within the cell at several stages of the designs. Two aspects of the cell were examined; the anodic flow to reduce bubble build up and the effect of the profile of the flow plate on the electrolyte flow and dispersion through the cell. The data presented in this section are from the final iteration of the MK 2 design and were used to produce the MK 3 design.

For this analysis the interior geometry of the cell is divided into five sections: the Inlet, Inlet Feeder, Exposed electrode area, Outlet feeder and Outlet as shown in Figure 4.21. For all the images containing simulations, the cell is displayed on its side, with the electrolyte flowing from left to right.

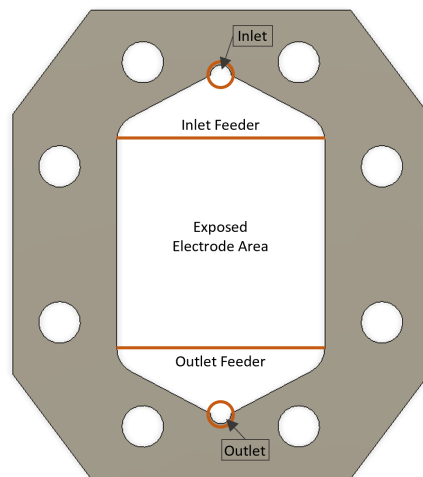


FIGURE 4.21: Schematic of cell sections.

4.5.1 Mesh Refinement

The meshes used in the simulations were automatically generated by the CFD software, with the mesh resolution factor being adjusted to produce different mesh levels. The number of elements and nodes generated at each resolution factor is shown in 4.4. A suitable Mesh Resolution Factor (MRF) was chosen

by comparing simulation flow results with experimental results. Different MRF changed the predictions made by the model as shown in Figure 4.22.

The flow trajectories in the cell chamber changed considerably as the meshing (number of nodes / elements) was increased (decrease in MRF), as well as the definition of the simulation. The flow traces covered much more of the cell compartment in Figure 4.22 a and b compared to a lower meshing level, as seen in Figure 4.22 f and g, where the flow traces do not enter the corners towards the right hand side of the image. Additionally the higher meshed simulations show much more evenly distributed flow, with a higher flow rate data presented (blue-red colour gradient).

Mesh	Mesh Resolution Factor	Number of Nodes	Number of Elements
a	0.1	98071	316132
b	0.5	25576	73361
c	1	8634	23125
d	1.5	4582	10610
e	2	3131	6777
f	2.5	2724	5802
g	3	2728	5808

TABLE 4.4: Mesh resolution factor and resulting number of nodes / elements.

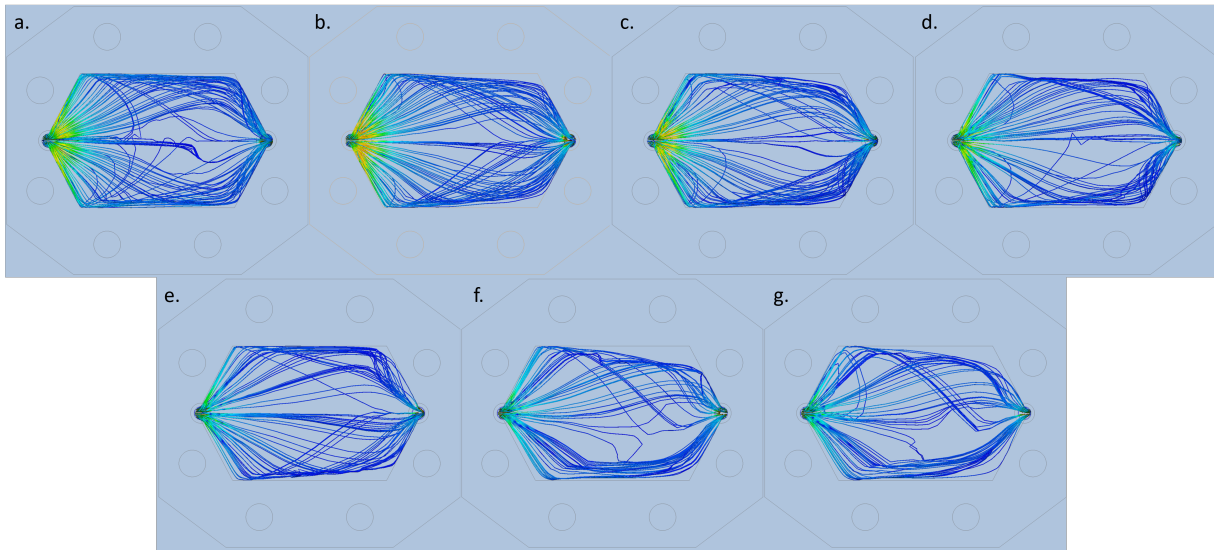


FIGURE 4.22: Flow traces, for each of the simulated mesh resolution factors, shown in Table 4.4.

Figure 4.23 shows the effect of the MRF on the distribution of the nodes within the cell. Image a has a MRF of 0.1, b is 1.5 and c is 3. The difference between the concentration and number of nodes can easily be seen, especially in the areas around the input and output. The MRF was chosen as the independent variable as this concentrates the nodes in the areas most likely to have an effect on the turbulence and therefore flow through the cell. A MRF of 0.5 was chosen for future simulations, as it provides a high level of accuracy whilst keeping the simulation time to a reasonable length.

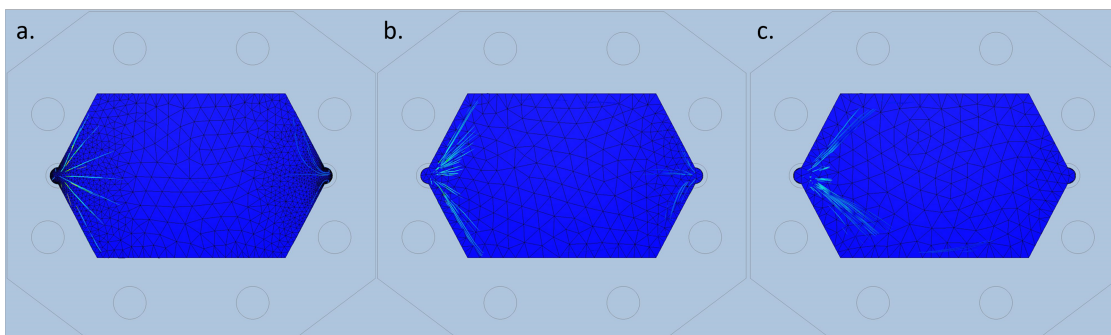


FIGURE 4.23: Node maps for 3 of the simulated mesh resolution factors: a is 0.1, b is 1.5 and c is 3.

4.5.2 Bubble dispersion

During initial testing of the MK 2 cell design, it was found that bubbles were becoming trapped in the platinum mesh anode, reducing the wet surface area of the electrode and negatively impacting the efficiency of the cell, as discussed in section 4.4.2. In order to solve this, several design variations were examined using simulation of the cell to adequately visualise the flow of the electrolyte through the anodic compartment. The effect of these bubbles is further discussed in section 5.2.1.

The most effective way to prevent this bubble build up was to change the flow plate behind the anode, so that the inlet feeder section is sealed. This change increased the flow at the inlet feeder in front of the anode, producing low pressure behind the anode where the cross sectional area of the outlet feeder is much larger than that of the plate in front of the anode. This caused the majority of the flow to pass through the anode removing the trapped bubbles. The outlet feeder was left open in front of the anode to prevent gas build up. Figure 4.24 shows the original and modified flow plate, whilst Figure 4.25 shows the original and modified flow paths.

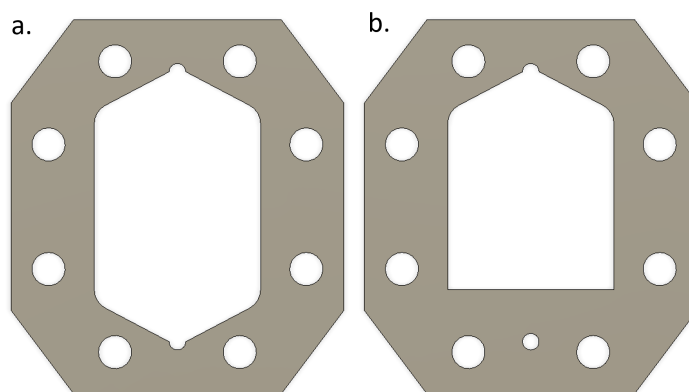


FIGURE 4.24: Designs of the anodic flow plate: a. original plate for the dual flow design, b. new single entry point design.

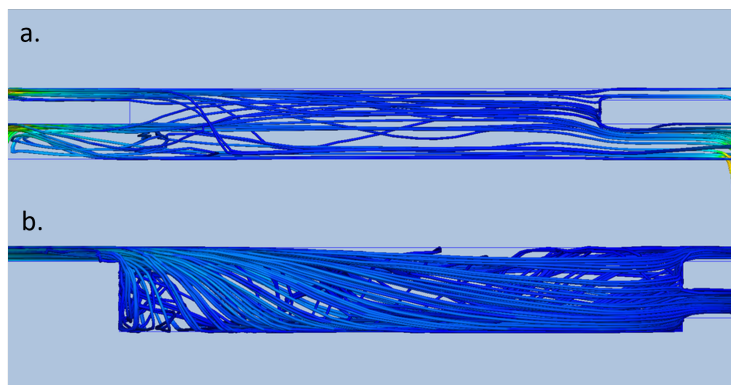


FIGURE 4.25: Simulated flow paths for anodic chamber: a. original dual inlet design, b. new single inlet design.

In Figure 4.25 the flow is from left to right. The anode (platinum mesh), although not modelled, is situated between the two flow plates indicated by the areas where the flow enters the anodic compartment (on the left) and leaves (on the right). By removing the bottom inlet from Figure 4.25 a, the flow into the cell is concentrated through the top inlet. Retaining the wider outlet behind the anode (bottom right), means the preferential flow passes through the anodic mesh, with this flow dislodging bubbles building up in the mesh. This flow can be seen in the increased number of traces moving from top to bottom in 4.25 comparing b to a.

4.5.3 Flow Path

The CFD modelling was also used to examine the electrolyte flow through different internal cell geometries, with five different aspects being examined: the feeder profile, inlet and outlet profile, cell restrictions and cell obstructions.

Several flow plates were examined with the most interesting shown in Figure 4.26. The characteristics examined included: tapered feeds and collectors, rounded feeds and collectors, obstructions across the cell, and restrictions in the cell. The flow rate at the inlet of the cell is equivalent to 60 mL/min, with the thickness of

all plates being 3 mm and a gaskets thickness of 1 mm giving 5 mm total thickness. The results of the flow simulations are shown in Figure 4.27 where each of the plates has been rotated 90°clockwise from Figure 4.26, so that the flow is modelled from left to right in Figure 4.27 of each of the plates. The lines observable in the figure displays the path of a 'seed' particle through the cell, with the colour scale showing their velocity in cm/s at a given point. It is key to note that the cell restrictions are the full width of the acrylic plate, but are not included in the accompanying gaskets.

Plate a was deemed to be the optimum flow plate profile for use in the cell; the restriction at the inlet causes relatively high pressure in that area as seen by the increased velocity of the seeds in the inlet area. This causes a comparatively even spread of flow across the full width of the inlet feeder area, which quickly settles into comparatively laminar flow trajectories over the centre of the exposed electrode area. Electrolyte that initially travels around the outside of the cell is reintroduced to the second half of the exposed electrode area increasing the amount of fresh electrolyte that reaches the electrode.

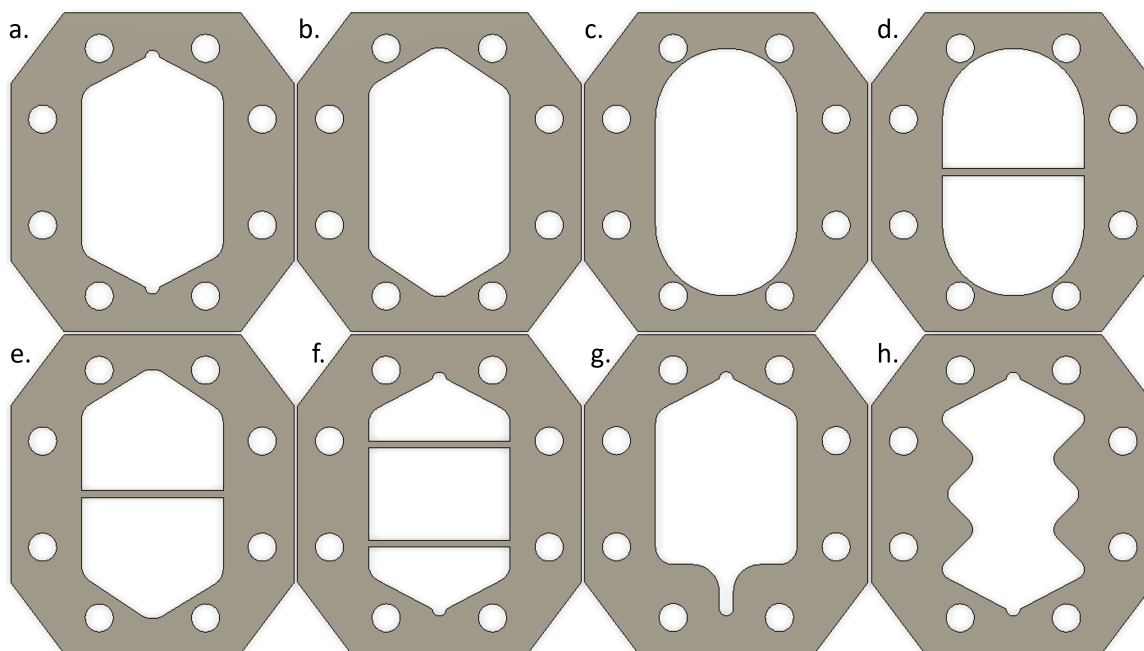


FIGURE 4.26: Designs of the flow plate: a. optimised plate, b. vectored unrestricted plate, c. circular unrestricted plate, d. circular unrestricted plate with obstruction, e. vectored unrestricted plate with obstruction, f. double obstructed plate, g. high restriction inlet plate, h. multiple equal restriction plate.

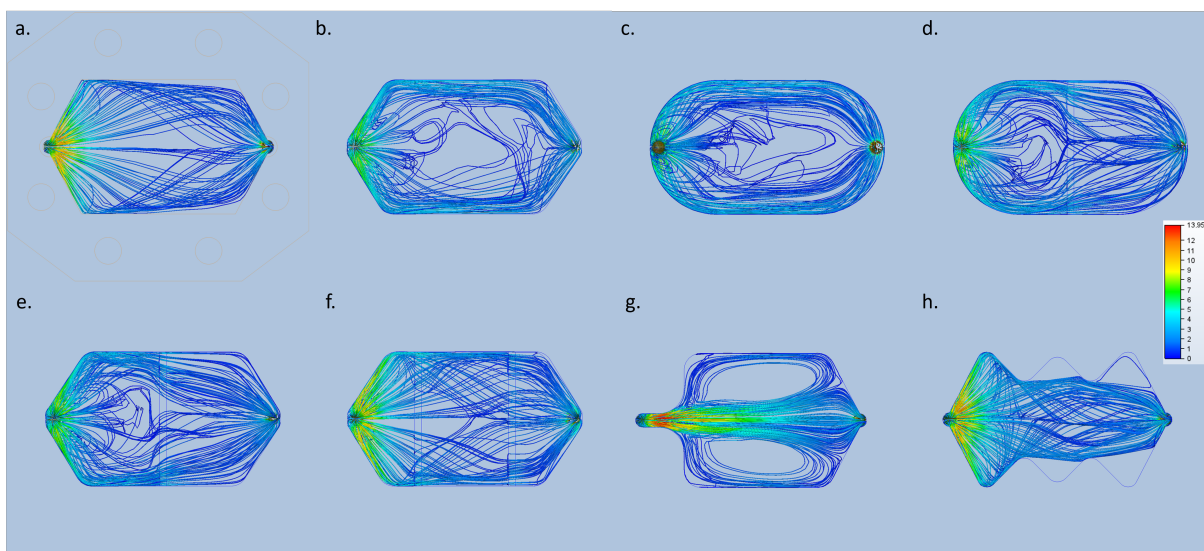


FIGURE 4.27: Top down view of the simulated flow paths for each of the flow plate designs presented in Figure 4.26, the colour scale shows velocity magnitude (cm/s).

Plate b has the delta shaped feeder profile of plate a, but the removal of the inlet restriction greatly reduces the velocity of the 'seed' at the inlet, as the electrolyte

is able to flow in the opposite direction to the outlet (moves to the left of the inlet rather than the right). This low flow rate, in the centre of the cell, causes the trace particles in this region to take a more indirect route through the cell with several stagnant areas being created in the centre of the cell (shown by the lack of traced particles in a given area). Most of the flow travels around the outside of the cell as a result of the reversed direction of flow at the inlet being forced against the flow plate's walls, meaning that the majority of the flow through the cell is pathed around the edge of the cell.

This effect was also seen in the hemispherical designs (plate c) with the smoother profile of the flow plate directing the flow at the edges in a more laminar way, also producing a relatively stagnant central region. Additionally some eddy currents were observed in the hemispherical designs. Both plates b and c showed low flow through the centre of the cell with large stagnant regions forming, increasing the diffusion distance from the fresh electrolyte to the electrode surface.

The presence of a single cell obstruction in the centre of the electrode exposed area, as seen in plates d and e (compared to c and b respectively), shows an improvement in flow distribution in the second half of the flow plate, with a much more laminar like flow over the second half of the exposed electrode area and into the outlet feeder. However the first half of the flow plate shows much more turbulence, with the 'seeds' changing direction more and in a smaller area. Whilst this increased turbulence in the first half, did not completely remove the stagnant areas, it did show a reduction in re-circulation (eddy currents). Additionally in the second half, after the cell obstruction, the flow distribution is more laminar in the horizontal plane than before the obstruction. In contrast, the vertical flow is almost non existent, with the majority of the flow only in a thin layer that very slowly disperses towards the outlet creating a large stagnant area in the top (from the perspective of the rotated figures) of the cell. Later practical trials (section 4.28) would show that these slight performance increases have significant

costs for piratical implementation.

Placing the cell obstruction later in the cell did not improve the flow distribution across the exposed electrode area. Earlier placement of the obstruction, between the inlet feeder and the exposed electrode area, did provide some improvement to evenness of the flow across the exposed electrode area, but was not as effective as the restriction at the inlet (plate a). Secondary obstructions (plate f), did improve the cell distribution of the flow, across the exposed electrode area. However the flow was reduced to an even thinner horizontal layer, than seen with a single obstruction, with significant stagnant area between the obstructions. Once again later practical trials (section 4.28) showed the difficulties of implementing this design practically.

With plate a showing considerable improvement from inlet restriction, the restriction was expanded further, producing plate g. This flow plate profile directs the majority of the flow over the centre of the exposed electrode area. However this focused flow is at a considerable velocity which may interfere with materials deposited on the electrode surface. Also, this flow is so focused that it creates significant stagnant areas on either side of the main flow, with considerable eddy currents forming around them, potentially recirculating depleted electrolyte. Moving the restriction further into the cell creates a high turbulence area before the restriction as the flow is concentrated in the central section, seen in Figure 4.27 h). The addition of restrictions later in the cell removes the eddy currents with the troughs between the restrictions becoming stagnant.

4.5.4 High Speed Imagery

The computational flow modelling was confirmed by analysing the data captured on a high speed camera as per section 3.7. The flow plates from Figure 4.26 were examined using the HSI with the frames from plates a, b and c seen in Figure 4.28. The flow rate was set to 60mL/min, the same as in section 4.5.3 with the images

in Figure 4.28 all being the frames taken one second after the ink entered the cell. The full method is described in section 3.7.

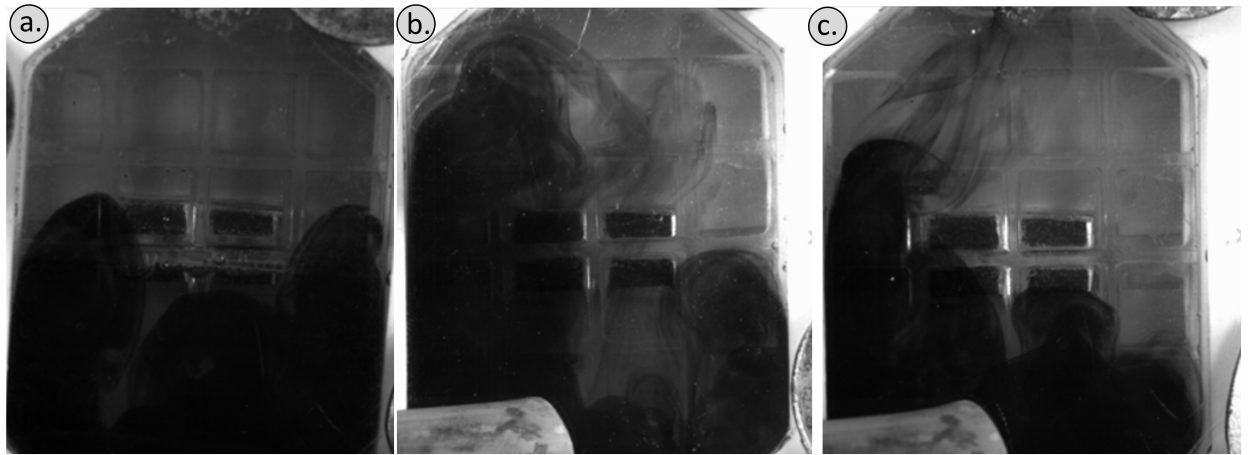


FIGURE 4.28: Images captured from HSI for flow plates a, b and c.

By comparing the CFD models for each plate (Figure 4.26) to the HSI, the accuracy of the CFD modelling can be observed, with Figure 4.28 showing the frame 1 second after the frame where the ink first enters the cell. Plate a has a relatively even spread of ink across the cell, with the ink strands flowing approximately the same distance within the 1 second, roughly as predicted by the CFD model. In plate b the ink moved much further around the outside of the cell than through the centre, within the 1 second, as the CFD model for Plate predicted proving that the lack of restriction at the inlet reduces the amount of flow through the centre of the cell. The lines of ink show turbulence in the cell as they often change direction and are quite dissipated. A similar effect was seen in plate c where the ink also travels around the outside of the cell. However the flow is much more laminar in the top of the cell, with the flow lines being much more defined than those of plate b and running in a much more parallel way.

The flow plates with the inclusion of the obstruction across the cell (d, e, f) proved impractical for usage within the cell as they caused considerable leaks to occur and as such are not presented in Figure 4.28 as the results proved too inconsistent.

The footage showed that the area before the restriction filled quickly, with the following sections taking much longer to be filled with ink, often with the recording terminating before the cell was filled with ink due to the exposure time available. The inclusion of a second cell obstruction resulted in more leaks in the cell making testing impossible. Plates g and h were not tested as they were deemed to be impractical designs for use in the cell.

Flow simulations become less accurate at lower flow speeds with the random movement of the individual molecules of the liquid becoming a larger factor determining their velocity. The HSI showed stronger mixing in the stagnant regions of the CFD modelling than predicted. A key limitation in the level of CFD used is that it cannot model diffusion mixing, as a result the CFD modelling is not entirely accurate, but can still be used to optimise cell designs effectively.

Cell Refresh Rate

By examining the time taken for the ink to fill or empty from the cell, the number of cell volumes required to fully refresh the cell can be determined. This value gives a comparable indication to the distribution of flow through each of the plates, highlighting the effects of any stagnate areas. A higher value will have lower flow distribution requiring more mixing to clear the cell, therefore requiring a larger amount of fluid to refresh the entire volume. Experimental results were quantified by recording the time taken for the cell to fill and, separately, empty with ink. The time taken for each cell is not comparable due to their different internal volumes, hence the need for Number of Cell Volumes for each flow plate, shown in Table 4.5.

Flow Plate	Internal Volume (mm^3)	Time for a Single Refresh (s)	Number of Cell Volumes to Refresh
A	31645.20	31.645	3.43
B	31940.45	31.994	4.04
C	34387.89	34.388	4.53
D	33747.89	33.748	5.56
E	31366.56	31.367	6.14

TABLE 4.5: Internal Volume, Volumetric refresh rates and the Number of Cell Volumes required for examined flow plates.

Plate A, clearly, has the lowest number of volumes required to empty the cell, making it the best design for refreshing the CO_2 saturated electrolyte. Although the ink is not completely comparable to the performance of the electrolyte, it still gives a rough indication of time each flow plate requires to completely refresh the cell. The key limitation of this method is that the ink behaves slightly differently to CO_2 saturated $KHCO_3$ in the cell, although the ink's progress is much easier to track through the cell. Additionally the exact point when the ink fills or empties the cell had some variation due to subjective error.

4.5.5 Proposed Cell Design

Having completed all testing, a cell design can be proposed for further development in future works. The modifications between the initial design and the MK 3 version make the cell stackable, where the anodic and cathodic channels have been offset, allowing for multiple compartments to be supplied from the same feed. This means that the cell could be used in stack as is possible in the FM01-LC cell (section 4.1.3) and as used by Rearden *et al.* in section 4.1.1, as well as in certain designs in the literature [125–127].

The key modification in this design is the setting of the anodic and cathodic electrolyte channels which allows for additional cells to be fed off the same supply,

as seen in Figure 4.29 where the connecting end plate hold the ports for both the anodic and cathodic electrolyte. A consequence of this change is that the profile of the flow gasket has been altered and will require additional modelling to optimise the flow path.

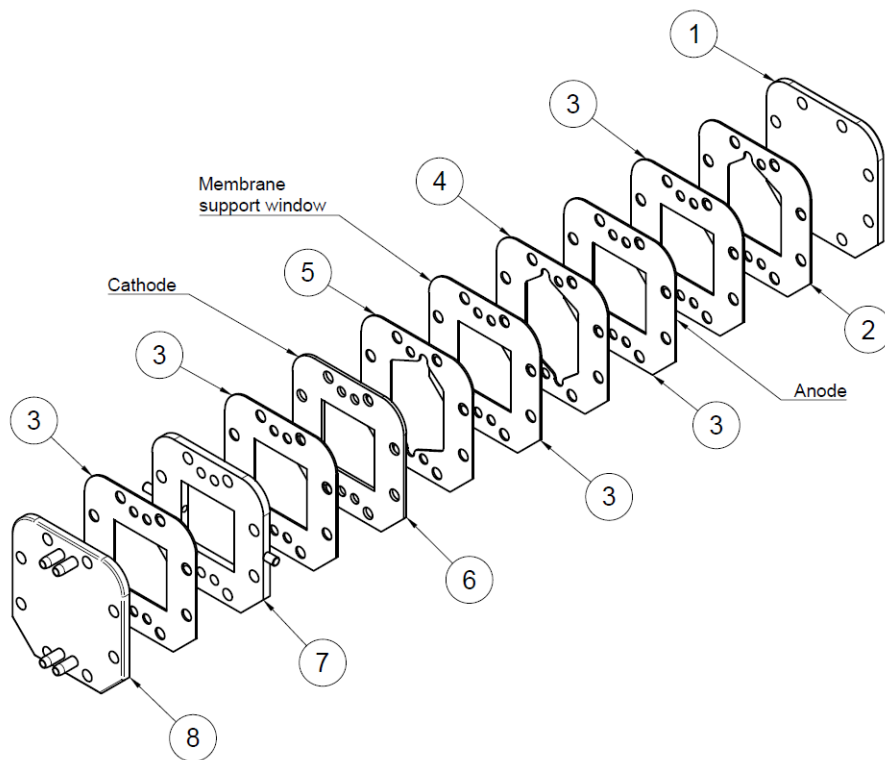


FIGURE 4.29: Exploded schematic drawing of the Proposed Cell Design.

Item	Part	Thickness	Material
1	Stoppered End Plate	5 mm	Acrylic
2	Anodic Gasket	1 mm	Silicone Rubber
3	Square gasket	1 mm	Silicone Rubber
4	Anodic Flow gasket	1 mm	Silicone Rubber
5	Cathodic Flow gasket	1 mm	Silicone Rubber
6	Cathode plate	3 mm	Acrylic
7	CO ₂ supply plate	5 mm	Acrylic
8	Connecting end plate	5 mm	Acrylic

TABLE 4.6: Parts table for the proposed cell design.

Figure 4.29 shows the exploded schematic drawing for the proposed cell design, with Table 4.6 detailing the associated parts. A 50 mm x 50 mm Nafion membrane should be mounted to a square gasket forming the membrane support window. The anode is again sandwiched between two square gaskets and a GDE can be utilised as the cathode in the cathode plate, using the CO₂ supply plate to introduce the CO₂ into the cell.

4.5.6 Conclusion

Improving the supply of CO₂ to the electrode and removal of subsequent products can be done by increasing the pump speed (examined further in section 5.2.1). However, this incurs three greater costs on the system: mechanically, the system must withstand a greater pressure; longevity, the parts will be more subject to wear; and; financially, cost of more power needed to run the pumps for the same amount of time. Improved flow profiles can effectively reduce the diffusion distance of the bulk electrolyte to the electrode surface, with little cost and may reduce pumping requirements.

In summary, inlet restriction has been shown to effectively reduce the amount of electrolyte that passes around the outside of the cell, with more even flow across the exposed electrode area. The internal geometry of the flow plates is also important with the harsher angles providing better flow distribution. Obstructions across the cell are effective at improving horizontal flow distribution, but greatly reduce vertical flow, whilst width restrictions improve vertical flow distribution, with reduced horizontal flow. Both obstructions and width restrictions produce significant stagnant areas, with possible eddy currents recirculating used electrolyte.

Works by Jeanty *et al.* [101] have shown that texturing the electrode surface can improve turbulence within the cell. This should be examined in future works once the size and configuration of the electrodes has been finalised.

Modelling provides a rapid and relatively cheap method of testing cell designs before they are manufactured, as well as providing more detailed insight into characteristics that are difficult to examine physically within the cell; quantifying velocity fields, pressure fields and flow profiles. Full-system modelling could examine fluid flow and apply these results to the wider system, finding the pressure acting on the cell walls to optimise cell geometry and be used to optimise the system's configuration.

Future studies should examine enhanced tapered feeders, more complex 3D configurations or larger alterations to cell geometry and re-positioning of the inlet and outlet.

4.6 Chapter Summary

In this chapter a review of the currently available electrochemical cells has been conducted, resulting in the design and refinement of an electrochemical flow cell

for CO₂ catalysis on an electrode up to 16 cm². CFD modelling has been conducted to optimise the electrolyte flow through the cell, with HSI used to confirm the accuracy of the modelling.

4.6.1 Cell and System Evaluation and Limitations

Despite several cell design refinements there are still a few issue to be resolved in the cell's design. A small amount of the gaseous products could be seen collecting in the cell and were therefore not included in the product analysis. Although this was deemed to have reached a steady state, with a consistent amount of product trapped in the cell, additional work should be conducted to further improve the internal geometry of the cell.

The limitation incurred by requiring the smallest amount of electrolyte possible to concentrate liquid products, consequently in-depth gas-liquid separation techniques could not be used. As the gaseous cathodic products are soluble in water, not all of the produced amount will be collected in the gas trap, with some being lost into the atmosphere through de-gasification in the bubbler.

4.6.2 Future Design Outlook

A key way to improve the cost of manufacturing the designed cell is to reduce the amount of Nafion used in its design. Alternate methods of sealing and mounting the membrane should be examined in order to use a smaller quantity. The current design uses a full profile Nafion cut out, having originally used a bonded acrylic plate, and then a gasket sandwich design. An improved sandwich design, where the gaskets better seal the edges of the membrane, or where the membrane is chemically attached to a gasket using a silicone based adhesive, would allow for a smaller amount of Nafion to be used reducing material costs. This is especially important due to the considerable increase in price of Nafion over the course of

this project, not to mention the environmental costs associated with its production and destruction. This could also be considered alongside the adaption of a MEA design, for the anodic side. By removing the need for electrolyte, the operating cost of the cell is reduced as well as the capital cost, as an anodic pump would no longer be needed. However the effect of this on the product efficiency and selectivity would need to be fully examined.

Whilst this cell has an 28x to 228x increase in electrode area, compared to that used by Rudd et al [93], it is still not suitable for commercial use, which utilise at least 1 m² electrodes. Further scale up is required for CO₂ electrolyzers to become an efficient and effective use of captured carbon, with additional factors such as preventing GDE wetting and electrode durability (maintained FE selectivity over time), to be explored further.

More in depth flow modelling should be conducted, using advanced software such as Ansys Fluent. This would produce much greater detail on the fluid models and allow for the simulation of gas bubbles being produced on the electrode surface.

With the known issue of pulsation affecting the wetting of the GDE and flooding of the gas chamber, electrolyte pressure regulation needs to be further developed. Inclusion of pressure relief valves and / or accumulators could overcome the problem. Alternatively, multiple pumps could be synchronised to dampen the pulsation effect. The inclusion of digital pressure sensors in the GDE gas chamber, combined with digital flow valves, would allow for instantaneous pressure regulation in the GDE gas chamber, ensuring a regulated and continuous supply of CO₂ to the electrodes surface. This is especially necessary for the proposed final design as each GDE gas chamber needs to be regulated independently.

Chapter 5

Cell Characterisation and Performance Optimisation

5.1 Introduction

Having designed and built the electrochemical cell, it needed to be characterised for its electrical and physical properties in order to establish the operational range of the cell and identify the variables for later test of its carbon dioxide conversion FE. As this study has stemmed from the research conducted by Ahn [95], and more recently Rudd [93], the starting operating parameters were as close to their works as possible, using 0.1 Molar potassium bicarbonate as the electrolyte and a 212 Nafion membrane. Detailed testing was conducted on several parameters to optimise the cell.

As discussed previously in section C.1.3, the resistance of the cell can be attributed to several factors including electrolyte concentration and electrode separation. Six parameters were selected for investigation in this chapter: electrolyte flow rate, electrode separation, electrolyte concentration, supplied gas, system configuration and electrode surface morphology.

5.1.1 Testing Profile

To produce an I-V curve, it is necessary to record the current at several different potentials. As the designed cell, only uses a two electrode setup, all potentials are measured across the cell not at the working electrode. The first profile consisted of applied potentials from 0 V to 10 V with a 0.5 V step. Each step lasted 10 mins to check for current stability in the cell, making sure the current had plateaued for consistent results. Preliminary testing showed no flow of electric current for cell potentials below 3.5 V.

In order to collect broader data beyond the Ohmic range of the cell, the testing profile adapted was started at 2 V. The intent was to explore cell optimisations that enable activity at lower potentials, up to 22 V, with a 0.5 V step. The cell was held at the given potential for 6 mins and then given a 2 min 'cool down' period as this was found to allow the cell to stabilise, removing any bubbles that had built up and replacing the electrolyte, from the previous step. The 6 min run at each step plus the 2 min cool required over 6 hours for multiple runs for each variable examined, not including time for cell assembly and experimental setup. This was deemed to be an inefficient use of the available time, so the potential step was increased to 1 V. From this improved profile the same detail could be observed, but in a shorter time period. The testing profile was refined again; 2 V to 22 V with a 1 V step between 2-4 V and 19-22 V with a 1.5 V step between 4-19 V. This greatly reduced the time per experimental run, without losing accuracy in the data obtained.

For this chapter, unless specified otherwise, the MK 2 cell was used without the membrane support plate. A 2 cm² copper plate was the cathode and the anode was a 50 x 50 mm platinum mesh, with a Nafion 212 membrane dividing the cell. The volume of KHCO₃ electrolyte in each half of the cell (and supporting system) was 150 mL. Results with error bars are presented in Appendix A

5.2 Results and Discussion

5.2.1 Effect of Flow Rate

The flow of the electrolyte was not considered in the cells used by Ahn [95] and Rudd [93], however it is a common factor seen in several published works as outlined below and commonly found throughout similar processes at the industrial level. Hara *et al.* [128] found that the pressure of the system, and stirring the electrolyte, directly affected the FE for CO₂RR of the cell with the partial current density of their cell being only 375 mA/cm² although this was at 30 atm pressure. Their FE peaks in the lower pressure region with stirring compared to without stirring, determined that the thickness of the diffusion layer on the electrode surface is decreased by stirring, resulting in an increase in the flux of CO₂ at the electrode surface.

Billy *et al.* [57] showed that the rate of electrolyte flow has a key role in the cell efficiency. They had the CO₂ bubbling directly into the cell, so the electrolyte was not used to transport the CO₂ into the cell, unlike the design used in this chapter. Increasing the electrolyte flow rate from 1.5ml/min to 3.2ml/min increased HCOO⁻ formation from 10% to 20% and the CO₂ consumption rate.

Wu *et al.* [102] found that electrolyte circulation improved cell efficiency for CO₂RR, when compared to other stationary electrodes. Therefore it is necessary to examine this property in optimising the cell, as it is suspected to impact several factors, such as local temperature, electrolyte depletion and gas bubble formation. Wu *et al.*'s cell design is examined in more detail on section 4.1.2.

Griffiths *et al.* [107] also showed how the increase in electrolyte flow rate affected the current density in the FM01-LC cell discussed in section 4.11.

Effect of Gas Bubbles

Zhang and Zeng [90] investigated the effect of gas bubbles on cell performance. They modelled the formation of bubbles on a metal electrode in stagnant electrolyte. Their work shows that for detachment to occur, the critical diameter of a bubble is a function of its buoyancy, expansion force and interfacial tension force. They also found that electrolyte concentration, investigated in section 5.2.3, has a considerable impact. With the addition of electrolyte circulation, the gas bubbles detach earlier from the metal surface, due to the additional forces acting on the bubbles. Notably, they demonstrated a small decrease in the cell voltage when flowing electrolyte was used. Bongenaar-Schlenter *et al.* [91] showed that presence of an electrolyte flow reduces the cell resistance. This suggested that the volume of the cell that is occupied by bubbles, in the inter-electrode gap is a key factor and that the effects from the bubble curtain, proposed by Zhang, could be overcome.

For the variation in flow rate through the cell, the MK 2 cell, section 4.4.2, was used without the membrane support plate. The voltage applied to the pumps shown in section 4.13 was varied at three different voltages in order to supply the electrolyte at various flow rates. This was calculated by using the flow calibration, as done previously, in Figure 3.1. The catholyte and anolyte were not mixed and pumped by separate pumps, at the specified applied voltage. 0 V acted as the control, with no electrolyte flow in the cell. 5 V was the minimum voltage required for the pumps to function, with a flow rate of 17 mL/min (0.3 mL/s). The maximum applicable voltage was 20 V, which had a flow rate of 122 mL/min (2 mL/s). A range of voltages was selected between these two end points.

Results & Discussion

Each pump voltage was tested three times with the average reading being presented in Figure 5.1. The optimum flow rate was found to be 50 mL/min (0.82

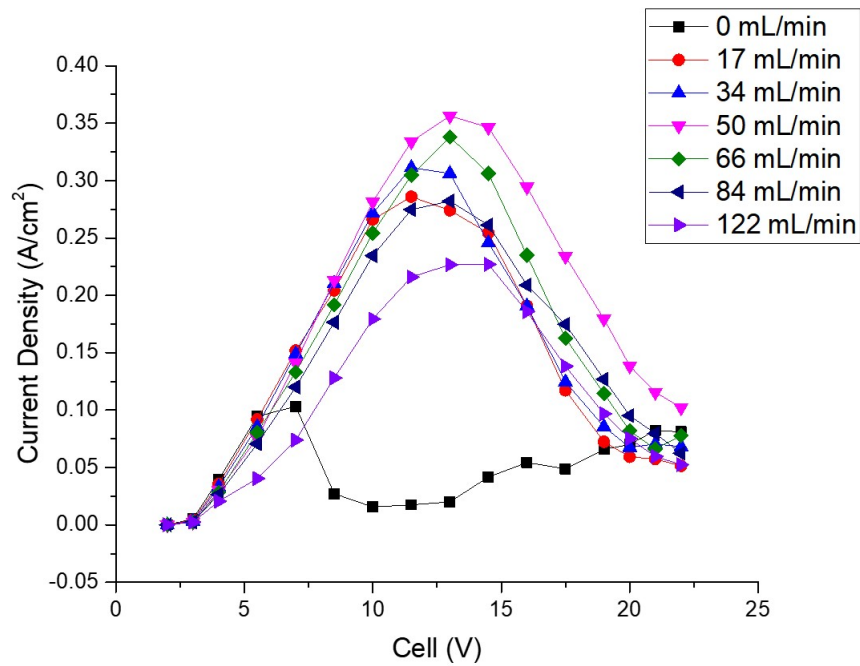


FIGURE 5.1: Plot of current density vs applied potential for varied electrolyte flow rates.

mL/s) which had one of the highest current densities at lower voltages and also peaked at the highest current density of 0.356 A/cm^2 at 13 V. Both 17 mL/min and 50 mL/min caused the cell performance to be equal until the 10 V mark where the performance of the 17 mL/min flow rate dropped off. The 50 mL/min continued to perform well up until 13 V, where it peaked at 0.35 A/cm^2 .

A flow rate of 122 mL/min was suspected to cause excessive interference between the two electrodes as the bicarbonate was moving at too great a speed increasing the distance between the electrodes. Whilst 17 mL/min caused stagnation of the cell from depletion of the electrolyte, 0 mL/min had one of the highest j at the start, up until the 5.5 V mark, where the electrolyte becomes depleted, causing the plateau and then drop in conductivity. 66 mL/min flow rate has a similar performance profile as the 50 mL/min flow rate, also peaking at 13 V, however it has a consistently lower j than the 50 mL/min flow rate and peaks at only 0.33 A/Cm^2 . The 84 mL/min flow rate performs even worse than the 66 mL/min flow rate, until 17.5 where it surpasses the performance of 66 mL/min and then has the

second highest j . Interestingly, the 84 mL/min flow rate peaks at approximately the same j as the 17 mL/min flow rate, although this is at 16 V versus the 17 mL/min flow rate's 14.5 V.

It is important to highlight that the flow rate of CO_2 was not increased with the rise in flow rate of the electrolyte. This meant that the electrolyte spent less time in the bubbler, with the same amount of CO_2 , so saturation of CO_2 will be lower at higher electrolyte flow rates. The fall in CO_2 saturation reduces the ability of the electrolyte to act as a buffer, contributing to the reduction in j . Having established that the 50 mL/min flow rate was optimum it was then used for all further testing. The drop in j , rather than a plateau, is attributed to pH build up within the cell which examined later in sections 5.2.4 and 5.2.5.

5.2.2 Effect of Electrode Separation

The distance between the electrodes was deemed to be an important factor by Nagai *et al.* [129] who showed that it had an effect on hydrogen production in the water splitting reaction. Both Passas [100] and Phillips *et al.* [98] showed this in their works, examined in section 4.1.1. It therefore stands that similar effects would be seen in the CO_2 reduction reaction (CO_2RR). The results can also be predicted using the equations examined in section C.1.3, which suggested the increase to the electrode spacing would increase the resistance of the cell, as per Ohm's law, section C.1.3.

By changing the thickness of the flow plates and gaskets (parts 3 and 4 in Figure 4.19) on the cathodic side of the membrane, the distance between the two electrodes could be varied. For these experiments the thickness of the anodic compartment remained constant at 2 mm to the Nafion from the platinum mesh, whilst the cathodic compartment was varied between the 4 different distances: 1 mm, 4 mm, 7 mm and 11 mm thicknesses. These distances were chosen due to

the available material thicknesses to produce a range of variables and their corresponding volumes are displayed in Table 5.1. The flow rate, optimised in section 5.2.1, was set at 50 mL/min.

Results and Discussion

Whilst Figure 5.2 shows little difference in current density for three of the distances, the 6 mm total separation has the optimum cell performance with the highest current density. Trend analysis shows that the closer the electrodes are, the more efficient the cell becomes.

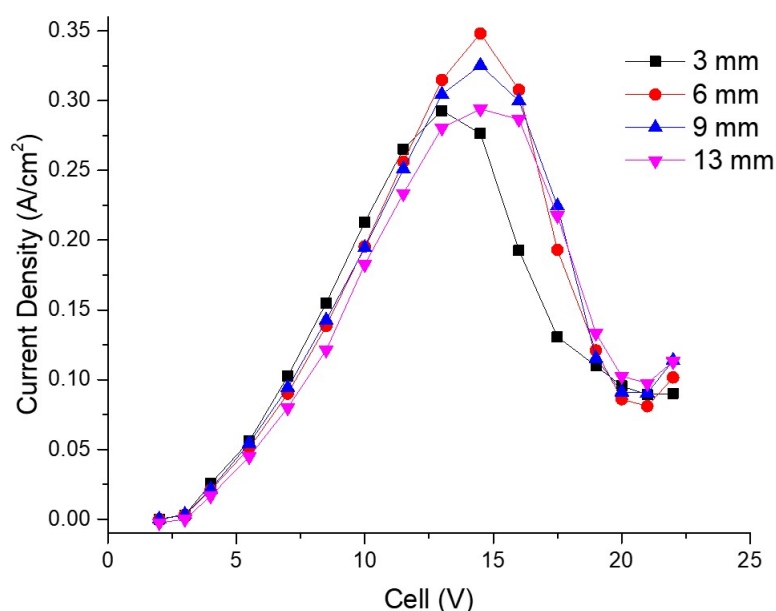


FIGURE 5.2: Plot of current density vs applied potential for different total separation distances between the two electrodes.

Total separation (mm)	Cathodic Distance (mm)	Cathodic Volume (mm ³)
3	1	2265.14
6	4	9060.56
9	7	15855.98
13	11	24916.54

TABLE 5.1: Electrode separations and resulting cathodic volumes.

In contrast, the 3 mm separation does not perform as expected. The graph demonstrates that the 3 mm separation (2 mm anodic, 1 mm cathodic) performs better up to the 11.5 V mark, where it starts to peak and then becomes the worst performing separation. The most likely limiting factor is the reduced internal cathodic volume as only 2.27 mL of electrolyte is directly in between the cathode and the membrane. This 227 mm³ volume does not allow much space for bubbles that are formed during the CO₂RR and therefore reduces the active surface area of the electrode, which could result in the reduced current density seen. There is also a case where the active surface area remains unchanged but the amount of electrolyte in the cell drops due to the bubbles and correspondingly there is less ion conductor (electrolyte) in the compartment causing a drop in current density.

As previously discussed in section C.1.3, current density is dependent upon $R_{\text{electrolyte}}$ which is affected by the distance between the electrodes. As the separation increases the resistance also increases, decreasing the current density at a given voltage. Additional distance between the electrodes means that there is more electrolyte between the electrodes. Although the resistance of the electrolyte, is relatively small there is still an increase in resistance and therefore a reduction in current density that passes through the cell. Equation C.4 shows that the increase in $R_{\text{Electrolyte}}$ will increase the specific resistance of the cell.

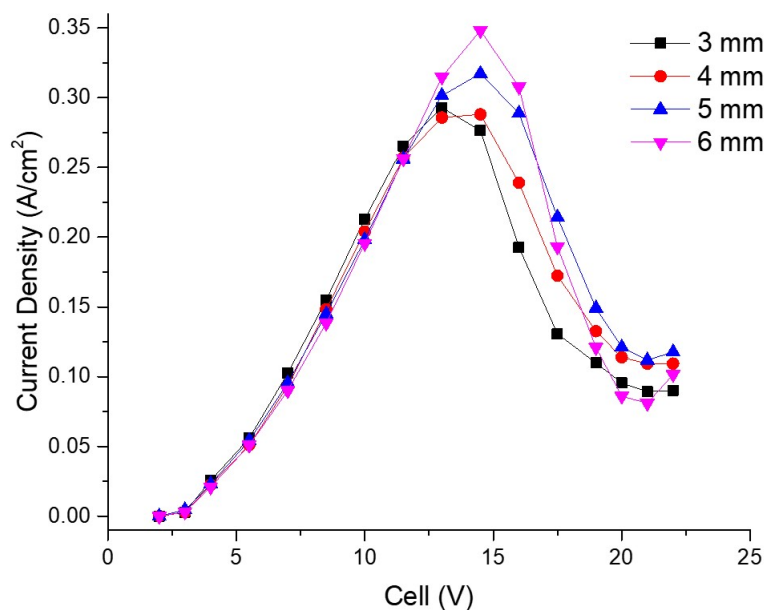


FIGURE 5.3: Plot of current density vs applied potential for different total separation distances of the electrodes between 3 mm and 6 mm.

A secondary experiment looked at additional separations between 3 mm and 6 mm, as shown in Figure 5.3. The 6 mm total spacing achieves the best peak current density, however this is at 15 V which is much higher than the cell would be expected to operate. On examination of the lower voltages, in Figure 5.4, the 3 mm total separation consistently out performs the other distances up to the 11.5 V mark where it becomes the worst performing cell, for reasons previously discussed. Therefore it was determined that the 3 mm was the optimum electrode separation to proceed to the product analysis stage with. However, if there is a considerable increase in bubbles generated due to another variable in the cell or refinement during FE testing, the total spacing will need to increase to 4 mm or 5 mm.

Once again the drop current density (above 15v), rather than a plateau, is attributed to pH build up within the cell which examined later in sections 5.2.4 and

5.2.5. More detailed Figures can be found in Appendix A

Total separation (mm)	Cathodic Distance (mm)	Cathodic Volume (mm ³)
3	1	2265
4	2	4530
5	3	6795
6	4	9060

TABLE 5.2: revised electrode separations and resulting cathodic volumes.

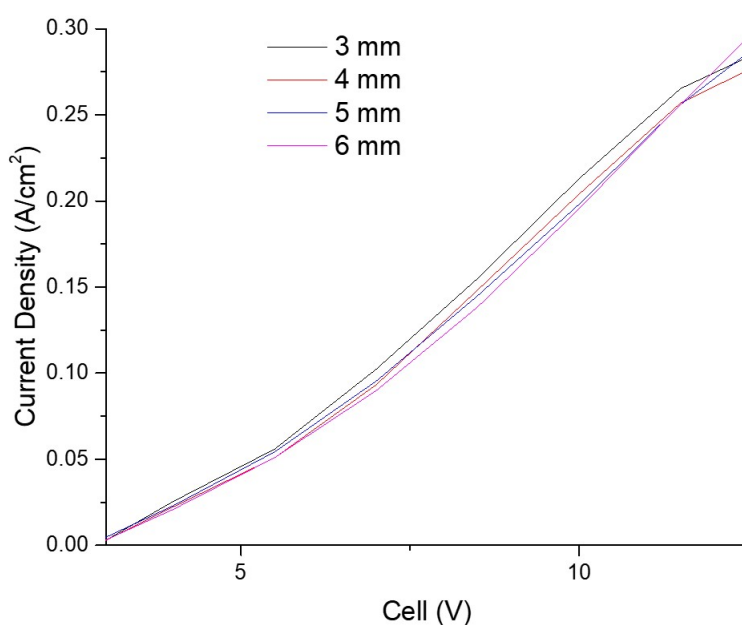


FIGURE 5.4: Plot of current density vs applied potential for total electrode separations between 3 mm and 6 mm, for applied potentials from 2.5 V to 12.5 V.

5.2.3 Effect of Electrolyte Concentration

High FE for methane and ethylene were observed by Hori and collaborators when 0.1–0.5 M HCO_3^- solutions were used [67, 130, 131]. They suggested that when a weak acid such as HCO_3^- was the supporting electrolyte, the pH near the electrode surface could be maintained lower than if a non-acid was used.

This higher $[H^+]$ concentration increased the yield of hydrocarbons in the reduction of CO_2 . Different electrolyte concentrations were examined: the 0.1 M value was taken from the works by Ahn [95] and more recently, Rudd [93] (the cell examined in section 4.1.1). The 0.01 M and 1.0 M variables were extrapolated from this value, with the remaining values selected during a second phase of testing in order to have sufficient data for machine learning optimisation.

For the variation in electrolyte concentration flowing through the cell, the cell was used as per section 4.5.5 with no physical changes being made. The flow rate, optimised in section 5.2.1, was set at 50 mL/min. The electrode spacing, optimised in section 5.2.2, was set at 3 mm total separation.

Results and Discussion

As expected, and shown in Figure 5.5, the 2.0 M electrolyte performed the best with the highest current density of the examined concentrations. However, liquid droplets were observed on several components of the system whilst examining the higher concentrations of $KHCO_3$. A thermometer was used to measure the temperature of the cathodic electrolyte after each electrolysis. The temperature for 2 M peaked at 76 °C, a considerable increase from the starting temperature of 19.5 °C. This heating effect was subsequently examined on the lower concentrations where the 0.2 M showed a thermal increase of only 5 °C, with lower concentrations not showing any significant change in temperature.

High FEs for C_2 products (as reported in current literature) are not seen at the high voltages used in these experiments, so temperature should not be a problem in later testing. It will have an effect on the conductivity of the electrolyte as rising temperature increases mobility of the dissolved ion [132]. Therefore the temperature increase will have affected the current density recorded for the higher molarities where the temperature increase was observed.

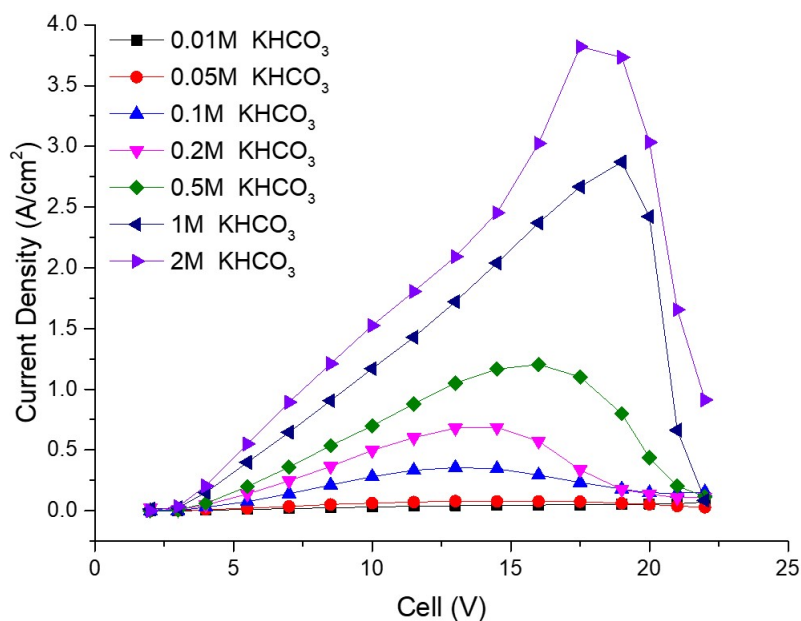


FIGURE 5.5: Plot of current density vs applied potential for different electrolyte concentrations.

Bicarbonate crystal growth was observed on several parts of the system whilst testing the 1.0 M and 2.0 M concentrations, suggesting that despite the highest current density, they may not be suitable for long durations. It is proposed that this increase in conductivity is attributed to the number of ions in the electrolyte.

Figure 5.5 shows that 0.2 M KHCO_3 has the highest current density. Kas *et al.* [72] saw the highest FE for ethylene at 0.1 M KHCO_3 suggesting this is the best concentration to use, although they also showed a higher CO FE which is not seen at higher concentrations. Varela *et al.* [133] also found that although current density is greater at higher molarities of KHCO_3 , the optimum concentration for ethylene FE is 0.1 M.

As the current focus of this project is the enhancement of ethylene it was decided to focus on the 0.1 M KHCO_3 , despite larger concentrations having higher peak current density (j).

Once again each parameter showed a drop in j after reaching a peak, rather than a

plateau, is attributed to pH build up within the cell which is examined in sections 5.2.4 and 5.2.5.

5.2.4 Effect of Supplied Gas

After the thermal observations in the previous section, it was decided to investigate the pH changes in the electrolyte. The experiments from section 5.2.3 were repeated for 0.01 M, 0.1 M and 1 M concentrations. It was found that for both the 0.1 M and the 1.0 M KHCO_3 had considerable pH changes. The cause and effects of this variation required further examination as they could have a considerable impact on the long term performance of the cell.

To examine the effects of the dissolved CO_2 , experiments were conducted at 0.1 M and 1 M KHCO_3 with CO_2 or N_2 being bubbled into the cathodic reservoir. Both gases were bubbled for 10 mins through the bubbler before the potentials were applied. For the variation in supplied gas to the electrolyte bubbler the cell was used as per section 4.5.5 with no physical changes being made. The flow rate, optimised in section 5.2.1, was set at 50 mL/min and the Electrode spacing (see section 5.2.2), at 3 mm total separation. The pH was measured using a digital pH probe as per section 3.4, in the anodic and cathodic reservoirs after every applied potential (before the two minute gap).

Results

Figure 5.6 shows current density versus voltage applied to the cell with 0.1M KHCO_3 , which was saturated with either CO_2 or N_2 , supplied to the bubbler at 48 mL/min. Figures 5.7 and 5.10 show the pH after each potential step for the CO_2 and N_2 electrolytes respectively. Figure 5.9 shows an identical setup but with 1.0M KHCO_3 , with Figures 5.8 and 5.11 again showing the pH after each potential step for the CO_2 and N_2 saturated electrolytes. The higher electrolyte

concentration was included despite the operating difficulties previously identified to show that the cell was not limited by the electrical conductivity of the electrolyte.

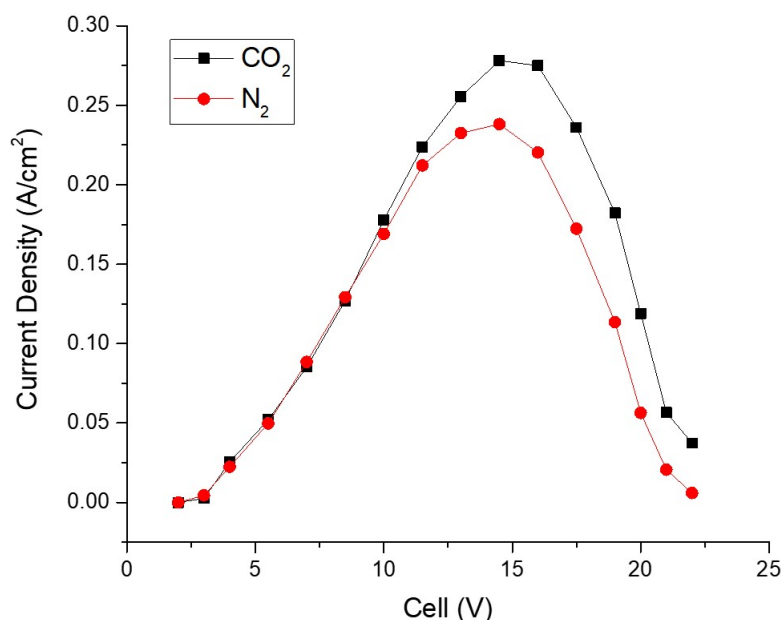


FIGURE 5.6: Plot of average current density vs applied potential for carbon dioxide and nitrogen at 0.1 M KHCO₃ circulated at 50 mL/min in dual reservoir system.

For the 0.1 M KHCO₃, Figure 5.6, the CO₂ saturated KHCO₃ reached a peak current density (j) of 0.279 A/cm² at 14.5 V, with the N₂ saturated KHCO₃ only reaching 0.23 A/cm² also peaking at 14.5 V after which the j begins to drop producing a bell shaped graph. Figure 5.7, shows the pH of the anodic and cathodic reservoirs for the CO₂ saturated 0.1 M KHCO₃, where the pH of both reservoirs remains relatively constant up to 13 V where the anodic reservoir begins to drop in pH down to 5.1 whilst the cathodic reservoir remains relatively constant. For Figure 5.8, the N₂ saturated 0.1 M KHCO₃, the pH for both start around 8.6 but after 4 V they show significant variation with the anodic pH steadily decreasing to 4.2 at 22 V whilst the Cathodic pH increased to 11.2.

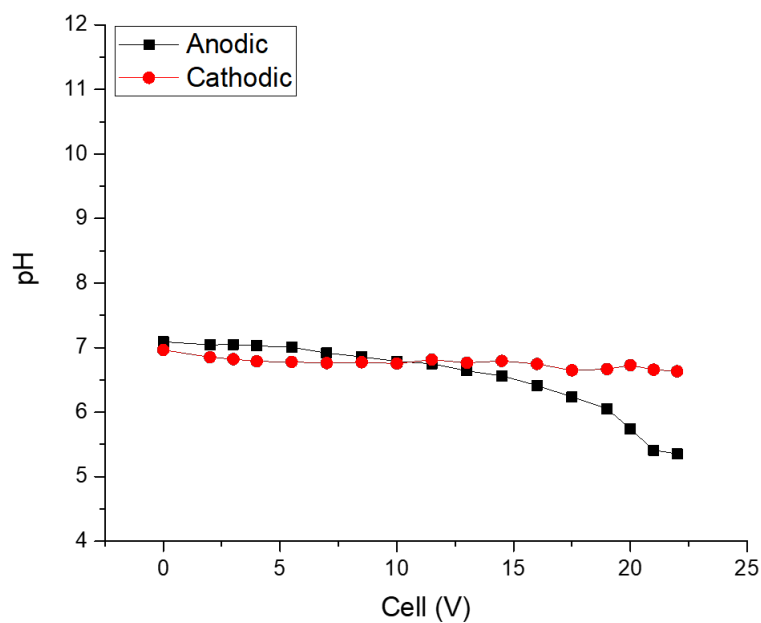


FIGURE 5.7: Plot of average pH of the electrolyte vs applied potential for carbon dioxide bubbled 0.1 M KHCO_3 circulated at 50 mL/min in a dual reservoir system.

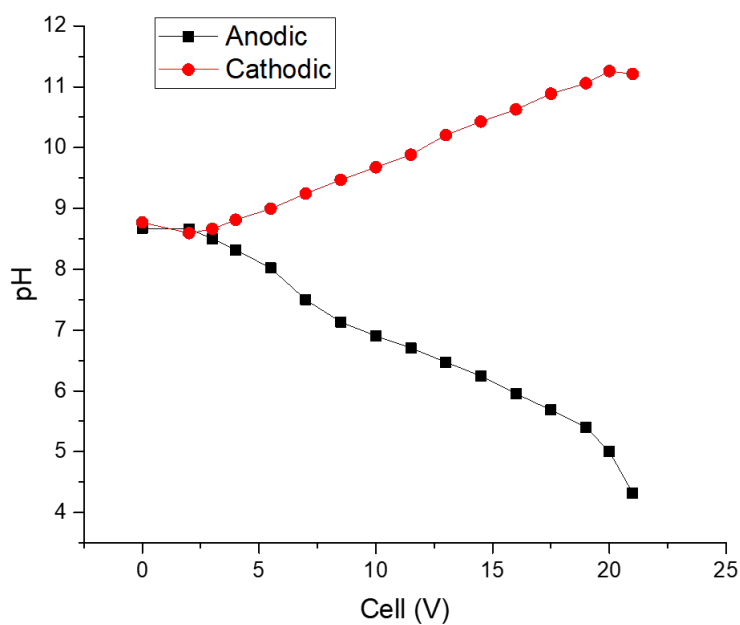


FIGURE 5.8: Plot of average pH of the electrolyte vs applied potential for nitrogen bubbled 0.1 M KHCO_3 circulated at 50 m/min in a dual reservoir system.

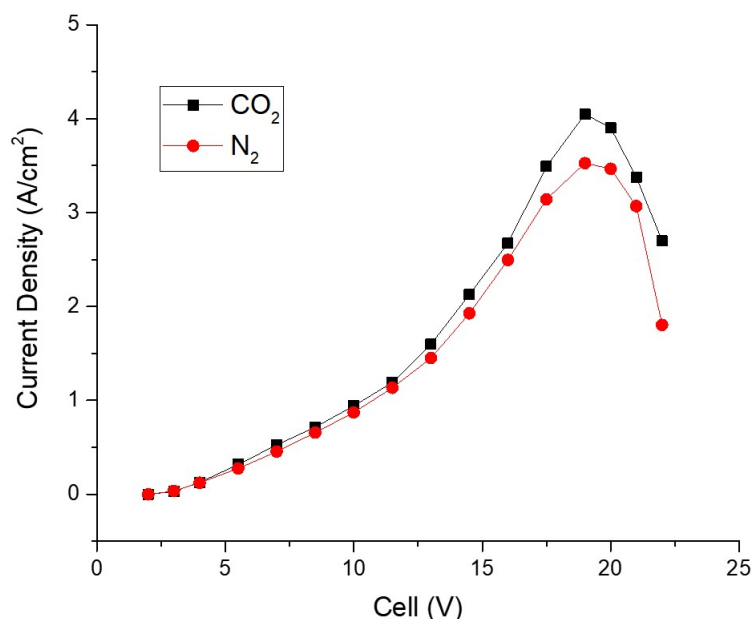


FIGURE 5.9: Plot of average current density vs applied potential for carbon dioxide and nitrogen at 1.0 M KHCO_3 circulated at 50 mL/min in dual reservoir system.

For the 1 M KHCO_3 , Figure 5.9, the CO_2 saturated KHCO_3 reached a peak current density of 4.05 A/cm^2 at 19 V, with the N_2 saturated KHCO_3 only reaching 3.52 A/cm^2 also peaking at 19 V after which the j begins to drop. Figure 5.10, shows the pH of the anodic and cathodic reservoirs for the CO_2 saturated 1 M KHCO_3 , where the pH of both reservoirs remains relatively constant up to 4 V with the cathodic pH around 7.6 and anodic around 8.3, after which the anodic pH decreases to around 7.5 between 8.5 V and 13 V before further decreasing to 5.4 pH. After 4V the cathodic pH steadily increases before remaining relatively constant around 8.8 pH mark. For Figure 5.11, the N_2 saturated 1 M KHCO_3 , the Anodic pH starts a 8.3 and steadily drops 6.5, at 17.5 V, before decreasing more rapidly to 5.4 at 22 V. The cathodic pH starts at 8.9 and increases steadily to 10.1 at 14.5 V before increasing more rapidly to 13.5 at 22 V.

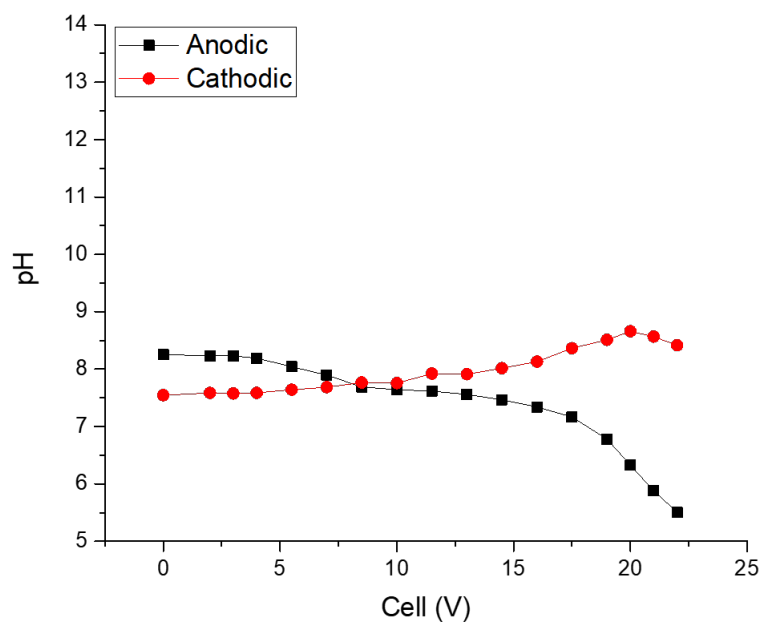


FIGURE 5.10: Plot of average pH of the electrolyte vs applied potential for carbon dioxide bubbled 1.0 M KHCO_3 circulated at 50 mL/min in a dual reservoir system.

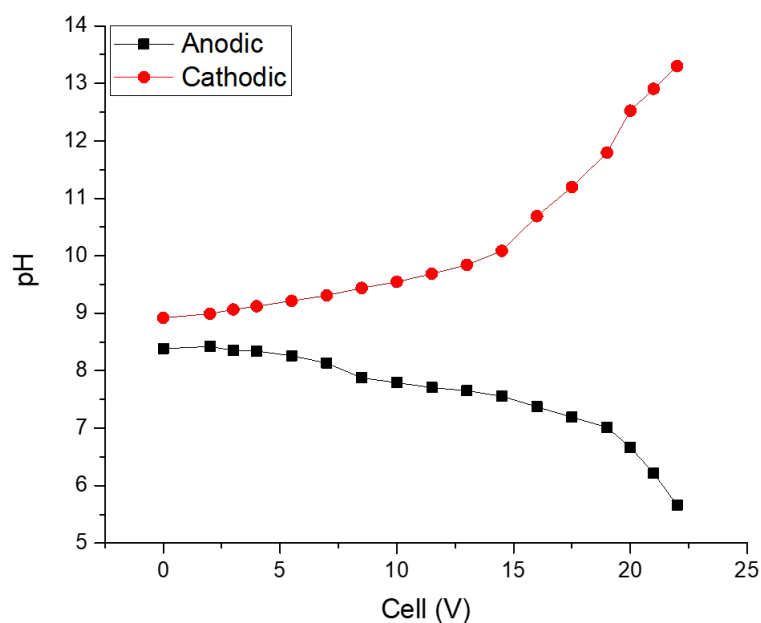


FIGURE 5.11: Plot of average pH of the electrolyte vs applied potential for nitrogen bubbled 1.0 M KHCO_3 circulated at 50 mL/min in a dual reservoir system.

Discussion

Under the nitrogen saturated conditions there is a clear pH change within the cell as seen when comparing Figure 5.7 with 5.8 and Figure 5.10 with 5.11. This shows that the cell can build up a considerable pH differential (Figure 5.8 versus 5.11), which can be clearly measured in the electrolyte reservoirs. This effect on the pH is not seen in the electrolyte reservoirs of the CO₂ saturated electrolyte (Figure 5.7 vs 5.10), due to the buffer effect of CO₂ in KHCO₃.

Examining Figure 5.6 whilst considering Figures 5.7 and 5.8, it can be observed that the CO₂ bubbled experiment obtains a higher current density whilst maintain a relatively constant pH. The same can be seen at 1.0 M KHCO₃, for Figure 5.9 utilising Figures 5.10 and 5.11 although there is a considerable difference between the endpoints of the 0.1 M KHCO₃ pH plots and the 1.0 M KHCO₃ pH plots.

As presented in Section C.3.1 the Electrolyte is a equilibrium of CO_{2(aq)}, HCO₃⁻ and CO₃²⁻, as seen in Figure C.3 a change in pH must be due to an change or imbalance in this equilibrium. As the drop in performance is not due to the electrolyte concentration or the amount of CO₂ present, the most likely cause of this is a mass transport issue caused by the membrane being unable to transport the OH⁻ ions fast enough.

5.2.5 Effect of System Configuration

With the pH changes observed in the previous section it was necessary to investigate their causes and potential ways in which they could be mitigated. The first consideration was the single reservoir system used by Jeanty et al (considered in section 4.1.2) whilst examining the continuous operation of an electrochemical cell converting CO₂ to CO [101]. The dual reservoir system, Figure 4.13 has been

shown to produce significant pH changes in the electrolyte and a change to a single reservoir system could have a significant effect on the pH of the catholyte and anolyte, improving current density. By mixing the acidic anolyte and the basic catholyte, the pH of the electrolyte could neutralise each other, producing a more stable system for CO₂RRs.

This change in system design would also allow for the testing of Nafion membrane alternatives, previously tried in section 4.4.2, as the build up of electrolyte on one side of the cell would be automatically re-balanced between the two halves of the cell.

The third consideration was re-routing the tubing connecting the cell to the reservoirs, seen in Figure 4.13 to allow the catholyte and anolyte to mix. The associated schematic is shown in Figure 5.12.

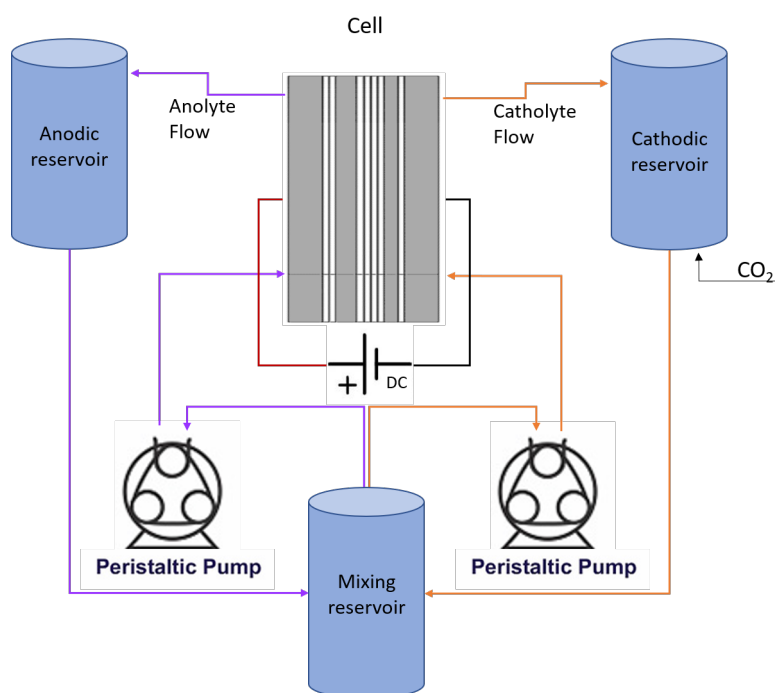


FIGURE 5.12: Schematic drawing of the designed system, modified for electrolyte mixing.

The cell was tested with the outputs from both electrolyte chambers being passed into a single, joint reservoir creating a Single Reservoir (SR) System. This was

compared against the Dual Reservoir (DR) System, where the anolyte and catholyte were kept separate.

For the variation in system configuration, the cell was used as per section 4.5.5 with no physical changes being made to the cell. The flow rate, optimised in section 5.2.1, was set at 0.054 mL/m (10v supplied to pumps). The electrode spacing, detailed in section 5.2.2, was set at 3mm total separation where the supplied gas was CO₂. The pH was measured using a digital pH probe as per section 3.4, in the anodic and cathodic reservoirs after every applied potential (before the 2 minute gap).

Results

Figure 5.13 shows that the SR system outperformed the DR configuration at 0.1 M KHCO₃, for current density at all applied voltages, with the highest current density at 0.75 A/cm² at 22 V, with no drop in current density. Unlike, as previously seen, the DR system which peaks at 0.279 A/cm² at 14.5 V before steadily decreasing to zero, in a bell curve shape. Figure 5.14 shows that the corresponding pH measured, in the combined reservoir of the SR system configuration, remains relatively constant at around 6.9 pH, for 0.1 M KHCO₃.

Figure 5.15 shows that for 1 M concentration, the SR configuration again has a higher j than the DR one, at all applied cell voltages, reaching a maximum value of 6.01 A/cm², at 22 V, compared to the 4.05 A/cm² at 19 V on the DR configuration, which then drops in j . Figure 5.16 shows the 1 M KHCO₃'s associated pH for the single reservoir system, which remains constant 7.8 pH mark.

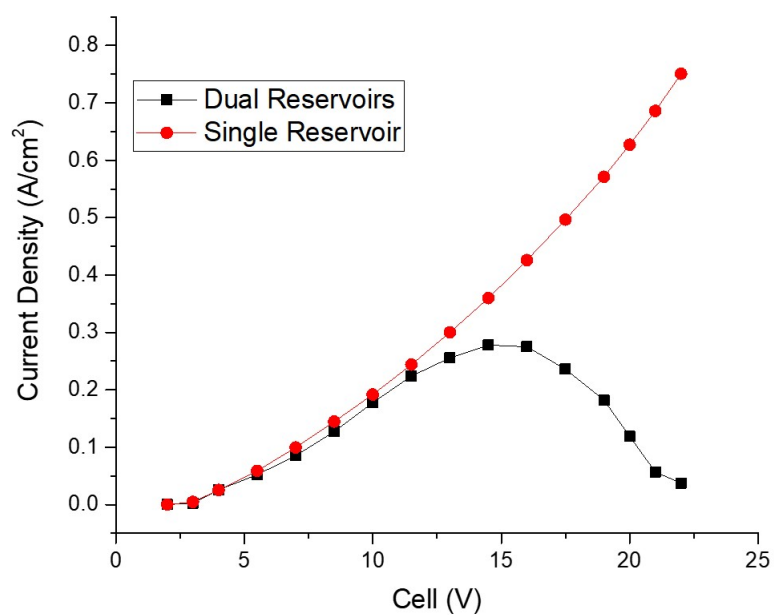


FIGURE 5.13: Plot of current density vs applied potential for combined and separate reservoirs at 0.1 M $KHCO_3$.

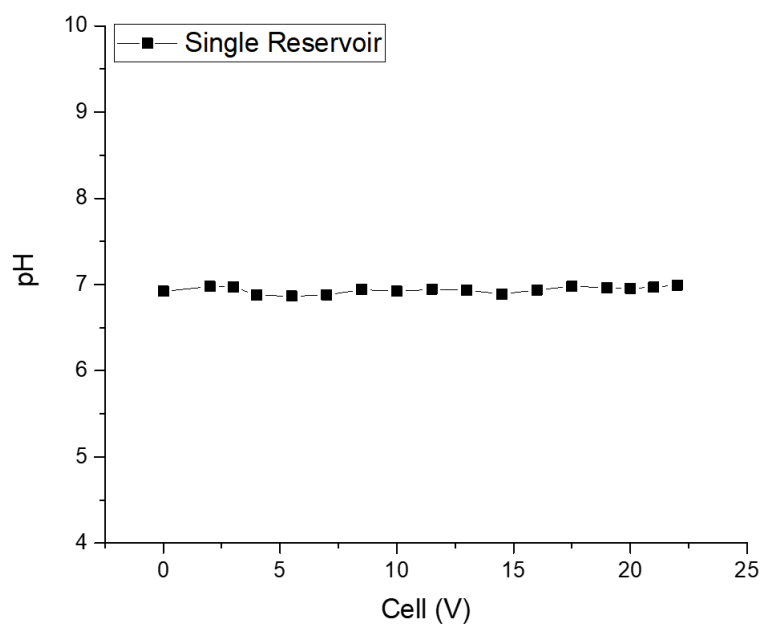


FIGURE 5.14: Plot of pH vs applied potential for carbon dioxide bubbled 0.1 M $KHCO_3$ in a single reservoir system.

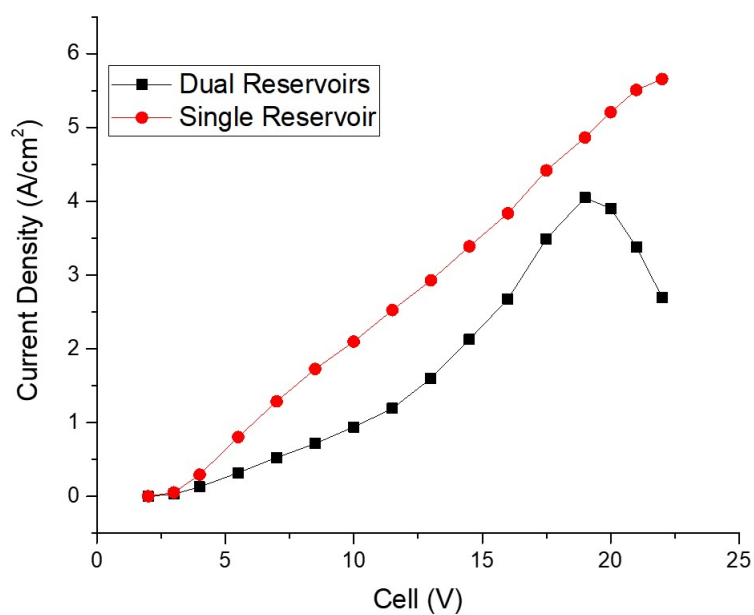


FIGURE 5.15: Plot of current density vs applied potential for combined and separate reservoirs at 1.0 M KHCO₃.

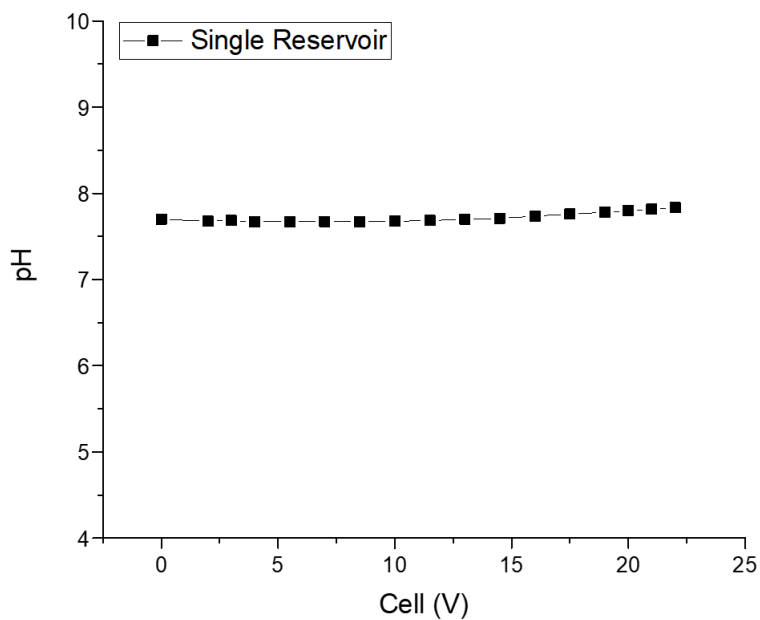


FIGURE 5.16: Plot of pH vs applied potential for carbon dioxide bubbled 1.0 M KHCO₃ in a single reservoir system.

Discussion

The key factor in Figures 5.13 and 5.15 is that the SR system configurations do not show a peak in j , unlike the DR system configuration as has been observed in previous experiments. From this, the drop in j for the DR systems can be attributed to proton distribution within the cell. The drop in j comes from the lack of protons in the cathodic side of the cell and the build up of protons in the anodic side of the cell, due to the proton transport limitations of the Nafion membrane. This causes an increase in resistance within the cell which reduces the amount of current that can be passed. The SR system configuration provides a way of preventing the proton differential by directly mixing the anolyte and catholyte after it leaves the cell.

A key issue is that the pH cannot be measured in the cell, due to the size of the available probe, and could only be effectively be monitored in the electrolyte reservoirs. The volume of the cell takes 2.8 seconds to be refreshed at a flow rate of 50mL/min. The approximately 14 mL volume of the cell is then diluted in a 1:8 ratio as it enters the reservoir, with approximately 25 mL being in the rest of the system. This means that the measured pH is much more neutralised than the pH at the electrode surface inside the cell.

With the limiting factor mechanism detailed, the profile of the DR system at 1 M (Figure 5.15) can be discussed. The DR at 1 M performs differently to the bell curve seen at 0.1 M which can be attributed to the increase in temperature, seen in section 5.2.3, for concentrations greater than 0.2 M KHCO_3 . As temperature increases the mobility of the ions in solution rises which means that the protons have more mobility and can pass through the Nafion membrane at a greater rate, lowering the pH imbalance and increasing the charge passed. However this increased current flow means that less heat is generated from the reduced resistance within the cell. This temperature increase does not increase linearly with the increase in applied potential across the cell meaning there is still a peak in j as the

ion mobility increase is insufficient to prevent the proton differential from occurring.

5.2.6 Effect of Electrode Surface Morphology

With the literature detailing several different nano materials for CO₂RR, section 2.2 it was important to investigate their effect on the j of the cell. Current density is the units of charge per unit of Surface Area (SA) but there are multiple ways of measuring the surface area. The cell is designed to hold an electrode of a specific Geometric Surface Area (SA_g) which cannot be increased without increasing the dimensions of the entire cell. However, it is possible to increase the Electrochemical Surface Area (SA_{ec}) without changing the geometrical surface area.

Method

The copper foam was electro-deposited, using scaled method from previous works [93, 95] for a 2 cm² electrode (SA_g). The foam and its properties are discussed in greater detail in Chapter 7, which concentrates on how the foams can be modified for product selectivity.

For the variation in electrode surface morphology, the cell design was used as in section 4.4.2 without the membrane support plate and with an additional gasket to increase the distance between the cathode and the membrane, allowing for the extra space occupied by the foam, creating a 4 mm total separation. The flow rate, optimised in section 5.2.1 above, was set at 50 mL/min, flowing through the DR system configuration. 0.1 M KHCO₃ was used, with CO₂ bubbled into the catholyte.

5.2.7 Foam Scaling

The foams were prepared as per section 3.1, with 0.01 M of applicable modifier in the electrolysis bath, on a 2 cm² copper plate. The foams that Rudd *et al.* [93]

deposited from a 15 seconds electrodeposition on their 7 mm² electrode were visually much thicker than the foam on the 2 cm² electrodes used in this work within the same deposition time, as shown in Figure 5.17. Consequently, the time was extended to obtain a foam of the same thickness, as per the works of Shin *et al.* [134]. 45 seconds was deemed suitable as it generated a similar foam to those presented in Rudd *et al.* [93], whilst allowing for the applied modifiers to have an effect on the rate of deposition. Faraday's law (C.39) was used to confirm that the same amount of deposition per electrode surface had occurred by ensuring that the charge passed per electrode surface area was the same for the 2 cm² electrode as the 7 mm².

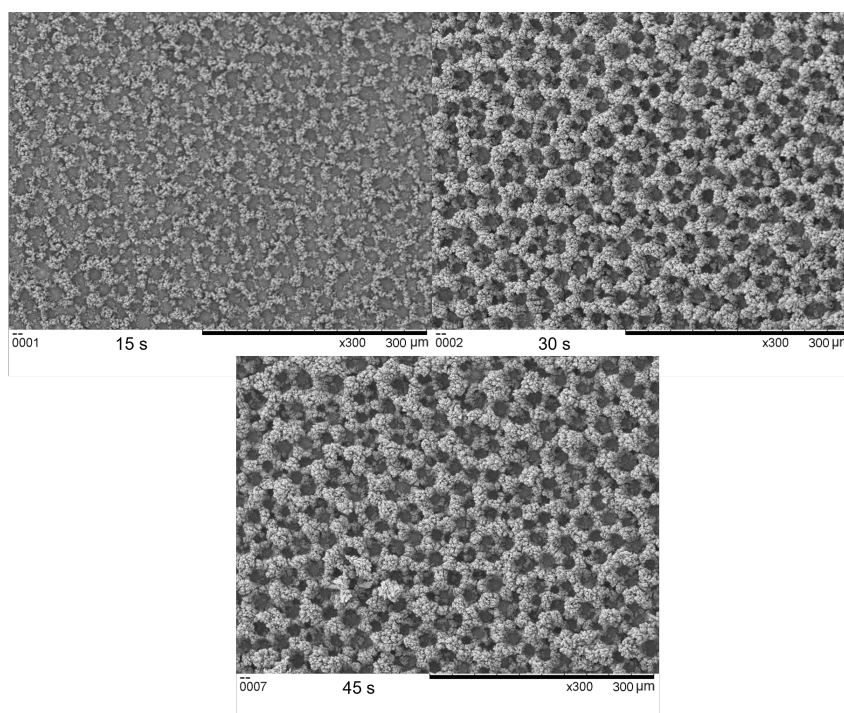


FIGURE 5.17: SEM images of a Plain foam after 15, 30 and 45 seconds of deposition.

Rudd *et al.* [93] deposited foams for 15 seconds and a much thicker foam was produced on that 7 mm² electrode than was evident on the 2 cm² electrodes used in this work within the same deposition time, as shown in Figure 5.17. Consequently, the time was extended to obtain a foam of the same thickness, as per the

works of Shin *et al.* [134]. 45 seconds was deemed suitable as it generated a similar foam to those presented in Rudd *et al.* [93], whilst allowing for the applied modifiers to have an effect on the rate of deposition.

Results and Discussion

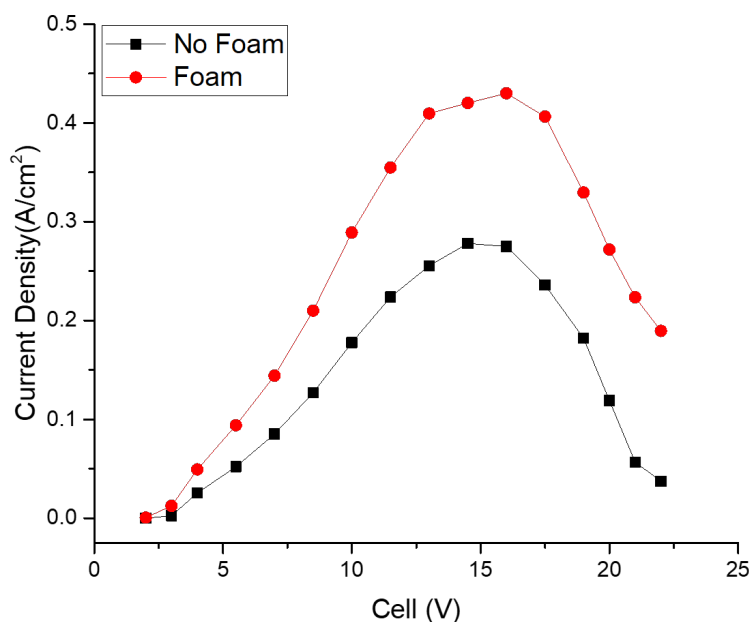


FIGURE 5.18: Plot of current density vs applied voltage for a Cu foam and a plain electrode, utilising 0.1 M KHCO_3 .

From Figure 5.18 it is clear to see that the foam considerably increases the conductivity of the cell, with the foam electrode reaching 0.43 A/cm^2 at 16 V versus the plate electrode only 0.28 A/cm^2 at 14.5 V. Whilst the geometric surface area of the electrode remains the same, the electrochemical surface area is greatly increased by the presence of the foam, allowing for much more interaction with the electrolyte, resulting in a higher current density. As presented in section C.2, electrical conductivity is highly dependent upon the electrochemical surface area, the foam allows for this to be increased without increasing the geometric surface area.

Although the foams had been examined previously, by Ahn *et al.* and Rudd *et al.* [93, 95] the foams had not been examined at this scale, shown by the difficulties in adapting the method. This section showed that the foams could successfully be grown on a larger electrodes, producing a similar performance increase.

5.3 Chapter Summary

In this chapter, the designed and built electrochemical cell, has been characterised for its electrical and physical properties. From this an optimum operating configuration has been established on which electrochemical testing can be conducted. These cell operating parameters are:

- Flow rate of 50 mL/min.
- 3 mm total separation, (1 mm cathodic 2 mm anodic)- to be increase to 4 mm total separation (2 mm cathodic) Cu foam inclusion.
- CO₂ saturating the electrolyte is vital for the operating stability of the cell, stabilising the pH.
- DR system configuration.
- Electrochemical surface area enhancement.

The limiting factor of the cell has been established as the proton transport across the Nafion membrane. The results from this chapter show that up to 10 V applied across the cell, pH imbalance is not seen and that operating the cell in a DR system configuration effectively separates the CO₂RR products, without pH limitation.

It should be noted that this optimisation gives no consideration to the products of the electrocatalysis, which will explored in Chapter 7. The parameters for optimised current, providing the minimum resistance in the cell, are far outside those

reported for high ethylene selectivity. Although no chemical analysis was performed, it was necessary to examine and optimise the cell physically and electrically before examining how the performed chemically under CO₂RR conditions.

5.4 Outlook and Future Work

In future more investigation could be conducted into further parameters, such as the effects of temperature, gas saturation approach, electrode surface area and cell configuration. More parameters could be optimised for conductivity, further reducing the over potential in the cell, however it is a priority to concentrate on product efficiency and selectivity if this technology is to progress.

In this chapter, two parameters were identified, that have not been investigated fully; the operating temperature of the cell and the geometric surface area of the cell and as such should be investigated in future works.

Temperature

As electrolytic conductivity is measured at a fixed temperature, as seen in section C.20, the conductivity will change with temperature. Miller *et al.* [132] discussed how the conductivity of the electrolyte increases as temperature increases due to the enhanced mobility of the ions in solution. Hayashi *et al.* [135] showed that the electrical conductivity, of saline water, varies with temperature, in a 'slightly non-linear', way, between 0 – 30°C, with Cardona *et al.* [136] showing that KHCO₃ behaves similarly. As such the current density of the designed cell should be investigated at different temperatures as this would allow for further refinement of the data collected in this chapter, during the collection of which temperature variation was observed.

Effect of Electrode Surface Area

Section 5.2.6 showed that an increase in electrochemical surface area improved current density. This SA increase was done through the utilisation of a copper foam and did not increase geometric SA. The cell was designed to be able to operate with an active electrode SA of 16 cm^2 ($4 \times 4 \text{ cm}$), however due to the limitation on the maximum geometric SA for foam deposition this increase electrode area was not investigated. By using the multiple electrode plates (section 4.4.1).

Chapter 6

Testing Optimisation and Machine Learning

6.1 Introduction

With the global COVID-19 pandemic, the way that research was able to be conducted greatly changed for a prolonged period of time. With the traditional trial and error (and subsequent refinement) approach constrained due to lack of access to lab facilities, a new optimisation method was required. Recent advances in Machine Learning (ML), and their increased use in materials science [137] has lead to the rapid growth of materials databases, the gradual spread of ML toolkits and the further development of algorithms. Recently ML has been applied to several CO₂RR electrocatalysis cells and cell components, as well as optimising a Microbial Fuel Cell for voltage output in a two-electrode cell, with multiple membranes [138]. ML was used in the design and screening of new electrocatalysts by Zhong *et al.* [139] and Zang *et al.* [140]. Wu *et al.* [141] used ML to screen 289 adsorbates for improving the efficiency of copper electrodes for CO₂RR.

In typical ML process, computers are trained on the provided data, using a given learning model. ML software can automatically learn from empirical data (training data) and then determine the linear or nonlinear relationships between the

data sets. Unlike traditional hard-coded approaches, where the algorithm is pre-programmed by a human expert, ML approaches learn directly from the data set, analysing the rules dominating the data set and build a model to make predictions. A trained ML model needs to make predictions to evaluate model accuracy for validation and further optimization. The valuation model should be verified to ensure the reliability of the prediction results. Usually, 80% of the samples are randomly selected as the training set and the remaining 20% of samples as the test set. This random running of the test set from samples is called cross-validation [142]. In addition to failing to make predictions accurately, an unsuccessful model will have a high bias (underfitting) if it finds insufficient data for applicable rules, or the algorithm is not flexible enough to reflect the relationship between input and output data. High variance (overfitting) occurs if the model is too complex and has too many parameters [140]. Feature engineering, extraction and selection is the critical next step to extract inputs to train a ML model from data, which is fundamental to ensure the applicability and feasibility of ML models. Then the ML algorithms are selected to build a model and learn from the data before the model can be finally, evaluated and optimised.

6.2 Method

Method selection

Several different algorithms have been proposed over the last decade to provide solutions for processing data [143]. The selection of the most appropriate ML model is key, as it significantly affects the ML performance [144]. ML methods can be divided into supervised [143], semi-supervised [145] and unsupervised [146] learning mainly determined by the amount of features (input data) and corresponding labels (output data) available. Due to the comparatively small data set produced by CO₂RR experiments, unsupervised learning

and semi-supervised learning algorithms for electrocatalyst are rarely reported. As such supervised learning will be used in this model, so that the relationship between input and output can be used to predict the output value when giving a specific input value.

Adaptive Network-based Fuzzy Inference System (ANFIS)

One of the most common techniques is Fuzzy Logic (FL) which enables effective data handling with uncertainty. This uncertainty arising from errors in the measurement instruments or the data is superimposed with noise. Another merit of using FL is the efficiency in modelling complex systems even if it has non-linearity in the input-output relationship, with FL successfully modelled data in several engineering applications [147–149].

FL can be thought as an extension to the tradition Boolean Logic (BL): a fuzzy set is an extension to the traditional binary set that contains only two elements (0, 1). BL deals with only two digits in the sense that a mapping of an element x to a group A is defined as either x is a member ($x \in A$) or not a member ($x \notin A$) of a group A ; if it is a member it is mapped with 1 otherwise it is mapped with 0. However, FL changes this idea to accept multi-valued mappings in the range (0-1). With this new prospective, partial degree of membership is applicable.

The first process in the fuzzy modelling is to fuzzify the input variables through membership functions (MFs) to obtain their corresponding fuzzy values. Any MF that satisfies the two features of convexity and normality can be nominated as a MF. The triangular and gaussian shapes are very popular MFs due to their mathematical simplicity in the learning process. Unlike mathematical equations that describe the relation between the inputs and the output, fuzzy systems formulate this relationship as an IF (antecedent) – THEN (consequence) rules. Usually, these rules are built either by experts or from the measured data. There are two

methods to obtain the rules from the data: Grid-Partitioning and Subtractive-Clustering. The latter is recommended because it ends up with the minimum number of rules.

Fuzzy rules are classified according to the rule's form which fall into two types: Mamdani-type and Sugeno-type. In both types, the antecedent represents a logical combination of the inputs and their fuzzy mapping. On the other hand, the consequence, which represents the output, is either a fuzzy mapping or a function of the inputs. Fortunately, to handle very complex systems, this function can be linear or non-linear. Examples of the two types of rules are shown in Equations 6.1 and 6.2, respectively:

$$\text{If } a_1 = MFa_1 \text{ and } a_2 = MFa_2 \text{ then } b = MF_b \quad (6.1)$$

$$\text{If } a_1 = MFa_1 \text{ and } a_2 = MFa_2 \text{ then } b = \int(a_1, a_2) \quad (6.2)$$

Where: MFa_1 and MFa_2 are two inputs membership functions; MF_b is the output's membership function; $\int(a_1, a_2)$ is a function of the two inputs.

The choice of the rule's type is application dependent. Usually, Mamdani-type is recommended in control applications while Sugeno-type is recommended in modelling applications. As soon as each rule has produced its output, they are aggregated together to produce a one final fuzzy output. Then, it is defuzzified to produce its corresponding crisp value. The defuzzification method is selected according to the rule's type. In case of Mamdani-type, the Centre of Area is the best nomination while the Weighted Average is recommended in case of Sugeno-type.

In 1993, Jang [150] proposed an integration between Adaptive Neural Networks

and FL to produce the Adaptive Network-based Fuzzy Inference System (ANFIS), which utilises the Sugeno-type fuzzy rules. The model is taught by a hybrid method of Least Square Estimator and Back Propagation, and is one of the most effective and efficient choice to model systems with non linearity. Accordingly, it has been applied in the current work to build the model of the electrolysis cell.

Optimisation method

Particle Swarm Optimisation (PSO) was developed from Metaheuristic Algorithms, with the main advantage, that it is a gradient-free technique. The goal of the optimiser is to find out the best set of values of the controlling parameters that minimise/maximise the controlled parameter. The optimisation process is considered either minimisation or maximisation depending upon the application. Most swarm optimisation technique are inspired by the natural behaviour of creatures such as birds as in PSO, ants as in Ant Colony Optimisation, bees as in Artificial Bee Colony, etc. They all share the same steps to reach the minimum/maximum location within the search space. Traditionally, they start by proposing a number of random solutions as an initial set of solutions, but each technique differs in the way it updates the position of the nodes. The critical challenge is to balance the exploration and exploitation phases, avoiding premature convergence, whilst still running efficiently. The solutions' positions are iteratively updated until the maximum number of iterations or a stopping criterion is reached. The comparison between one optimiser and another is usually based on the efficiency of reaching the optimal solution accurately and as fast as possible.

For this study PSO is utilised. In the PSO method the solution is produced when a set of particles forms a group. On each iteration, personal best (pbest) and global best (gbest) for each particle are compared and the particle moves to find the best solution in the search field.

As a swarm concept, PSO modelling concludes when a set of particles forms a group with a clear majority of the particles. Both *pbest* and *gbest* values are utilised by each particle and swarm (set of particles) when it moves to find the best solution, each iteration. Then updates its velocity $v(k+1)$ and position $p(k+1)$ from the previous velocity $v(k)$ and position $p(k)$.

The position and velocity for each particle is shown in Equations 6.3 and 6.4:

$$p(k+1) = p(k) + v(k+1) \quad (6.3)$$

$$v(k+1) = w * v(k) + c_1 * r_1 * (pbest - p) + c_2 * r_2 * (gbest - p) \quad (6.4)$$

Where: c_1 is the local weight experienced and c_2 represent the global weight experienced. The default values of c_1 & c_2 was 2, while r_2 and r_1 are the random variables changes from 0 to 1 and w is the weight of inertia, as shown in Equation 6.5.

$$w = w_{max} - tx \left(\frac{w_{max} - w_{min}}{Iter_{Max}} \right) \quad (6.5)$$

Where: w_{max} and w_{min} are the maximum and minimum weight of inertia, with the default values at 0.8 and 0.2 respectively. The maximum number of iterations was set to 100. PSO optimizer is easy and effective, it is applied in this study to obtain the optimum operating conditions, i.e. minimal electrode separation and applied voltage, with maximum current density.

6.3 Results and Discussion

ML has a minimum required sample data size to run accurately, as such it was not possible to conduct ML for all of the experiments conducted in this chapter, due to governmental regulations restricting access to the lab. Only the data from the Effect of Flow Rate (section 5.2.1), the Effect of Electrode separation (section

5.2.2) and the Effect of Electrolyte Concentration (section 5.2.3) proved to be of sufficient size.

Modelling Phase

The ANFIS model is built using the experimental data points, from three different cell parameters as examined previously; electrolyte flow rate: section 5.2.1, electrode separation section 5.2.2 and electrolyte concentration section 5.2.3. The inputs include time, electric voltage, electrical charge passed and specific experimental parameters.

The accuracy of the modelling is examined by training the experimental data until the minimum error of test data is obtained, with the training-to-testing ratio set at 80:20 (with 80% to and 20% used to validate the model). In addition, the mean squared error (MSE) and the root mean square error (RMSE) of the modelling, in relation to the dataset, is shown in Table 6.1. The lower the MSE and RMSE, the better a model fits a dataset. R^2 shows the proportion of the variance in the response variable of a regression model, which can be explained by the predictor variables. R^2 has a range of 0 to 1, with the higher the value, the better a model fits a dataset.

MSE			RMSE			Coefficient of determination (R^2)		
Train	Test	All	Train	Test	All	Train	Test	All
2.042e-02	0.0109	0.0175	0.1429	0.1042	0.1324	0.9902	0.9961	0.9924

TABLE 6.1: Statistical evaluation of the fuzzy-based model for electrode separation.

In Table 6.1, the lowest MSE and RMSE values from training and testing, as well as the R-squared values are shown. The model has high accuracy based on the low MSE and RMSE, and high coefficient of determination. Additionally the high correlation of the training and modelled data, shown in Figure 6.1, highlights the reliability and accuracy of the ANFIS modelling, with the training data shown as blue diamonds, with the modelled data as red asterisks.

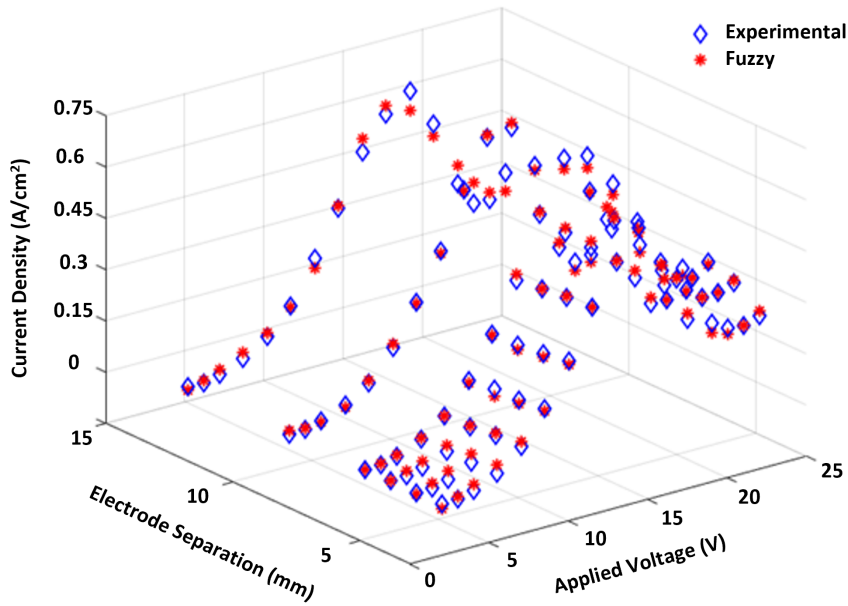


FIGURE 6.1: Fuzzy system validation plot showing fuzzy model fit for electrode separation.

MFs are used in the fuzzification and defuzzification steps, mapping the non-fuzzy input values to fuzzy linguistic terms and vice versa. Figure 6.2 displays the Gaussian-shaped MFs of the system inputs FL MFs. These MFs have a relatively consistent distribution, implying that the measured data was generated using uniformly distributed input values. This distribution enables the ANFIS model to accurately select the input–output relationship.

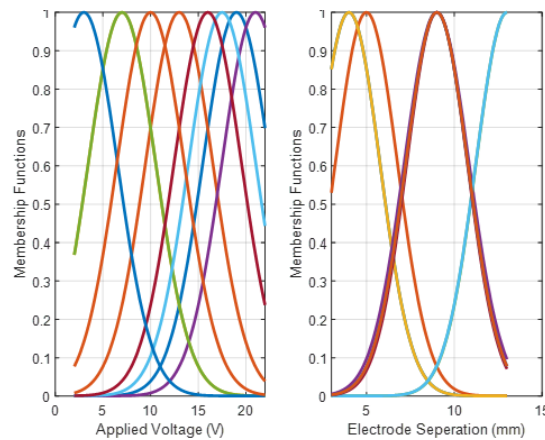


FIGURE 6.2: Membership Functions of the inputs of the ANFIS model of the electrode separation experiment.

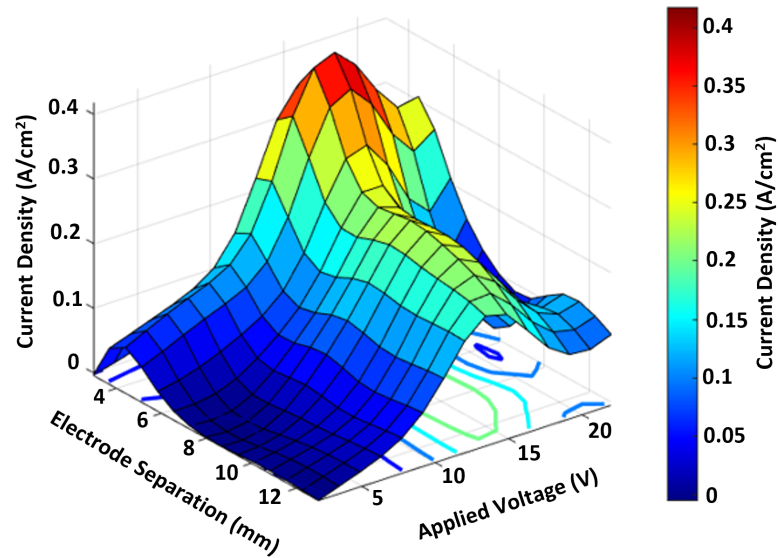


FIGURE 6.3: 3D plot of ML model for electrode separation.

Examining the input–output relationship caused by the investigated system helps in comprehending the influence of the inputs on the output. Figure 6.3 depicts a 3D surfaces plot of one of the models using the electrode separation data. This data has been discussed previously (section 5.2.2), a key difference shown here is the peak in current density, at 5.3 mm separation and 15 V applied voltage, which has been predicted by the modelling. Additionally, the gaps in-between the experientially obtained data sets are also available for analysis.

Optimisation Phase

PSO is a metaheuristic optimisation algorithm; the optimization procedure must be carried out repeatedly to avoid finding the false optimisation points. Therefore, the PSO technique was repeated 30 times.

Figure 6.4 shows the comprehensive outcomes of the PSO optimisation process for the electrode separation experiment. It shows that the data is fully converged at 70 iterations. For PSO it is much easier to operate with numbers of equal scale, the easiest way to do this was to increase the current density values to whole

numbers, rather than decimals. The current density values were converted to 'cost' values, this was done by multiplying each value by 20, as such 'best cost' directly relates to optimum current density.

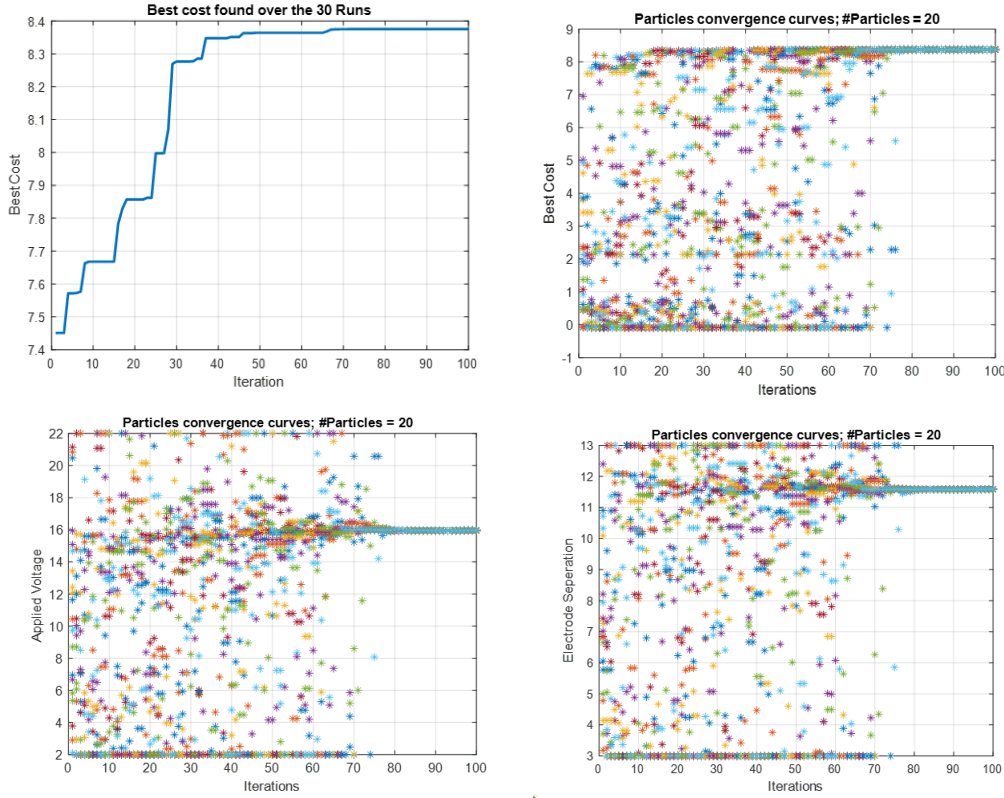


FIGURE 6.4: Cost estimate and particle convergence curves for electrode separation

30 runs (of 100 iterations) were completed with the optimum cost function presented in Figure 6.5. Table 6.2 shows the difference between the experimental and model results where the experimentally obtained optimum in section 5.2.2 was an electrode separation of 6 mm and an applied voltage of 14.5 V. However the ML optimisation found a new optimum with a current density at 0.44 A/cm² with a separation of 5.3 mm and applied voltage of 15.9 V.

Method	Applied Voltage	Electrode Separation	Power
Experimental	14.5 V	6 mm	0.35 A/cm ²
Machine Learning	15.9 V	5.3 mm	0.42 A/cm ²

TABLE 6.2: Machine Learning results for electrode separation.

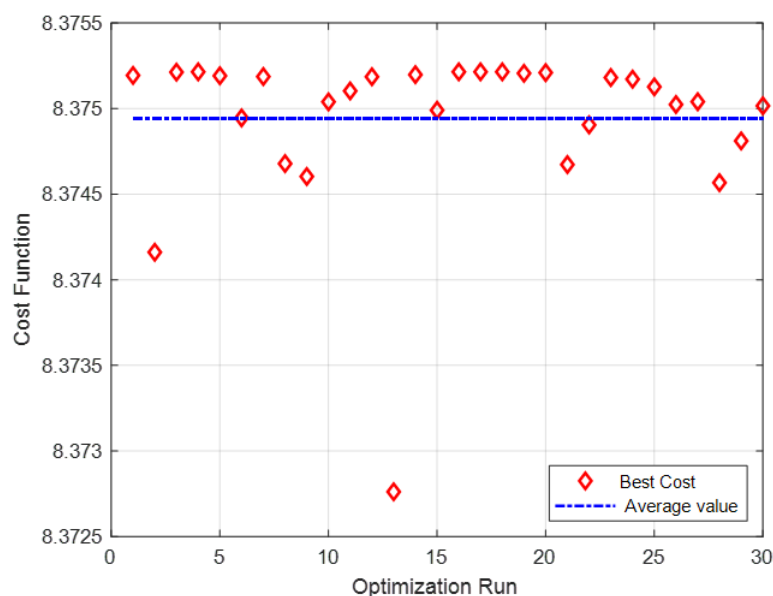


FIGURE 6.5: Results of 30 optimisation runs, with average cost function plotted.

Table 6.3 shows the ML optimum parameters found for each of the three experimental parameters examined, along with the experimentally obtained highest current density. For electrode separation the experimentally obtained optimum current density was found at 13 V, 6 mm total separation, through the ML technique a new optimum of 0.42 A/cm² was found at 15.9 V 5.3 mm total separation. The optimum flow rate was deemed to be 50mL/Min in section 5.2.1, with the ANFIS and PSO finding a higher optimum current density of 0.39 A/cm² at 56 mL/min. For the electrolyte concentration data explained in section 5.2.3, the optimum concentration remains at 2 M KHCO₃. As this was one of the experimental limits, although the ANFIS model can predict performance outside of experimental parameter, the MSE and RMSE are much higher making the data much less

reliable. However the ML still produced an improved optimum current density, 4.11 A/cm² at 17.7 V compared to 3.73 A/cm² at 17.5 V.

Experiment	Testing Parameter ML	Applied Voltage ML	Current Density ML	Current Density Experimental
Electrode Separation	5.3 mm	15.9 V	0.42 A/cm ²	0.35 A/cm ²
Flow Rate	56 mL/min	12.8 V	0.39 A/cm ²	0.36 A/cm ²
Electrolyte Concentration	2 M KHCO ₃	17.7 V	4.11 A/cm ²	3.73 A/cm ²

TABLE 6.3: Machine Learning results.

6.4 Conclusion

ML is an effective tool for optimising the cell, especial when lab availability is limited. The combination of Figures 6.3 and 6.1 demonstrates the potential of using an ANFIS models to efficiently predict intermediate data from experimental results, with PSO to find the optimum cell operating parameters from these models. The produced models had high accuracy and high correlation based on the minimal error between the modelled data and the coefficient of determination as shown in Table 6.1.

Three of the cell parameters, examined in the previous chapter, were optimized to increase current density in the cell: Electrode Separation, Electrolyte Flow Rate and Electrolyte Concentration, with notable increases in current density found for each examined parameter. These results were used to improve the MK 2 (Section 4.4.2) design into the MK 3 design (Section 4.4.3).

6.5 Contributions

Dr Hegazy, Dr Abdelkareem, Dr Waqas Tanveer contributed to the initial development of the ML works, section 6 with Dr Fabio Caraffini providing further expertise and developing the code used.

Chapter 7

Cell and CO₂ Electrocatalysts Integration

7.1 Introduction

In the previous chapter the cell was optimised for current density, however most of the applied potentials used are known to produce low FE for C₂ products. As such it is necessary to explore how the cell could be modified to improve FE selectivity towards C₂ products and away from hydrogen evolution.

Metal foams have been examined by several works [62, 134, 151–154], Shin *et al.* [134] were the first to report "self-supported nanoramified (dendritic) deposits" (foams) utilising the hydrogen evolution reaction. They used the production of hydrogen bubbles as a dynamic negative template for the metal crystal to form around, resulting in 3D free-standing metal foams. The highly porous dendritic walls greatly increased the cathodic electrochemical surface area without increasing the geometric area, and only slightly increasing the geometric volume.

Figure 7.1 shows a simplified schematic of the formation process for the metal foams. Where there are hydrogen bubbles deposition cannot occur because there are no metal ions available to generate the porous structured deposits. The pore

size of the foam increases as substrate distance increases, as the hydrogen bubbles coalesce.

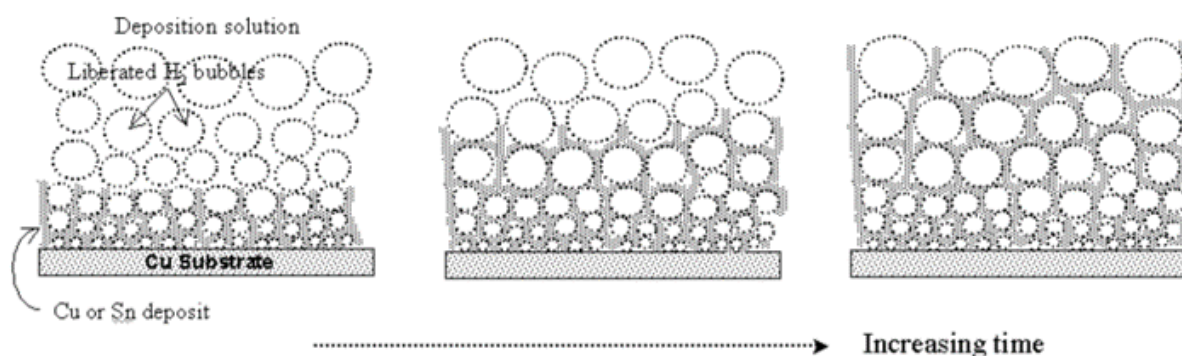


FIGURE 7.1: Reproduced with permission from Shin *et al.*[134]: Simplified description of the formation process of the metal foams. A series of gas bubbles, evolve on the substrate and then act as a dynamic negative template during the metal deposition, as the metal deposits between gas bubbles forming the foam structure. The pore size of the foam increases with the distance away from the substrate because of the coalescence of hydrogen bubbles.

Shin *et al.*[151] further refined their control of the foams by examining the effects of adjusting the deposition conditions. They reduced pore size by adding bubble stabilizers (e.g. acetic acid) which suppressed the coalescence of bubbles and reduced the wall thickness of the pores by adding HCl, with the catalytic effect of chloride ions impacting the copper deposition reaction. Kim *et al.*[152] examined the effects of several other additives to the deposition bath on the growth and structure of the foams. Additives such as Cl⁻, polyethylene glycol and 3-mercaptopropane-1-sulphonic acid were found to change the morphology of foam. Additionally they found that 3 A cm⁻² was the optimum for potential foam growth as higher voltages proved too unstable for the foam structure to grow properly, resulting in collapse. This was attributed to the deposition solution being agitated excessively by hydrogen bubbles being evolved too vigorously.

Dutta *et al.* [154] further developed Shin's work, investigating the effects of time on the deposition of the foam before examining the copper foams in a CO₂RR.

They used 30 mL per compartment of CO₂-saturated 0.5 M NaHCO₃ electrolyte in a custom-built, airtight, glass H-cell with a Nafion 117 membrane. A 1 cm² Cu cathode was used with a bright Pt foil (15 mm × 5 mm) serving as the counter electrode and a Ag/AgCl reference electrode. The foam electrode showed enhanced production rates for hydrogen, ethylene, ethane, formate and carbon monoxide, with a notable reduction in methane production when compared to a copper electrode without a foam. Dutta *et al.* [62] then examined the effect of other metal foams finding that Ag also shows enhanced performance by the use of a metal foam.

Previous work by Rudd [93] examined ways of altering the electrodeposition bath to improve the selectivity of electrocatalysis products. This study tested the effects of HCl concentration and urea in the electrodeposition bath. Other research found that the presence of nitrogen containing moieties can modify the properties of the copper catalyst, adjusting product selectivity and current densities, promote C-C bond formation and lead to greater product selectivity [155, 156].

Several papers have discussed ways to improve (FE) for specific products. Song *et al.* [157] highlighted some effective molecular motifs for the construction of organic/inorganic hybrids for CO₂ reduction. They noted the effectiveness of poly(acrylamide) for ethylene selectivity, as previously established by Ahn *et al.* [95]. The most effective motif for ethylene selectivity is poly-N-(6-aminohexyl) acrylamide, found at 87% FE by Chen *et al.* [158]. Buckley *et al.*'s [159] work on polyallylamine was also identified by Song *et al.*'s review as showing a FE selectivity for C₂ products.

As seen above in section 5.2.6, foams have been shown to improve the performance of the cell. It was decided to examine the effects of the foams, and subsequent modified foams, on the FE of the products of the cell from CO₂RR. The works of Chen, Ahn and Buckley [95, 158, 159] all showed good FEs, with two having used amines, as highlighted in Song *et al.*'s [157] review. Other potential

amino acid were examined by Xie *et al.* [155] who found that the intermediate CHO was stabilized by interacting with the -NH_3^+ of the adsorbed glycine. This improved the hydrocarbon generation, regardless of the morphology of the copper electrodes. Xie examined several amino acids including glycine, DL-alanine, DL-leucine, DL-tryptophan, DL-tyrosine and DL-arginine but lysine was not considered. L-Lysine was examined by Wei *et al.* [160] for formate production in a thermo-catalytic system on a Ru complex catalyst. Other amino acids were examined all with lower yields. It appeared that lysine had not been used as a metal foam modifier for CO₂ electrocatalysis.

The literature review suggested a knowledge gap in the research, presenting the opportunity to examine the effects that different amides and amines have on product selectivity of the designed cell. The organic modifiers selected were: poly acrylamide (PA), (poly) sodium acrylate (PSA), D-lysine (DL), L-lysine (LL), polyallylamine (PAA) & poly-D-lysine (PDL), all shown in Figure 7.1. Additionally, a foam with no modifier (Plain), and an electrode with no Cu foam (Plate), were also examined.

Each modifier was selected for a specific reason. PAA is a primary amine polymer with a single carbon in the amine branch. It was highlighted in previous works providing a baseline for subsequent experiments. In contrast, PA is a polymer with a primary amide branch and PSA is a polymer with carboxyl groups. These can be used to show the difference between the three groups: amine, amide and carboxyl, on the deposition of the foam.

Chen *et al.*'s [158] work found the highest reported FE for ethylene, using a 6 carbon primary amine with an amino acid in a polymer chain. He did not examine the effects of lysine which has a similar structure, lacking the tertiary carbon that forms the polymer chain. Lysine has two primary amides and a carbonyl group. The presence of the carbonyl and a primary amide is similar in composition to

the amide group of PA but with an additional carbon, whilst also having a second primary amine at the end of the carbon chain resulting in the same active group as PAA. The two primary amines also mean that lysine can polymerise in two different ways; ϵ -poly and α -poly, as seen in Table 7.1. LL and DL are lysine monomers, with LL as the enantiomer of the DL.

If only the α -poly lysine is formed then it would have a similar, ordered branched, structure to that of Chen's work, whereas an ϵ -poly lysine would produce an unbranched polymer. It is difficult to select a single form of polymerisation and as such PDL forms a dendrimer structure as seen in Figure 7.2 from Hedge *et al.* [161]. Due to limited availability and time, PDL was supplied in a Phosphate-Buffered Saline solution, containing HCl, which, as previously discussed, is known to affect the morphology of metal foams. Table 7.1 summarises the selected foam modifiers, which were prepared following the method detailed in section 3.1.

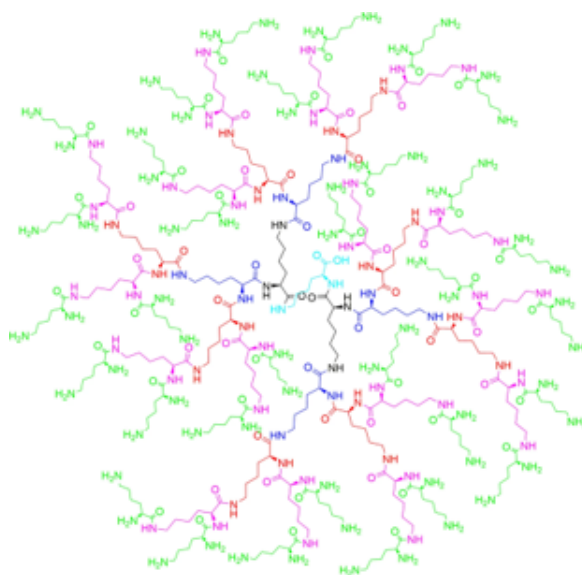


FIGURE 7.2: Reproduced with permission from Hedge *et al.* [161]: Structure of 5.0 G poly(L-lysine) dendrimer.

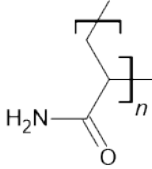
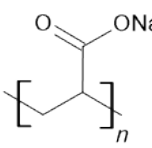
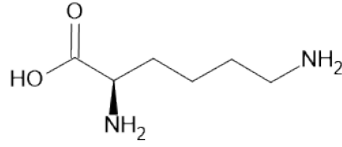
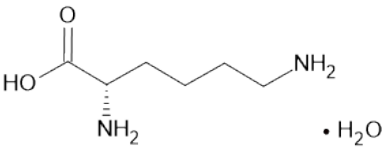
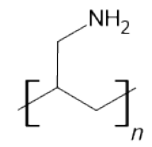
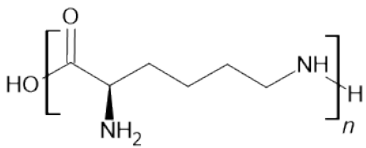
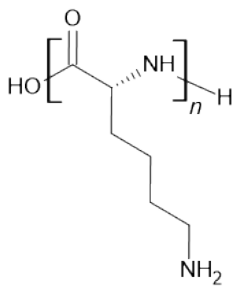
Mod	Full Name	Structural Formula	Molecular Weight (g/mol)	Molecular Formula
PA	Poly Acrylamide		5 M - 6 M	$(C_3H_5NO)_n$
PSA	(Poly)Sodium Acrylate		5100	$(C_3H_4O_2 \cdot Na)_n$
DL	D-Lysine		146.19	$C_6H_{14}N_2O_2$
LL	L-Lysine hydrate		164.19	$C_6H_{14}N_2O_2 \cdot H_2O$
PAA	Pollyallyamine		15,000	$(C_3H_7N)_n$
PDL	Poly-D-Lysine		50 K - 150 K	$(C_6H_{12}N_2O)_n$
				

TABLE 7.1: Selected foam modifiers.

7.2 Material Characterisation

7.2.1 SEM

SEM analysis was used to examine the structure of the Cu foams. Figures 7.3 and 7.4 show SEM images of the Cu foams at 120x and 500x magnification respectively. Table 7.2 summarises the analyses of Figures 7.3 and 7.4, showing the average pore diameter and wall thicknesses of the Cu foams, as well as their respective standard deviations.

Foam	Pore diameter	stdev	Wall thickness	stdev
Plain	535	102.59	320	33.16
PA	374	110.11	157	33.02
PSA	182	33.11	99	26.5
DL	439	88.88	245	40.28
LL	344	61.03	230	40.4
PAA	273	51.23	238	48.06
PDL	447	171.46	206	124.57

TABLE 7.2: Average pore diameter and wall thickness for each Cu foam in μm .

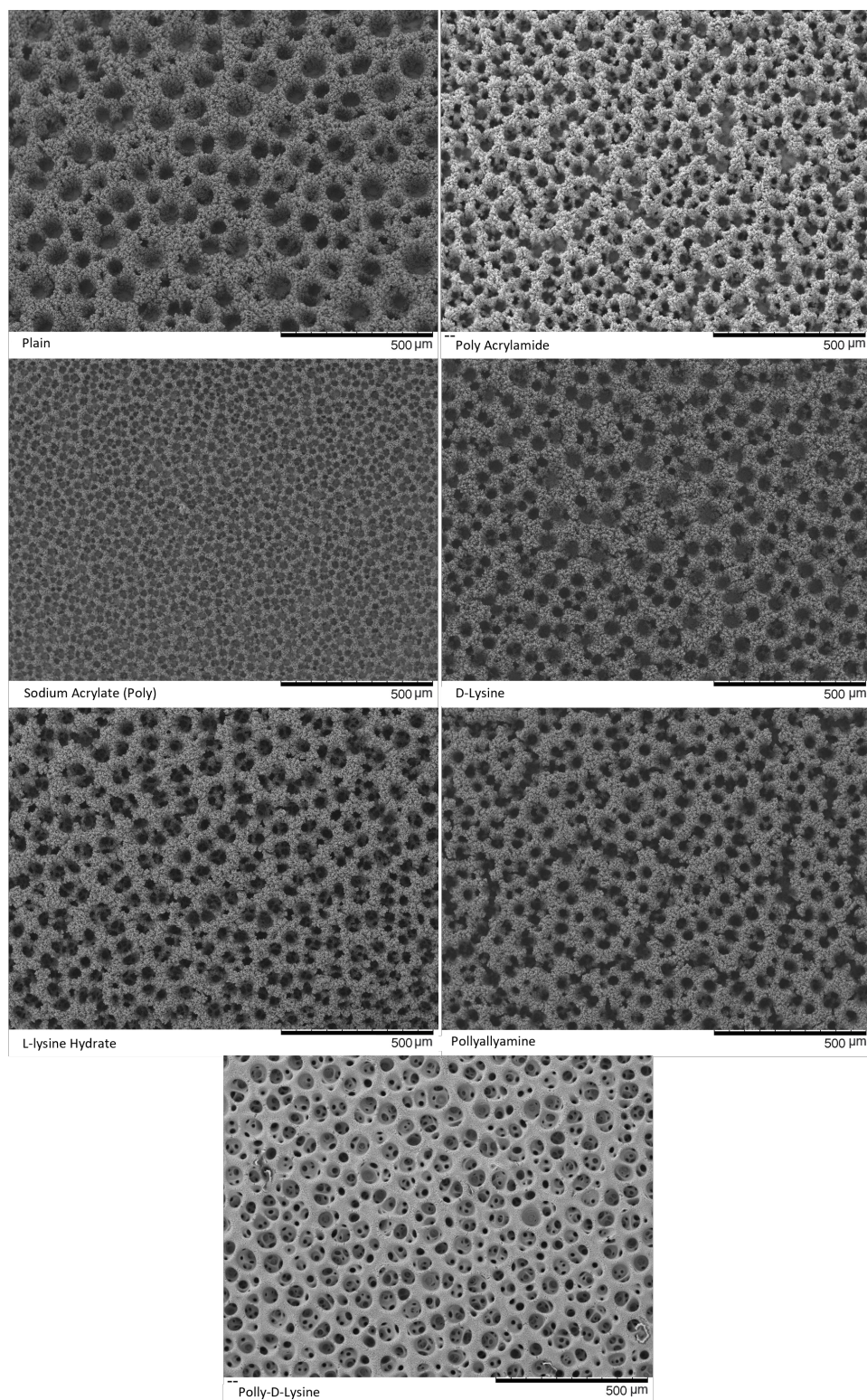


FIGURE 7.3: SEM images of the Plain and modified foams before electrocatalysis at 120x magnification.

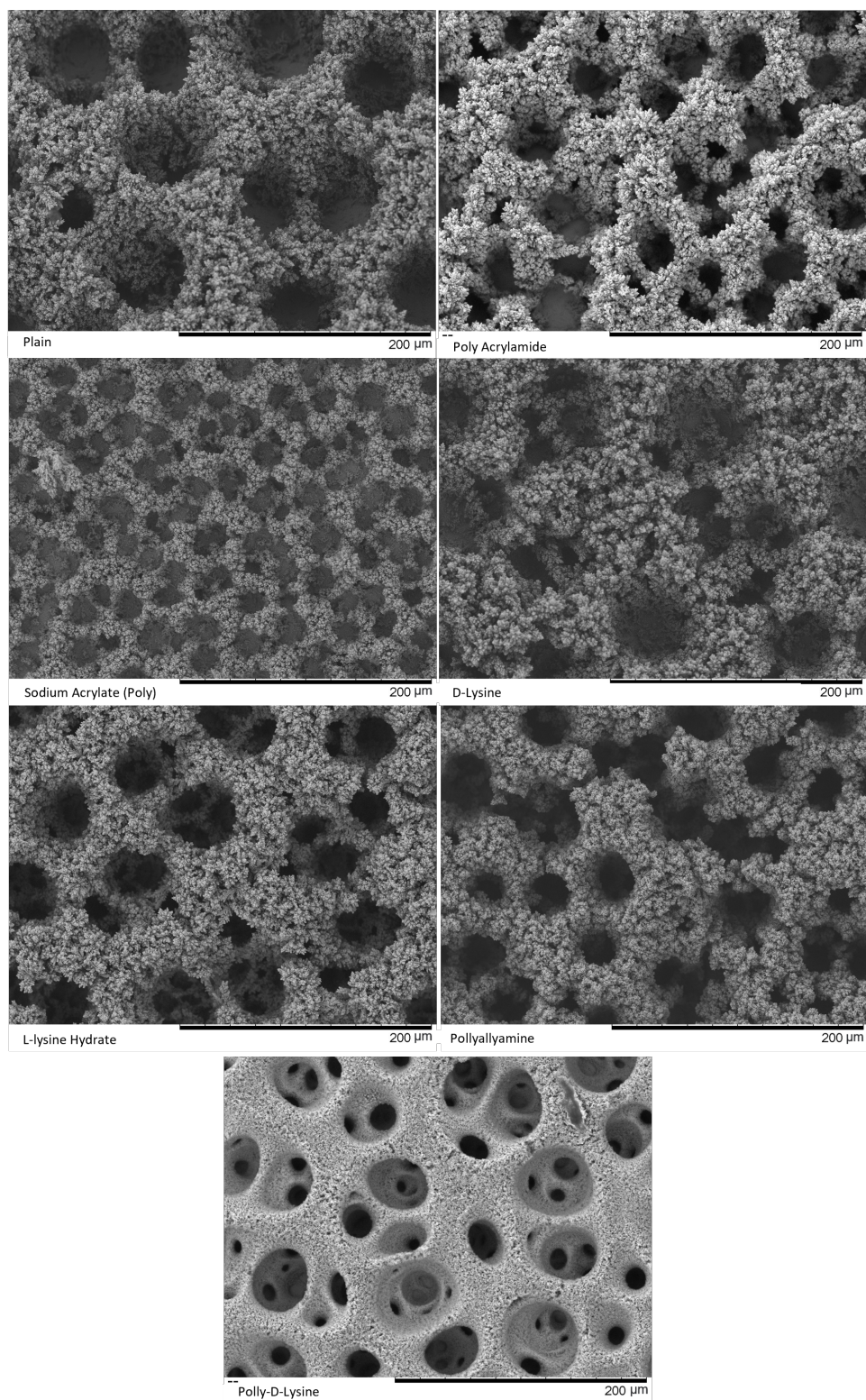


FIGURE 7.4: SEM images of the Plain and modified foams before electrocatalysis at 500x magnification.

7.2.2 EDX

Energy Dispersive X-ray Spectroscopy (EDX) analysis was conducted as per the method in section 3.3 for each of the Cu foams. The individual EDX spectra for each foam are presented in Appendix B, with the results summarised in Table 7.3. Carbon was excluded from the analysis as it is a known adventitious contaminant. The map spectra and associated SEM images are presented in Figure 7.5.

Foam	Cu	O	S	Cl
Plain	81.17	17.39	1.44	-
PA	83.04	15.92	1.04	-
PSA	90.28	8.93	0.78	-
DL	95.47	4.39	0.15	-
LL	85.7	12.55	1.76	-
PAA	94.16	5.36	0.48	-
PDL	56.73	20.29	1.64	21.33

TABLE 7.3: Atomic % of Cu, O, S and Cl for each of the foams.

7.2.3 Discussion

All the modified foams have a smaller average pore size and wall thickness than the Plain foam. PDL and DL are the next closest in average pore diameter size. PA and LL have relatively similar pore diameters, but the standard deviation for PA is much higher. Additionally PA has a smaller wall thickness than LL suggesting the reason for the variation in pore diameter. PAA has a smaller average pore diameter than PA and LL at 273 μm , plus a smaller standard deviation at 51 μm .

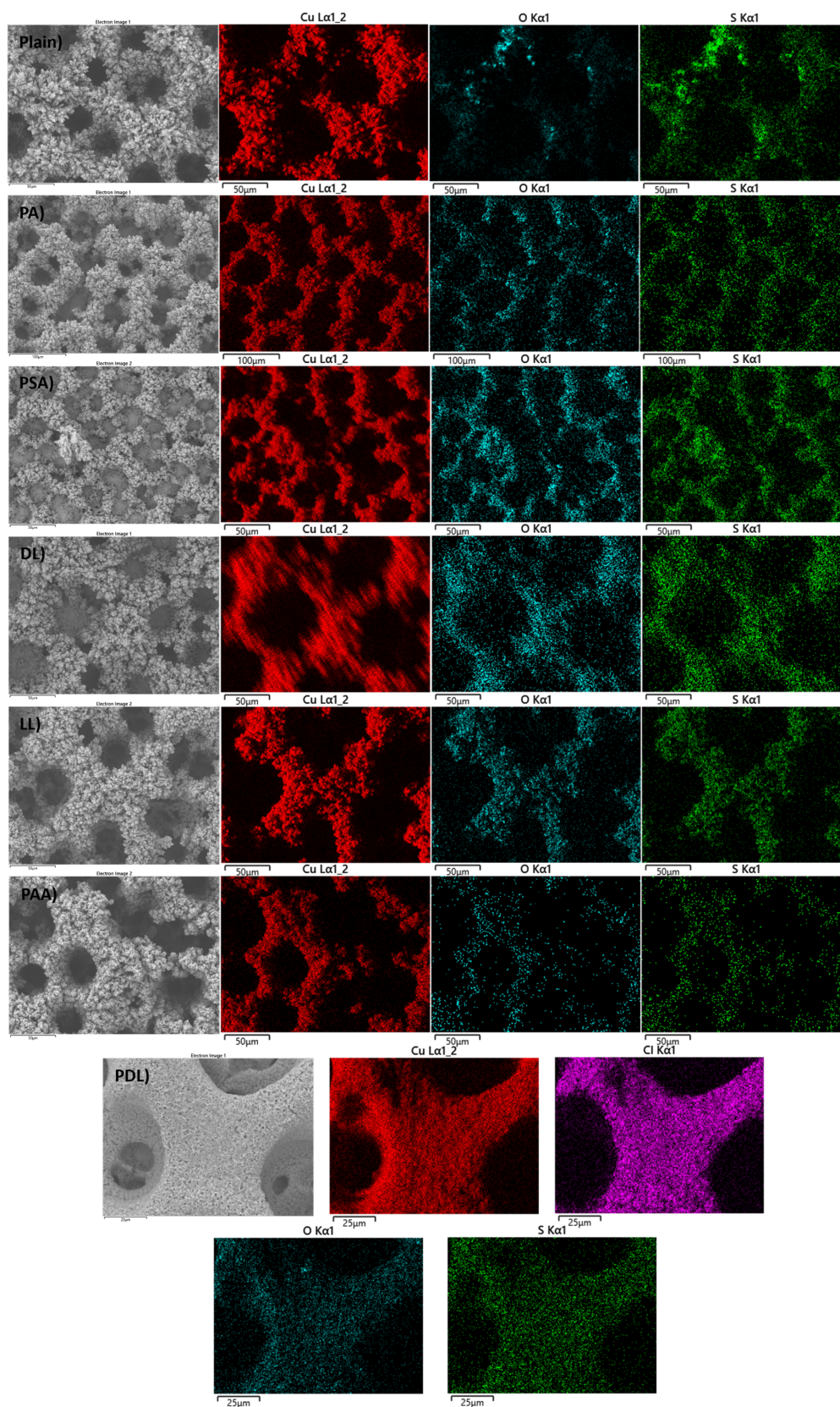


FIGURE 7.5: EDX map spectra for each of the Cu foams, and cosponsoring SEM images.

PSA has notably smaller pore size and wall thickness, (evident in Figures 7.3 and 7.4) as well as the much smaller wall thickness at 182 μm . It also has the smallest standard deviation in wall thickness observed in Table 7.2. This suggests that the PSA has a similar effect on the growth of the Cu foam as the acetic acid used by Shin *et al.* [151] as a hydrogen bubble stabilizer. They also saw reduced wall thickness and pore diameter with increase in acetic acid concentration.

Figures 7.3 and 7.4 show the clear effect of HCl on the morphology of the foam as discussed in Rudd *et al.*[93]. The foam appears very differently with a distinct dendritic structure compared to the other foams. Whilst it has a comparable average pore size, PDL's standard deviation is much higher at 171 μm than DL's 89 μm . The same is true for wall thickness: PDL's average is relatively comparable at 206 μm , but has by far the largest standard deviation at 125 μm .

All the foams are more than 80 % (atomic weight) copper apart from the PDL foam which has the considerable addition of chlorine. They all contain copper oxide, as shown by the oxygen presence in the foams map spectra, in Figure 7.5, as well as sulphur inclusion in the metal foam. The sulphur and oxide in the map spectra follows the shape of the Cu foam quite closely. Figure 7.5 shows that the Cu foam has both sulphur inclusions from the sulphuric acid in the deposition bath and copper oxide in its structure.

7.3 Affect of Applied Voltage on CO₂ Electrolysis using Organic Modified Cu Foams

The effect of each of the Cu foams was examined under CO₂RR conditions at different applied voltages. The foams were characterised by their FE for each product at 3 V, 4 V and 5 V, selected around the purposed optimum at 4 V (section 4.4.2). Due to low liquid product concentrations, preliminary NMR was not viable so it was decided to focus on gaseous products at this stage. The foams

were prepared as per section 3.1, with 0.01 M of applicable modifier in the electrolysis bath, on a 2 cm² copper plate. CO₂RR was conducted in the MK 3 cell without the GDE adaption. Each electrolysis lasted 15 mins, with the last of the products collected one minute after the applied voltage was stopped.

7.3.1 Results

Copper Plate

Figure 7.6 shows the FE of the collected product gases for the copper plate (Plate) electrode.

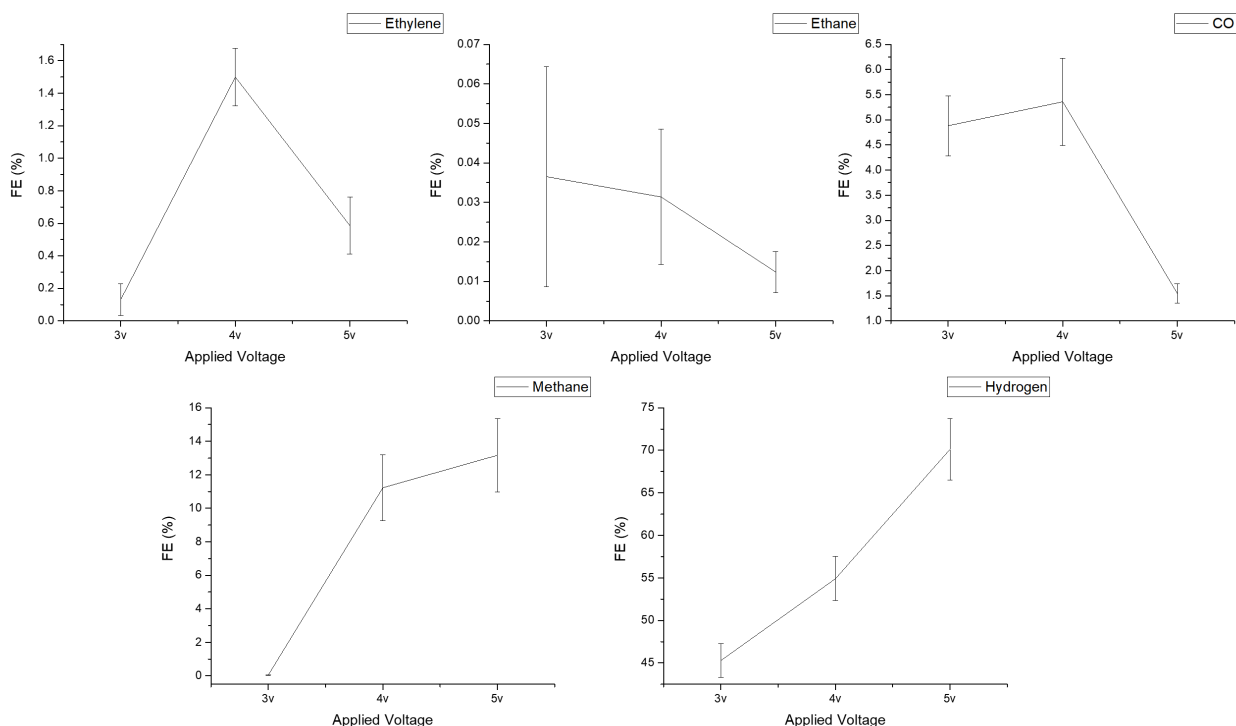


FIGURE 7.6: CO₂ electrolysis FE for all detected gaseous product for copper plate electrodes, in CO₂ saturated 0.1M KHCO₃ electrolyte, at three different applied voltages.

For the Plain copper plate (no foam) methane is the highest FE of the desired products present at 13.1% at 5 V, CO is the next highest product at 5.4%, with ethylene at 1.5%. Methane is almost non existent at 3 V however it greatly increases at higher voltages up to 11% at 4 V and 13% at 5 V. Ethylene is low at

0.1% for 3 V, peaks at 1.5% for 4 V and drops again to 0.5% for 5 V. CO is relatively constant around 5% from 3 V and 4 V, but then drops to 1.5% for 5 V. Ethane is found in trace amounts throughout and does not change considerably. Hydrogen is the dominant product of the copper plate electrode, at 45% at 3 V steadily increasing to 70% at 5 V.

Plain Copper Foam

Figure 7.7 shows the FE of the collected product gases, for the un-modified foam (Plain) electrode.

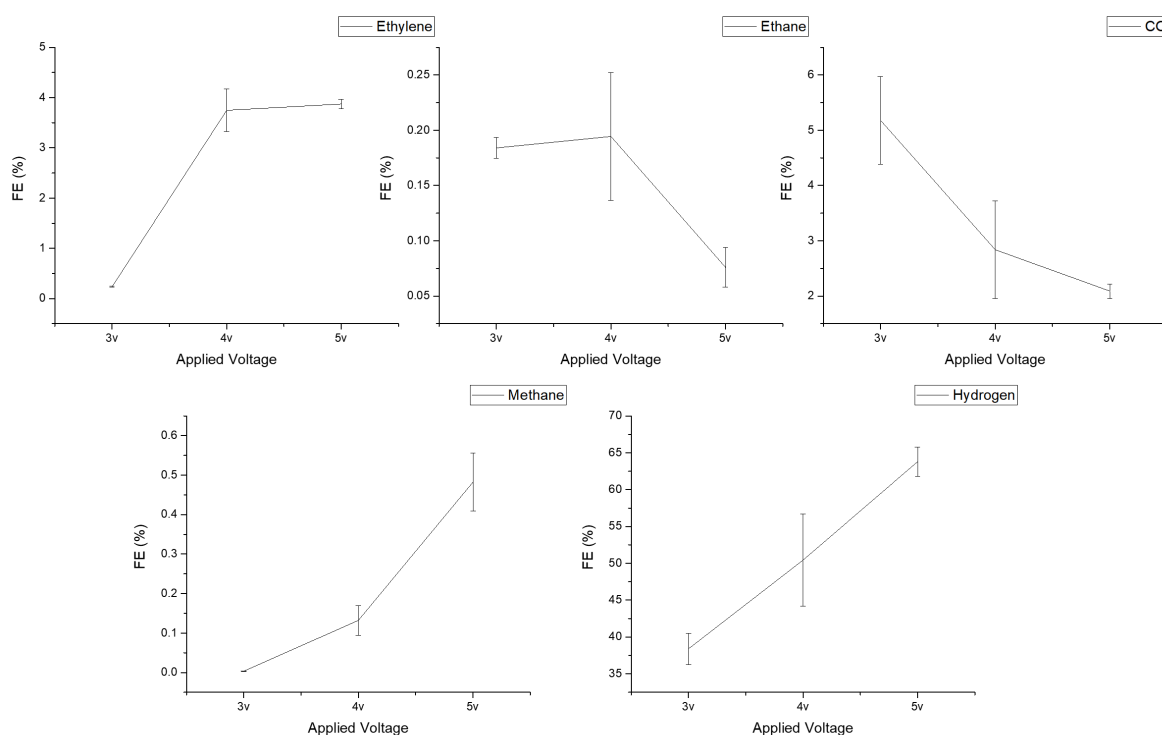


FIGURE 7.7: CO₂ electrolysis FE for all detected gaseous product for the unmodified copper foams on copper plate electrodes, in CO₂ saturated 0.1M KHCO₃ electrolyte, at three different applied voltages.

For the Plain copper foam, CO is the highest desired product at 5.2% at 3 V, ethylene is the second highest product at 3.9% at 5 V. Ethylene starts very low at 0.2% then increases and levels out at around 3.8% after 4 V applied voltage. CO starts high, at 5.2% but steadily drops with applied voltage to 2% at 5 V. Methane has

a slight increase in FE % with increase in applied voltage from trace amounts to 0.5%. Ethane fluctuates very slightly in trace amounts. Hydrogen starts low at 38% at 3 V and then increases to 50% at 4 V and then further increases to 63.5% at 5 V.

Poly Acrylamide

Figure 7.8 shows the FE % of the collected product gases, for the Poly Acrylamide modified foam (PA) electrode.

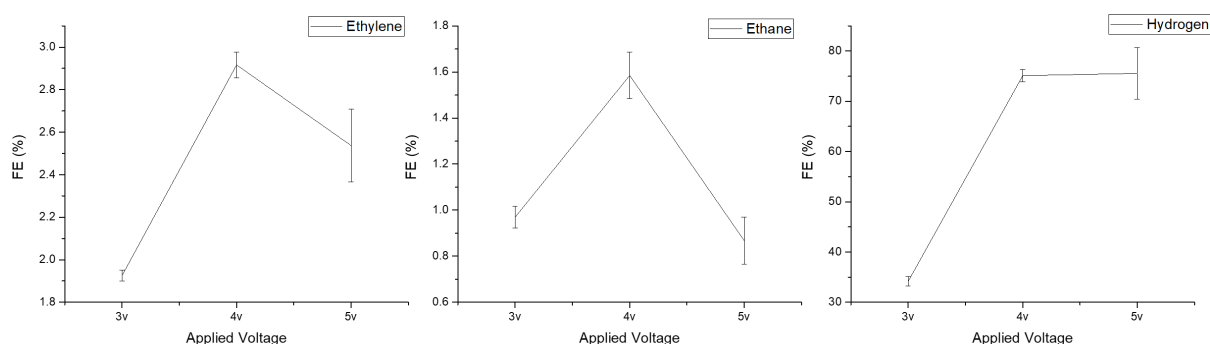


FIGURE 7.8: CO₂ electrolysis FE for all detected gaseous product for Poly Acrylamide modified copper foams on copper plate electrodes, in CO₂ saturated 0.1M KHCO₃ electrolyte, at three different applied voltages

For the PAA modified Cu foam, ethylene is the highest desired product detected at 2.9% at 4 V, followed by ethane at 1.6% also at 4 V, most notably no C₁ products were detected. Ethylene starts low at 1.9% at 3 V then peaks at 2.9% at 4 V before dropping again to 2.5% at 5 V. Ethane follows a similar trend to ethylene, starting low at 1% for 3 V then peaking at 1.5% for 4 V and drops back down to 0.9% at 5 V. At 3 V, hydrogen is low at 34% at 3 V before it doubles to 75% at 4 V and 5 V.

(Poly) Sodium Acrylate

Figure 7.9 shows the FE of the collected product gases, for the Sodium Acrylate (Poly) modified foam (PSA) electrode.

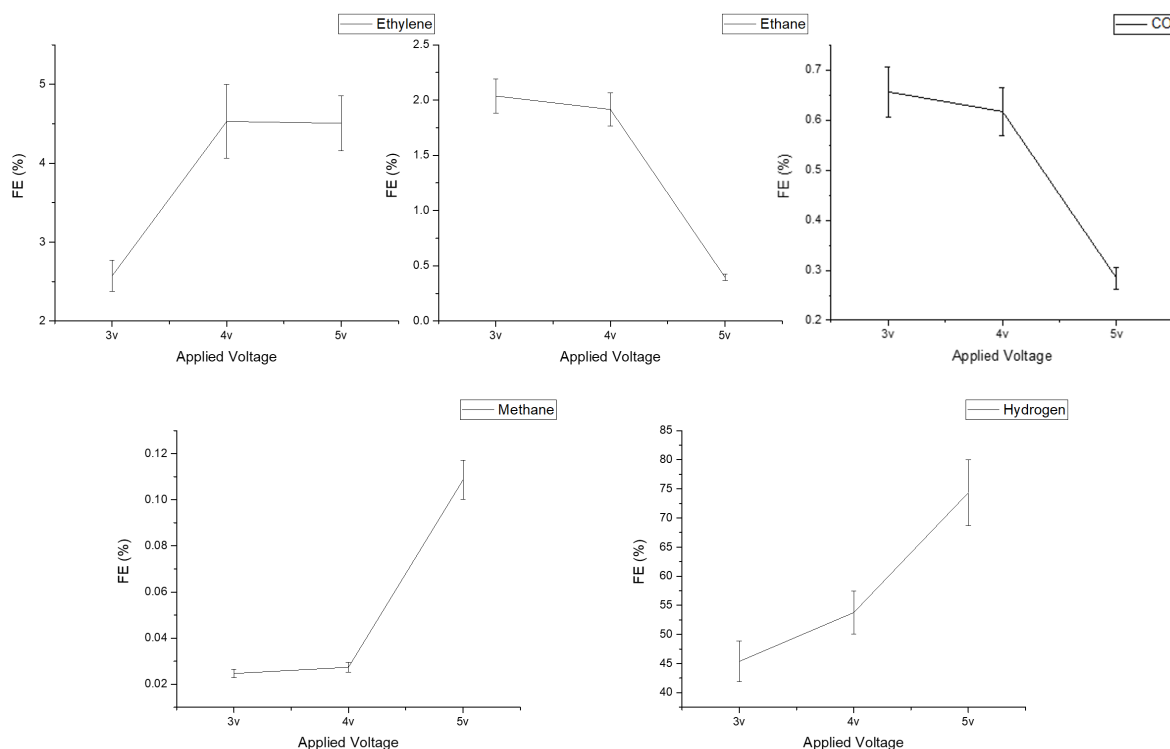


FIGURE 7.9: CO₂ electrolysis FE for all detected gaseous product for Sodium Acrylate (Poly) modified copper foams on copper plate electrodes, in CO₂ saturated 0.1M KHCO₃ electrolyte, at three different applied voltages.

For the PSA modified Cu foam, ethylene is the highest desired product detected at 4.5% at 4 V, followed by ethane at 2%. CO was the next highest at 0.6% at 3 V, with trace amounts of methane found. Ethylene starts at 2.5% at 3 V then increases to approximately 4.5% at 4 V and 5 V. Ethane starts at around 2% for 3 V and 4 V and drops down to 0.4% at 5 V. CO is relatively constant at 3 V and 4 V at 0.65% and 0.61% respectively, before dropping to 0.28% at 5 V. Trace amounts of methane are found, at 0.02% at 3 V and 4 V increasing to 0.1% at 5 V. Hydrogen is at 45% at 3 V increases to 54% at 4 V then to 74% at 5 V.

D-Lysine

Figure 7.10 shows the FE of the collected product gases for the D-Lysine modified foam (DL) electrode.

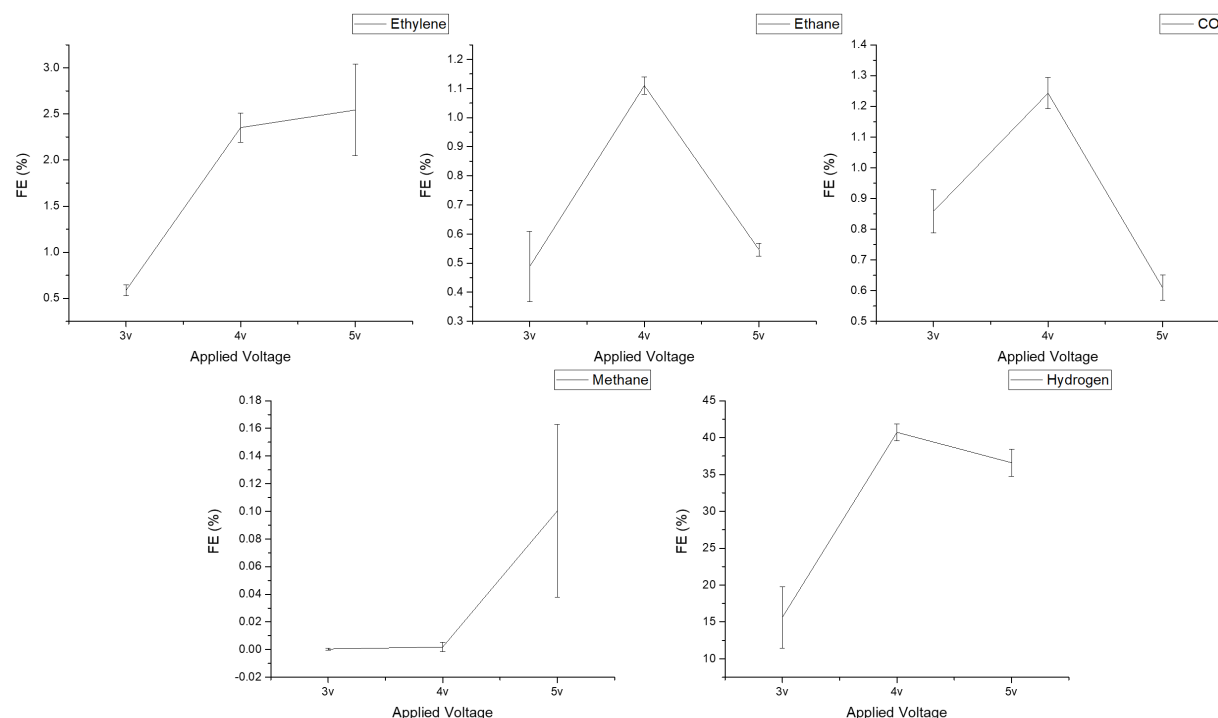


FIGURE 7.10: CO₂ electrolysis FE for all detected gaseous product for D-Lysine modified copper foams on copper plate electrodes, in CO₂ saturated 0.1M KHCO₃ electrolyte, at three different applied voltages.

For the DL modified copper foam, ethylene was the highest desired product detected, at 2.5% at 5 V, with the next highest product being CO at 1.2% at 4 V, closely followed by ethane at 1.1% at 4 V with trace amounts of methane. Ethylene starts at 0.6% at 3 V then increases to approximately 2.4% at 4 V and 5 V. CO starts low at 0.85% at 3v then peaks at 1.2% at 4v, before dropping at 0.6% at 5 V. Ethane follows a similar trend to CO, starting low at 0.5% at 3 V, peaking at 1.1% at 4 V then drops to 0.5% at 5 V. Trace amounts of methane were detected, with a considerable increased at 5 V. Hydrogen is 15% at 3 V then peaks with 40% FE at 4 V before declining slightly to 36.5% at 5 V.

L-lysine Hydrate

Figure 7.11 shows the FE of the collected product gases, for the L-Lysine modified foam (LL) electrode.

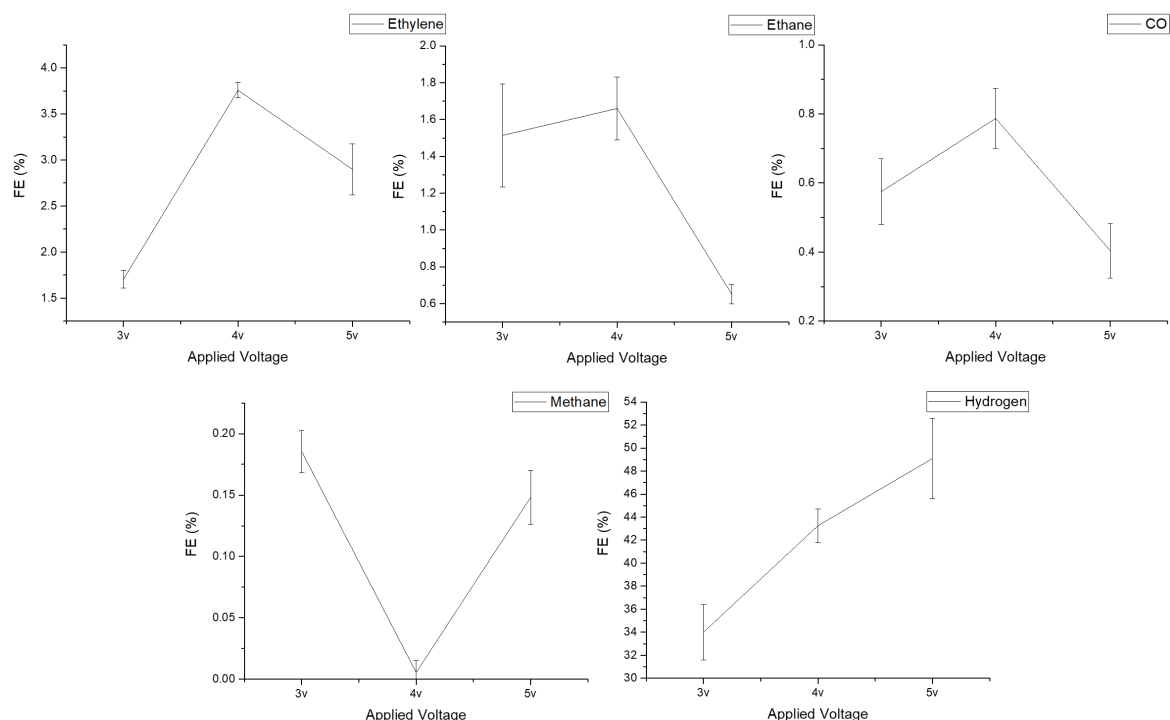


FIGURE 7.11: CO₂ electrolysis FE for all detected gaseous product for L-Lysine modified copper foams on copper plate electrodes, in CO₂ saturated 0.1M KHCO₃ electrolyte, at three different applied voltages.

For the LL modified copper foam, ethylene is the highest desired detected product at 3.8% at 4 V, followed by ethane at approximately 1.5% at 3 V and 4 V. CO is at 0.78% at 4 V, with trace amounts of methane. Ethylene starts at 1.7% at 3 V and increases to 3.7% at 4 V before dropping to 2.9% at 5 V. Ethane remains relatively constant at 1.5% and 1.7% at 3 V and 4 V respectively, with a notable decrease to 0.65% at 5 V. CO is 0.57% at 3 V, increases to 0.79% at 4 V and drops again to 0.4% at 5 V. Methane is found in trace amounts. Hydrogen is at 34% at 3 V with an increase to 43% at 4 V, with a further increase to 49% at 5 V.

Pollyallyamine

Figure 7.12 shows the FE of the collected product gases, for the Pollyallyamine modified foam (PAA) electrode.

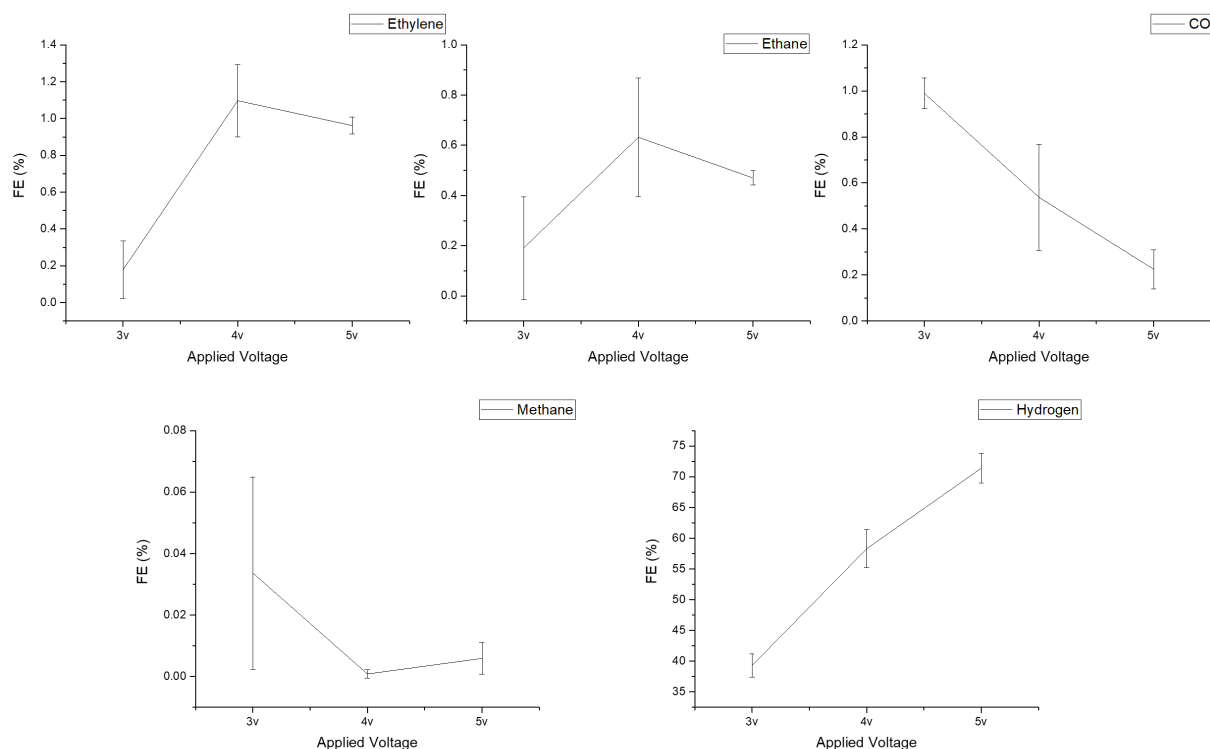


FIGURE 7.12: CO₂ electrolysis FE for all detected gaseous product for Polyallylamine modified copper foams on copper plate electrodes, in CO₂ saturated 0.1M KHCO₃ electrolyte, at three different applied voltages.

For the PAA modified copper foam, ethylene is highest of the desired products at 1.1% at 3 V followed at CO as the next highest gaseous product at 1% at 3 V, and ethane at 0.6% at 4 V with trace amounts of methane. Ethylene FE starts low at 0.2% at 3 V, increases at 1.1% at 4 V and then plateaus between 4 V and 5 V around 1%. Ethane FE is 0.19% at 3 V then increases, peaking at 0.63% at 4 V before falling to 0.46% at 5 V. CO FE is highest 0.99% at 3 V and then drops steadily to 0.54% at 4 V and further to 0.23% at 5 V. Methane FE is at trace levels at all applied voltages. Hydrogen FE is 39% at 3 V before steadily rising to 58% at 4 V and then rising further to 71% at 5 V.

Poly-D-Lysine

Figure 7.13 shows the FE of the collected product gases, for the Poly-D-Lysine modified foam (PDL) electrode.

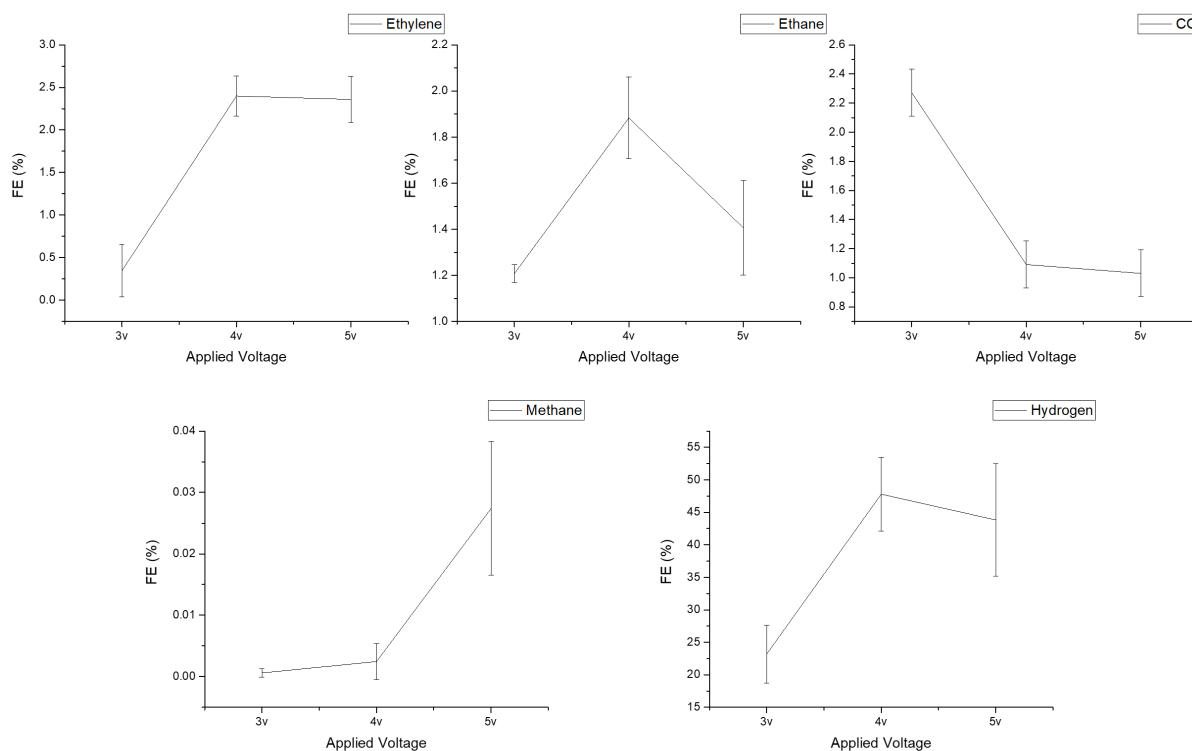


FIGURE 7.13: CO₂ electrolysis FE for all detected gaseous product for Poly-D-Lysine modified copper foams on copper plate electrodes, in CO₂ saturated 0.1M KHCO₃ electrolyte, at three different applied voltages.

For the PDL modified copper foam, ethylene is highest of the desired products at 2.4% at 3 V and 4 V followed at CO next highest at 2.3% at 3 V and then ethane at 1.9% at 4 V with trace amounts of methane. Ethylene FE starts at 0.3% at 3 V and rises to 2.4% at 4 V where it levels off at around 2.4% at 5 V. Ethane FE is at 1.2% at 3 V, reaches 1.9% at 4 V, before dropping to 1.4% at 5 V. CO FE is highest at 2.3% at 3 V, but then falls, with increased applied voltage, to 1.1% at 4 V where it remains relatively constant with 1.0% FE at 5 V. Once again methane is at trace levels at all applied voltages. Hydrogen FE starts at 23% at 3 V, then increases to 48% at 4 V, then shows a slight decrease to 44% at 5 V.

Comparison of Foam Modifiers at Set Voltages

To select the best modified foams for further testing, Figures 7.14, 7.15 and 7.16, were produced, showing the ethylene, ethane, carbon monoxide and hydrogen FE for each modifier at the applied voltages. Methane levels are not presented as they were only detected in trace amounts apart from on the Plate electrode.

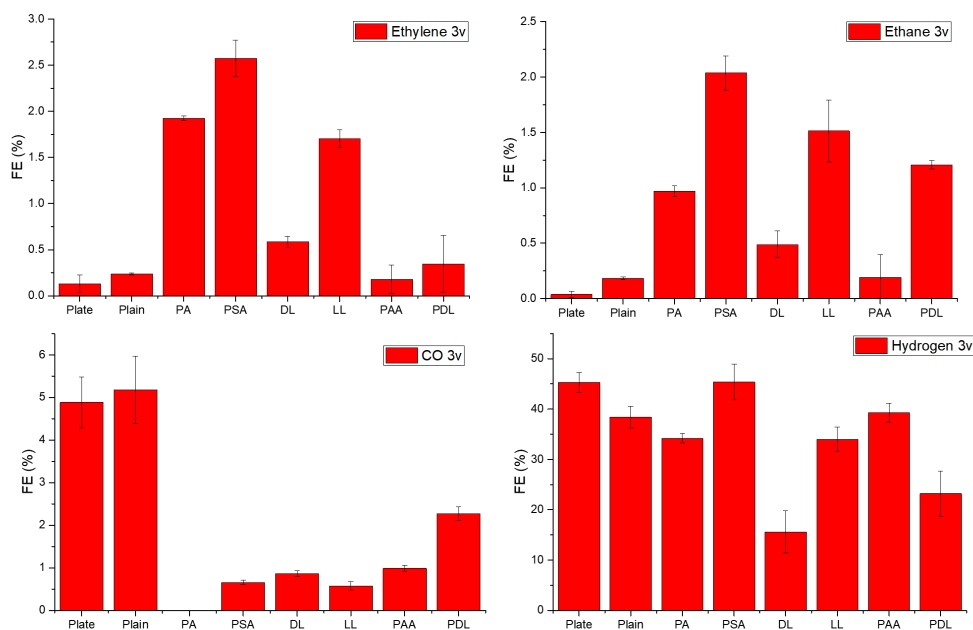


FIGURE 7.14: Bar charts for the FE of ethylene, ethane and hydrogen at 3 V for each of the different cathodes.

The bar charts at Figure 7.14 show that PSA has the highest ethylene FE at 3 V, at 2.6%. PA has the 2nd highest at 1.9% followed by LL at 1.7% with all other cathodes performing at less than 0.75%. For ethane at 3 V, PSA is again the highest at 2%, followed by LL at 1.5% and then PDL 1.2%. PA is the 4th highest at 1%, with all other being less than 0.5%. The Plain and Plate electrodes clearly have a much higher FE for CO at 3 V; 5.2% and 4.9% FE respectively. PDL shows a 2.3% FE at 3 V with PAA at 1%. All other electrodes are less than 1% FE for CO at 3 V, notably with no CO detected for PA. For hydrogen at 3 V, PSA is the highest at 45.4% very closely followed by the Plate at 45.3% with PAA and Plain being

the next two highest at 39% and 38.4% respectively. PA and LL are very close at 34.2% and 34%. Notably, PDL is lower at 23.2% and DL is even lower at 15.6%.

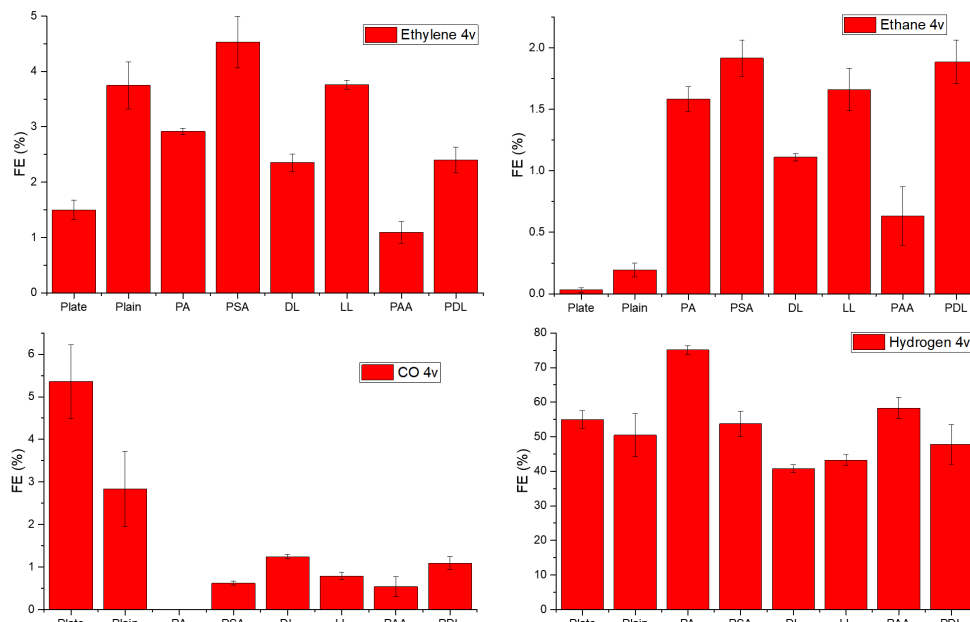


FIGURE 7.15: Bar charts for the FE of ethylene, ethane and hydrogen at 4 V for each of the different cathodes.

Figure 7.15 shows that at 4 V PSA has the highest FE for ethylene at 4.5%, with LL and Plain as the next highest at 3.8% and 3.7% respectively. PA is the next highest at 2.9% with DL and PDL both at 2.4%. PAA has a lower ethylene FE than Plate, 1.1% compared to 1.5%. PSA and PDL have the highest FE for ethane at 1.9%, with PSA being very slightly higher. LL is the 3rd highest at 1.7% closely followed by PA at 1.6%. DL has an ethane FE of 1.1% and PAA is significantly lower at 0.6%. Plain is even lower than PAA, at 0.2% with Plate only producing trace amounts. Plate clearly has the highest FE for CO at 4 V at 5.4% with Plain as the second highest at 2.8%. PDL, DL and LL have similar FEs for CO at 1.1%, 1.2% and 1% respectively. PAA and PSA both competitively have low FEs for CO at 0.5% and 0.6% with PA once again having no detectable FE for CO. DL is the lowest for hydrogen FE at 40.7% with LL and PDL also lower than Plain at 43.3%,

47.8% and 50.4%. PSA has a hydrogen FE of 53.8%, with Plate being at 55%. PA is by far the highest at 75%.

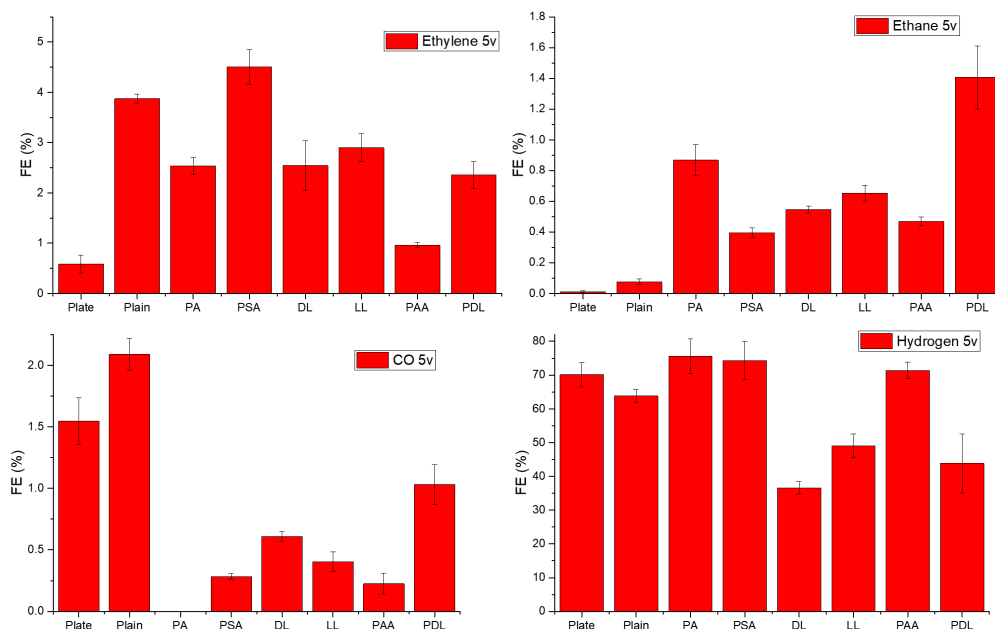


FIGURE 7.16: Bar charts for the FE of ethylene, ethane and hydrogen at 5 V for each of the different cathodes.

The 5 V patterns can be seen in Figure 7.16 which shows the findings at 4V where PSA has the highest ethylene FE at 4.5% with Plain as the next highest at 3.9%. LL is the 3rd highest at 2.9%, followed by PA and DL both at 2.5%, with PDL not far away at 2.4%. PAA is much lower at 1% and the Plate is even lower at 0.6%. PDL has the highest FE for ethane at 5 V, at 1.4% almost twice the value of the next highest which is PA at 0.87%. LL has a FE of 0.65% with DL slightly lower at 0.54%. PAA is slightly higher than PSA 0.47% and 0.4% with Plain and Plate producing trace amounts. Plain has the highest FE for CO at 2.1% whilst Plate is the second highest at 1.5%. PDL has a CO FE of 1% with all other modifiers having less than 1% FE. Most notably once again PA showed undetectable FE for CO. DL has the lowest FE for hydrogen at 5 V at 36%, PDL is the next lowest at 44%, with LL at 49%. Plain is next at 64% with Plate and PAA being relatively

close together at 70.1% and 71.4%. PSA and PA have the highest hydrogen FE 74% and 76%.

7.3.2 Discussion

Generally, at 3 V, FE is low for all detected products. At 4 V, most C₂ products either peaked in FE or remained at relatively constant levels up to 5 V. The general trend across all electrodes was an increase in FE of carbon based products up to 4V before either remaining relatively constant or dropping. A notable exception was the methane FE of the Plate and Plain electrodes which further increased from 4V to 5V. Some of the modified foam electrodes also show this behaviour, though still only trace amounts. Hydrogen FE increases with all voltages and electrodes except the three lysine foams. Both PDL and DL show a decrease in hydrogen FE from 4 V to 5 V suggesting that DL has a hydrogen quenching effect between 4V and 5V as this drop is also seen in the PDL electrode.

Plate and Plain have clear selectivity for C₁ products and are very similar at 3 V with trace amounts of C₂ products. Although Plain shows approximately twice the C₂ products as Plate, they are by far the highest FE for CO with trace methane FE from all electrodes. They also show comparatively high hydrogen FEs. This trend changes slightly at 4 V where the effect of the foam can be seen; Plain has twice the ethylene FE of Plate, but also approximately half the CO FE whilst maintaining relatively comparable hydrogen FEs. The key difference between the Plate and Plain is that Plate has an 11% FE for methane, whilst all the foams, not just Plain, have methane FEs in trace amounts. A similar situation is seen at 5 V, where Plate continues to be the only one to have a considerable FE for methane. Additionally Plain has the second highest CO FE at 5 V, only surpassed by Plate, whilst having the lowest ethylene and ethane FEs.

The key difference attributable to the presence of the Cu foam is the increased

FE for ethylene at 4 V and 5 V. On the topic of C₂ selectivity, PA has a clear selectivity for C₂ products in the gas phase as no C₁ products (CO or methane) were detected at any applied voltage. With the Plate having clear selectivity for C₁ gaseous products, all the foams show enhanced C₂ gaseous products. This suggests that the inclusion of the oxide layer seen in the EDX analysis is key for product selectivity.

PSA has the highest ethylene FE at all applied voltages, as well as the highest ethane at 3 V and 4 V, although by a small margin. It also has one of the highest hydrogen FE, with a clear difference from the lysine modified foams, especially at 3 V and 5 V. This suggests that the presence of a carboxyl group in the deposition bath, used to form the foam, may increase ethylene selectivity through the effects seen to the growth of the foams as observed in the SEM analysis. The impact of the carboxyl group in the PSA is also highlighted by comparing it to PAA where there are two differences: the average length of the polymer chain, 5.1K versus 15K (molecular weights), and the branched chain. With both branched chains being the same length, the key difference is the amide of PAA versus PSA's carboxyl group. PAA has a lower FE for C₂ products than PSA at all applied voltages, with PSA being 4x higher at 3 V, and at least 2x higher at 4 V, with only ethylene FE higher at 5 V.

It is useful to compare PA to PSA and PAA, as previously discussed above. Interestingly PA's FEs for C₂ gaseous products lies between those of PSA and PAA at all applied voltages, apart from ethane at 5 V which out performs both PSA and PAA. It is noted that PA has the lowest hydrogen FE (of the three foams) at 3 V, but then has the highest (of all electrodes) at 4 V, before having comparable FEs to PSA and PAA at 5 V.

The drop in CO for Plate is clearly in response to the increase in hydrogen production, up to 70% from around 50%. A similar effect is seen in all the foams as

CO FEs drop from 4 V to 5 V with an increase in hydrogen FE. However the lysine foams clearly show a lower FE for hydrogen at 5 V, also having the lowest FE for hydrogen at 4 V. This reinforces the previously mentioned quenching effect; PDL's FE for hydrogen, is not always as low as DL's, although it is consistently lower than that of the Plain. Similar patterns are found for LL, less the drop in hydrogen FE between 4 V and 5 V; it is consistently at a lower point than the Plate and Plain foam, at all applied voltages.

7.3.3 Summary

Three foams were selected for further testing: DL, LL, PDL. The DL showed a quenching effect as well as PDL, LL has a similar structure and following a literature search, these foams appear not to have been previously investigated. The Plain foam was also selected to form a baseline for all observed effects. Although these three modifiers did not perform particularly well on ethylene FE, they are often more selective for ethane, always out performing the Plain foam. The significantly different hydrogen FEs for the lysine modified foams, suggest an enhanced selectivity for a liquid product, compare to the Plain.

In addition to the reduction in modifiers it was also necessary to reduce the number of applied potentials. 4 V and 5 V were taken forward because 4 V proved optimum for wanted products on most modifiers and 5 V has the highest current density and therefore is more likely to concentrate liquid products, making them easier to detect. 3 V was discounted as although the FE% can be high for wanted products and low for hydrogen, the overall charge passed is low and unlikely to effectively concentrate liquid products.

7.4 Affect of Time on CO₂ Electrolysis using Organic Modified Cu Foams

To fully understand the effect of the foam on the CO₂ electrolysis, the liquid products should also be analysed. In the previous experiment they were too dilute to detect using ¹H NMR so to increase the concentration, the duration of the electrolysis was increased, with samples taken at regular intervals alongside reducing the amount of electrolyte in the system.

For this second set of experiments, the electrodes were prepared as per section 3.1. The duration of each electrolysis was 30 mins at 4 V with the last of the gaseous products collected from the gas trap 1 min after the end of the electrolysis and a 4ml sample of the catholyte was taken. 4 ml of fresh electrolyte was then added to the catholyte and the gas syringe and trap were emptied, before the next 30 min electrolysis was conducted. The volume of the electrolyte was halved to 75 ml in each half of the cell, to help concentrate liquid product, whilst ensuring the electrolyte was saturated with CO₂ in the bubbler. Six cumulative 30 min CO₂RR were conducted; 30 mins was selected to allow for the GC runtime and reset in between sample collection. FEs for the first 30 mins are not reported as liquid product concentrations were too low for repeatable data. Individual plots with standard deviation are presented in Appendix B.

7.4.1 Results

Figure 7.17 shows the product FEs for each of the examined foams over 3 hours at 4 V. It was found that the total FE drops over time for all of the examined Cu foam electrodes. PDL has the lowest total FE until 2 hours, where it has a similar FE as DL, thereafter it performs similarly to DL and LL. DL and LL remain in line with Plain until the 2 hour point, where they drop more than Plain.

PDL has the highest j at 30 mins, remained relatively constant to the 1 hour mark, before dropping steadily to have the lowest j at 3 hours. Plain has similar j to PDL after the first 30 mins, but performs very differently for the rest of the CO₂RR. The j for Plain drops considerably up to the 1 hour point, after which it drops at a more steady rate, falling just lower than that of PDL after 2.5 hours, before maintaining a higher j at the 3 hour mark. DL and PDL performed very similarly, both having passed a lower charge in the first 30 mins than PDL and Plain. However in the second 30 mins Plain's j remains relatively constant, similar to PDL, passing a higher charge than Plain, after which performance reflects Plain but decreases at a slightly lower rate.

Ethanol

The FE for ethanol in all cases drops over time, before starting to level out around the 2.5 hour mark. LL starts 6% higher than the other foams, but after dropping steadily, ends lower than Plain and relatively equal to DL, which similarly to Plain, showed a slight increase in the last 30 mins. PDL although being the third lowest after 30 mins, dropped much more rapidly than the other foams in the second 30 mins, before levelling off and surpassing DL after 2 hours, and both DL and Plain at the 2.5 hour mark, before being the lowest again at the 3 hour end point.

Acetic Acid

For acetic acid, all of the modified foams have a higher FE than the Plain foam. LL and DL perform similarly through the course of the 3 hours, dropping steadily until the 2 hour mark, where LL shows a slight increase in FE, before dropping to a marginally higher level than the other foams, which are all at a relatively comparable level.

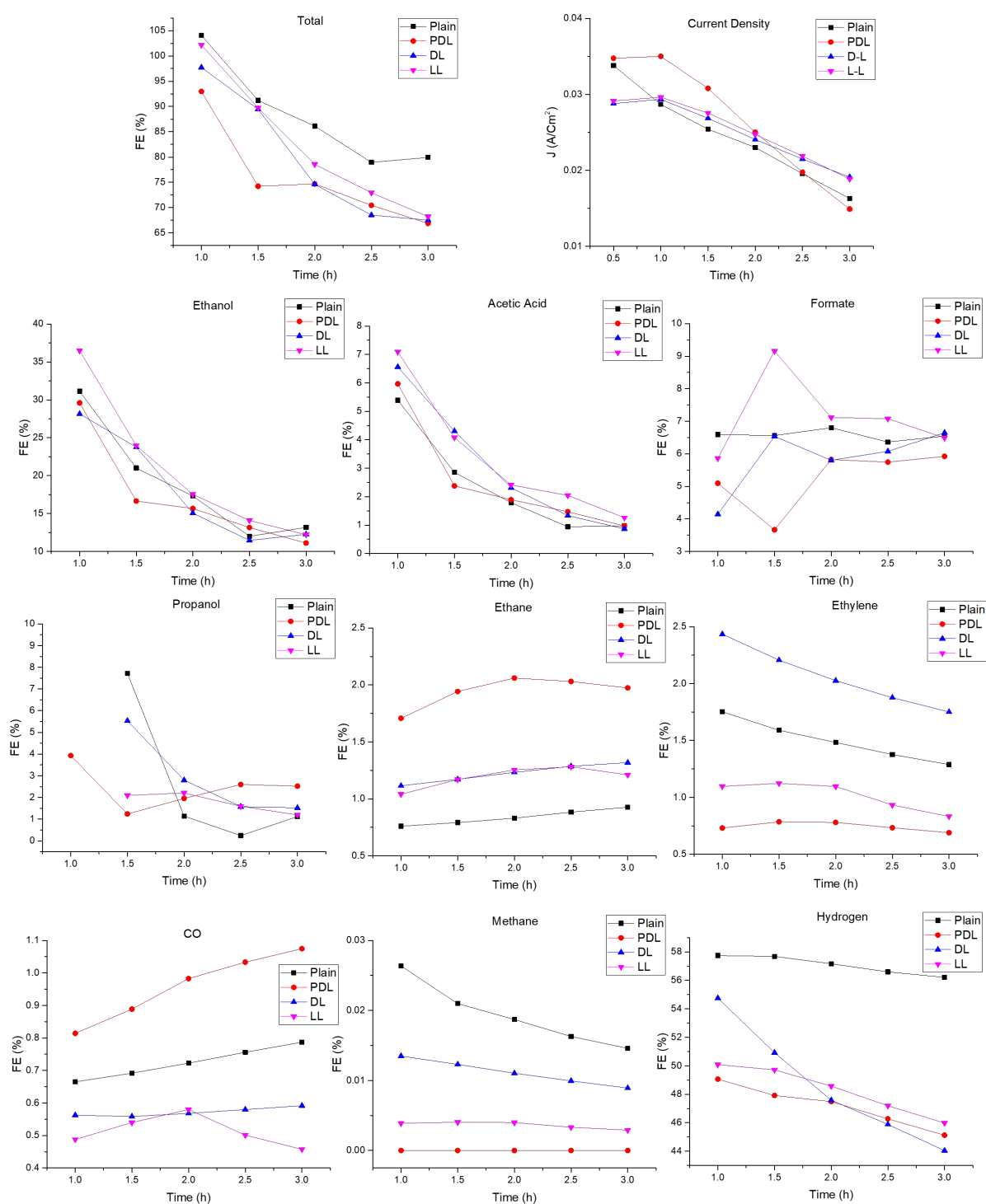


FIGURE 7.17: FE for each foam modifier and un-modified foam over 3 hours.

Formate

For the FE of formate, Plain remains relatively constant throughout the course of the 3 hour CO₂RR. Both DL and LL end at approximately the same FE as Plain, with PDL only 0.6% lower, and LL, PDL and DL having an FE 0.7%, 1.4% and 2.5% lower than Plain after the second 30 mins. With Plain remaining constant after the third 30 mins, the key difference is the considerable increase in FE by both DL and LL, although PDL strangely drops in FE during the same period. These trends do not continue in the fourth period where DL and LL both drop, PDL increases and LL and PDL trend towards the Plain foam. Between 2 and 3 hours, PDL remains constant whilst LL remains constant before decreasing in FE, and DL steadily increases in FE. Plain, DL and LL were all at a relatively comparable FE for formate after 3 hours.

Propanol

Only PDL reliably showed propanol at the 1 hour mark, whilst all of the foams showed propanol at 1.5 hours, with PDL propanol FE dropping considerably in that third 30 min period. Plain has the highest FE for propanol at the 1.5 hour mark, but then drops considerably at the 2 hour mark, with DL also having a comparatively high 1.5 hour propanol FE, before also dropping at the same point, although not as much as Plain. At 2.5 hours Plain has a very low FE of propanol, at 0.25%, but it increases back to 1.1% after 3 hours. Although LL has the lowest starting point for propanol FE, it remains relatively constant throughout the remaining 1.5 hours.

Ethane

PDL has highest FE for ethane throughout the 3 hours of CO₂RR, remaining relatively constant throughout, with a slight peak at 2 hours. DL and LL are relatively comparable in FE throughout the CO₂RR, with LL at the 1 hour and 3 hour

mark having a slightly lower FE than DL, with them both being approximately 1% lower in FE than PDL throughout. Plain is the lowest in FE throughout the 3 hours, with a slight upwards trend, from 0.76% at 1 hour to 0.92% after 3 hours. All of the foams shown a slight up trend in ethane FE over time.

Ethylene

DL has the highest ethylene FE of all the foams, with Plain approximately 1% behind, then LL another 1% behind. DL and Plain have a steady downtrend over time with DL decreasing slightly more than Plain; 0.6% versus 0.5%. LL has a lower FE than Plain but does not follow the same trend, with FE remaining constant at approximately 1.1% until 2 hours before following a similar downwards trend as DL and Plain. PDL has the lowest ethylene FE throughout with a slight peak around the 1.5 hour mark.

Carbon Monoxide

PDL showed a clear upwards trend in CO FE, surpassing 1% FE at the 2 hour mark. Plain shows a similar increase as PDL, though approximately 1% lower and to a lesser extent as it never reaches 0.8% FE. DL remains relatively constant at around 0.55% throughout. LL has a slight peak, of 0.1%, at the 2 hour mark, before dropping to 0.46% after 3 hours.

Methane

Methane was only found in trace amounts resulting in little difference FE, especially when experimental variation is considered.

Hydrogen

Plain has by far the highest hydrogen FE at around 57% throughout the 3 hours, with a slight downtrend. DL has a significantly higher hydrogen FE than the

other lysine foams at 55%, but the FE drops considerably, matching LL at approximately 47% at the 2 hour mark, then dropping further to 44% after 3 hours. PDL and LL follow a similar, slight downwards, trend starting at 49% and 50% at the 1 hour mark, decreasing to 45% and 46% respectively.

7.4.2 Discussion

There is a key difference between the way that liquid and gaseous products were analysed in this series of experiments. The gaseous products were collected in their entirety, less what was trapped in the cell (an estimated 1mL), after each 30 min CO₂RR. However only a sample of the liquid products was taken, with the same volume replaced to prevent dilution of the liquid products as much as possible. This meant that the FE for liquid products of each 30 mins had to be mathematically calculated rather than directly interpreted from the raw data.

The total FE should remain relatively constant around the 100% mark, however it dropped steadily over time. Due to the product collection methods used, the most likely cause is that volatile liquid products are stripped from the electrolyte when they pass through the CO₂ bubbler. As only liquid products are left in the system after each CO₂RR and only the liquid products (other than formate) reduce considerably in FE over time. Formate is not volatile enough to be stripped off and is continuously produced throughout the 3 hours, to maintain a relatively constant FE.

Lui *et al.* [162] found a decrease in hydrogen FE on Cu₂O electrodes in the first 3 hours, but it remained constant or increased for Cu electrodes in the same time period. This supports what can be seen in Figure 7.17 where the hydrogen FE remains comparatively constant for Plain and drops for the lysine modified foams. Additionally they showed very low FE for methane throughout, with ethylene FE steadily decreasing over time as evident in Figure 7.17. Kas *et al.* [72] also saw similar behaviours on Cu nanoparticles.

With PDL having the highest average current density it is not surprising that it has the lowest total FE. Additionally PDL displays ethane selectivity, having the highest ethane FE throughout the 3 hours but also the lowest ethylene FE. Notably both the PDL and Plain show current densities similar to those seen in Rudd *et al.* [93] after 30 mins (and up to 1 hour for PDL), where they reported 37.6 A/cm² for foam CF-18H-100U and 29.4 A/cm² for foam CF-18H, with comparable FEs for Propanol of 3.93 % in this work of 4.93 % for foam CF-18H-100U and 3.34 % for foam CF-18H.

The delay in propanol FE peak suggests that this product is produced at a later stage of electrolysis, as other C₂ products drop in FE, with formate also showing a considerable change in FE activity at 1.5 hour mark.

Pletcher *et al.* [92] discussed the effect of recycling reactant solution between the cell and a reservoir. They showed that although this design style benefits from a high linear flow rate it has a high current density and rate of conversion (mole/unit area of electrode) at the start. This conversion rate drops over time "as the concentration of reactant decreases; a high fractional conversion requires a long electrolysis time" [92]. Alternatively, by replacing the electrolyte, through continuous addition of fresh electrolyte, the rate of conversion can be maintained but the fractional conversion remains low.

Tang *et al.* [163] presented suggested various pathways for C₃ products, from known intermediates (Presented by Johnson *et al.* [164], Figure C.1) with the red boxes in Figure 7.18 highlighting the possible C₃ intermediates, the majority of which are propanol based intermediates.

It is also important to note that the lysine modified foams again showed a reduced FE of hydrogen when compared to the Plain foam.

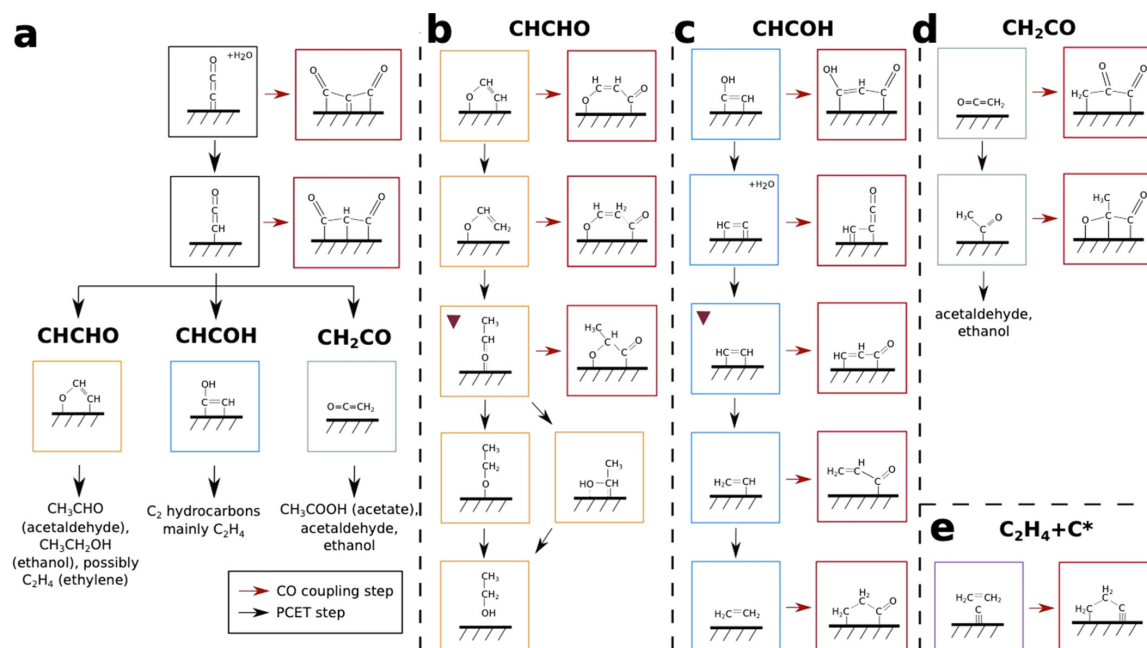


FIGURE 7.18: Reproduced from Tang *et al.* [163]: Pathways toward various C₂ products through CCO*, C₃ intermediates are boxed in red. (a) Trifurcation starts from CHCO* where CHCHO* (orange), CHCOH* (blue), and CH₂CO* (green) may form; it is postulated that ethylene can form from either CHCHO* (major product) or CHCOH* (minor product). (b) Intermediates and coupling mechanisms within the CHCHO* pathway. (c) Intermediates and coupling mechanisms within the CHCOH* pathway. (d) Exclusive intermediates and coupling mechanisms within the CH₂CO* pathway. (e) Ethylene coupling with atomic carbon. The inverted triangle (Brown triangle down solid) denotes the two most promising coupling steps to form C₃ products.

7.4.3 Summary

Considerable FE for ethanol were achieved after an hour of electrolysis, with LL at 37.2%, and both acetic acid and formate showing up to 7% FE at this point. The FEs for carbon products in these experiments are much lower than those reported in the literature. Billy *et al.* [57] discusses how the availability of CO₂ in cells impacts the selectivity of the products produced suggesting that the cell is mass transport limited. The relatively small amount of CO₂ that can be saturated into the electrolyte is insufficient for higher C₂ product FEs especially when considering the comparatively long distance between the electrode and the CO₂ source in the system. Most cells studied previously bubble directly into the cell reducing the CO₂ to bulk distance. The low solubility of CO₂, approximately 33 mM at STP

[165], limits mass transfer and consequently the current density and an aqueous-fed electrolyser only reaches values up to 35 mA /cm² [166]. In summary there is a lack of CO₂ reaching the electrode surface, due to the limited amount that is brought in through the saturated electrolyte.

7.5 Affect of GDE Inclusion on CO₂ Electrolysis using Organic Modified Cu Foams

It has been suggested in the previous section that the cell is currently mass transport limited. The most effective way to overcome this is to reduce the diffusion distance from the source of the CO₂ (currently the bulk electrolyte) to the electrode surface. The best method to achieve this is to introduce the CO₂ directly at the electrode surface through the use of a GDE.

For the adaption to a GDE electrode, the same electrodeposition method was used as in section 3.1, with the amount of electrolyte in the cathodic side of the cell further reduced to 25 ml of 0.1 M KHCO₃, with 75ml in the anodic side. Due to the small volume of catholyte used there was no cathodic circulation of electrolyte using the pump, on the cathodic side, therefore a syringe was used to recirculate the electrolyte ensuring that the bubbles did not build up inside the cathodic chamber and reduce the surface area of the cathode. The duration of each electrolysis was 15 mins per voltage with the last of the gaseous products collected from the gas trap 1 minute after the end of the electrolysis. As the GDEs are not homogeneous it was necessary to manually adjust the pressure of CO₂ applied to the gas compartment, so that CO₂ bubbles were just breaking through the GDE electrode.

7.5.1 Results

Figure 7.19 shows the FE for liquid and gaseous products for each Cu foam, grown on a Torbay carbon paper GDE, in a CO₂RR at -4 V for 15 mins. The geometrical current density of the Cu foam GDE has been calculated by normalizing the current to the outer surface area of the foam, as is the standard convention for reporting current densities of GDEs [167–170].

The GDE foams have the highest FE for ethanol, with LL as the highest of the three at 55%, followed by DL at 51% and PDL at 48% in clear contrast to the Plain foam at 38% FE. PDL has the highest FE for acetic acid at 4 V, at 18.6% DL and Plain were comparable around 12% with LL as the lowest at 11%. For formate FE, LL is the highest at 19% with PDL and DL similar at 11% and 11.6% respectively. Plain shows comparatively little formate FE at only 3.8%.

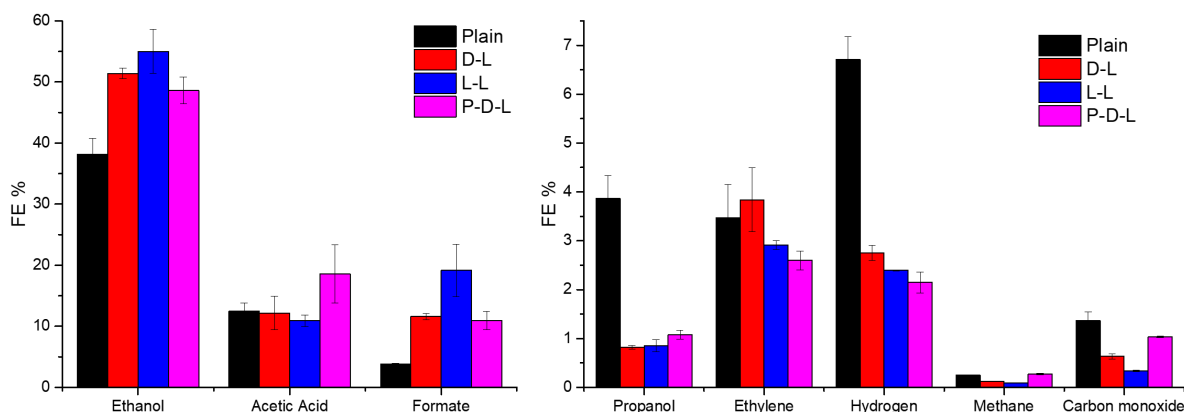


FIGURE 7.19: FE for each foam modifier and un-modified foam over 3 hours.

Plain has the highest FE for propanol at 3.9% with all of the lysine modified foams at around 1% FE. Ethylene FE is highest 3.9% for the DL foam, with the Plain foam at 3.5%. LL and PDL show a FE for ethylene at 3% and 2.6% respectively. Plain has more than double the FE of the lysine modified foams at 6.7% compared to 2.8% for DL, with 2.4% for LL and 2.1% for PDL. Methane was detected in trace

amounts. For CO FE at 4 V Plain is at 1.4%, PDL is at 1%, DL is at 0.6% and LL is at 0.3%.

Figure 7.20 shows the FE for liquid and gaseous products for each Cu foam, grown on a Torbay carbon paper electrode, in a CO₂RR at 5 V for 15 mins. It shows that LL has the highest FE for ethanol at 5 V, at 28.6% with DL at 26.5% and PDL at 23.4%. Plain has a considerably lower ethanol FE 19.1%. For acetic acid at 5 V, LL has the highest FE at 10.5% with PDL at 7.2%, DL at 6.4% and Plain as the lowest at 5%. PDL has the highest formate FE at 5 V, at 7.7% followed by LL at 5.2%. DL has a FE of 2.4% and Plain is at 1.8%.

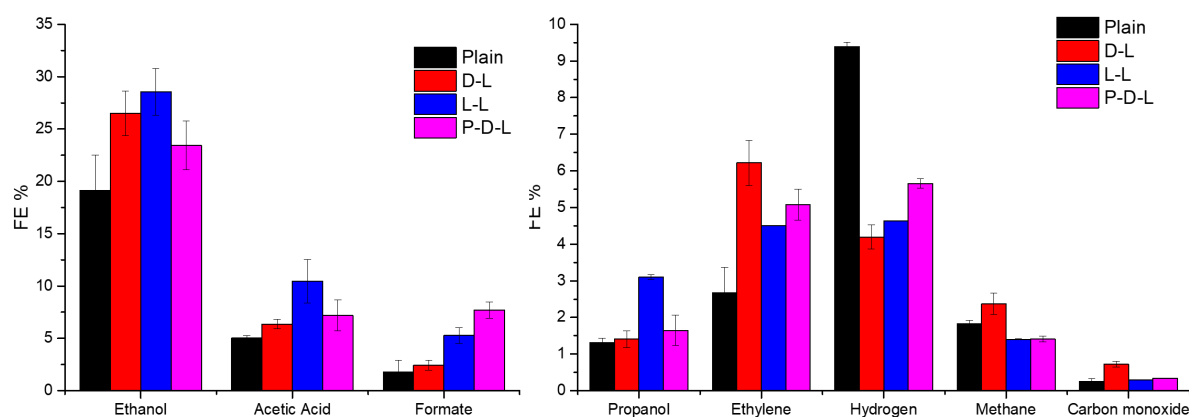


FIGURE 7.20: FE for each foam modifier and un-modified foam over 3 hours.

FE for propanol at 5 V is highest at 3.1% on LL, with PDL and LL comparable at 1.6% and 1.4% and Plain as the lowest at 1.3%. For ethylene at 5 V, FE is highest at 6.2% on DL, PDL is at 5.1%, LL at 4.5% and Plain at 2.7%. Plain has the highest hydrogen FE at 9.4% with PDL at 5.7%, LL at 4.6% and DL at 4.2%. Methane's highest FE at 5 V is DL at 2.3% followed by LL and PDL at 1.4% then Plain at 1.8%. CO FE is highest at 0.7% for DL recording PDL at 0.3, LL and Plain at 0.3%.

7.5.2 Discussion

The Plain foam has the highest FE for hydrogen at both examined voltages, whilst the lysine foams are all considerably lower, again showing the hydrogen quenching effect discussed earlier. Ethanol FE shows similar performance between the two voltages, with almost identical distributions, though 5 V has almost half the FE of that seen at 4 V.

The experimental run time was limited to 15 mins due to the instability of the GDE structure. GDE are known to be susceptible to flooding (electrolyte entering the gas phase). Another limitation is that the carbon paper is not homogenous, therefore not all electrodes are identical, causing flooding at different pressures and after different durations. Some cells lasted more than 20 mins others did not make 15 mins so it is difficult to successfully characterise the GDE.

7.5.3 Summary

The GDE setup shows clear selectivity for ethanol, with lysine enhancing this selectivity. 4 V has been shown to be the optimum applied voltage for ethanol FE, and the lowest hydrogen FE. However ethylene and methane FE is highest at 5 V.

7.6 *In Situ* Surface Study on the Interface of Cu-foam Electrodes using EXAFS

Previous studies [93] as well as the work in this chapter, have shown that CO₂ can be converted to propanol and morphological changes of the Cu foam can impact the conversion performance. Following this, a better understanding of the chemistry at the interface of the copper electrode was desired, especially the role of the Cu valence state and formation of transient oxide species, as computational studies [164, 171] have indicated that subsurface oxygen or oxide phases can affect the CO₂ conversion selectivity for C₂ products.

It is challenging to detect the presence of oxygen, *ex-situ*, since exposure to air causes surface oxidation of the copper. Additionally the chemical speciation of the Cu electrode during electrolysis are rapidly changing due to interaction of Cu with the CO₂ conversion intermediates which are mobile causing a restructuring of the surface. This is particularly the case with CO which coordination adducts with copper [172].

Conventional X-ray absorption spectroscopy (XAS) acquisition time is approximately 10 to 30 min, and electron energy loss spectroscopy (EELS) requires a time-scale in minutes for spectrum acquisition. However the metal centres are known to reach a steady state within a couple of minutes during the CO₂RR, as Chang *et al.* found [173] through *in-situ* Raman. The CuO_x achieves a steady-state condition due to the co-occurrence of electrochemical reduction and spontaneous oxidation caused by the trace oxidants in the electrolyte [174]. As a result of these factors, operando energy dispersive Extended X-ray Absorption Fine Structure (EXAFS) at the I20 beamline, Diamond Light Source Ltd, was used to identify the chemical speciation on Cu foams.

7.6.1 Experimental

In-situ Energy Dispersive EXAFS was performed over an energy range of 8.8 to 9.7 KeV, with spectra acquired using a FReLoN detector. Acquisition times were in the order of 0.5 to 8.5 ms per single accumulation (130 ms/spectrum) after optimizing counts, while avoiding detector saturation (0.5 ms was used to avoid saturation even during bubble formation). To improve spectral signal-to-noise ratio, spectra were averaged over time and several experimental runs. Electrochemistry was conducted (using the available Ivium potentiostat) at a constant voltage using a copper foam on carbon paper (Toray 060) working electrode, Ni foam counter electrode and Ag/AgCl reference electrode. A Bespoke Diamond designed two-phase flow cell was used at the I20 beam line as shown in Figure 7.22. CO₂ gas was bubbled into the 1 M NaOH electrolyte feed solution, maintaining saturation, and then pumped round the cell, using I20's peristaltic pump. This was performed simultaneously with Cu K edge X-ray absorption spectroscopy measurements. The reactions were followed by EXAFS for up to 360 seconds, with the data being analysed using Diamond's DAWN analysis software.

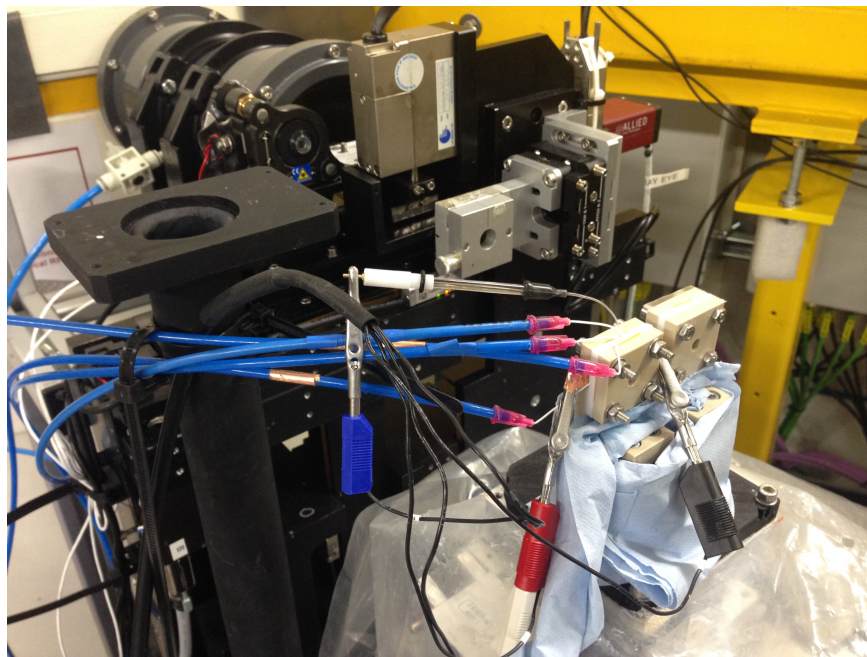


FIGURE 7.21: Instrumental set-up used for the EXAFS study. The examined copper foam is in the left electrochemical cell, with the background reference cell on the right.

In Figure 7.21 the studied foam is in the left electrochemical cell, which is connected to electrolyte flow (through the blue tubes) and the electrical connections to the Ivium potentiostat. The background shows a Kapton ended vacuum tube between the primary and experimental radiation shields. The copper foams were prepared as per section 3.1.

7.6.2 Results and Discussion

Figure 7.22 shows the results of placing the reference standards within the reference cell, and testing without the presence of electrolyte. Figure 7.23 shows the EXAFS spectra for reference standards for CuO, Cu₂O and Cu Foil. A clear peak for copper foil at 2.25 Å is attributed to the Cu-Cu Interatomic distance, supported by Lin *et al.*'s [174] findings. The Cu-O bond can clearly be seen in both figures to have an interatomic distance of 1.45 Å, with Cu₂O also seen at 2.7 Å. Dutta *et al.* [86] also found Cu-Cu at 2.25 Å and Cu-O at 1.5 Å.

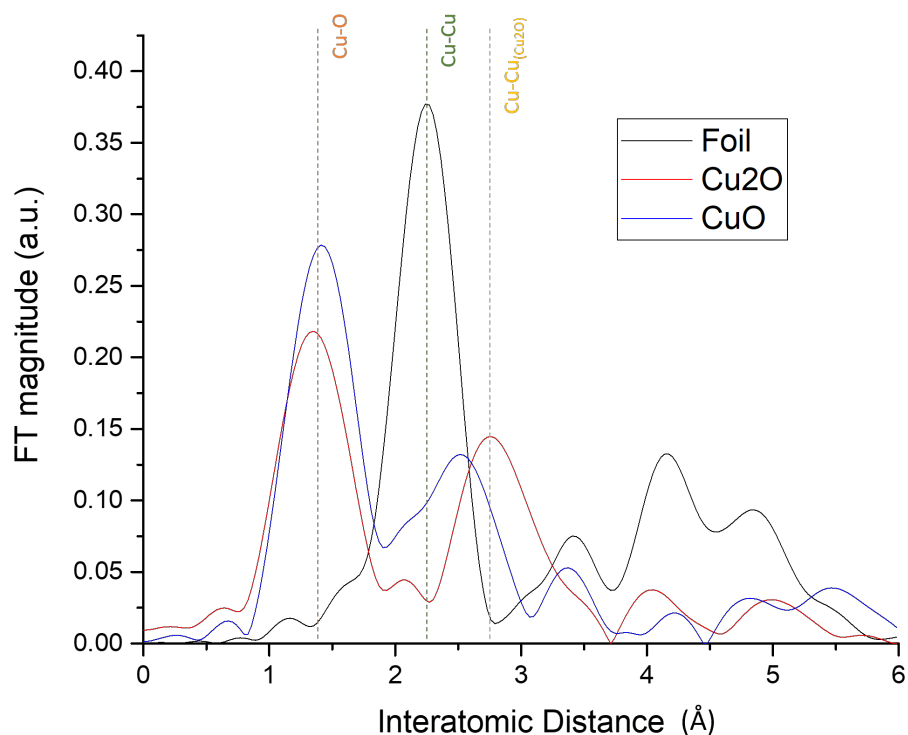


FIGURE 7.22: EXAFS spectra for reference standards for CuO, Cu₂O and Cu Foil.

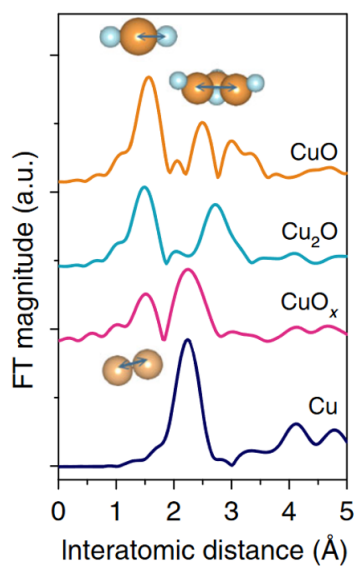


FIGURE 7.23: Reproduced with permission from Lin *et al.*[174], Wavelet transformed-EXAFS of prepared CuO_x and the references.

Figure 7.24 shows the averaged EXAFS spectra for a Cu foam under a -1.00 V vs Ag/AgCl, in a 1 M NaOH electrolyte saturated with Ar. Before applying voltage, the EXAFS spectra showed signals corresponding to a mixture of Cu₂O and CuO. The Cu foam is quickly oxidised and reaches a steady state, shown by the reduction in the relative magnitude for the Cu-O and the Cu₂O peaks, and the increase in the Cu-Cu peak within 90 seconds.

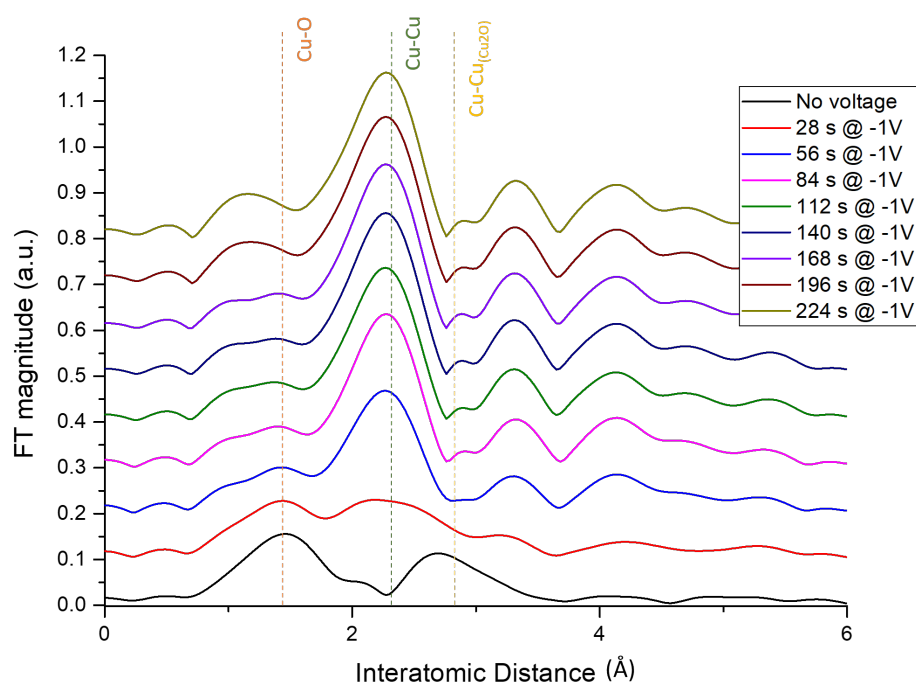


FIGURE 7.24: Averaged EXAFS spectra for Cu foam at -1 V in Ar saturated 1 M NaOH electrolyte before and during the electrolysis.

Figure 7.25 shows the averaged EXAFS spectra for a Cu foam under a -1.00 V versus Ag/AgCl, in a 1M NaOH electrolyte saturated with CO₂. Similarly to the Ar saturated electrolysis, the Cu foam is quickly reduced, with a similar reduction relative magnitude for the Cu-O and the Cu₂O peaks, and increase in the Cu-Cu peak. However the Cu foam is not fully reduced as there is still a considerable peak at just under the 1.45 Å interatomic distance of the Cu-O. Additionally, there is the emergence of an additional peak, just below the Cu-Cu peak (at 2.25 Å), at around 1.8 Å.

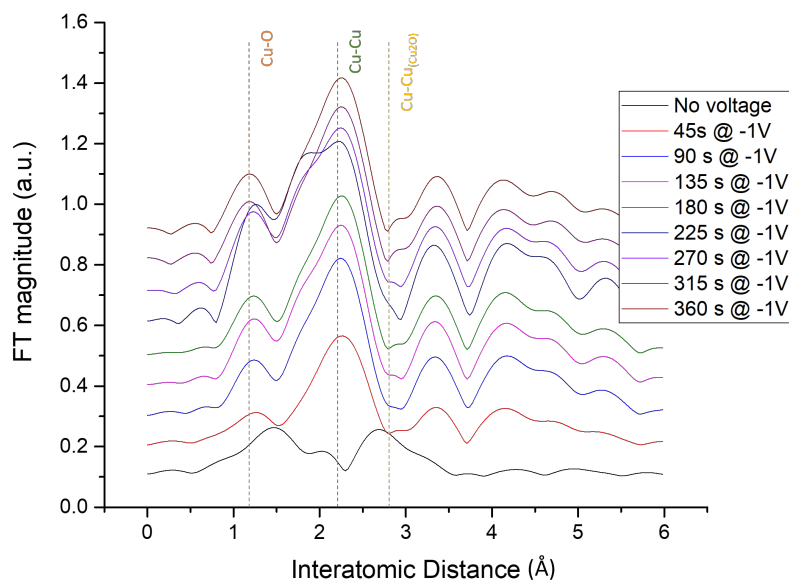


FIGURE 7.25: Averaged EXAFS spectra for Cu foam at -1 V in CO₂ saturated 1 M NaOH electrolyte before and during the CO₂RR.

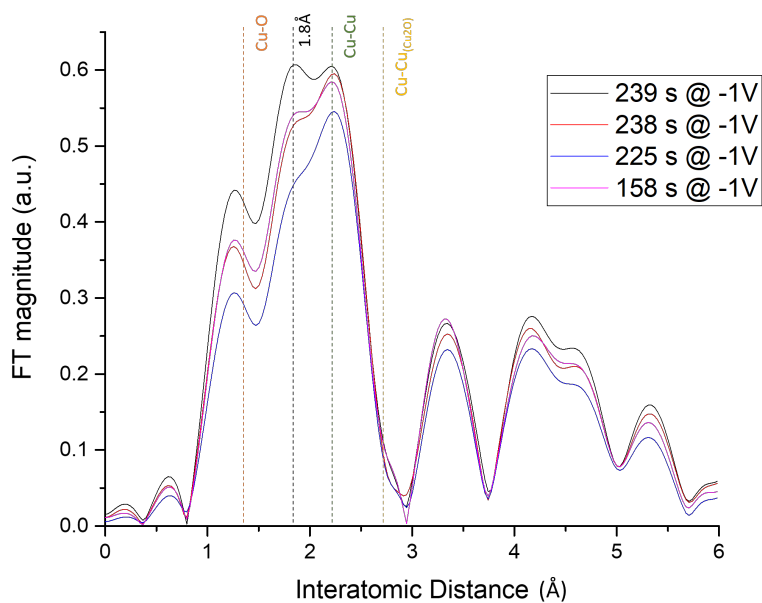


FIGURE 7.26: Selected EXAFS spectra for Cu foam at -1 V in CO₂ saturated 1 M NaOH electrolyte before and during the CO₂RR.

Figure 7.26 presents the individually selected EXAFS spectra from the same data set as Figure 7.25, where the additional peak at 1.8 Å can be more easily seen. Published works have attributed the 1.8 Å peak to Cu-C bonds, with Alikhani *et al.*[175] finding that the interatomic distance for Cu(CO)₂ the Cu-C is 1.831 Å and for CuCO the Cu-C is 1.976 Å. Additionally Pike *et al.*[176] found the interatomic distance for Cu-C to be within the range of 1.80-1.86 Å.

7.6.3 Conclusion

Lin *et al.*[174] showed an enhanced FE for ethanol using their Redox Shuttle method where square wave voltammetry re-oxidises the foam inbetween CO₂RRs. It can therefore be hypothesised that the Cu foam is still partially oxidised, in a steady state, during CO₂RRs explaining the enhanced selectivity for ethanol seen in earlier sections of this chapter. This combined with the presence of the peak at 1.8 Å shows that the Cu foam can form a bond with CO₂ present in the electrolyte and/or the carbon monoxide generated during electrolysis with it being previously reported that the presence of subsurface oxygen can steer the selectivity of the CO₂RR to C₂ products.

7.6.4 Acknowledgments

This work is part of project SP25525, titled 'How does carbon dioxide convert to n-propanol? An EXAFS study.' performed at Beamline I-20 at diamond light source.

Research staff involved include: Dr Enrico Andreoli, Dr Jennifer Rudd, Dr Sandra Hernandez-Aldave, Dr Waqas Tanveer, Odin Bain.

Thanks to Dr Luke Keenan for his assistance in data collection and analysis

7.7 Conclusion and Outlook

The presence of copper oxide, seen in the EDX analysis, has been shown to enhance the selectivity for C₂ products in section 7.3, with the EXAFS analysis showing that a hybrid copper/copper oxide electrode is maintained during electrolysis, for at least the unmodified foam. Further work needs to be conducted to corroborate the EXAFS analysis and confirm the allocation of the 1.8 Å as the Cu-CO interatomic distance, through specific modelling.

Lysine and its derivatives have shown promise for CO₂RR enhancement of C₂ products and a hydrogen quenching effect. The effects of lysine should be developed further; examination in a 3 electrode cell will produce results which can be compared with other studies found in the literature. Additionally the effects of PDL without the presence of HCl should be examined.

Chapter 8

Conclusions

This study sought to advance the development of CO₂ electrolyzers towards the integration of novel catalysts using copper foams to enhance product selectivity and productivity. The thesis had three main aims. Firstly, it sought to design, develop, and characterise electrochemical cells to be operated over a wide range of applied potentials for CO₂ conversion. Secondly, to perform experimental characterisations to quantify and minimise the electrical losses within the cells through current density versus potential measurements. Finally, to integrate novel additive-modified copper foams as CO₂ electrocatalysts to enhance C₂ product selectivity.

With regards to the first of these goals, Chapter 4 examined electrochemical cells currently available on the market and others reported in the literature. From this, a novel design was developed and further refined through computational fluid dynamic modelling (CFD) and practical application resulting in the creation of a cell that could be optimised for electrical conductance in Chapter 5. The CFD modelling demonstrated the effects of various features in the profile of the flow plate particularly the inlet restrictions, outer body geometry and cell restrictions. Having designed a cell that was optimised for electrolyte flow, the cell was further modified into the final design iteration (MK3), also through the electrical characterisations described in Chapter 5. In this version the cell's reliability and

durability were improved to allow for multiple hour runs required for the CO₂ electrolysis presented in Chapter 7. The design had also been adapted to facilitate the inclusion of a gas diffusion electrode, in the attempt to enhance the supply of CO₂ to the electrode surface. At the end of Chapter 4, a proposed future design iteration is presented, possibly enabling the cell to work as a stacked electrolyser, where multiple cathodes and anodes operate in close proximity as is commonly seen in commercially available stacked cell designs.

In relation to the second goal to quantify and minimise the electrical losses within the cells, Chapter 5 examined the effects of several parameters on the current density. The electrolyte flow rate was optimised and a value of 50 mL/min was found to be the most effective. Thereafter focus was placed on the effect of electrode separation on cell performance. An electrode spacing of 3 mm emerged as the optimal distance, whilst a separation of 4 mm was adopted to allow integration of copper catalyst foams. The third examined parameter was the impact of different electrolyte concentrations and 2 M KHCO₃ was shown to result in the highest current density. A key aspect noticed in these three experiments was that the profile of the *j*-*V* curve had a bell shape, rather than a typical linear response. The cause of this behaviour was investigated by using nitrogen-saturated electrolyte to amplify the pH imbalance observed during operation between the cathodic and anodic compartments, separately circulating catholyte and anolyte through a Dual Reservoir system. In such a case, the cell experienced proton transport limitation across the Nafion membrane, affecting electrical current flow at high voltages, resulting in the observed bell shape. A single reservoir system, where catholyte and anolyte are combined, was then implemented to verify that pH neutralisation overcame the current drop resulting in a typical linear ohmic conductor response. The final examined parameter was the effect of using a copper foam instead of a copper plate electrode. The high electrochemical surface area of the copper foam resulted in an increased current density over a copper

plate electrode of the same geometric surface area. Machine learning algorithms were applied to verify the experiential optimum parameter values affecting cell current density. This computer modelling study was conducted during the pandemic due to lab access restrictions.

To address the final goal, Chapter 7 examined how additive-modified copper foam electrodes can enhance the selectivity for C₂ products from CO₂ catalysis. The faradaic efficiency of CO₂RR products were determined with an emphasis on identifying C₂ products. A number of organic compounds were selected as modifiers for use in the deposition of copper foam electrodes, referenced to those reported in the literature as a guidance. The deposited foams were characterised using SEM and EDX analytical techniques. The foams were then utilised for CO₂ electrocatalysis at different voltages applied across the cell for 15 minutes. These data were used to determine the optimum potential across the cell for CO₂RR to C₂ products, with a single limitation of only being able to analyse gaseous products due to low liquid product concentrations. The cell and supporting system were then adapted to allow increasing the concentration of liquid products for electrolysis extended to 3 hours. Through this adaptation, a clear selectivity for ethanol was observed, along with a considerable hydrogen quenching effect by lysine-modified copper foams. The final testing required another cell and system change to include the integration of a gas diffusion electrode at the cathode. This last modification allowed for detectable amounts of liquid products to be generated within a 15 minute electrolysis, as the catholyte was no longer required to transport CO₂ into the cell, greatly reducing the volume of electrolyte required. Once again a clear selectivity for ethanol was seen with the lysine-modified foams showing an even stronger hydrogen quenching effect. To conclude Chapter 7, synchrotron *in-situ* EXAFS analyses were conducted to show that the copper foam remained in a partially oxidised state during CO₂ electrocatalysis. The EXAFS FT magnitude spectrum also showed a 1.8 Å peak which

could be attributed to Cu-CO species formed during CO₂ catalysis.

8.1 Future works

Future Designs

There are several ways in which the design of the cell could be further refined, after the proposed cell design in presented section 4.5.5. The method of membrane mounting should be examined in order to reduce the amount of membrane required, considering the current limitations on the postreduction of PFSA's and reducing costs. Additional MEA based design adaptations should be considered. By removing the need for electrolyte, the operating and setup costs can be reduced, though product efficiency and selectivity would need to be maintained.

Additional scale up is required to make the CO₂ electrolyzers commercial viable, even with the maximum electrode area of 16 cm². Most commercial electrolyzers utilise at least 1 m² electrodes. With this increase in scale factors such as temperature moderations, electrolyte flow and GDE wetting will become more substantial and require additional study.

Specialised flow modelling should be conducted, using advanced software such as Ansys Fluent, which could produce much greater detail on the fluid models and allow for the simulation of gas bubbles being produced on the electrode surface.

Ways to mitigate the pulsation of pumps enhancing the effect of GDE wetting and flooding of the gas side will need to be further developed, most likely by the inclusion of dampeners or accumulators, although gravity designs are being developed currently.

Digitalisation and monitoring in each of the chambers will allow for much finer control of variables, however this will come at a considerable cost increase and

will need to be evaluated thoroughly.

Future system analysis

As has been shown at several point in the theory as well as in the literature, temperature and pressure both have significant affect on the system. The key considerations of this is the effect on the solubility of CO₂ in the electrolyte as well as the electrolytes conductivity and the rate of transport through the membrane. Future studies couldl examine these properties and identify potential ways to improve performance.

Future Machine Optimisation

With the rapid progress in AI technologies, additional way in which it can be used to streamline and enhance piratical experimentation should be thoroughly investigated in-order to further scientific advancement across all fields.

Future Electrocatalysts

The conducted EXAFS analysis showed that a hybrid copper/copper oxide electrode is maintained during electrolysis, for at least the unmodified foam. Further investigation to corroborate the EXAFS analysis and confirm the allocation of the 1.8 Å as the Cu-CO interatomic distance, will improve the understanding of the reaction mechanisms this technology utilises.

Lysine modified foams have shown promise for CO₂RR favouring C₂ products with a considerable hydrogen quenching effect. This should be developed further to identify the particular components of lysine that produce this effect.

Bibliography

1. Jonnes, J. *Empires of light : Edison, Tesla, Westinghouse, and the race to electrify the world* / Jill Jonnes. eng. ISBN: 9780375758843 (Random House, New York, 2004).
2. Hammerstrom, D. J. AC Versus DC Distribution Systems Did We Get it Right? doi:10.1109/PES.2007.386130 (2007).
3. Liu, X., Wang, P. & Loh, P. C. A Hybrid AC/DC Microgrid and Its Coordination Control. *IEEE Transactions on Smart Grid* **2**, 278–286. doi:10.1109/TSG.2011.2116162 (2011).
4. *Microgeneration strategy* tech. rep. (Department of Energy & Climate Change, June 2011). https://assets.publishing.service.gov.uk/government/uploads/system/uploads/attachment_data/file/48114/2015-microgeneration-strategy.pdf.
5. Morgan, J., Littlewood, J., Jones, P. & Alam, M. *Testing and validation of 'building as power station technologies' in practice, to maximise energy efficiency and user comfort and minimise carbon emissions* Future Technology Press Sustainability in Energy and Buildings: Research Advances, 6, pp.20-28. 2017.
6. Masters, C. Voltage rise: the big issue when connecting embedded generation to long 11 kV overhead lines. English. *Power Engineering Journal* **16**, 5–12(7). ISSN: 0950-3366. https://digital-library.theiet.org/content/journals/10.1049/pe_20020101 (1 2002).

7. Quezada, V., Abbad, J. & Roman, T. Assessment of energy distribution losses for increasing penetration of distributed generation. *IEEE Transactions on Power Systems* **21**, 533–540. doi:10.1109/TPWRS.2006.873115. <https://ieeexplore.ieee.org/abstract/document/1626356> (2006).
8. Lopes, J. P., Hatziargyriou, N., Mutale, J., Djapic, P. & Jenkins, N. Integrating distributed generation into electric power systems: A review of drivers, challenges and opportunities. *Electric Power Systems Research* **77**. Distributed Generation, 1189–1203. ISSN: 0378-7796. doi:<https://doi.org/10.1016/j.epsr.2006.08.016>. <https://www.sciencedirect.com/science/article/pii/S0378779606001908> (2007).
9. Mahmud, N. & Zahedi, A. Review of control strategies for voltage regulation of the smart distribution network with high penetration of renewable distributed generation. *Renewable and Sustainable Energy Reviews* **64**, 582–595. ISSN: 1364-0321. doi:<https://doi.org/10.1016/j.rser.2016.06.030>. <https://www.sciencedirect.com/science/article/pii/S136403211630243X> (2016).
10. Jouny, M., Luc, W. & Jiao, F. General Techno-Economic Analysis of CO₂ Electrolysis Systems. *Industrial & Engineering Chemistry Research* **57**, 2165–2177. doi:10.1021/acs.iecr.7b03514. eprint: <https://doi.org/10.1021/acs.iecr.7b03514>. <https://doi.org/10.1021/acs.iecr.7b03514> (2018).
11. Okoye-Chine, C. G. *et al.* Conversion of carbon dioxide into fuels—A review. *Journal of CO₂ Utilization* **62**, 102099. ISSN: 2212-9820. doi:<https://doi.org/10.1016/j.jcou.2022.102099>. <https://www.sciencedirect.com/science/article/pii/S2212982022002189> (2022).
12. Centi, G. & Perathoner, S. Status and gaps toward fossil-free sustainable chemical production. *Green Chem.* **24**, 7305–7331. doi:10.1039/D2GC01572B. <http://dx.doi.org/10.1039/D2GC01572B> (19 2022).
13. Bilgen, S. Structure and environmental impact of global energy consumption. *Renewable and Sustainable Energy Reviews* **38**, 890–902 (2014).

14. Nejat, P, Jomehzadeh, F, Taheri, M. M., Gohari, M & Majid, M. A global review of energy consumption, CO₂ emissions and policy in the residential sector (with an overview of the top ten CO₂ emitting countries). *Renewable and Sustainable Energy Reviews* **43**, 843–862 (2015).
15. *Annual Energy Outlook* (2005).
16. Crompton, P & Wu, Y. Energy consumption in China: past trends and future directions. *Energy economics* **27**, 195–208 (2005).
17. Ekholm, T, Krey, V, Pachauri, S & Riahi, K. Determinants of household energy consumption in India. *Energy Policy* **38**, 5696–5707 (2010).
18. Lazard. *Lazard's Levelized Cost of Energy Analysis— Version 11.0* 2018.
19. Department, I. E. A. R. E. T. *Comparative Analysis of International Offshore Wind Energy Development* 2018.
20. Hassellöv, I.-M., Turner, D. R., Lauer, A. & Corbett, J. J. Shipping contributes to ocean acidification. *Geophysical Research Letters* **40**, 2731–2736. doi:10.1002/grl.50521 (2013).
21. Jonson, J. E. *et al.* Impact of excess NO_x emissions from diesel cars on air quality, public health and eutrophication in Europe. *Environmental Research Letters* **12**, 094017 (2017).
22. Hutchinson, E. J. & Pearson, P. J. An evaluation of the environmental and health effects of vehicle exhaust catalysts in the UK. *Environmental health perspectives* **112**, 132 (2004).
23. Solomon, S, Plattner, G, Knutti, R & Friedlingstein, P. Irreversible climate change due to carbon dioxide emissions. *Proceedings of the national academy of sciences* **106**, 1704–1709 (2009).
24. Earth System Research Laboratories, G. M. L. *Trends in Atmospheric Carbon Dioxide (CO₂)* https://gml.noaa.gov/ccgg/trends/gl_trend.html. https://gml.noaa.gov/ccgg/trends/gl_trend.html.

25. Krupa, S. V. & Kickert, R. The greenhouse effect: impacts of ultraviolet-B (UV-B) radiation, carbon dioxide (CO₂), and ozone (O₃) on vegetation. *Environmental Pollution* **61**, 263–393 (1989).
26. Hansen, J. *et al.* Ice melt, sea level rise and superstorms: evidence from paleoclimate data, climate modeling, and modern observations that 2C global warming could be dangerous. *Atmospheric Chemistry and Physics* **16**, 3761–3812. doi:10.5194/acp-16-3761-2016. <https://acp.copernicus.org/articles/16/3761/2016/> (2016).
27. McGlade, C. & Ekins, P. The geographical distribution of fossil fuels unused when limiting global warming to 2 °C. *Nature* **517**, 187–190. ISSN: 1476-4687. doi:10.1038/nature14016. <https://doi.org/10.1038/nature14016> (2015).
28. Jenkinson, D. S., Adams, D. E. & Wild, A. Model estimates of CO₂ emissions from soil in response to global warming. *Nature* **351**, 304–306. ISSN: 1476-4687. doi:10.1038/351304a0. <https://doi.org/10.1038/351304a0> (1991).
29. Norby, R. J. & Luo, Y. Evaluating Ecosystem Responses to Rising Atmospheric CO₂ and Global Warming in a Multi-Factor World. *The New Phytologist* **162**, 281–293. ISSN: 0028646X, 14698137. <http://www.jstor.org/stable/1514501> (2022) (2004).
30. Joos, F., Plattner, G.-K., Stocker, T. F., Marchal, O. & Schmittner, A. Global Warming and Marine Carbon Cycle Feedbacks on Future Atmospheric CO₂. *Science* **284**, 464–467. doi:10.1126/science.284.5413.464. <https://www.science.org/doi/abs/10.1126/science.284.5413.464> (1999).
31. Goldemberg, J. *World energy assessment. Energy and the challenge of sustainability* 2001.
32. Olah, G. A., Prakash, G. K. S. & Goepfert, A. Anthropogenic Chemical Carbon Cycle for a Sustainable Future. *Journal of the American Chemical Society* **133**. PMID: 21612273, 12881–12898. doi:10.1021/ja202642y. eprint: <https://doi.org/10.1021/ja202642y>

- [//doi.org/10.1021/ja202642y](https://doi.org/10.1021/ja202642y). <https://doi.org/10.1021/ja202642y> (2011).
33. Olah, G. A., Goeppert, A. & Prakash, G. K. S. Chemical Recycling of Carbon Dioxide to Methanol and Dimethyl Ether: From Greenhouse Gas to Renewable, Environmentally Carbon Neutral Fuels and Synthetic Hydrocarbons. *The Journal of Organic Chemistry* **74**. PMID: 19063591, 487–498. doi:10.1021/jo801260f. eprint: <https://doi.org/10.1021/jo801260f>. <https://doi.org/10.1021/jo801260f> (2009).
34. COP21 Paris Agreement in (2015). http://ec.europa.eu/clima/policies/international/negotiations/paris/index_en.htm.
35. Working Group III Contribution to the Fifth Assessment Report of the Intergovernmental Panel on Climate Change in (2014).
36. Campbell, M. Technology Innovation Advancements for Shell Cansolv CO₂ capture solvents. *Energy Procedia* **63**. 12th International Conference on Greenhouse Gas Control Technologies, GHGT-12, 801–807. ISSN: 1876-6102. doi:<https://doi.org/10.1016/j.egypro.2014.11.090>. <https://www.sciencedirect.com/science/article/pii/S1876610214019055> (2014).
37. Singh, A. & Stéphenne, K. Shell Cansolv CO₂ capture technology: Achievement from First Commercial Plant. *Energy Procedia* **63**. 12th International Conference on Greenhouse Gas Control Technologies, GHGT-12, 1678–1685. ISSN: 1876-6102. doi:<https://doi.org/10.1016/j.egypro.2014.11.177>. <https://www.sciencedirect.com/science/article/pii/S1876610214019924> (2014).
38. Zhu, Z. *et al.* Greening of the Earth and its drivers. *Nature climate change* **6**, 791–795 (2016).
39. Alcalde, J. *et al.* A criteria-driven approach to the CO₂ storage site selection of East Mey for the acorn project in the North Sea. *Marine and Petroleum Geology* **133**, 105309. ISSN: 0264-8172. doi:<https://doi.org/10.1016/j.j>

- marpetgeo . 2021 . 105309. <https://www.sciencedirect.com/science/article/pii/S0264817221004128> (2021).
40. Tucker, O., Holley, M., Metcalfe, R. & Hurst, S. Containment Risk Management for CO₂ Storage in a Depleted Gas Field, UK North Sea. *Energy Procedia* **37**. GHGT-11 Proceedings of the 11th International Conference on Greenhouse Gas Control Technologies, 18-22 November 2012, Kyoto, Japan, 4804–4817. ISSN: 1876-6102. doi:<https://doi.org/10.1016/j.egypro.2013.06.390>. <https://www.sciencedirect.com/science/article/pii/S1876610213006334> (2013).
 41. Al-Shargabi, M., Davoodi, S., Wood, D. A., Rukavishnikov, V. S. & Minaev, K. M. Carbon Dioxide Applications for Enhanced Oil Recovery Assisted by Nanoparticles: Recent Developments. *ACS Omega* **7**, 9984–9994. doi:10.1021/acsomega.1c07123. eprint: <https://doi.org/10.1021/acsomega.1c07123>. <https://doi.org/10.1021/acsomega.1c07123> (2022).
 42. Burrows, L. C. *et al.* A Literature Review of CO₂, Natural Gas, and Water-Based Fluids for Enhanced Oil Recovery in Unconventional Reservoirs. *Energy & Fuels* **34**, 5331–5380. ISSN: 0887-0624. doi:10.1021/acs.energyfuels.9b03658. <https://doi.org/10.1021/acs.energyfuels.9b03658> (2020).
 43. Of Sciences Engineering, N. A. & Medicine. *Gaseous Carbon Waste Streams Utilization: Status and Research Needs* ISBN: 978-0-309-48336-0. doi:10.17226/25232. <https://nap.nationalacademies.org/catalog/25232/gaseous-carbon-waste-streams-utilization-status-and-research-needs> (The National Academies Press, Washington, DC, 2019).
 44. *Global Roadmap for Implementing CO₂ Utilization* in (2016). https://assets.ctfassets.net/xg0gv1arhdr3/27vQZEvrxaQiQEAsGyoSQu/44ee0b72ceb9231ec53ed180cb759614/CO2U_ICEF_Roadmap_FINAL_2016_12_07.pdf.
 45. Doddrell, N. H., Lawson, T., Raines, C. A., Wagstaff, C. & Simkin, A. J. Feeding the world: impacts of elevated CO₂ on nutrient content of greenhouse grown fruit crops and options for future yield gains. *Horticulture*

- Research* **10**, uhad026. ISSN: 2052-7276. doi:10.1093/hr/uhad026. eprint: <https://academic.oup.com/hr/article-pdf/10/4/uhad026/50015163/uhad026.pdf>. <https://doi.org/10.1093/hr/uhad026> (Feb. 2023).
46. Lack, E. & Seidlitz, H. in *Extraction of Natural Products Using Near-Critical Solvents* (eds King, M. B. & Bott, T. R.) 101–139 (Springer Netherlands, Dordrecht, 1993). ISBN: 978-94-011-2138-5. doi:10.1007/978-94-011-2138-5_5. https://doi.org/10.1007/978-94-011-2138-5_5.
 47. BP. *BP Statistical Review of World Energy June 2016* tech. rep. (BP, 2016). <https://oilproduction.net/files/especial-BP/bp-statistical-review-of-world-energy-2016-full-report.pdf>.
 48. Krause, R. *et al.* Industrial application aspects of the electrochemical reduction of CO₂ to CO in aqueous electrolyte. *Chemie Ingenieur Technik* **92**, 53–61 (2020).
 49. Haas, T., Krause, R., Weber, R., Demler, M. & Schmid, G. Technical photosynthesis involving CO₂ electrolysis and fermentation. *Nature Catalysis* **1**, 32–39 (2018).
 50. Matthews, T. *et al.* On the route to commercialization of a CO₂ electrolyzer: Lessons learned from an industry effort to fight climate change in *Abstracts of papers of the American Chemical Society* **249** (2015).
 51. Kaczur, J. J., Yang, H., Liu, Z., Sajjad, S. D. & Masel, R. I. Carbon dioxide and water electrolysis using new alkaline stable anion membranes. *Frontiers in chemistry* **6**, 263 (2018).
 52. Bhanage, B. M. *Transformation and utilization of carbon dioxide* Inorganic, Organic, Physical and Analytical Chemistry. ISBN: 978-3-642-44987-1. http://inis.iaea.org/search/search.aspx?orig_q=RN:45049477 (Springer, Germany, 2014).
 53. Le Quéré, C. *et al.* Global Carbon Budget 2018. *Earth System Science Data* **10**, 2141–2194. doi:10.5194/essd-10-2141-2018. <https://essd.copernicus.org/articles/10/2141/2018/> (2018).

54. *Plastics - the Facts 2021* tech. rep. (Plastics Europe, 2021). eprint: <https://plasticseurope.org/wp-content/uploads/2021/12/Plastics-the-Facts-2021-web-final.pdf>. <https://plasticseurope.org/wp-content/uploads/2021/12/Plastics-the-Facts-2021-web-final.pdf>.
55. Geyer, R., Jambeck, J. R. & Law, K. L. Production, use, and fate of all plastics ever made. *Science Advances* **3**, e1700782. doi:10.1126/sciadv.1700782. eprint: <https://www.science.org/doi/pdf/10.1126/sciadv.1700782>. <https://www.science.org/doi/abs/10.1126/sciadv.1700782> (2017).
56. *2017 UK GREENHOUSE GAS EMISSIONS, PROVISIONAL FIGURES* tech. rep. (Department for Business, Energy & Industrial Strategy, Mar. 2018). https://assets.publishing.service.gov.uk/government/uploads/system/uploads/attachment_data/file/695930/2017_Provisional_Emissions_statistics_2.pdf.
57. Billy, J. T. & Co, A. C. Experimental Parameters Influencing Hydrocarbon Selectivity during the Electrochemical Conversion of CO₂. *ACS Catalysis* **7**, 8467–8479. doi:10.1021/acscatal.7b02373. <https://pubs.acs.org/doi/10.1021/acscatal.7b02373> (2017).
58. Merino-Garcia, I., Alvarez-Guerra, E., Albo, J. & Irabien, A. Electrochemical membrane reactors for the utilisation of carbon dioxide. *Chemical Engineering Journal* **305**. SI: New concepts in membrane reactors: from membrane design to tissue engineering, 104–120. ISSN: 1385-8947. doi:<https://doi.org/10.1016/j.cej.2016.05.032>. <https://www.sciencedirect.com/science/article/pii/S1385894716306556> (2016).
59. Genovese, C., Ampelli, C., Perathoner, S. & Centi, G. Electrocatalytic conversion of CO₂ to liquid fuels using nanocarbon-based electrodes. *Journal of Energy Chemistry* **22**, 202–213. ISSN: 2095-4956. doi:[https://doi.org/10.1016/S2095-4956\(13\)60026-1](https://doi.org/10.1016/S2095-4956(13)60026-1). <https://www.sciencedirect.com/science/article/pii/S2095495613600261> (2013).

60. Nitopi, S. *et al.* Progress and Perspectives of Electrochemical CO₂ Reduction on Copper in Aqueous Electrolyte. *Chemical Reviews* **119**. PMID: 31117420, 7610–7672. doi:10.1021/acs.chemrev.8b00705. eprint: <https://doi.org/10.1021/acs.chemrev.8b00705>. <https://doi.org/10.1021/acs.chemrev.8b00705> (2019).
61. Kuhl, K. P. *et al.* Electrocatalytic Conversion of Carbon Dioxide to Methane and Methanol on Transition Metal Surfaces. *Journal of the American Chemical Society* **136**. PMID: 25259478, 14107–14113. doi:10.1021/ja505791r. eprint: <https://doi.org/10.1021/ja505791r>. <https://doi.org/10.1021/ja505791r> (2014).
62. Dutta, A., Morstein, C. E., Rahaman, M., Cedeño López, A. & Broekmann, P. Beyond Copper in CO₂ Electrolysis: Effective Hydrocarbon Production on Silver-Nanofoam Catalysts. *ACS Catalysis* **8**, 8357–8368. doi:10.1021/acscatal.8b01738. <https://doi.org/10.1021/acscatal.8b01738> (2018).
63. Hori, Y. *Modern Aspects of Electrochemistry*. 42 New York 2008.
64. Bagger, A., Ju, W., Varela, A. S., Strasser, P. & Rossmeisl, J. Electrochemical CO₂ Reduction: A Classification Problem. *ChemPhysChem* **18**, 3266–3273. doi:<https://doi.org/10.1002/cphc.201700736>. eprint: <https://chemistry-europe.onlinelibrary.wiley.com/doi/pdf/10.1002/cphc.201700736>. <https://chemistry-europe.onlinelibrary.wiley.com/doi/abs/10.1002/cphc.201700736> (2017).
65. DeWulf, D. W. Electrochemical and Surface Studies of Carbon Dioxide Reduction to Methane and Ethylene at Copper Electrodes in Aqueous Solutions. *Journal of The Electrochemical Society* **136**, 1686. doi:10.1149/1.2096993 (1989).
66. Montoya, J. H., Peterson, A. A. & Nørskov, J. K. Insights into C-C Coupling in CO₂ Electroreduction on Copper Electrodes. *ChemCatChem* **5**, 737–742. doi:<https://doi.org/10.1002/cctc.201200564>. eprint: <https://chemistry-europe.onlinelibrary.wiley.com/doi/pdf/10.1002/cctc.201200564>

- cctc . 201200564. <https://chemistry-europe.onlinelibrary.wiley.com/doi/abs/10.1002/cctc.201200564> (2013).
67. Hori, Y., Murata, A. & Takahashi, R. Formation of hydrocarbons in the electrochemical reduction of carbon dioxide at a copper electrode in aqueous solution. *J. Chem. Soc., Faraday Trans. 1* **85**, 2309–2326. doi:10.1039/F19898502309. <http://dx.doi.org/10.1039/F19898502309> (8 1989).
68. Lum, Y., Yue, B., Lobaccaro, P., Bell, A. T. & Ager, J. W. Optimizing C–C Coupling on Oxide-Derived Copper Catalysts for Electrochemical CO₂ Reduction. *The Journal of Physical Chemistry C* **121**, 14191–14203. doi:10.1021/acs.jpcc.7b03673. eprint: <https://doi.org/10.1021/acs.jpcc.7b03673>. <https://doi.org/10.1021/acs.jpcc.7b03673> (2017).
69. Lv, W. *et al.* Electrodeposition of nano-sized bismuth on copper foil as electrocatalyst for reduction of CO₂ to formate. *Applied Surface Science* **393**, 191–196. ISSN: 0169-4332. doi:<https://doi.org/10.1016/j.apsusc.2016.10.017>. <https://www.sciencedirect.com/science/article/pii/S0169433216321122> (2017).
70. Lv, W., Zhou, J., Kong, F., Fang, H. & Wang, W. Porous tin-based film deposited on copper foil for electrochemical reduction of carbon dioxide to formate. *International Journal of Hydrogen Energy* **41**, 1585–1591. ISSN: 0360-3199. doi:<https://doi.org/10.1016/j.ijhydene.2015.11.100>. <https://www.sciencedirect.com/science/article/pii/S0360319915308004> (2016).
71. Cheng, T., Xiao, H. & Goddard, W. A. Nature of the Active Sites for CO Reduction on Copper Nanoparticles; Suggestions for Optimizing Performance. *Journal of the American Chemical Society* **139**. PMID: 28810738, 11642–11645. doi:10.1021/jacs.7b03300. eprint: <https://doi.org/10.1021/jacs.7b03300>. <https://doi.org/10.1021/jacs.7b03300> (2017).

72. Kas, R., Kortlever, R., Yilmaz, H., Koper, M. T. M. & Mul, G. Manipulating the Hydrocarbon Selectivity of Copper Nanoparticles in CO₂ Electrorreduction by Process Conditions. *ChemElectroChem* **2**, 354–358. doi:<https://doi.org/10.1002/celc.201402373>. <https://chemistry-europe.onlinelibrary.wiley.com/doi/abs/10.1002/celc.201402373> (2015).
73. Dongare, S., Singh, N. & Bhunia, H. Electrocatalytic reduction of CO₂ to useful chemicals on copper nanoparticles. *Applied Surface Science* **537**, 148020. ISSN: 0169-4332. doi:<https://doi.org/10.1016/j.apsusc.2020.148020>. <https://www.sciencedirect.com/science/article/pii/S016943322032777X> (2021).
74. Loiudice, A. *et al.* Tailoring Copper Nanocrystals towards C₂ Products in Electrochemical CO₂ Reduction. *Angewandte Chemie International Edition* **55**, 5789–5792. doi:<https://doi.org/10.1002/anie.201601582>. eprint: <https://onlinelibrary.wiley.com/doi/pdf/10.1002/anie.201601582>. <https://onlinelibrary.wiley.com/doi/abs/10.1002/anie.201601582> (2016).
75. Gorginpour, F. & Zali-Boeini, H. Synergistic effect of copper nanocrystals-nanoparticles incorporated in a porous organic polymer for the Ullmann C–O coupling reaction. *Molecular Catalysis* **504**, 111460. ISSN: 2468-8231. doi:<https://doi.org/10.1016/j.mcat.2021.111460>. <https://www.sciencedirect.com/science/article/pii/S2468823121000778> (2021).
76. Zhang, Z., Zhang, J., Jia, A.-P., Lu, J.-Q. & Huang, W. Morphology-Dependent CO Reduction Kinetics and Surface Copper Species Evolution of Cu₂O Nanocrystals. *The Journal of Physical Chemistry C* **124**, 21568–21576. doi:10.1021/acs.jpcc.0c06425. eprint: <https://doi.org/10.1021/acs.jpcc.0c06425>. <https://doi.org/10.1021/acs.jpcc.0c06425> (2020).
77. Huang, J. *et al.* Copper-comprising nanocrystals as well-defined electrocatalysts to advance electrochemical CO₂ reduction. *Journal of Energy Chemistry* **62**, 71–102. ISSN: 2095-4956. doi:<https://doi.org/10.1016/j.jechem>.

- 2021.03.009. <https://www.sciencedirect.com/science/article/pii/S2095495621001297> (2021).
78. Conte, A., Baron, M., Bonacchi, S., Antonello, S. & Aliprandi, A. Copper and silver nanowires for CO₂ electroreduction. *Nanoscale* **15**, 3693–3703. doi:10.1039/D2NR06687D. <http://dx.doi.org/10.1039/D2NR06687D> (8 2023).
79. Lyu, Z. *et al.* Controlling the Surface Oxidation of Cu Nanowires Improves Their Catalytic Selectivity and Stability toward C₂+ Products in CO₂ Reduction. *Angewandte Chemie International Edition* **60**, 1909–1915. doi:<https://doi.org/10.1002/anie.202011956>. eprint: <https://onlinelibrary.wiley.com/doi/pdf/10.1002/anie.202011956>. <https://onlinelibrary.wiley.com/doi/abs/10.1002/anie.202011956> (2021).
80. Li, Y. *et al.* Structure-Sensitive CO₂ Electroreduction to Hydrocarbons on Ultrathin 5-fold Twinned Copper Nanowires. *Nano Letters* **17**. PMID: 28094953, 1312–1317. doi:10.1021/acs.nanolett.6b05287. eprint: <https://doi.org/10.1021/acs.nanolett.6b05287>. <https://doi.org/10.1021/acs.nanolett.6b05287> (2017).
81. Kung, C.-W. *et al.* Copper Nanoparticles Installed in Metal–Organic Framework Thin Films are Electrocatalytically Competent for CO₂ Reduction. *ACS Energy Letters* **2**, 2394–2401. doi:10.1021/acsenergylett.7b00621. eprint: <https://doi.org/10.1021/acsenergylett.7b00621>. <https://doi.org/10.1021/acsenergylett.7b00621> (2017).
82. Kim, C., Möller, T., Schmidt, J., Thomas, A. & Strasser, P. Suppression of Competing Reaction Channels by Pb Adatom Decoration of Catalytically Active Cu Surfaces During CO₂ Electroreduction. *ACS Catalysis* **9**, 1482–1488. doi:10.1021/acscatal.8b02846. eprint: <https://doi.org/10.1021/acscatal.8b02846>. <https://doi.org/10.1021/acscatal.8b02846> (2019).
83. Rayer, A. V. *et al.* Electrochemical carbon dioxide reduction to isopropanol using novel carbonized copper metal organic framework derived electrodes.

- Journal of CO₂ Utilization* **39**, 101159. ISSN: 2212-9820. doi:<https://doi.org/10.1016/j.jcou.2020.101159>. <https://www.sciencedirect.com/science/article/pii/S2212982019311898> (2020).
84. Wuttig, A. & Surendranath, Y. Impurity Ion Complexation Enhances Carbon Dioxide Reduction Catalysis. *ACS Catalysis* **5**, 4479–4484. doi:[10.1021/acscatal.5b00808](https://doi.org/10.1021/acscatal.5b00808). eprint: <https://doi.org/10.1021/acscatal.5b00808>. <https://doi.org/10.1021/acscatal.5b00808> (2015).
85. Hori, Y. *et al.* “Deactivation of copper electrode” in electrochemical reduction of CO₂. *Electrochimica Acta* **50**, 5354–5369. ISSN: 0013-4686. doi:<https://doi.org/10.1016/j.electacta.2005.03.015>. <https://www.sciencedirect.com/science/article/pii/S0013468605002410> (2005).
86. Dutta, A. *et al.* CO₂ electrolysis – Complementary operando XRD, XAS and Raman spectroscopy study on the stability of Cu_xO foam catalysts. *Journal of Catalysis* **389**, 592–603. ISSN: 0021-9517. doi:<https://doi.org/10.1016/j.jcat.2020.06.024>. <https://www.sciencedirect.com/science/article/pii/S0021951720302578> (2020).
87. Kuhl, K. P., Cave, E. R., Abram, D. N. & Jaramillo, T. F. New insights into the electrochemical reduction of carbon dioxide on metallic copper surfaces. *Energy Environ. Sci.* **5**, 7050–7059. doi:[10.1039/C2EE21234J](https://doi.org/10.1039/C2EE21234J). <http://dx.doi.org/10.1039/C2EE21234J> (5 2012).
88. Nikolić, N., Branković, G., Pavlović, M. & Popov, K. The effect of hydrogen co-deposition on the morphology of copper electrodeposits. II. Correlation between the properties of electrolytic solutions and the quantity of evolved hydrogen. *Journal of Electroanalytical Chemistry* **621**, 13–21. ISSN: 1572-6657. doi:<https://doi.org/10.1016/j.jelechem.2008.04.006>. <https://www.sciencedirect.com/science/article/pii/S0022072808001629> (2008).
89. Krutzsch, W. C. & Cooper, P. en. in (eds Karassik, I. J., Messina, J. P., Cooper, P. & Heald, C. C.) 4th Edition (McGraw-Hill Education, New York, 2008).

- ISBN: 9780071460446. <https://www.accessengineeringlibrary.com/content/book/9780071460446/toc-chapter/chapter1/section/section3>.
90. Zhang, D & Zeng, K. Evaluating the Behavior of Electrolytic Gas Bubbles and Their Effect on the Cell Voltage in Alkaline Water Electrolysis. *Industrial and Engineering Chemistry Research* **51**, 13825–13832. <https://pubs.acs.org/doi/10.1021/ie301029e> (2012).
91. Bongenaar-Schlenter, B. E., Janssen, L. J. J., Van Stralen, S. J. D. & Barendrecht, E. The effect of the gas void distribution on the Ohmic resistance during water electrolytes. *Journal of Applied Electrochemistry* **15**, 537–548 (1985).
92. Pletcher, D., Green, R. A. & Brown, R. C. D. Flow Electrolysis Cells for the Synthetic Organic Chemistry Laboratory. *Chemical Reviews* **118**. PMID: 28921969, 4573–4591. doi:10.1021/acs.chemrev.7b00360. eprint: <https://doi.org/10.1021/acs.chemrev.7b00360>. <https://doi.org/10.1021/acs.chemrev.7b00360> (2018).
93. Rudd, J. A. *et al.* Investigation into the Re-Arrangement of Copper Foams Pre- and Post-CO₂ Electrocatalysis. *Chemistry* **3**, 687–703. ISSN: 2624-8549. doi:10.3390/chemistry3030048. <https://www.mdpi.com/2624-8549/3/3/48> (2021).
94. Perry, S. C., de León, C. P. & Walsh, F. C. Review—The Design, Performance and Continuing Development of Electrochemical Reactors for Clean Electrosynthesis. *Journal of The Electrochemical Society* **167**, 155525. doi:10.1149/1945-7111/abc58e. <https://doi.org/10.1149/1945-7111/abc58e> (2020).
95. Ahn, S. *et al.* Poly-Amide Modified Copper Foam Electrodes for Enhanced Electrochemical Reduction of Carbon Dioxide. *ACS Catalysis* **8**, 4132–4142. doi:10.1021/acscatal.7b04347 (2018).
96. Esrafilzadeh, D. *et al.* Room temperature CO₂ reduction to solid carbon species on liquid metals featuring atomically thin ceria interfaces. *Nature Communications* **10**, 865. ISSN: 2041-1723. doi:10.1038/s41467-019-08824-8. <https://doi.org/10.1038/s41467-019-08824-8> (2019).

97. Instrumentation, P. R. *Low Volume Separated Cell* <https://pinerresearch.com/shop/products/cells-and-glassware/low-volume-cells/low-volume-separated-cell/> (2023).
98. Phillips, R., Edwards, A., Rome, B., Jones, D. R. & Dunnill, C. W. Minimising the ohmic resistance of an alkaline electrolysis cell through effective cell design. *International Journal of Hydrogen Energy* **42**, 23986–23994. ISSN: 0360-3199. doi:<https://doi.org/10.1016/j.ijhydene.2017.07.184>. <https://www.sciencedirect.com/science/article/pii/S0360319917330203> (2017).
99. Rearden, A., Mandale, S., Glover, K., Phillips, R. & Dunnill, C. W. Optimizing the Design of an Alkaline Water Splitting Device Test cell for Renewable Energy Storage as Hydrogen. *Archives of Chemistry and Chemical Engineering* **2**, 1–9. doi:10.5281/zenodo.3964220. <https://doi.org/10.5281/zenodo.3964220> (July 2020).
100. Passas G. Dunnill, C. Water Splitting Test Cell for Renewable Energy Storage as Hydrogen Gas. *Journal of Fundamentals of Renewable Energy and Applications* **5**, 188. doi:10.4172/20904541.1000188 (Sept. 2015).
101. Jeanty, P. *et al.* Upscaling and continuous operation of electrochemical CO₂ to CO conversion in aqueous solutions on silver gas diffusion electrodes. *Journal of CO₂ Utilization* **24**, 454–462. ISSN: 2212-9820. doi:<https://doi.org/10.1016/j.jcou.2018.01.011>. <http://www.sciencedirect.com/science/article/pii/S2212982017307084> (2018).
102. Wu, J. *et al.* Electrochemical Reduction of Carbon Dioxide II. Design, Assembly, and Performance of Low Temperature Full Electrochemical Cells. *Journal of The Electrochemical Society* **160**. <https://iopscience.iop.org/article/10.1149/2.030309jes> (2013).
103. Marshall, R. & Walsh, F. A review of some recent electrolytic cell designs. *Surface Technology* **24**, 45–77. ISSN: 0376-4583. doi:[https://doi.org/10.1016/0376-4583\(83\)90001-1](https://doi.org/10.1016/0376-4583(83)90001-1) (1983).

- 1016/0376-4583(85)90015-9. <https://www.sciencedirect.com/science/article/pii/0376458385900159> (1985).
104. Dell, R. M. Industrial electrochemistry (second edition) by Derek Pletcher and Frank C. Walsh, Chapman and Hall, London, 1990, pp. xvi + 653, price £65.00. ISBN 0 412 30410 4. *Journal of Chemical Technology & Biotechnology* **52**, 427–428. doi:<https://doi.org/10.1002/jctb.280520317>. eprint: <https://onlinelibrary.wiley.com/doi/pdf/10.1002/jctb.280520317>. <https://onlinelibrary.wiley.com/doi/abs/10.1002/jctb.280520317> (1991).
105. Rivera, F. F., de León, C. P., Nava, J. L. & Walsh, F. C. The filter-press FM01-LC laboratory flow reactor and its applications. *Electrochimica Acta* **163**, 338–354. ISSN: 0013-4686. doi:<https://doi.org/10.1016/j.electacta.2015.02.179>. <https://www.sciencedirect.com/science/article/pii/S0013468615005009> (2015).
106. Rivera, F. F., de León, C. P., Walsh, F. C. & Nava, J. L. The reaction environment in a filter-press laboratory reactor: the FM01-LC flow cell. *Electrochimica Acta* **161**, 436–452. ISSN: 0013-4686. doi:<https://doi.org/10.1016/j.electacta.2015.02.161>. <https://www.sciencedirect.com/science/article/pii/S0013468615004697> (2015).
107. Griffiths, M., de León, C. P. & Walsh, F. C. Mass transport in the rectangular channel of a filter-press electrolyzer (the FM01-LC reactor). *AIChE Journal* **51**, 682–687. doi:<https://doi.org/10.1002/aic.10311>. eprint: <https://aiche.onlinelibrary.wiley.com/doi/pdf/10.1002/aic.10311>. <https://aiche.onlinelibrary.wiley.com/doi/abs/10.1002/aic.10311> (2005).
108. Enciso-Pérez, R., Velasco-Martínez, G., Gómez, J. A. D. & Rodríguez-Torres, I. Computational Fluid Dynamics of an Electrolytic Cell FM01-LC. *ECS Transactions* **20**, 103. doi:10.1149/1.3268377. <https://dx.doi.org/10.1149/1.3268377> (2009).

109. Vázquez, L., Alvarez-Gallegos, A., Sierra, F., Ponce de León, C. & Walsh, F. Simulation of velocity profiles in a laboratory electrolyser using computational fluid dynamics. *Electrochimica Acta* **55**, 3437–3445. ISSN: 0013-4686. doi:<https://doi.org/10.1016/j.electacta.2009.08.066>. <https://www.sciencedirect.com/science/article/pii/S0013468609010986> (2010).
110. Walsh, F. C. & Ponce de León, C. Progress in electrochemical flow reactors for laboratory and pilot scale processing. *Electrochimica Acta* **280**, 121–148. ISSN: 0013-4686. doi:<https://doi.org/10.1016/j.electacta.2018.05.027>. <https://www.sciencedirect.com/science/article/pii/S0013468618310430> (2018).
111. Brown, C., Pletcher, D., Walsh, F., Hammond, J. & Robinson, D. Local mass transport effects in the FM01 laboratory electrolyser. *Journal of Applied Electrochemistry* **22**. Cited by: 98, 613 – 619. doi:10.1007/BF01092609. <https://www.scopus.com/inward/record.uri?eid=2-s2.0-0026900059&doi=10.1007%2fBF01092609&partnerID=40&md5=7d89657fbd3d262c39f1de2213cf2449> (1992).
112. Vázquez, L., Alvarez-Gallegos, A., Sierra, F., Ponce de León, C. & Walsh, F. CFD evaluation of internal manifold effects on mass transport distribution in a laboratory filter-press flow cell. *Journal of Applied Electrochemistry* **43**. doi:10.1007/s10800-013-0530-9 (Apr. 2013).
113. Vázquez, L., Alvarez-Gallegos, A., Sierra, F., de León, C. P. & Walsh, F. Prediction of mass transport profiles in a laboratory filter-press electrolyser by computational fluid dynamics modelling. *Electrochimica Acta* **55**, 3446–3453. ISSN: 0013-4686. doi:<https://doi.org/10.1016/j.electacta.2009.08.067>. <https://www.sciencedirect.com/science/article/pii/S0013468609010998> (2010).

114. Castañeda, L., Antaño, R., Rivera, F. F. & Nava, J. L. Computational fluid dynamic simulations of single-phase flow in a spacer-filled channel of a filter-press electrolyzer. *Int. J. Electrochem. Sci* **12**, 7351–7364 (2017).
115. Bengoa, C, Montillet, A, Legentilhomme, P & Legrand, J. Characterization and Modeling of the Hydrodynamic Behavior in the Filter-Press-Type FM01-LC Electrochemical Cell by Direct Flow Visualization and Residence Time Distribution. *Industrial & engineering chemistry research*. **39**, 2199–2206. ISSN: 0888-5885 (2000-07-01).
116. Wu, L., Arenas, L. F., Graves, J. E. & Walsh, F. C. Flow Cell Characterisation: Flow Visualisation, Pressure Drop and Mass Transport at 2D Electrodes in a Rectangular Channel. *Journal of The Electrochemical Society* **167**, 043505. doi:10.1149/1945-7111/ab7b49. <https://dx.doi.org/10.1149/1945-7111/ab7b49> (2020).
117. Downs, C. *Using the C-Flow LAB cell for laboratory electrochemistry* tech. rep. (C-Tech Innovation). eprint: <https://www.ctechinnovation.com/wp-content/uploads/2019-C-Flow-LAB-Case-Study.pdf>. <https://www.ctechinnovation.com/product/c-flow-5x5/>.
118. Ltd, C.-T. I. *C-Flow LAB 5x5 Instruction Manual* tech. rep. (12C-Tech Innovation Ltd Capenhurst Technology Park Capenhurst Chester UK CH1 6EH, May 2019). eprint: <https://www.ctechinnovation.com/wp-content/uploads/C-Flow-LAB-5x5-Manual-2021.pdf>. <https://www.ctechinnovation.com/product/c-flow-5x5/>.
119. Ltd, C.-T. I. *C-Flow LAB 5x5 Datasheet* tech. rep. (12C-Tech Innovation Ltd Capenhurst Technology Park Capenhurst Chester UK CH1 6EH). eprint: <https://www.ctechinnovation.com/wp-content/uploads/Laboratory-Electrochemical-Cell-C-Flow-LAB-5x5-Datasheet-2021.pdf>. <https://www.ctechinnovation.com/product/c-flow-5x5/>.

120. Gupta, N., Gattrell, M. & MacDougall, B. Calculation for the cathode surface concentrations in the electrochemical reduction of CO₂ in KHCO₃ solutions. *Journal of Applied Electrochemistry* **36**, 161–172. ISSN: 1572-8838. doi:10.1007/s10800-005-9058-y. <https://doi.org/10.1007/s10800-005-9058-y> (2006).
121. Li, H. & Oloman, C. The Electro-Reduction of Carbon Dioxide in a Continuous Reactor. *Journal of Applied Electrochemistry* **35**, 955–965. ISSN: 1572-8838. doi:10.1007/s10800-005-7173-4. <https://doi.org/10.1007/s10800-005-7173-4> (2005).
122. Baumgartner, L. M., Koopman, C. I., Forner-Cuenca, A. & Vermaas, D. A. Narrow Pressure Stability Window of Gas Diffusion Electrodes Limits the Scale-Up of CO₂ Electrolyzers. *ACS Sustainable Chemistry & Engineering* **10**, 4683–4693. doi:10.1021/acssuschemeng.2c00195. <https://doi.org/10.1021/acssuschemeng.2c00195> (2022).
123. Moyle, M. P., Morrison, R. B. & Churchill, S. W. Detonation characteristics of hydrogen-oxygen mixtures. *AIChE Journal* **6**, 92–96. doi:<https://doi.org/10.1002/aic.690060118>. <https://aiche.onlinelibrary.wiley.com/doi/abs/10.1002/aic.690060118> (1960).
124. Woldu, A. R. *et al.* Electrochemical reduction of CO₂: Two- or three-electrode configuration. *International Journal of Energy Research* **44**, 548–559. doi:<https://doi.org/10.1002/er.4904>. eprint: <https://onlinelibrary.wiley.com/doi/pdf/10.1002/er.4904>. <https://onlinelibrary.wiley.com/doi/abs/10.1002/er.4904> (2020).
125. Arenas, L. F., de León, C. P. & Walsh, F. C. Critical Review—The Versatile Plane Parallel Electrode Geometry: An Illustrated Review. *Journal of The Electrochemical Society* **167**, 023504. doi:10.1149/1945-7111/ab64ba. <https://dx.doi.org/10.1149/1945-7111/ab64ba> (2020).
126. Endrődi, B. *et al.* Multilayer Electrolyzer Stack Converts Carbon Dioxide to Gas Products at High Pressure with High Efficiency. *ACS Energy Letters* **4**.

- PMID: 31328172, 1770–1777. doi:10.1021/acsenergylett.9b01142. eprint: <https://doi.org/10.1021/acsenergylett.9b01142>. <https://doi.org/10.1021/acsenergylett.9b01142> (2019).
127. Perry, S. C., ki Leung, P., Wang, L. & Ponce de León, C. Developments on carbon dioxide reduction: Their promise, achievements, and challenges. *Current Opinion in Electrochemistry* **20**, Innovative Methods in Electrochemistry Electrochemical Engineering, 88–98. ISSN: 2451-9103. doi:<https://doi.org/10.1016/j.coelec.2020.04.014>. <https://www.sciencedirect.com/science/article/pii/S2451910320300958> (2020).
128. Hara, K. Electrochemical Reduction of CO₂ on a Cu Electrode under High Pressure. *Journal of The Electrochemical Society* **141**, 2097. doi:10.1149/1.2055067. <https://doi.org/10.1149/1.2055067> (1994).
129. Nagai, N., Takeuchi, M., Kimura, T. & Oka, T. Existence of optimum space between electrodes on hydrogen production by water electrolysis. *International Journal of Hydrogen Energy* **28**, 35–41. ISSN: 0360-3199. doi:[https://doi.org/10.1016/S0360-3199\(02\)00027-7](https://doi.org/10.1016/S0360-3199(02)00027-7). <https://www.sciencedirect.com/science/article/pii/S0360319902000277> (2003).
130. Hori, Y., Murata, A., Takahashi, R. & Suzuki, S. Enhanced formation of ethylene and alcohols at ambient temperature and pressure in electrochemical reduction of carbon dioxide at a copper electrode. *J. Chem. Soc., Chem. Commun.*, 17–19. doi:10.1039/C39880000017. <http://dx.doi.org/10.1039/C39880000017> (1988).
131. Hori, Y., Takahashi, R., Yoshinami, Y. & Murata, A. Electrochemical Reduction of CO at a Copper Electrode. *The Journal of Physical Chemistry B* **101**, 7075–7081. doi:10.1021/jp970284i. eprint: <https://doi.org/10.1021/jp970284i>. <https://doi.org/10.1021/jp970284i> (1997).
132. Miller, R. L., Bradford, W. L. & Peters, N. E. *Specific conductance: theoretical considerations and application to analytical quality control* (US Government Printing Office Washington, DC, USA, 1988).

133. Varela, A. S., Kroschel, M., Reier, T. & Strasser, P. Controlling the selectivity of CO₂ electroreduction on copper: The effect of the electrolyte concentration and the importance of the local pH. *Catalysis Today* **260**, Surface Analysis and Dynamics (SAND), 8–13. ISSN: 0920-5861. doi:<https://doi.org/10.1016/j.cattod.2015.06.009>. <https://www.sciencedirect.com/science/article/pii/S0920586115003594> (2016).
134. Shin, H.-C., Dong, J. & Liu, M. Nanoporous Structures Prepared by an Electrochemical Deposition Process. *Advanced Materials* **15**, 1610–1614. doi:<https://doi.org/10.1002/adma.200305160>. <https://onlinelibrary.wiley.com/doi/abs/10.1002/adma.200305160> (2003).
135. Hayashi, M. Temperature-Electrical Conductivity Relation of Water for Environmental Monitoring and Geophysical Data Inversion. *Environmental Monitoring and Assessment* **96**, 119–128. ISSN: 1573-2959. doi:[10.1023/B:EMAS.0000031719.83065.68](https://doi.org/10.1023/B:EMAS.0000031719.83065.68). <https://doi.org/10.1023/B:EMAS.0000031719.83065.68> (2004).
136. De Jesús-Cardona, H., del Moral, C. & Cabrera, C. R. Voltammetric study of CO₂ reduction at Cu electrodes under different KHCO₃ concentrations, temperatures and CO₂ pressures. *Journal of Electroanalytical Chemistry* **513**, 45–51. ISSN: 1572-6657. doi:[https://doi.org/10.1016/S0022-0728\(01\)00598-8](https://doi.org/10.1016/S0022-0728(01)00598-8). <https://www.sciencedirect.com/science/article/pii/S0022072801005988> (2001).
137. Butler, K. T., Davies, D. W., Cartwright, H., Isayev, O. & Walsh, A. Machine learning for molecular and materials science. *Nature* **559**, 547–555. ISSN: 1476-4687. doi:[10.1038/s41586-018-0337-2](https://doi.org/10.1038/s41586-018-0337-2). <https://doi.org/10.1038/s41586-018-0337-2> (2018).
138. Tsompanas, M.-A., You, J., Wallis, L., Greenman, J. & Ieropoulos, I. Artificial neural network simulating microbial fuel cells with different membrane materials and electrode configurations. *Journal of Power Sources* **436**, 226832. ISSN: 0378-7753. doi:<https://doi.org/10.1016/j.jpowsour.2018.07.009> (2018).

- 2019.226832. <https://www.sciencedirect.com/science/article/pii/S0378775319308250> (2019).
139. Zhong, M. *et al.* Accelerated discovery of CO₂ electrocatalysts using active machine learning. *Nature* **581**, 178–183. ISSN: 1476-4687. doi:10.1038/s41586-020-2242-8. <https://doi.org/10.1038/s41586-020-2242-8> (2020).
140. Zhang, N. *et al.* Machine Learning in Screening High Performance Electrocatalysts for CO₂ Reduction. *Small Methods* **5**, 2100987. doi:<https://doi.org/10.1002/smt.202100987>. eprint: <https://onlinelibrary.wiley.com/doi/pdf/10.1002/smt.202100987>. <https://onlinelibrary.wiley.com/doi/abs/10.1002/smt.202100987> (2021).
141. Wu, D., Zhang, J., Cheng, M.-J., Lu, Q. & Zhang, H. Machine Learning Investigation of Supplementary Adsorbate Influence on Copper for Enhanced Electrochemical CO₂ Reduction Performance. *The Journal of Physical Chemistry C* **125**, 15363–15372. doi:10.1021/acs.jpcc.1c05004. eprint: <https://doi.org/10.1021/acs.jpcc.1c05004>. <https://doi.org/10.1021/acs.jpcc.1c05004> (2021).
142. Toyao, T. *et al.* Machine Learning for Catalysis Informatics: Recent Applications and Prospects. *ACS Catalysis* **10**, 2260–2297. doi:10.1021/acscatal.9b04186. eprint: <https://doi.org/10.1021/acscatal.9b04186>. <https://doi.org/10.1021/acscatal.9b04186> (2020).
143. Jordan, M. I. & Mitchell, T. M. Machine learning: Trends, perspectives, and prospects. *Science* **349**, 255–260. doi:10.1126/science.aaa8415. eprint: <https://www.science.org/doi/pdf/10.1126/science.aaa8415>. <https://www.science.org/doi/abs/10.1126/science.aaa8415> (2015).
144. Mitchell, J. B. O. Machine learning methods in chemoinformatics. *WIREs Computational Molecular Science* **4**, 468–481. doi:<https://doi.org/10.1002/wcms.1183>. eprint: <https://wires.onlinelibrary.wiley.com/doi/pdf/>

- 10.1002/wcms.1183. <https://wires.onlinelibrary.wiley.com/doi/abs/10.1002/wcms.1183> (2014).
145. Tran, K. & Ulissi, Z. W. Active learning across intermetallics to guide discovery of electrocatalysts for CO₂ reduction and H₂ evolution. *Nature Catalysis* **1**, 696–703. ISSN: 2520-1158. doi:10.1038/s41929-018-0142-1. <https://doi.org/10.1038/s41929-018-0142-1> (2018).
146. Hinton, G. & Sejnowski, T. J. *Unsupervised Learning: Foundations of Neural Computation* ISBN: 9780262288033. doi:10.7551/mitpress/7011.001.0001. <https://doi.org/10.7551/mitpress/7011.001.0001> (The MIT Press, May 1999).
147. Cheng, P.-C., Peng, B.-R., Liu, Y.-H., Cheng, Y.-S. & Huang, J.-W. Optimization of a Fuzzy-Logic-Control-Based MPPT Algorithm Using the Particle Swarm Optimization Technique. *Energies* **8**, 5338–5360. ISSN: 1996-1073. doi:10.3390/en8065338. <https://www.mdpi.com/1996-1073/8/6/5338> (2015).
148. Lin, J., Wang, K., Yan, B. & Tarng, Y. Optimization of the electrical discharge machining process based on the Taguchi method with fuzzy logics. *Journal of Materials Processing Technology* **102**, 48–55. ISSN: 0924-0136. doi:[https://doi.org/10.1016/S0924-0136\(00\)00438-6](https://doi.org/10.1016/S0924-0136(00)00438-6). <https://www.sciencedirect.com/science/article/pii/S0924013600004386> (2000).
149. Nassef, A. M. *et al.* Fuzzy-modeling with Particle Swarm Optimization for enhancing the production of biodiesel from Microalga. *Energy Sources, Part A: Recovery, Utilization, and Environmental Effects* **41**, 2094–2103. doi:10.1080/15567036.2018.1549171. eprint: <https://doi.org/10.1080/15567036.2018.1549171>. <https://doi.org/10.1080/15567036.2018.1549171> (2019).
150. Jang, J.-S. ANFIS: adaptive-network-based fuzzy inference system. *IEEE Transactions on Systems, Man, and Cybernetics* **23**, 665–685. doi:10.1109/21.256541 (1993).

151. Shin, H.-C. & Liu, M. Copper Foam Structures with Highly Porous Nanostructured Walls. *Chemistry of Materials* **16**, 5460–5464. doi:10.1021/cm048887b. <https://doi.org/10.1021/cm048887b> (2004).
152. Kim, J.-H., Kim, R.-H. & Kwon, H.-S. Preparation of copper foam with 3-dimensionally interconnected spherical pore network by electrodeposition. *Electrochemistry Communications* **10**, 1148–1151. ISSN: 1388-2481. doi:<https://doi.org/10.1016/j.elecom.2008.05.035>. <https://www.sciencedirect.com/science/article/pii/S1388248108002269> (2008).
153. Dutta, A., Rahaman, M., Mohos, M., Zanetti, A. & Broekmann, P. Electrochemical CO₂ Conversion Using Skeleton (Sponge) Type of Cu Catalysts. *ACS Catalysis* **7**, 5431–5437. doi:10.1021/acscatal.7b01548. <https://doi.org/10.1021/acscatal.7b01548> (2017).
154. Dutta, A., Rahaman, M., Luedi, N. C., Mohos, M. & Broekmann, P. Morphology Matters: Tuning the Product Distribution of CO₂ Electroreduction on Oxide-Derived Cu Foam Catalysts. *ACS Catalysis* **6**, 3804–3814. doi:10.1021/acscatal.6b00770. <https://doi.org/10.1021/acscatal.6b00770> (2016).
155. Xie, M. S. *et al.* Amino acid modified copper electrodes for the enhanced selective electroreduction of carbon dioxide towards hydrocarbons. *Energy Environ. Sci.* **9**, 1687–1695. doi:10.1039/C5EE03694A. <http://dx.doi.org/10.1039/C5EE03694A> (5 2016).
156. Han, Z., Kortlever, R., Chen, H.-Y., Peters, J. C. & Agapie, T. CO₂ Reduction Selective for C₂ Products on Polycrystalline Copper with N-Substituted Pyridinium Additives. *ACS Central Science* **3**. PMID: 28852699, 853–859. doi:10.1021/acscentsci.7b00180. <https://doi.org/10.1021/acscentsci.7b00180> (2017).
157. Song, D. *et al.* Electrochemical CO₂ reduction catalyzed by organic/inorganic hybrids. *eScience* **3**, 100097. ISSN: 2667-1417. doi:<https://doi.org/>

- 10.1016/j.esci.2023.100097. <https://www.sciencedirect.com/science/article/pii/S2667141723000071> (2023).
158. Chen, X. *et al.* Electrochemical CO₂-to-ethylene conversion on polyamine-incorporated Cu electrodes. *Nature Catalysis* **4**, 20–27. ISSN: 2520-1158. doi:10.1038/s41929-020-00547-0. <https://doi.org/10.1038/s41929-020-00547-0> (2021).
159. Buckley, A. K. *et al.* Electrocatalysis at Organic–Metal Interfaces: Identification of Structure–Reactivity Relationships for CO₂ Reduction at Modified Cu Surfaces. *Journal of the American Chemical Society* **141**, 7355–7364. doi:10.1021/jacs.8b13655. <https://doi.org/10.1021/jacs.8b13655> (2019).
160. Wei, D., Junge, H. & Beller, M. An amino acid based system for CO₂ capture and catalytic utilization to produce formates. *Chem. Sci.* **12**, 6020–6024. doi:10.1039/D1SC00467K. <http://dx.doi.org/10.1039/D1SC00467K> (17 2021).
161. Hegde, N., Velingkar, V. & Prabhakar, B. An Update on Design and Pharmacology of Dendritic Poly(l-lysine). *International Journal of Peptide Research and Therapeutics* **25**, 1539–1562. ISSN: 1573-3904. doi:10.1007/s10989-018-9798-2. <https://doi.org/10.1007/s10989-018-9798-2> (2019).
162. Liu, G. *et al.* CO₂ reduction on pure Cu produces only 2.
163. Tang, M. T., Peng, H.-J., Stenlid, J. H. & Abild-Pedersen, F. Exploring Trends on Coupling Mechanisms toward C₃ Product Formation in CO₂R. *The Journal of Physical Chemistry C* **125**, 26437–26447. doi:10.1021/acs.jpcc.1c07553. eprint: <https://doi.org/10.1021/acs.jpcc.1c07553>. <https://doi.org/10.1021/acs.jpcc.1c07553> (2021).
164. Johnson, D., Qiao, Z. & Djire, A. Progress and Challenges of Carbon Dioxide Reduction Reaction on Transition Metal Based Electrocatalysts. *ACS Applied Energy Materials* **4**, 8661–8684. doi:10.1021/acsaem.1c01624. <https://doi.org/10.1021/acsaem.1c01624> (2021).

165. Carroll, J. J., Slupsky, J. D. & Mather, A. E. The Solubility of Carbon Dioxide in Water at Low Pressure. *Journal of Physical and Chemical Reference Data* **20**, 1201–1209. ISSN: 0047-2689. doi:10.1063/1.555900. eprint: https://pubs.aip.org/aip/jpr/article-pdf/20/6/1201/8183456/1201_1_online.pdf. <https://doi.org/10.1063/1.555900> (Nov. 1991).
166. Li, M. *et al.* Toward Excellence of Transition Metal-Based Catalysts for CO₂ Electrochemical Reduction: An Overview of Strategies and Rationales. *Small Methods* **4**, 2000033. doi:<https://doi.org/10.1002/smt.202000033>. <https://onlinelibrary.wiley.com/doi/abs/10.1002/smt.202000033> (2020).
167. Kas, R. *et al.* Three-dimensional porous hollow fibre copper electrodes for efficient and high-rate electrochemical carbon dioxide reduction. *Nature Communications* **7**, 10748. ISSN: 2041-1723. doi:10.1038/ncomms10748. <https://doi.org/10.1038/ncomms10748> (2016).
168. Whipple, D. T. & Kenis, P. J. A. Prospects of CO₂ Utilization via Direct Heterogeneous Electrochemical Reduction. *The Journal of Physical Chemistry Letters* **1**, 3451–3458. doi:10.1021/jz1012627. <https://doi.org/10.1021/jz1012627> (2010).
169. Furuya, N., Yamazaki, T. & Shibata, M. High performance RuPd catalysts for CO₂ reduction at gas-diffusion electrodes. *Journal of Electroanalytical Chemistry* **431**, 39–41. ISSN: 1572-6657. doi:[https://doi.org/10.1016/S0022-0728\(97\)00159-9](https://doi.org/10.1016/S0022-0728(97)00159-9). <https://www.sciencedirect.com/science/article/pii/S0022072897001599> (1997).
170. Kim, B., Ma, S., Molly Jhong, H.-R. & Kenis, P. J. Influence of dilute feed and pH on electrochemical reduction of CO₂ to CO on Ag in a continuous flow electrolyzer. *Electrochimica Acta* **166**, 271–276. ISSN: 0013-4686. doi:<https://doi.org/10.1016/j.electacta.2015.03.064>. <https://www.sciencedirect.com/science/article/pii/S0013468615006465> (2015).

171. Perryman, J. T. & Velázquez, J. M. Design Principles for Multinary Metal Chalcogenides: Toward Programmable Reactivity in Energy Conversion. *Chemistry of Materials* **33**, 7133–7147. doi:10.1021/acs.chemmater.1c01983. <https://doi.org/10.1021/acs.chemmater.1c01983> (2021).
172. Eren, B. *et al.* Activation of Cu(111) surface by decomposition into nanoclusters driven by CO adsorption. *Science* **351**, 475–478. doi:10.1126/science.aad8868. <https://www.science.org/doi/abs/10.1126/science.aad8868> (2016).
173. Chang, C.-J. *et al.* Quantitatively Unraveling the Redox Shuttle of Spontaneous Oxidation/Electroreduction of CuOx on Silver Nanowires Using in Situ X-ray Absorption Spectroscopy. *ACS Central Science* **5**, 1998–2009. doi:10.1021/acscentsci.9b01142. <https://doi.org/10.1021/acscentsci.9b01142> (2019).
174. Lin, S.-C. *et al.* Operando time-resolved X-ray absorption spectroscopy reveals the chemical nature enabling highly selective CO₂ reduction. *Nature Communications* **11**, 3525. ISSN: 2041-1723. doi:10.1038/s41467-020-17231-3. <https://doi.org/10.1038/s41467-020-17231-3> (2020).
175. Alikhani, M. E. & Manceron, L. The copper carbonyl complexes revisited: Why are the infrared spectra and structures of copper mono and dicarbonyl so different? *Journal of Molecular Spectroscopy* **310**. Spectroscopy of Radicals and Ions in Memory of Marilyn Jacox, 32–38. ISSN: 0022-2852. doi:<https://doi.org/10.1016/j.jms.2014.12.015>. <https://www.sciencedirect.com/science/article/pii/S0022285214002653> (2015).
176. Pike, R. D. Structure and Bonding in Copper(I) Carbonyl and Cyanide Complexes. *Organometallics* **31**, 7647–7660. doi:10.1021/om3004459. <https://doi.org/10.1021/om3004459> (2012).
177. Tomita, Y., Teruya, S., Koga, O. & Hori, Y. Electrochemical Reduction of Carbon Dioxide at a Platinum Electrode in Acetonitrile-Water Mixtures. *Journal of The Electrochemical Society* **147**, 4164. doi:10.1149/1.1394035 (2000).

178. Costentin, C., Drouet, S., Robert, M. & Savéant, J.-M. A Local Proton Source Enhances CO₂ Electroreduction to CO by a Molecular Fe Catalyst. *Science* **338**, 90–94. doi:10.1126/science.1224581 (2012).
179. Hatsukade, T., Kuhl, K. P., Cave, E. R., Abram, D. N. & Jaramillo, T. F. Insights into the electrocatalytic reduction of CO₂ on metallic silver surfaces. *Phys. Chem. Chem. Phys.* **16**, 13814–13819. doi:10.1039/C4CP00692E. <http://dx.doi.org/10.1039/C4CP00692E> (27 2014).
180. Stevens, G. B., Reda, T. & Raguse, B. Energy storage by the electrochemical reduction of CO₂ to CO at a porous Au film. *Journal of Electroanalytical Chemistry* **526**, 125–133. doi:10.1016/S0022-0728(02)00688-5 (2002).
181. Hori, Y., Murata, A. & Takahashi, R. Formation of hydrocarbons in the electrochemical reduction of carbon dioxide at a copper electrode in aqueous solution. *J. Chem. Soc., Faraday Trans. 1* **85**, 2309–2326. doi:10.1039/F19898502309. <http://dx.doi.org/10.1039/F19898502309> (8 1989).
182. Li, C. W. & Kanan, M. W. CO₂ Reduction at Low Overpotential on Cu Electrodes Resulting from the Reduction of Thick Cu₂O Films. *Journal of the American Chemical Society* **134**, 7231–7234. doi:10.1021/ja3010978 (2012).
183. Rosen, J. *et al.* Mechanistic Insights into the Electrochemical Reduction of CO₂ to CO on Nanostructured Ag Surfaces. *ACS Catalysis* **5**, 4293–4299. doi:10.1021/acscatal.5b00840 (2015).
184. Zhu, W. *et al.* Monodisperse Au Nanoparticles for Selective Electrocatalytic Reduction of CO₂ to CO. *Journal of the American Chemical Society* **135**, 16833–16836. doi:10.1021/ja409445p (2013).
185. Zhu, W. *et al.* Active and Selective Conversion of CO₂ to CO on Ultrathin Au Nanowires. *Journal of the American Chemical Society* **136**, 16132–16135. doi:10.1021/ja5095099 (2014).
186. Song, Y. *et al.* High-Selectivity Electrochemical Conversion of CO₂ to Ethanol using a Copper Nanoparticle/N-Doped Graphene Electrode. *ChemistrySelect* **1**, 6055–6061. doi:10.1002/slct.201601169 (2016).

187. Sen, S., Liu, D. & Palmore, G. T. R. Electrochemical Reduction of CO₂ at Copper Nanofoams. *ACS Catalysis* **4**, 3091–3095. doi:10.1021/cs500522g (2014).
188. W, T. C., B, N. A. & ANDREW, K. *pat.* 5266421. [https://worldwide.espacenet.com/patent/search/family/025379509/publication/US5266421A?q=pn=US5266421\(1993\)](https://worldwide.espacenet.com/patent/search/family/025379509/publication/US5266421A?q=pn=US5266421(1993)).
189. Yasin I. Irfan, B. An analysis of SPEEK as a suitable alternative for Nafion in a proton electrolyte membrane in PEM fuel cells. *University of Michigan Undergraduate Research Journal* **17**. doi:<https://doi.org/10.3998/umurj.5508>. <https://journals.publishing.umich.edu/umurj/article/id/5508/> (2024).
190. Mamlouk, M. in *Comprehensive Renewable Energy (Second Edition)* (ed Letcher, T. M.) Second Edition, 473–504 (Elsevier, Oxford, 2022). ISBN: 978-0-12-819734-9. doi:<https://doi.org/10.1016/B978-0-12-819727-1.00103-5>. <https://www.sciencedirect.com/science/article/pii/B9780128197271001035>.
191. Millikan, R., Bishop, E. & Society, A. T. *Elements of Electricity: A Practical Discussion of the Fundamental Laws and Phenomena of Electricity and Their Practical Applications in the Business and Industrial World* <https://books.google.co.uk/books?id=dZM3AAAAMAAJ> (American Technical Society, 1917).
192. Wu, Y. C. & Berezansky, P. A. Low Electrolytic Conductivity Standards. *J Res Natl Inst Stand Technol* **100**. PMC4887229, 521–527. ISSN: 1044-677X. doi:10.6028/jres.100.039. <https://doi.org/10.6028/jres.100.039> (1995).
193. *Potassium Bicarbonate Handbook* tech. rep. (Armand Products Company, 469 North Harrison Street Princeton, NJ 08543-5297). <https://www.armandproducts.com/content/pdfs/PotBiVs6.PDF>.
194. Hori, Y., Wakebe, H., Tsukamoto, T. & Koga, O. Electrocatalytic process of CO selectivity in electrochemical reduction of CO₂ at metal electrodes in aqueous media. *Electrochimica Acta* **39**, 1833–1839. ISSN: 0013-4686. doi:[https://doi.org/10.1016/0013-4686\(94\)00133-9](https://doi.org/10.1016/0013-4686(94)00133-9).

- [//doi.org/10.1016/0013-4686\(94\)85172-7](https://doi.org/10.1016/0013-4686(94)85172-7).<https://www.sciencedirect.com/science/article/pii/0013468694851727> (1994).
195. Peterson, A. A., Abild-Pedersen, F., Studt, F., Rossmeisl, J. & Nørskov, J. K. How copper catalyzes the electroreduction of carbon dioxide into hydrocarbon fuels. *Energy Environ. Sci.* **3**, 1311–1315. doi:10.1039/C0EE00071J. <http://dx.doi.org/10.1039/C0EE00071J> (9 2010).
196. Montoya, J. H., Shi, C., Chan, K. & Nørskov, J. K. Theoretical Insights into a CO Dimerization Mechanism in CO₂ Electroreduction. *The Journal of Physical Chemistry Letters* **6**. PMID: 26266498, 2032–2037. doi:10.1021/acs.jpcclett.5b00722. eprint: <https://doi.org/10.1021/acs.jpcclett.5b00722>. <https://doi.org/10.1021/acs.jpcclett.5b00722> (2015).
197. Kortlever, R., Shen, J., Schouten, K. J. P., Calle-Vallejo, F. & Koper, M. T. M. Catalysts and Reaction Pathways for the Electrochemical Reduction of Carbon Dioxide. *The Journal of Physical Chemistry Letters* **6**. PMID: 26722779, 4073–4082. doi:10.1021/acs.jpcclett.5b01559. eprint: <https://doi.org/10.1021/acs.jpcclett.5b01559>. <https://doi.org/10.1021/acs.jpcclett.5b01559> (2015).
198. Cheng, T., Xiao, H. & Goddard, W. A. I. Free-Energy Barriers and Reaction Mechanisms for the Electrochemical Reduction of CO on the Cu(100) Surface, Including Multiple Layers of Explicit Solvent at pH 0. *The Journal of Physical Chemistry Letters* **6**. PMID: 26562750, 4767–4773. doi:10.1021/acs.jpcclett.5b02247. eprint: <https://doi.org/10.1021/acs.jpcclett.5b02247>. <https://doi.org/10.1021/acs.jpcclett.5b02247> (2015).
199. Lum, Y., Cheng, T., Goddard, W. A. I. & Ager, J. W. Electrochemical CO Reduction Builds Solvent Water into Oxygenate Products. *Journal of the American Chemical Society* **140**. PMID: 30009595, 9337–9340. doi:10.1021/jacs.8b03986. eprint: <https://doi.org/10.1021/jacs.8b03986>. <https://doi.org/10.1021/jacs.8b03986> (2018).

200. Feaster, J. T. *et al.* Understanding Selectivity for the Electrochemical Reduction of Carbon Dioxide to Formic Acid and Carbon Monoxide on Metal Electrodes. *ACS Catalysis* **7**, 4822–4827. doi:10.1021/acscatal.7b00687. eprint: <https://doi.org/10.1021/acscatal.7b00687>. <https://doi.org/10.1021/acscatal.7b00687> (2017).
201. Liu, X. *et al.* pH effects on the electrochemical reduction of CO₂ towards C₂ products on stepped copper. *Nature Communications* **10**, 32. ISSN: 2041-1723. doi:10.1038/s41467-018-07970-9. <https://doi.org/10.1038/s41467-018-07970-9> (2019).
202. Garza, A. J., Bell, A. T. & Head-Gordon, M. Mechanism of CO₂ Reduction at Copper Surfaces: Pathways to C₂ Products. *ACS Catalysis* **8**, 1490–1499. doi:10.1021/acscatal.7b03477. eprint: <https://doi.org/10.1021/acscatal.7b03477>. <https://doi.org/10.1021/acscatal.7b03477> (2018).
203. Chernyshova, I. V., Somasundaran, P. & Ponnurangam, S. On the origin of the elusive first intermediate of CO₂ electroreduction. *Proceedings of the National Academy of Sciences* **115**, E9261–E9270. doi:10.1073/pnas.1802256115. eprint: <https://www.pnas.org/doi/pdf/10.1073/pnas.1802256115>. <https://www.pnas.org/doi/abs/10.1073/pnas.1802256115> (2018).
204. Marepally, B. C. *et al.* in *Horizons in Sustainable Industrial Chemistry and Catalysis* (eds Albonetti, S., Perathoner, S. & Quadrelli, E. A.) 7–30 (Elsevier, 2019). doi:<https://doi.org/10.1016/B978-0-444-64127-4.00001-X>. <https://www.sciencedirect.com/science/article/pii/B978044464127400001X>.
205. Lasia, A. Hydrogen evolution reaction. *Handbook of fuel cells* **2** (2010).
206. Liu, M. *et al.* Enhanced electrocatalytic CO₂ reduction via field-induced reagent concentration. *Nature* **537**, 382–386. ISSN: 1476-4687. doi:10.1038/nature19060. <https://doi.org/10.1038/nature19060> (2016).
207. Qi, K. *et al.* Unlocking direct CO₂ electrolysis to C₃ products via electrolyte supersaturation. *Nature Catalysis* **6**, 319–331. ISSN: 2520-1158. doi:10.1038/

- s41929-023-00938-z. <https://doi.org/10.1038/s41929-023-00938-z> (2023).
208. Sonoyama, N., Kirii, M. & Sakata, T. Electrochemical reduction of CO₂ at metal-porphyrin supported gas diffusion electrodes under high pressure CO₂. *Electrochemistry Communications* **1**, 213–216. ISSN: 1388-2481. doi:[https://doi.org/10.1016/S1388-2481\(99\)00041-7](https://doi.org/10.1016/S1388-2481(99)00041-7). <https://www.sciencedirect.com/science/article/pii/S1388248199000417> (1999).
209. Jones, J.-P., Prakash, G. K. S. & Olah, G. A. Electrochemical CO₂ Reduction: Recent Advances and Current Trends. *Israel Journal of Chemistry* **54**, 1451–1466. doi:<https://doi.org/10.1002/ijch.201400081>. eprint: <https://onlinelibrary.wiley.com/doi/pdf/10.1002/ijch.201400081>. <https://onlinelibrary.wiley.com/doi/abs/10.1002/ijch.201400081> (2014).
210. Jhong, H.-R., Ma, S. & Kenis, P. J. Electrochemical conversion of CO₂ to useful chemicals: current status, remaining challenges, and future opportunities. *Current Opinion in Chemical Engineering* **2**. Nanotechnology / Separation engineering, 191–199. ISSN: 2211-3398. doi:<https://doi.org/10.1016/j.coche.2013.03.005>. <https://www.sciencedirect.com/science/article/pii/S2211339813000294> (2013).
211. Bard, A. & Faulkner, L. *Electrochemical Methods: Fundamentals and Applications* ISBN: 9780471043720. <https://books.google.co.uk/books?id=kv56QgAACAAJ> (Wiley, 2000).
212. Nguyen, T. N. & Dinh, C.-T. Gas diffusion electrode design for electrochemical carbon dioxide reduction. *Chem. Soc. Rev.* **49**, 7488–7504. doi:10.1039/D0CS00230E. <http://dx.doi.org/10.1039/D0CS00230E> (21 2020).
213. Dean, J. A. *Lange's Handbook of Chemistry* 1999.
214. Sullivan, B. P. & Krist K. and Guard, H. E. *Electrochemical and electrocatalytic reactions of carbon dioxide* English (Elsevier, Amsterdam; New York, 1993).

215. Pedersen, O., Colmer, T. & Sand-Jensen, K. Underwater Photosynthesis of Submerged Plants – Recent Advances and Methods. *Frontiers in plant science* **4**, 140. doi:10.3389/fpls.2013.00140 (May 2013).
216. Rahman, F. U. *Laminar Flow and Turbulent Flow* Sept. <https://theconstructor.org/fluid-mechanics/laminar-turbulent-flow/559432/>.
217. Lacassagne, T., EL Hajem, M., Champagne, J.-Y. & Simoëns, S. Turbulent mass transfer near gas-liquid interfaces in water and shear-thinning dilute polymer solution. *International Journal of Heat and Mass Transfer* **194**, 122975. ISSN: 0017-9310. doi:<https://doi.org/10.1016/j.ijheatmasstransfer.2022.122975>. <https://www.sciencedirect.com/science/article/pii/S0017931022004483> (2022).

Appendix A

Supplementary Information 1

Additional content for Chapter 5

A.1 Detailed graphs

This section contains graphs with additional details.

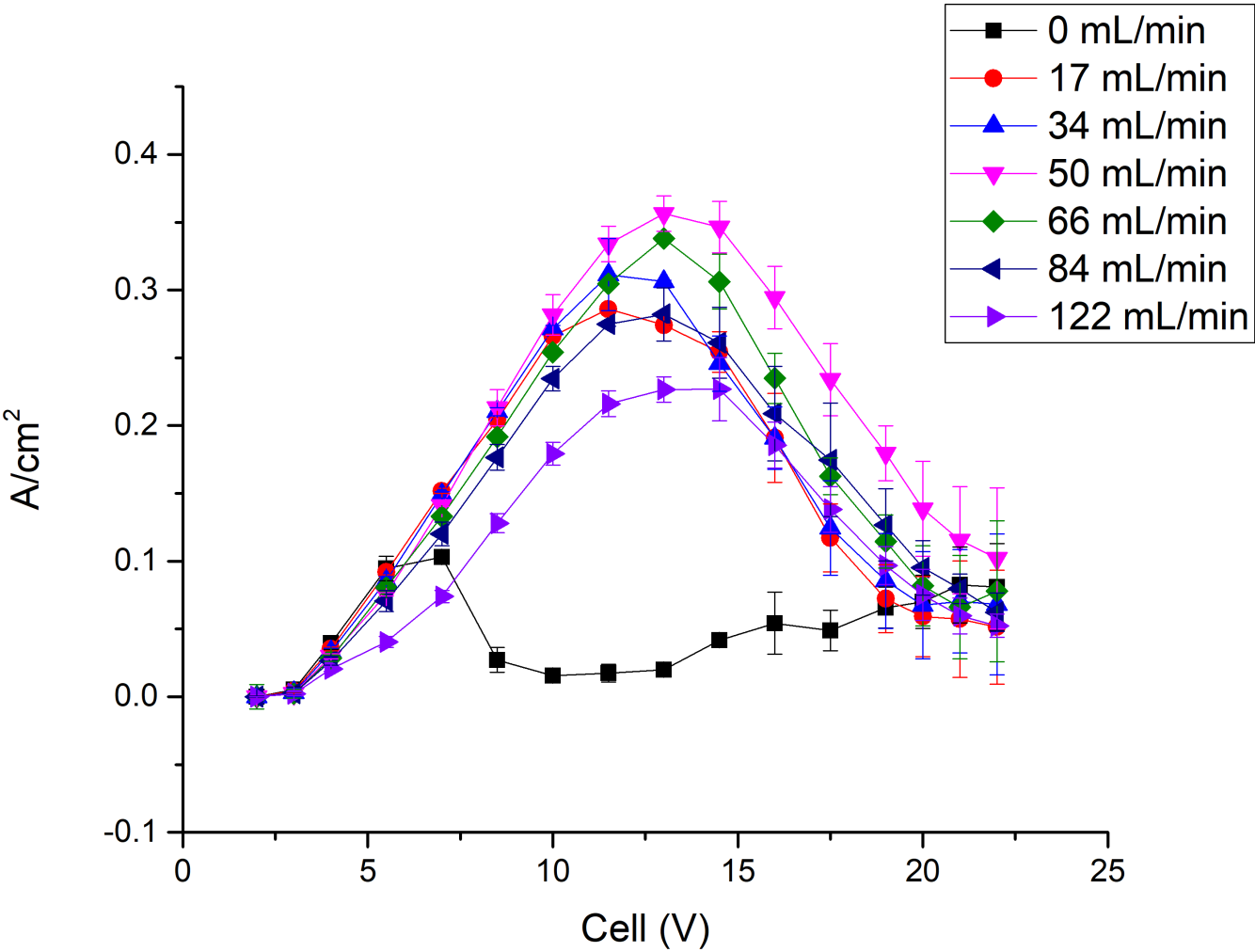


FIGURE A.1: Plot of current density vs applied potential for varied electrolyte flow rates.

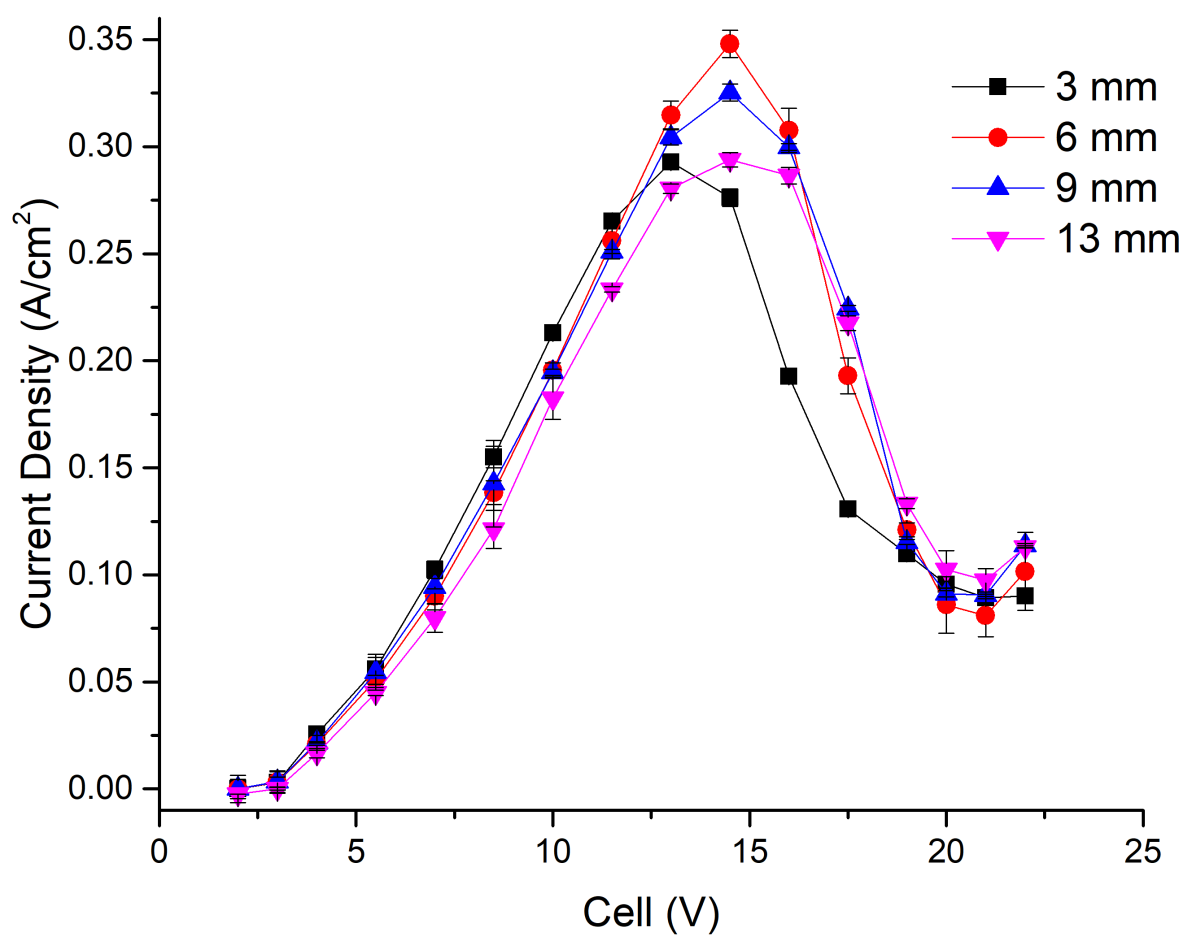


FIGURE A.2: Plot of current density vs applied potential for different total separation distances between the two electrodes.

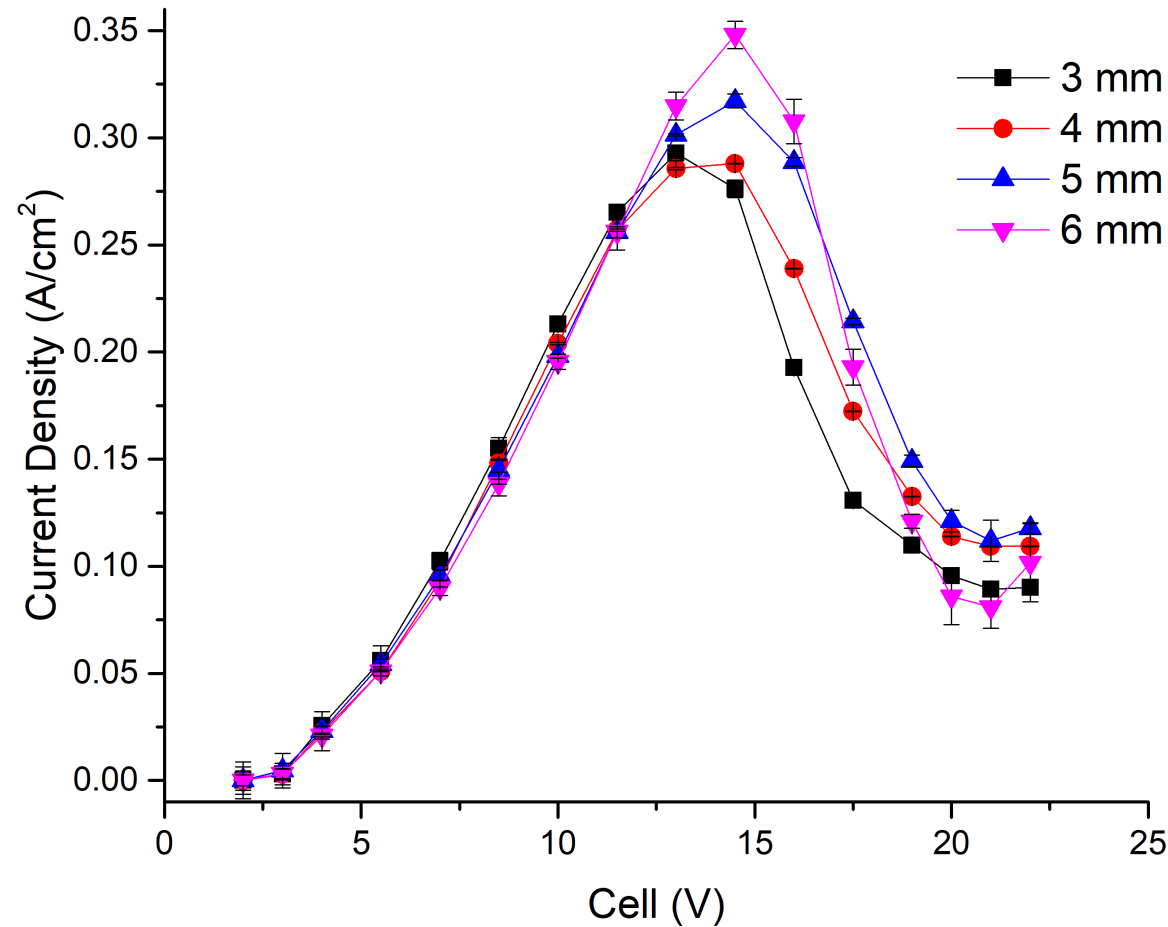


FIGURE A.3: Plot of current density vs applied potential for different total separation distances of the electrodes between 3 mm and 6 mm.

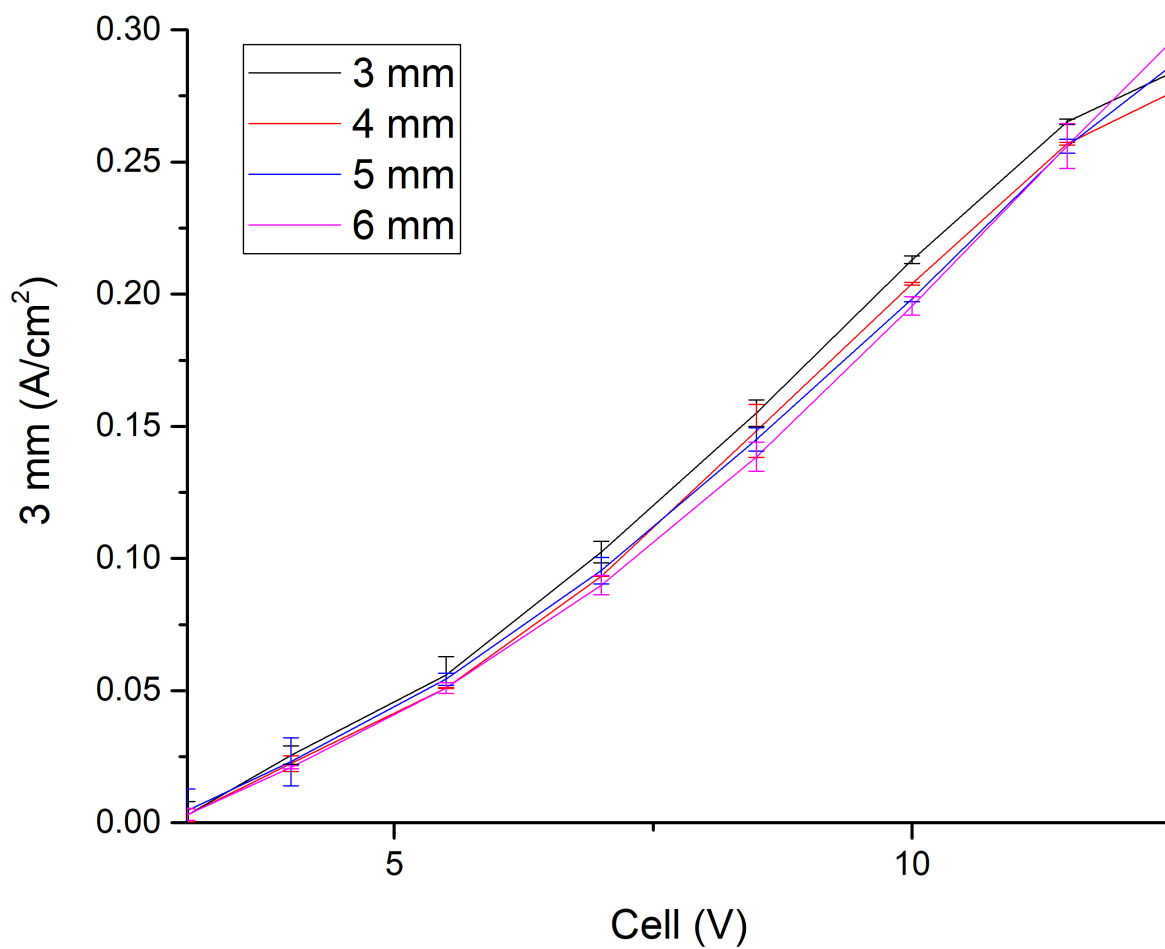


FIGURE A.4: Plot of current density vs applied potential for total electrode separations between 3 mm and 6 mm, for applied potentials from 2.5 V to 12.5 V.

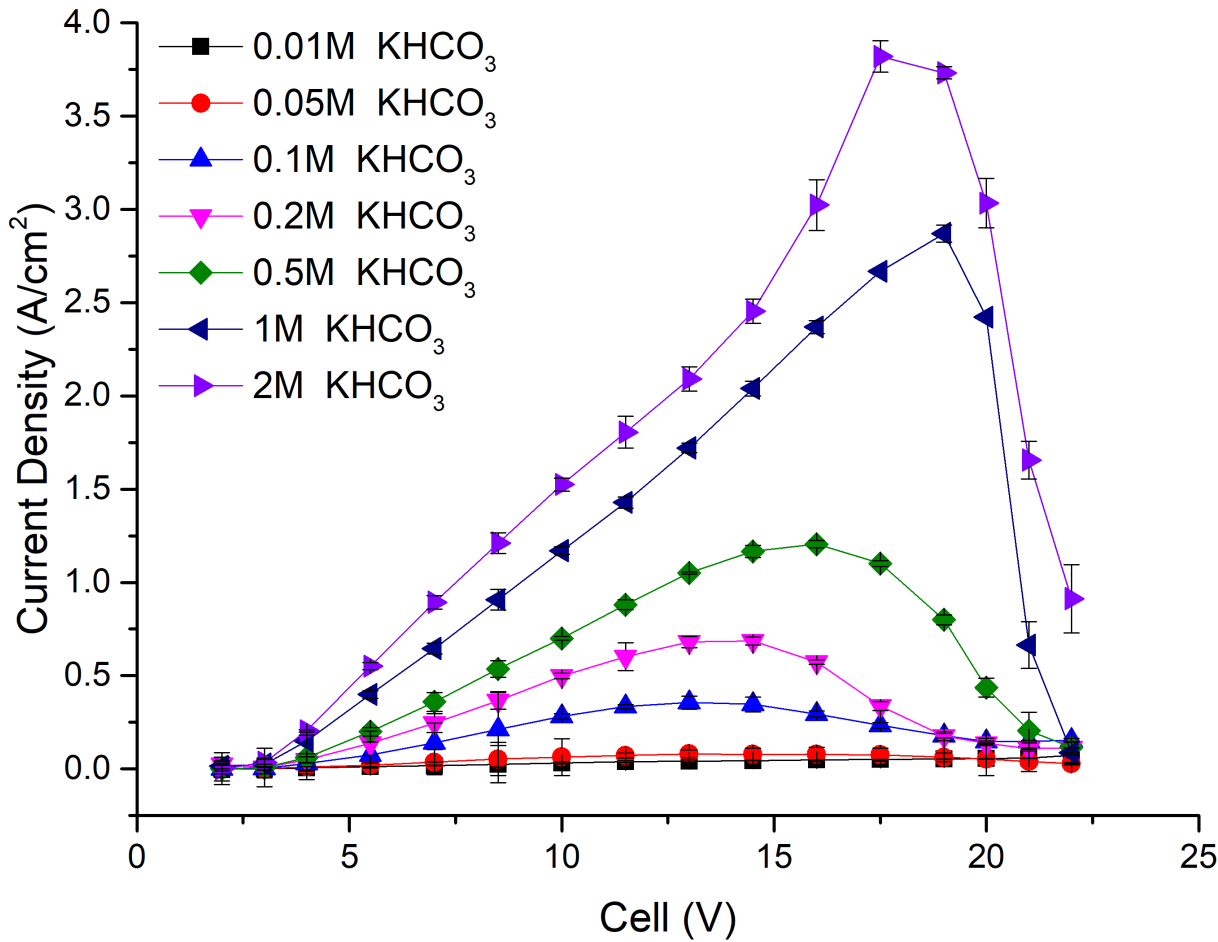


FIGURE A.5: Plot of current density vs applied potential for different electrolyte concentrations.

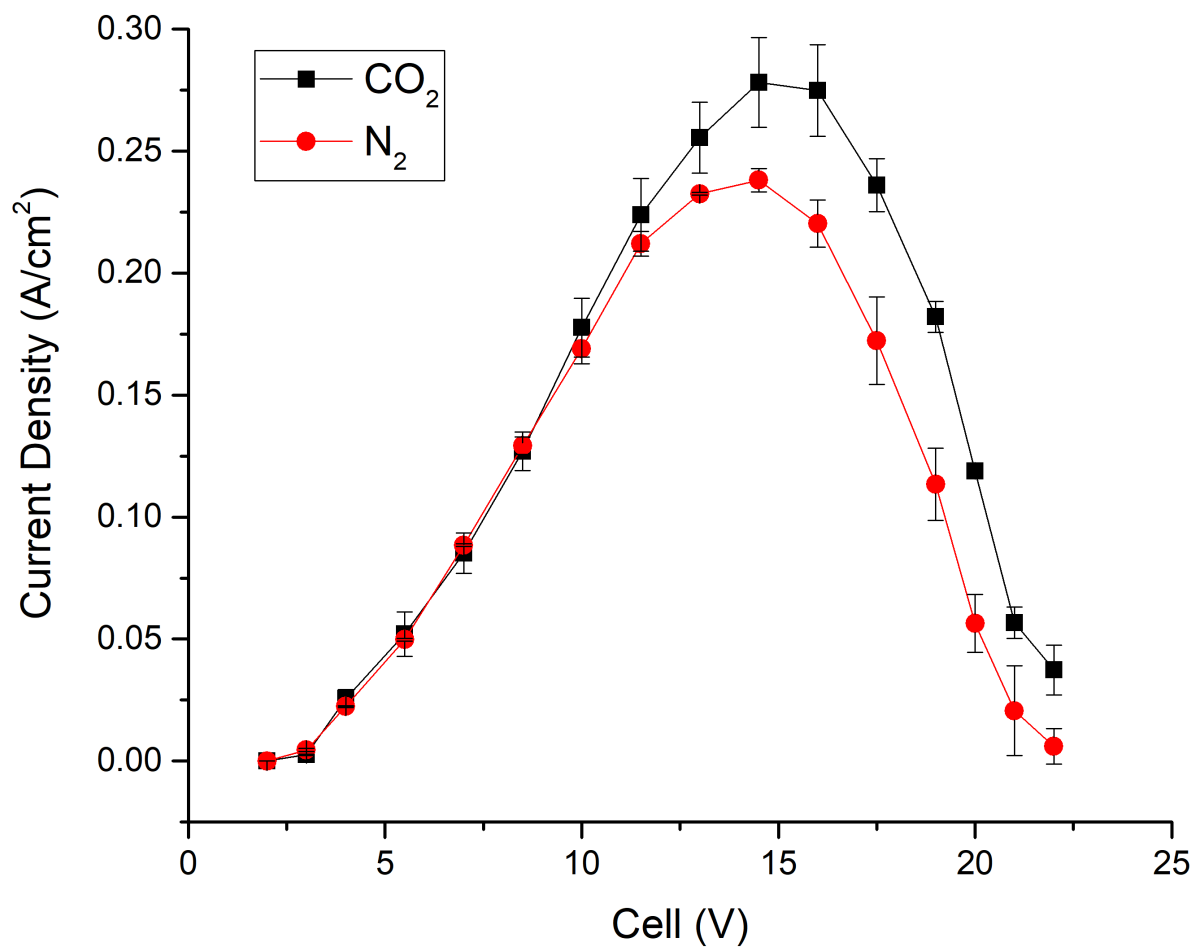


FIGURE A.6: Plot of average current density vs applied potential for carbon dioxide and nitrogen at 0.1 M KHCO₃ circulated at 50 mL/min in dual reservoir system.

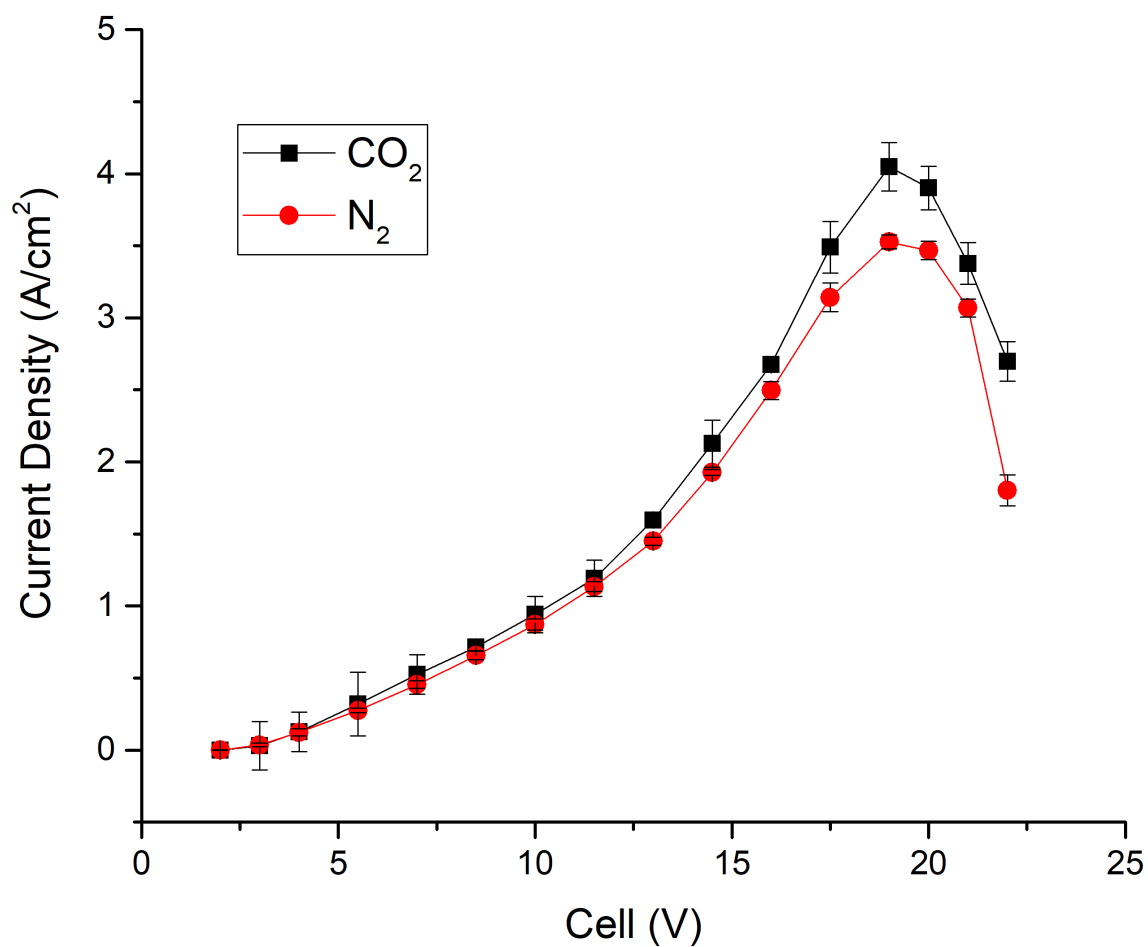


FIGURE A.7: Plot of average current density vs applied potential for carbon dioxide and nitrogen at 1.0 M KHCO₃ circulated at 50 mL/min in dual reservoir system.

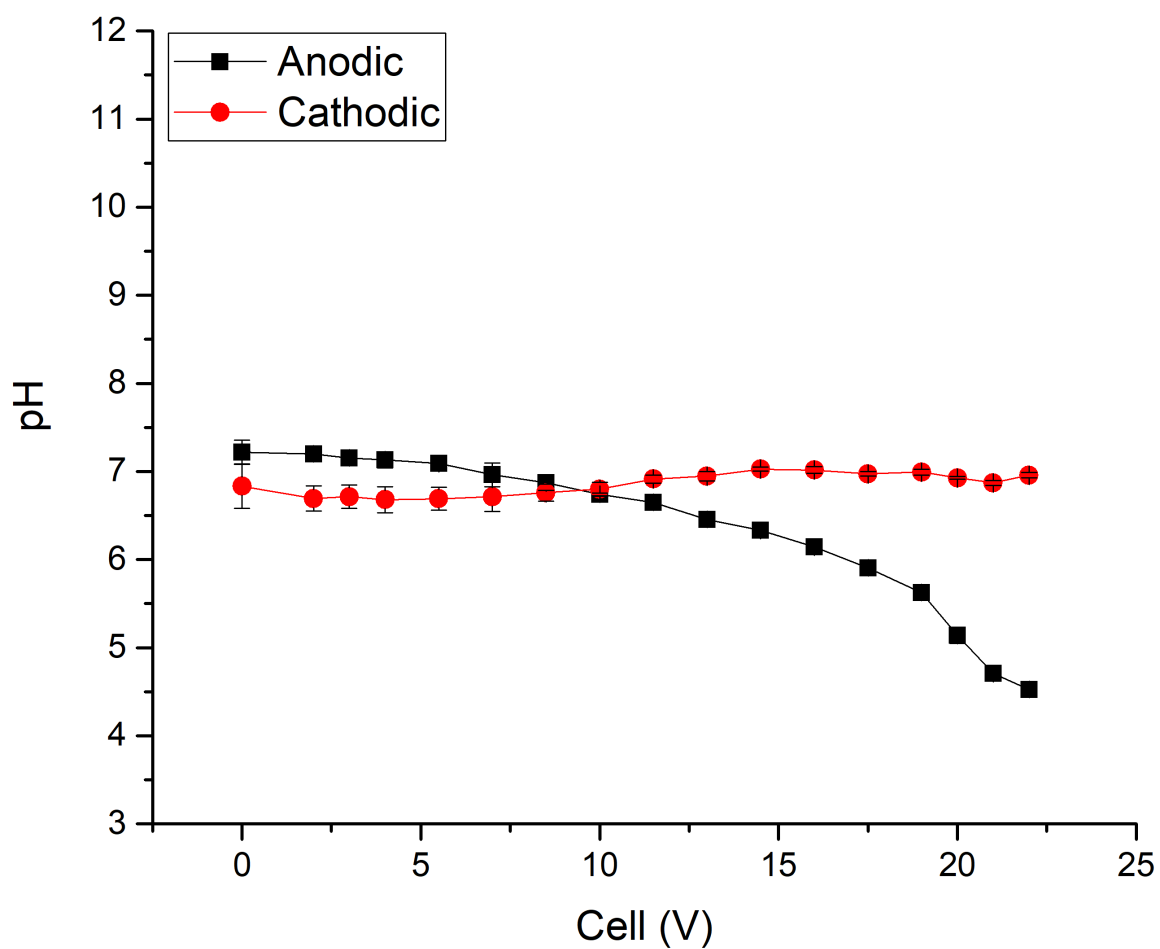


FIGURE A.8: Plot of average pH of the electrolyte vs applied potential for carbon dioxide bubbled 0.1 M KHCO_3 circulated at 50 mL/min in a dual reservoir system.

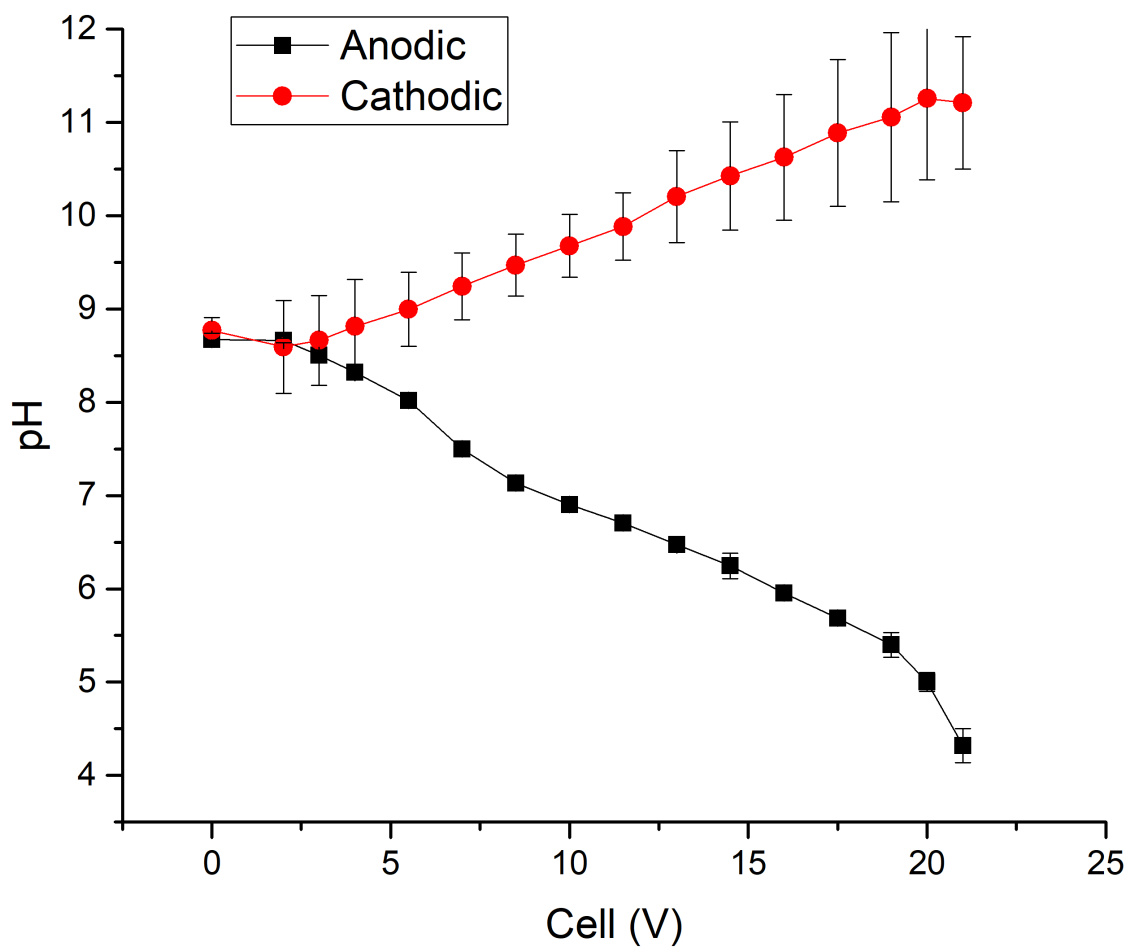


FIGURE A.9: Plot of average pH of the electrolyte vs applied potential for nitrogen bubbled 0.1 M KHCO_3 circulated at 50 m/min in a dual reservoir system.

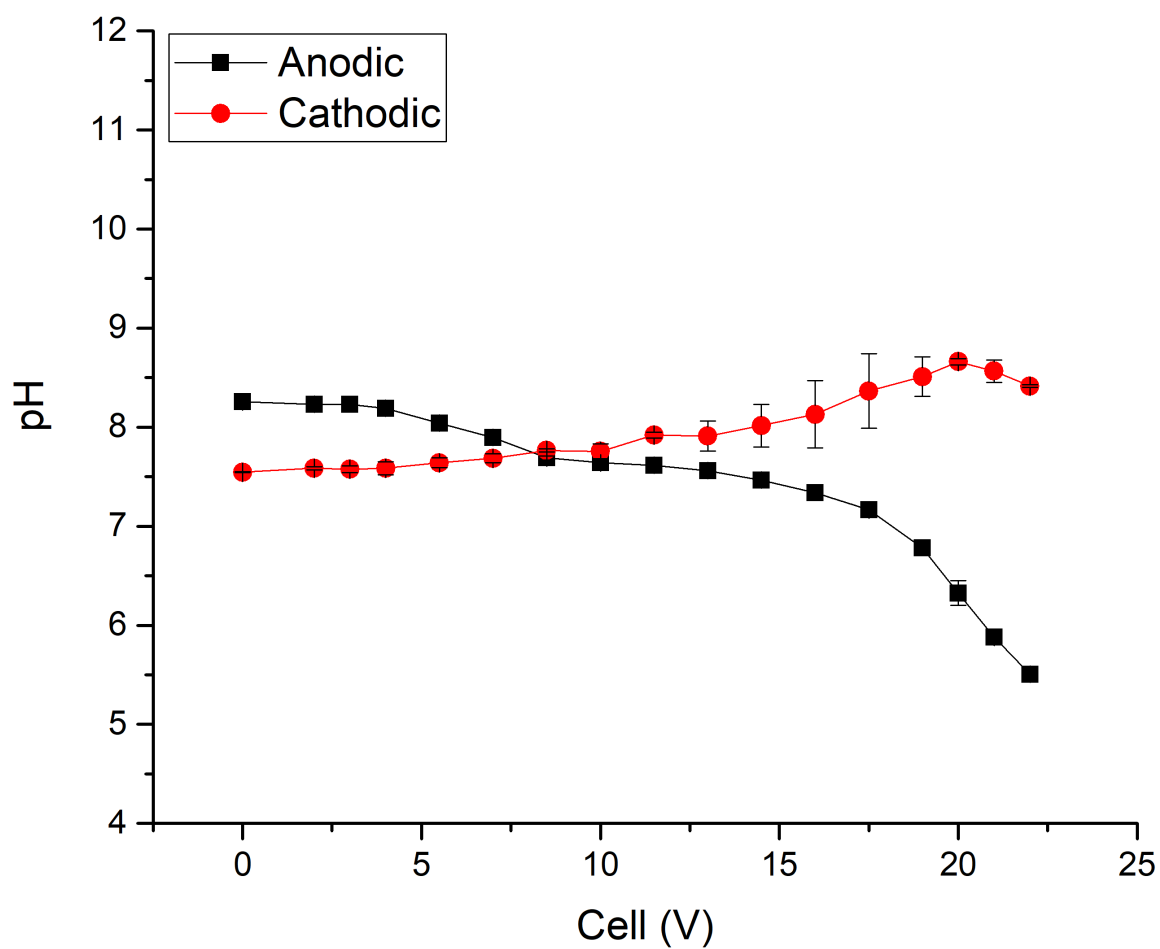


FIGURE A.10: Plot of average pH of the electrolyte vs applied potential for carbon dioxide bubbled 1.0 M KHCO_3 circulated at 50 mL/min in a dual reservoir system.

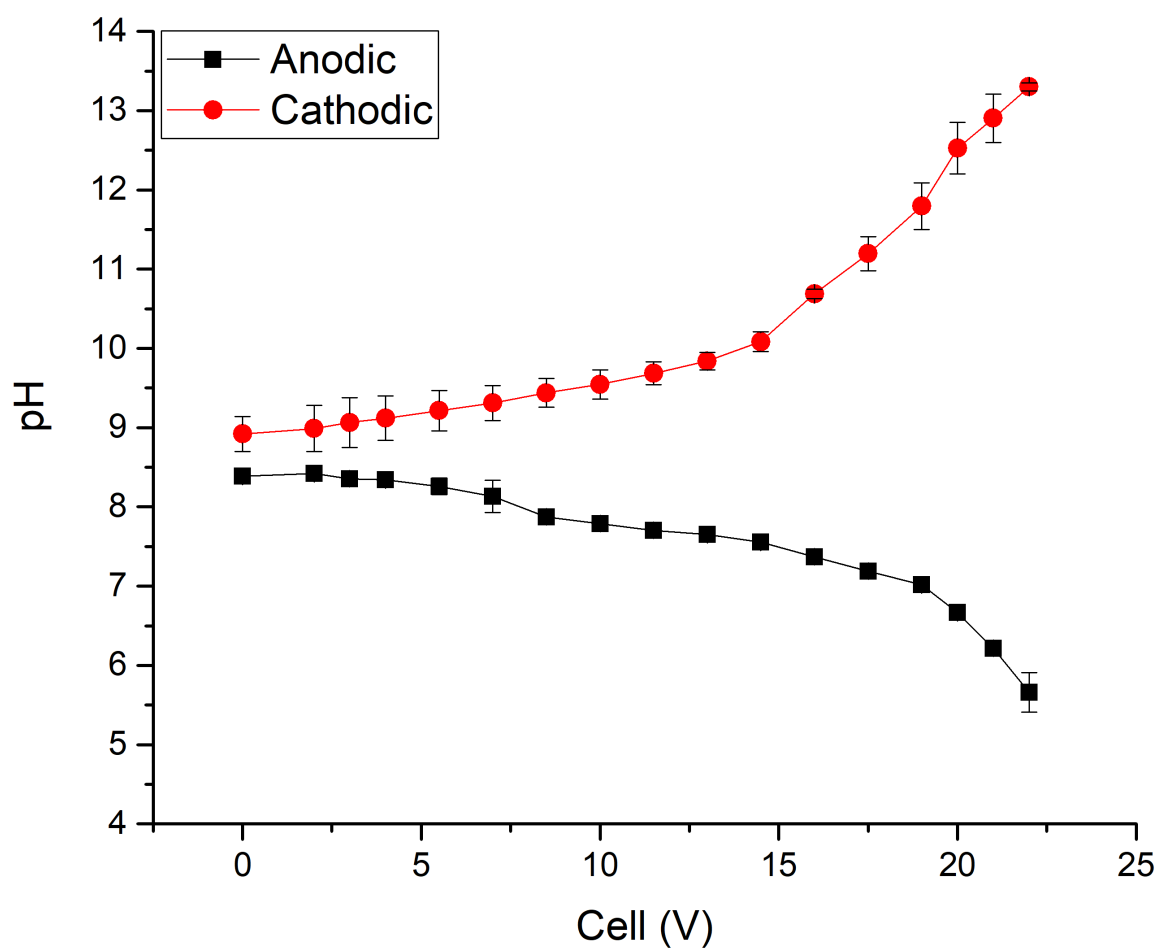


FIGURE A.11: Plot of average pH of the electrolyte vs applied potential for nitrogen bubbled 1.0 M KHCO_3 circulated at 50 mL/min in a dual reservoir system.

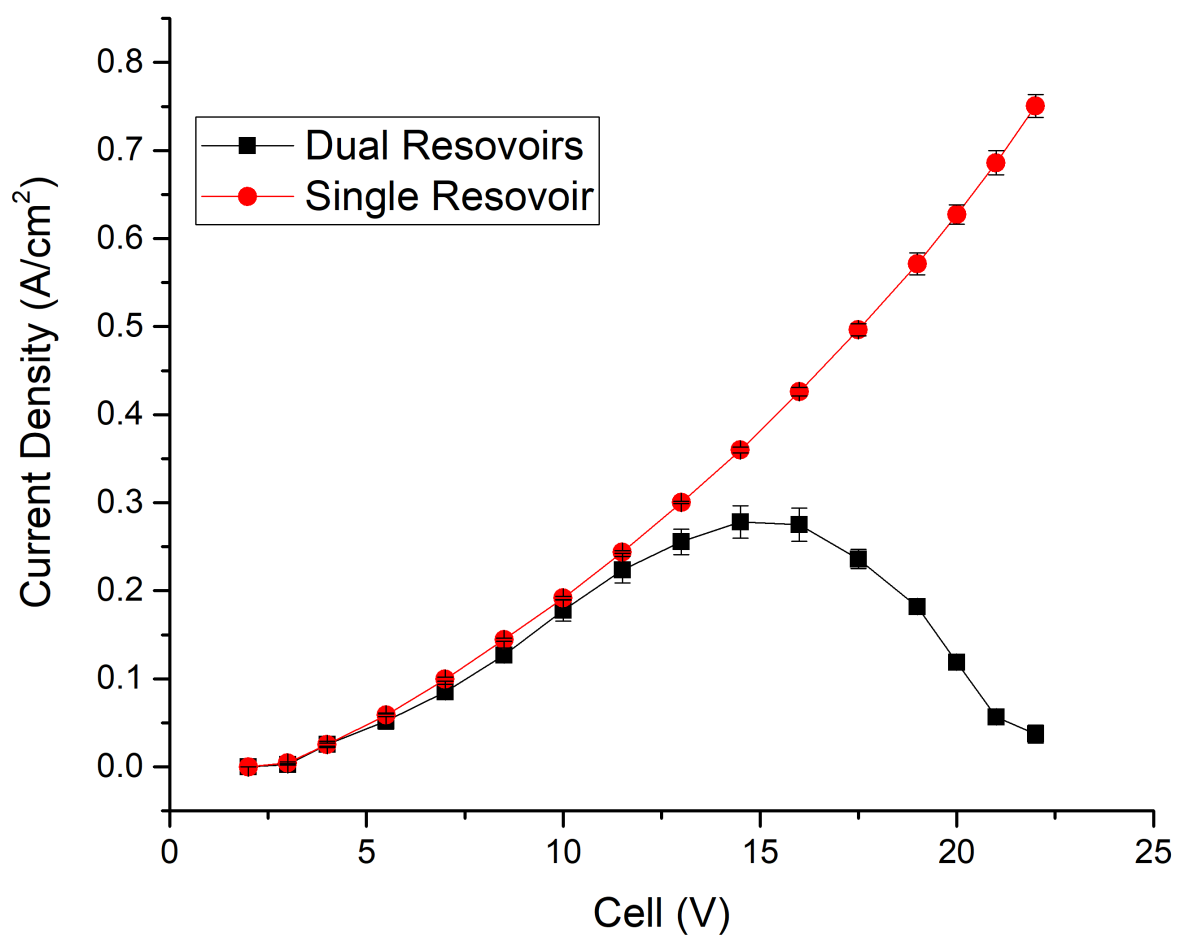


FIGURE A.12: Plot of current density vs applied potential for combined and separate reservoirs at 0.1 M KHCO₃.

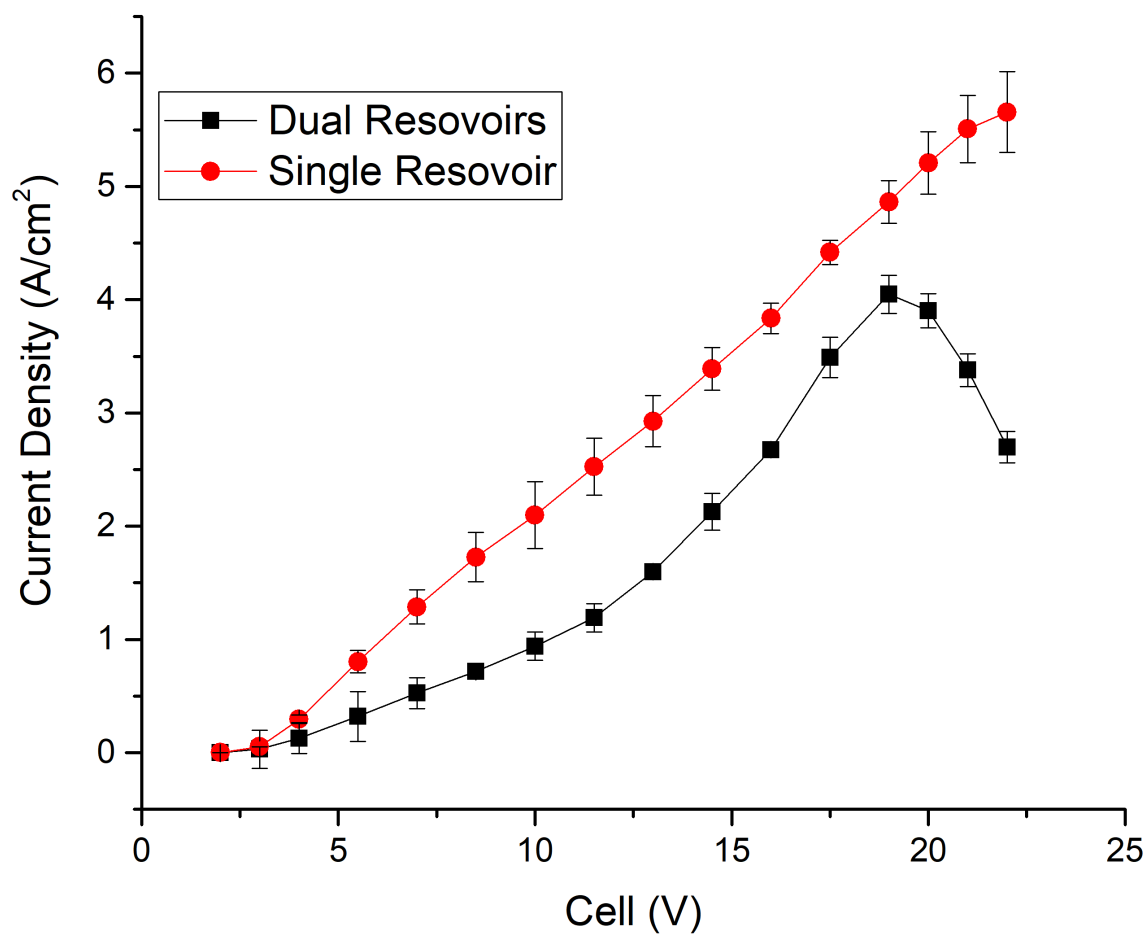


FIGURE A.13: Plot of current density vs applied potential for combined and separate reservoirs at 1.0 M KHCO_3 .

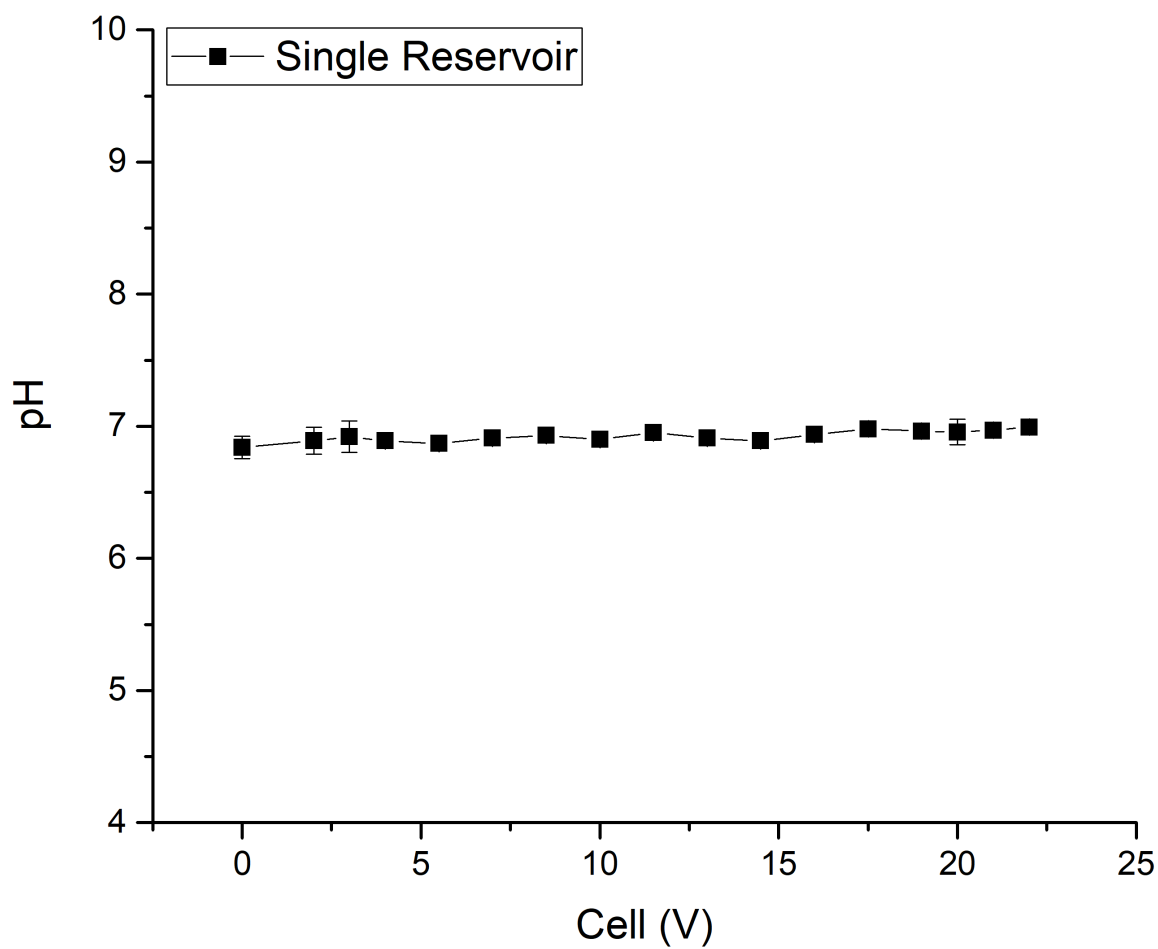


FIGURE A.14: Plot of pH vs applied potential for carbon dioxide bubbled 0.1 M KHCO_3 in a single reservoir system.

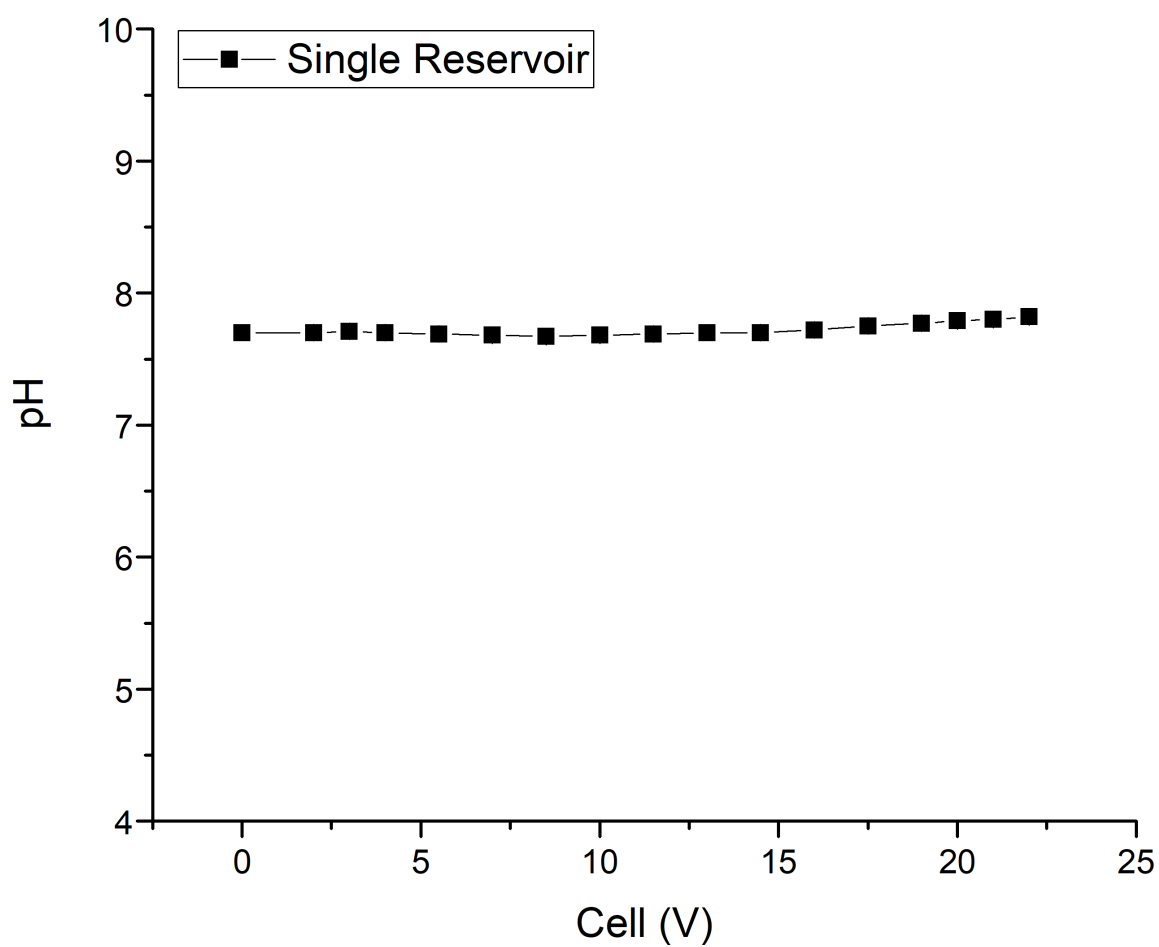


FIGURE A.15: Plot of pH vs applied potential for carbon dioxide bubbled 1.0 M KHCO_3 in a single reservoir system.

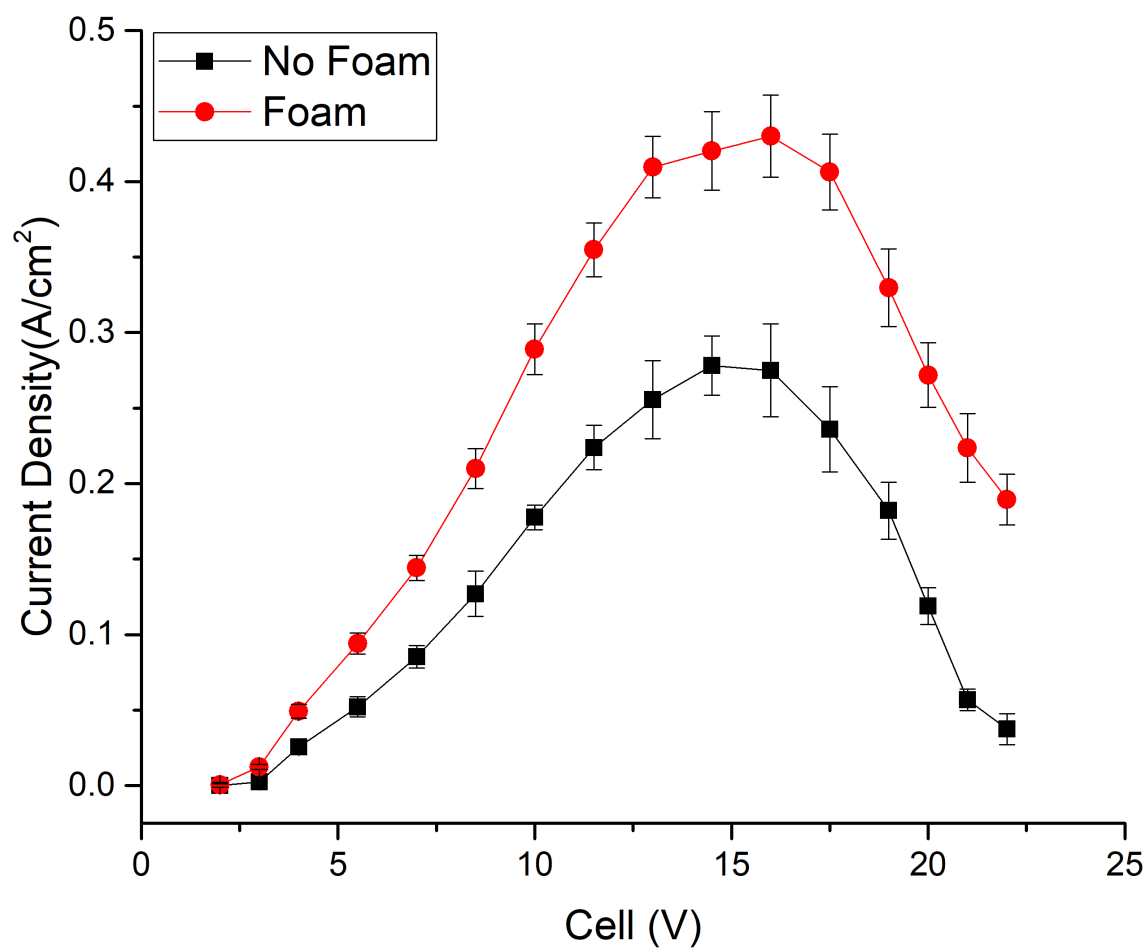


FIGURE A.16: Plot of current density vs applied voltage for a Cu foam and a plain electrode, utilising 0.1 M KHCO₃.

A.2 Matlab code for J/V curve

```
clear all;
clc;
close all;

%Open file and replaces occurrences of a tab, A or V with a space; use a
%switch statement and a for loop to cycle through each file in turn
Nfiles = 4;

for f=1:Nfiles

switch f
    case 1
        File = '21-01-2020 12-28-05.txt';
    case 2
        File = '21-01-2020 15-17-17.txt';
    case 3
        File = '22-01-2020 12-10-53.txt';
    case 4
        File = '22-01-2020 14-28-26.txt';

end

Input = fopen(File);
text = fscanf(Input,'%c');
tabs = strfind(text,'\t');
Achar = strfind(text,'A');
```

```
Vchar = strfind(text,'V');
text(tabs) = ' ';
text(Achar) = ' ';
text(Vchar) = ' ';

%Pass the revised format to a new file named "New.txt"
Converted = fopen('New.txt','w');
fwrite(Converted, text);

%Import V and I data from New.txt
Data = importdata('New.txt');
V = Data.data(:,1);
I = Data.data(:,2);

%Identify unique values of V and the number of different values
Vvals = unique(V);

%Remove all values outside Vmin and Vmax
Vmin = 1.99;
Vmax = 25;
Vvals(Vvals<Vmin) = nan;
Vvals(Vvals>Vmax) = nan;
Vvalsnan = isnan(Vvals);
Vvals = Vvals(~Vvalsnan);

NV = size(Vvals,1);
Iav = zeros(size(Vvals));
Idev = zeros(size(Vvals));
```

```
%Cycle through each value of V in turn and find all entries in I
%corresponding to that value; take the mean and standard deviation
%of these values
```

```
for i=1:NV
    Vtemp = V;
    Vtemp(Vtemp~=Vvals(i)) = nan;
    Itemp = I.*Vtemp;
    Vtemp(Vtemp==0) = 1;
    Itemp = Itemp./Vtemp;
    Inan = isnan(Intemp);
    Itemp = Itemp(~Inan);
    Iav(i) = mean(Intemp);
    Idev(i) = std(Intemp);
end
```

```
%Output a file named "Means.txt" containing all of the V values and the
%corresponding average I value
```

```
OPData = [Vvals.'; Iav.'; Idev.'];
OPName = ['Values-',File];
Output = fopen(OPName, 'w');
fprintf(Output,'%s %s %s\r\n','V / V','I / A','dI / A');
fprintf(Output, '%f %f %f\r\n', OPData);
fclose(Output);
fclose(Converted);

end
```


Appendix B

Supplementary Information 2

Additional content for chapter 7

B.1 Matlab code for Q calculation

```
clear all;
clc;
close all;

%Set number of files
Nfiles = 1;

%Set up vector to store integral values
Q = zeros(Nfiles,1);

for f=1:Nfiles
%Select file
switch f
    case 1
        File = '12-10-2021 17-42-11.txt';
    case 2
```

```

        File = '09-03-2021 16-34-20.txt ';
    case 3
        File = '09-03-2021 16-54-52.txt ';
    end

%Open file and replaces occurrences of a tab, colon, A or V with a space; us
%switch statement and a for loop to cycle through each file in turn
Input = fopen(File);
text = fscanf(Input,'%c');
tabs = strfind(text,sprintf('\t'));
Achar = strfind(text,'A');
Vchar = strfind(text,'V');
Cols = strfind(text,':');
Spaces = strfind(text,' ');
text(tabs) = ' ';
text(Achar) = ' ';
text(Vchar) = ' ';
text(Cols) = ' ';
text(Spaces) = ' ';

%Pass the revised format to a new file named "New.txt"
Converted = fopen('New.txt','w');
fwrite(Converted, text);

%Import V and I data from New.txt
Data = importdata('New.txt');
Hours = Data.data(:,1);
Mins = Data.data(:,2);

```

```
Secs = Data.data(:,3);
V = Data.data(:,4);
I = Data.data(:,5);

%Calculate total time in s from Hour, Mins and Secs entries
t = (3600.*Hours)+(60.*Mins)+Secs;
t = t-t(1);

%Integrate I with respect to t
Q(f) = trapz(t,I);

%Plot I vs t
figure
scatter(t,I,15,'o','MarkerEdgeColor','k','MarkerFaceColor','k','LineStyle','none')
set(gca,'FontSize',14)
set(gca,'FontName','Arial');
xlabel('\it{t}\rm / s')
ylabel('\it{I}\rm / A')
xlim([0,max(t)]);
ylim([0,1.1*max(I)]);

%Display Q value on command line
disp([File,':',num2str(Q(f)),' C']);

end
```

B.2 Additional Results

B.2.1 EDX

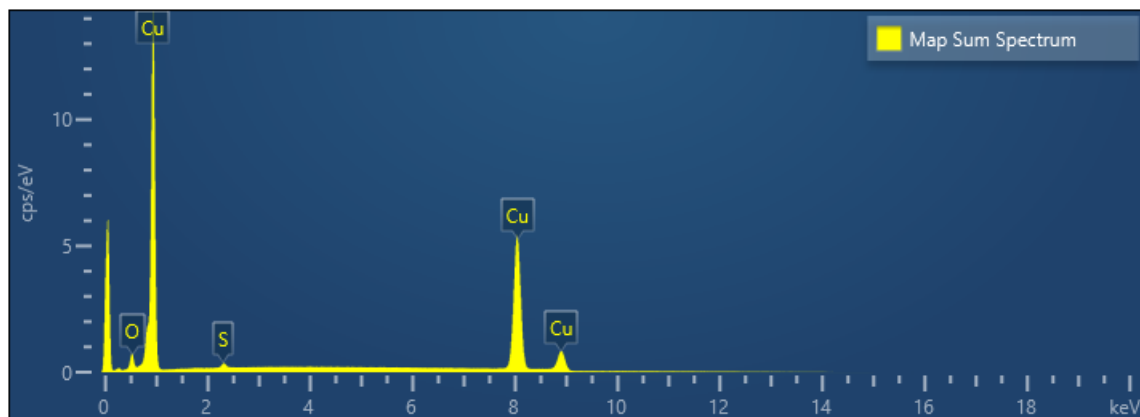


FIGURE B.1: EDX spectra for Plain Cu foam

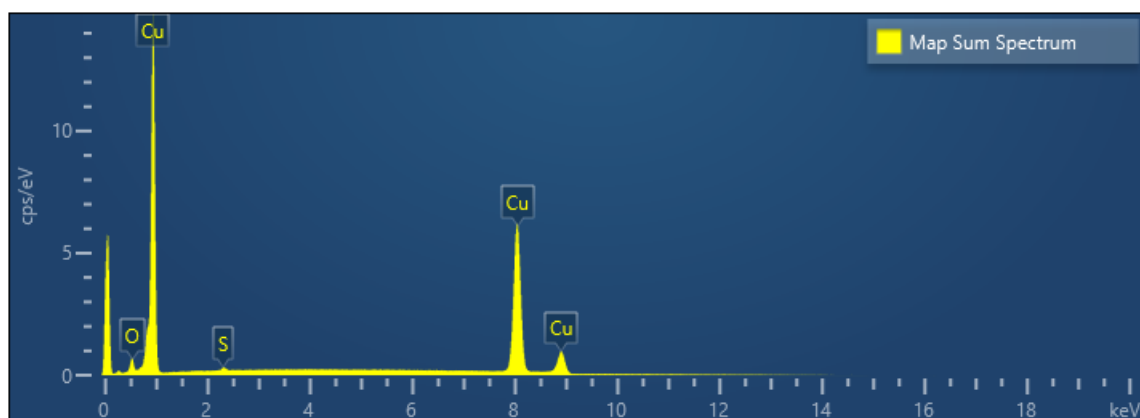


FIGURE B.2: EDX spectra for PA Cu foam

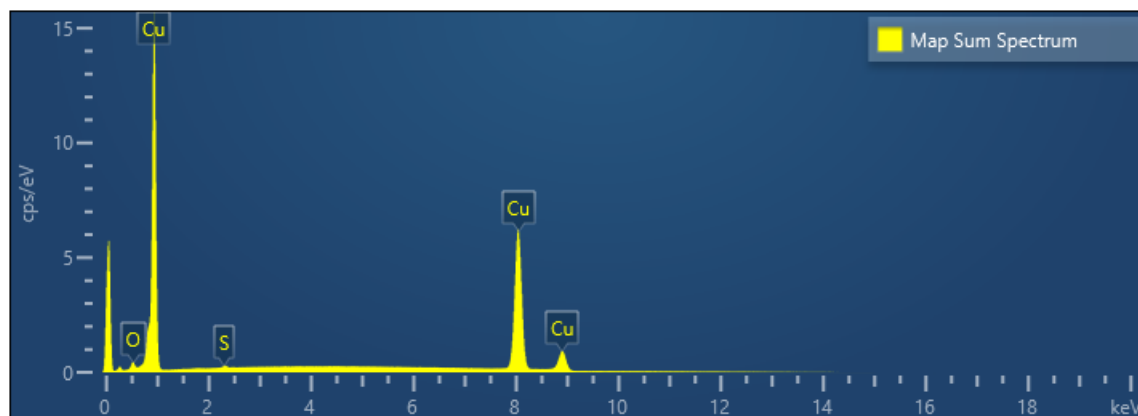


FIGURE B.3: EDX spectra for PSA Cu foam

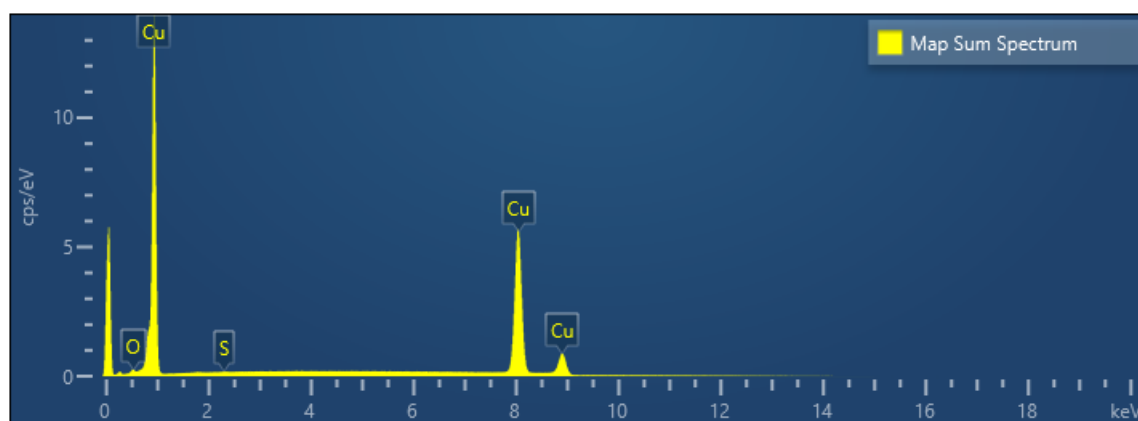


FIGURE B.4: EDX spectra for DL Cu foam

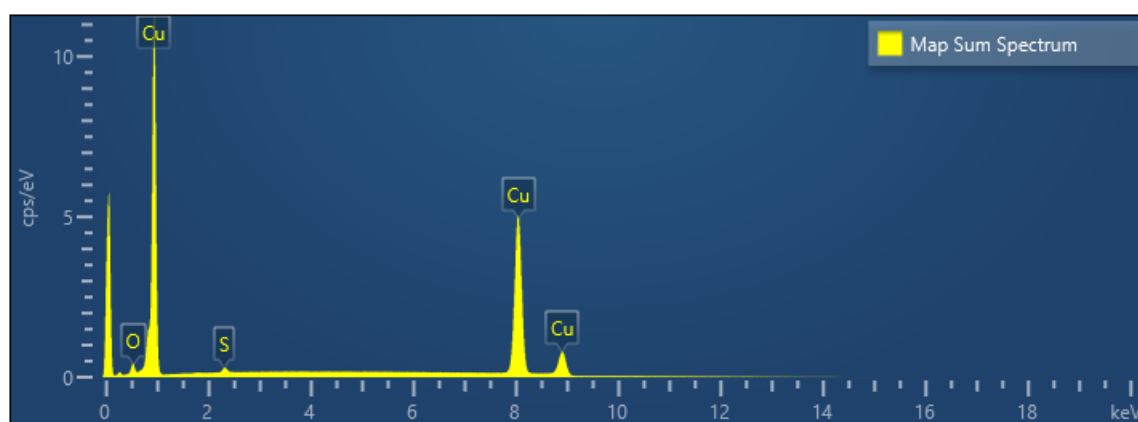


FIGURE B.5: EDX spectra for LL Cu foam

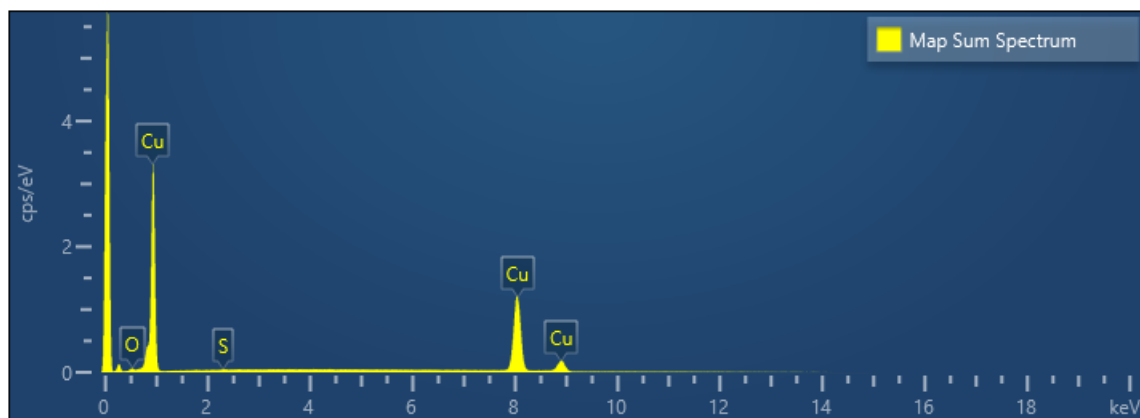


FIGURE B.6: EDX spectra for PAA Cu foam

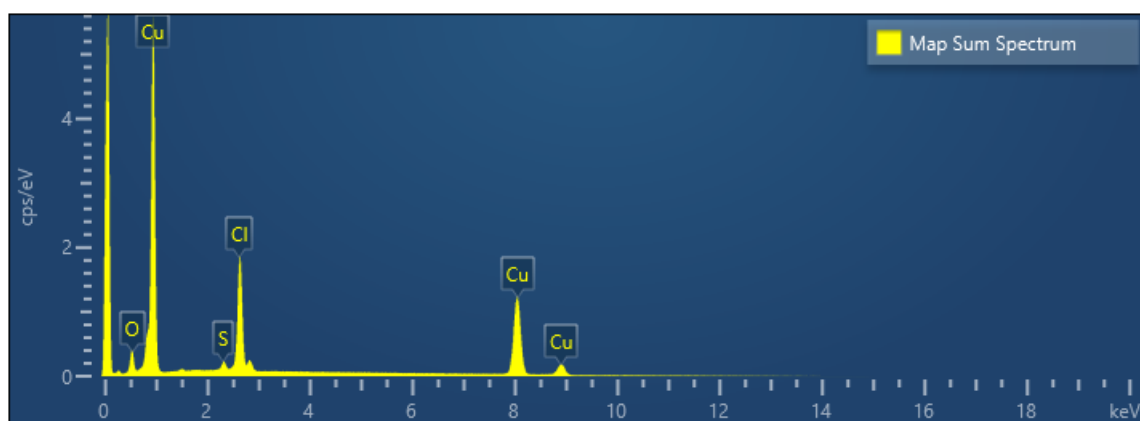
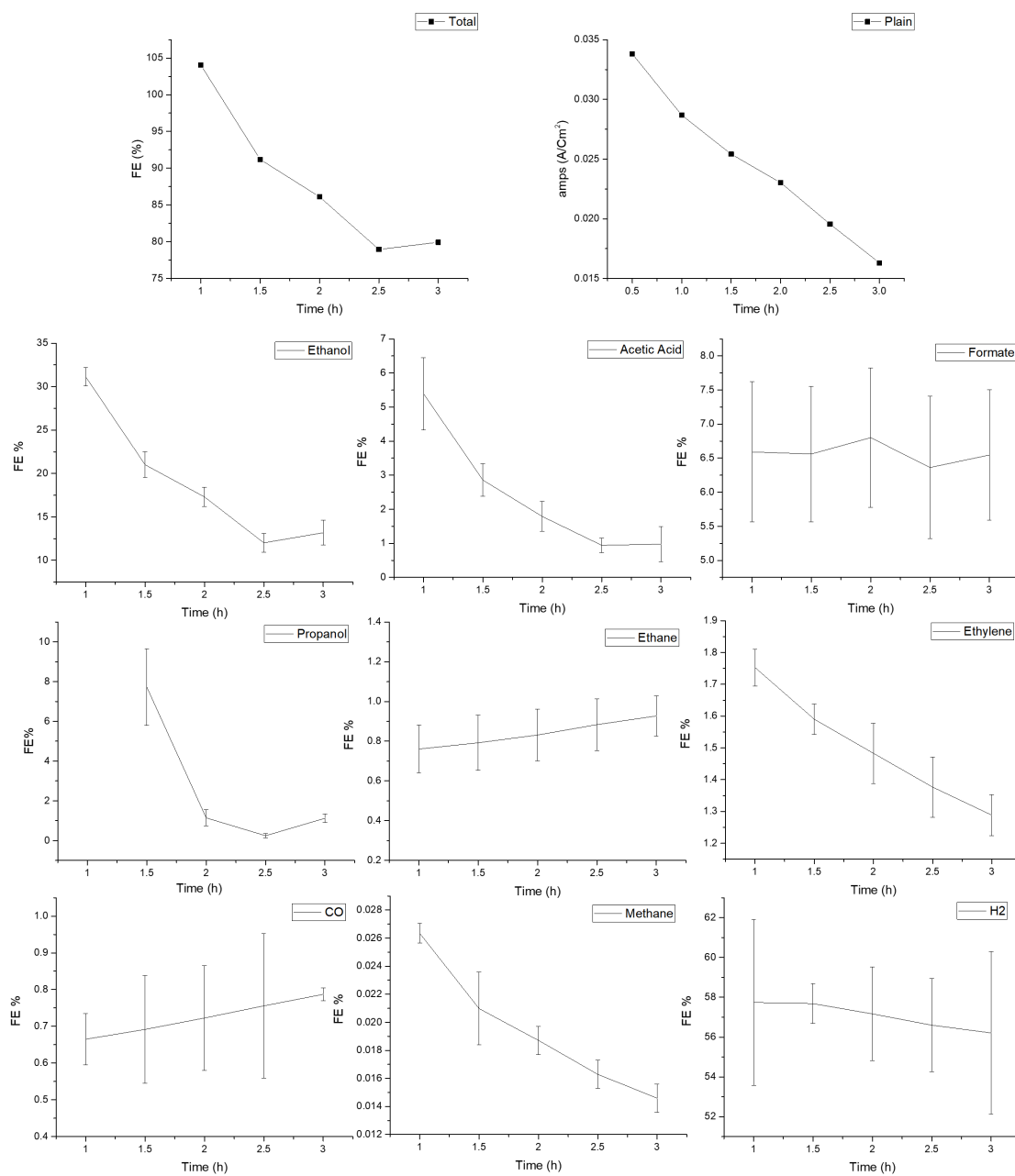


FIGURE B.7: EDX spectra for PDL Cu foam

B.2.2 Time plots

FIGURE B.8: Plots for Plain foam over 3 hours of CO₂RR at 4 V

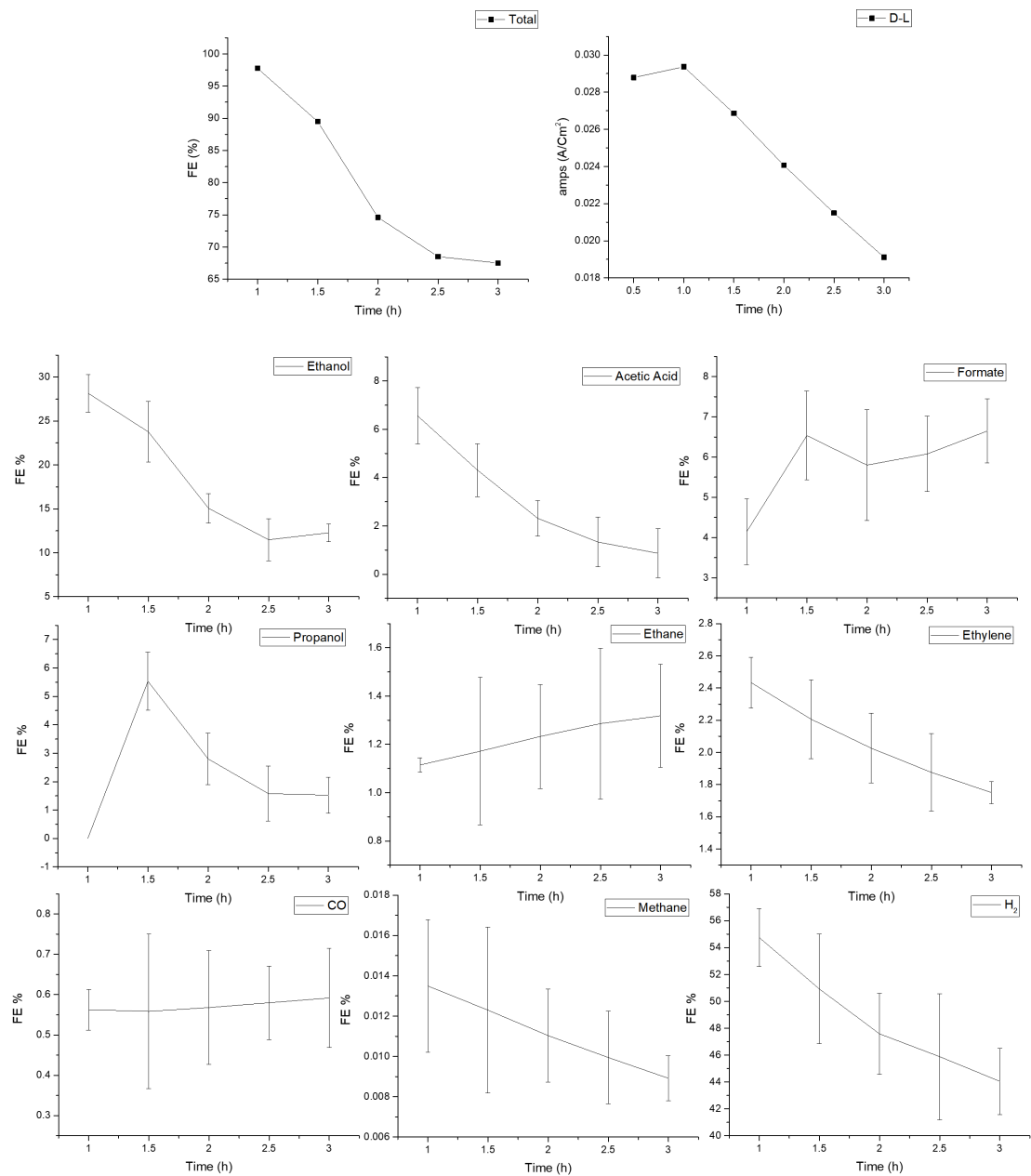
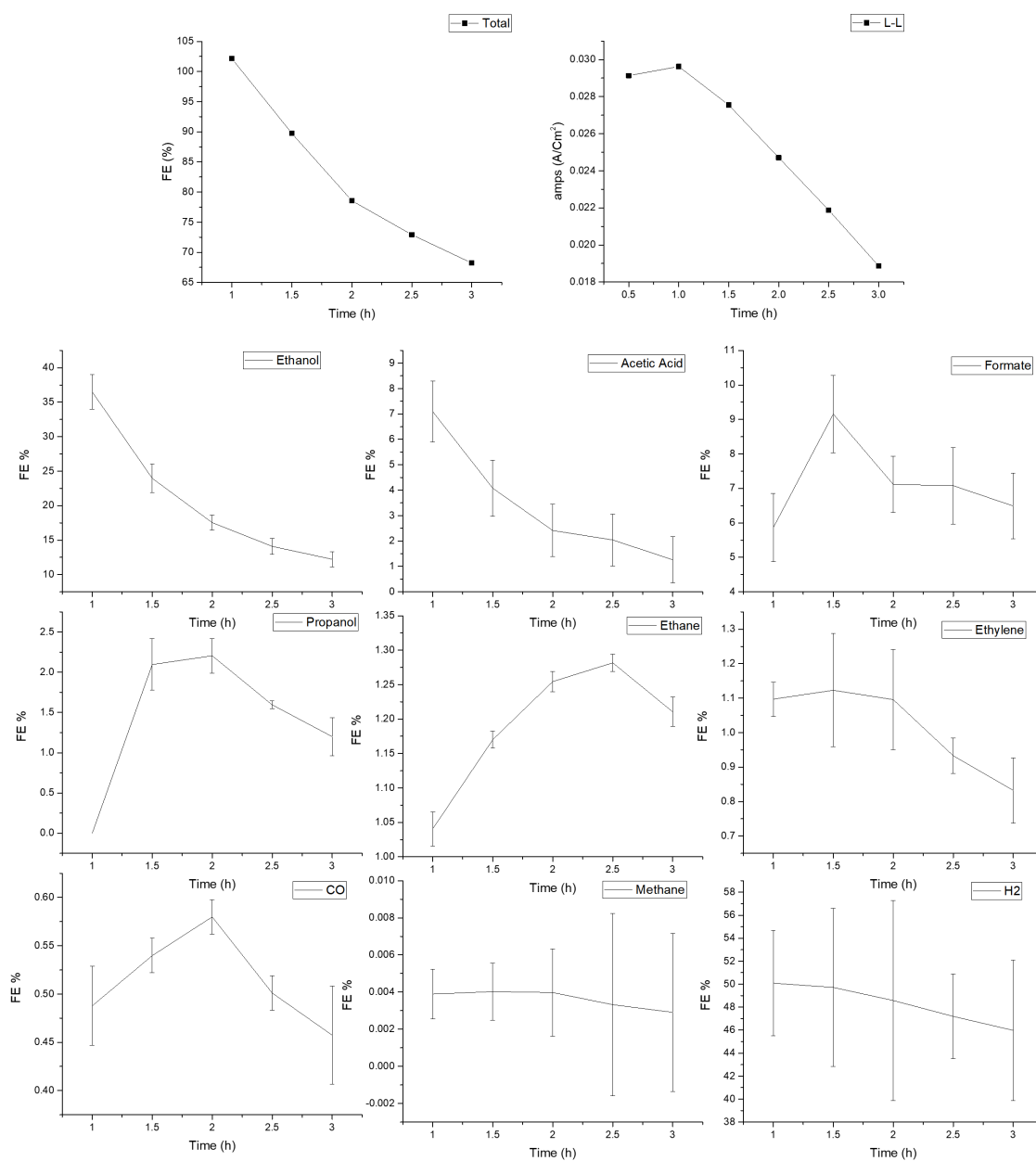
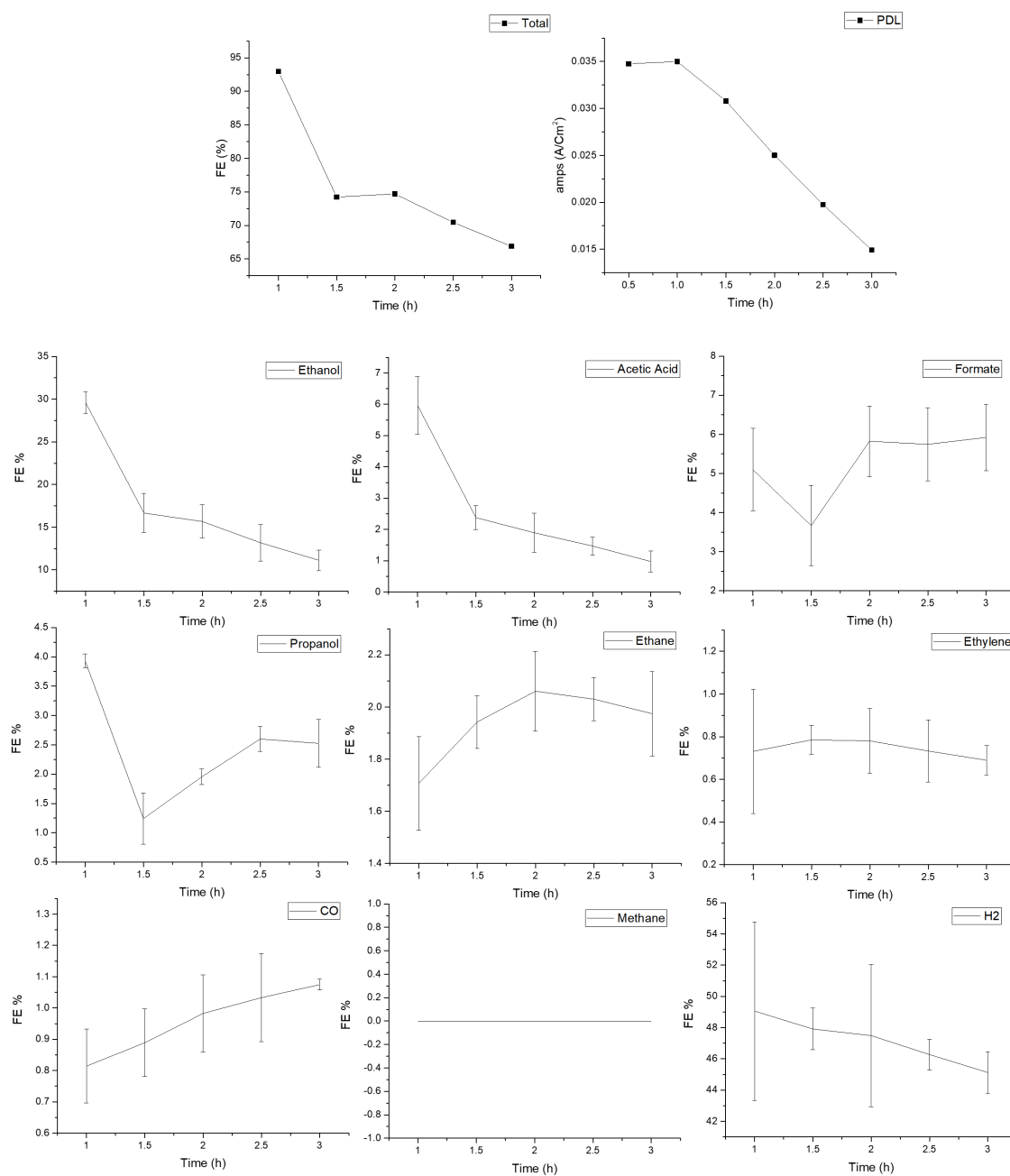


FIGURE B.9: Plots for DL foam over 3 hours of CO₂RR at 4 V

FIGURE B.10: Plots for LL foam over 3 hours of CO₂RR at 4 V

FIGURE B.11: Plots for PDL foam over 3 hours of CO₂RR at 4 V

Appendix C

Background Theory

In order to successfully design an electrochemical cell based on the works of Sunyik [95] and Rudd [93], it is necessary to fully understand the function of each component in the electrocatalytic cell and how they interact with each other. In this chapter electrocatalytic concepts will be examined.

C.1 Cell Components

In an electrocatalytic cell there are three key components: the electrodes, the electrolyte and the membrane.

C.1.1 Electrodes

Arguably the most important part of the electrochemical cell is the electrodes used. They act as the interface between the electrical circuit and the electrolyte. It is on these that the reduction and oxidation reactions occur, with heavy influence on the selectivity of each of the possible reactions.

Electrode Compositions

Many different metals have been examined for use as the working electrode, such as; platinum [177], iron [178], silver [179] and gold [180].

Each of these materials has a selectivity for a different products, resulting in different Faradaic Efficiencies (FE) (Discussed in section C.2.4) for each material. Copper has been found to be the best material for direct conversion of CO₂ to C₂ products [65, 181]. Various forms of copper have been examined, such as copper-oxide (Cu^(II)O) electrodes [182]. Nanomaterials have also been shown to affect the products of the electrocatalysis [183–185]. Copper has been tested with nanoparticles [186] and copper nano-foams [93, 95, 155, 156, 158, 159, 187], which are further discussed in Chapter 7.

Traditional Electrodes

The electrodes that have been more traditionally seen in the literature are at a two phase boundary, either solid to gas, or solid to liquid. These electrodes are commonly made from sheet metals as they are a cheap and readily available material that is easy to work with. However, when ultra high purity is required, metal foils are often used, with them being mounted on conductive carbon blocks, retaining the strength and rigidity required, whilst only using a minimal amount of expensive material. Alternatively, a mesh can be used as they have a greatly increased surface area to volumes ratio, whilst still providing some rigidity and strength.

Gas Diffusion Electrodes (GDE)

In more recent literature, GDE are becoming more and more prevalent. They are designed to interface at a three phase boundary within the cell, between the solid electrode, the gaseous reactants and the liquid electrolyte. Cells using this set style of GDE are much more effective at reacting gaseous reactants than cells that use a dissolved reactant approach.

C.1.2 Membranes

In electrocatalysis it is necessary to separate sections of the cell; mixing anolyte and catholyte can cause unwanted reactions to occur. However the electrical connection needs to be maintained and early designs used salt bridges to connect the two physically separated electrolytes. More recently membranes have been developed to optimise electrical conductivity whilst maintain the separation of the electrolytes. The two key variations are Proton Exchange Membranes (PEM) and Anion Exchange Membranes.

PEM are semipermeable membranes, that conduct protons, whilst acting as a reactant barrier, blocking other species such as oxygen and hydrogen. They can be either pure polymer membranes or composite membranes, where other materials are embedded in a polymer matrix.

One of the most commonly used and commercially available PEM materials is the fluoropolymer (PFSA) Nafion, a DuPont product [188]. While Nafion is an ionomer with a perfluorinated backbone like Teflon there are many other structural motifs used, such as polyaromatic polymers and partially fluorinated polymers.

Proton-exchange membranes are primarily characterized by proton conductivity, methanol permeability, and thermal stability, with fluorocarbon membranes performing well, as well as their high durability, Low Surface Energy and chemical resistance. Recently however, the difficulties of manufacturing these materials and the health risks associated with their by-products, has lead to their use being phased out globally, where possible. leading to numerous works attempting to find alternatives that perform as well, such as Sulphonated Aromatic Polymers [189].

AEM are polymer membranes that contains positive ionic groups, for example quaternary ammonium groups such as $\text{R-N}^+(\text{CH}_3)_3$, and mobile negatively charged

anions [190].

C.1.3 Electrolyte

Water is a relatively poor conductor of electricity, and so a salt is used to increase the specific conductivity of the solution. A higher ionic conductivity relates directly to a lower resistance of the electrolyte, which affects the overall cell performance. The voltage drop due to the electrolytic solution is expressed using Ohm's law.

Ohm's Law

In electrical circuits, it is often desirable to specify the voltage at a certain component, the difference in voltage between the two sides of the component, is referred to as the voltage drop. As in Ohm's law, this voltage drop is proportional to the current flowing through the component, multiplied by its resistance.

Ohm's law states that the current conducted between two points is directly proportional to the voltage across the two points [191].

$$I = \frac{V}{R} \quad (\text{C.1})$$

Where: I is the current through the conductor in amperes, V is the voltage measured across the cell in volts, and R is the resistance of the conductor in ohms. More specifically, Ohm's law states that resistance is constant, independent of the current. This can be adapted to Equation C.2 to normalise the current for the electrode surface area:

$$j = \frac{V}{R_{SA}} \quad (\text{C.2})$$

Where: j is the current density in $A \cdot cm^{-2}$, R_{SA} is the area specific resistance of the cell ($\Omega \cdot cm^2$).

Since the potential difference of a cell is not affected by the area of the electrodes immersed in electrolyte or of the distance between them, it is seen from Ohm's law that a change in the current passed must be due to change in the total resistance within the cell. This internal resistance is directly proportional to the distance between the electrodes, and inversely proportional to the area of the immersed electrode. If the external resistance of a cell is represented by R_e , and the internal resistance by R_i , then Ohm's law takes the form [191]:

$$j = \frac{E}{R_e + R_i} \quad (C.3)$$

The R_i can be further defined, by separating the resistance of the cell in into two components; membrane resistance $R_{Membrane}$ and electrolyte resistance $R_{Electrolyte}$ [98]:

$$R_i = R_{Membrane} + R_{Electrolyte} \quad (C.4)$$

$R_{Membrane}$ is relative to the surface area, thickness and resistivity of the membrane used. $R_{Electrolyte}$ is a function of electrolyte resistivity and distance between the electrode.

Ohms law can also be expressed as:

$$IR = \frac{IL}{A\kappa} = \frac{jL}{\kappa} \quad (C.5)$$

Where: I is the current in amperes, j is the current density in $A \cdot cm^{-2}$, L is electrode spacing in cm, A is the cross-sectional area in cm^2 , and κ is the conductivity in $S \cdot cm^{-1}$. showing that a reduction in voltage at the same current density it is key to increase conductivity.

Historically, aqueous electrolytes have been used due to their wide availability and ease of use inside an electrolysis cell. Their resistance can be determined by:

$$\sigma = R \frac{A}{L} \quad (\text{C.6})$$

Where: σ is the resistivity, R is the resistance, A is the cross-sectional area in cm^2 , and L is electrode spacing in cm.

From this equation σ is an intensive variable, which is independent of the dimensions of the cell, however R is an extensive variable, meaning that it is dependent upon the dimensions of the system. This can be used as a model to predict the effects of the several experiments upon the cell: electrode spacing, surface area of cell, electrolyte concentration (effecting R).

Using Equation C.6: If $A_1 < A_2$ and $L_1 < L_2$ then an increase in cross-sectional area, Equation C.10, results in an decrease in resistance. Although a increase in electrode spacing, Equation C.11, increases the resistance.

$$R_{11} = R(A_1, L_1) \quad (\text{C.7})$$

$$R_{21} = R(A_2, L_1) \quad (\text{C.8})$$

$$R_{12} = R(A_1, L_2) \quad (\text{C.9})$$

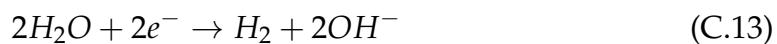
$$R_{21} < R_{11} \quad (\text{C.10})$$

$$R_{12} > R_{11} \quad (\text{C.11})$$

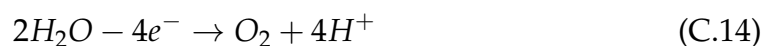
C.2 Electrochemical Concepts

A heterogeneous electrochemical reaction is a process where charge is passed to or from an electrode. If it is a reduction reaction then it is deemed to be a cathodic

process, where a species is reduced by an electron from the electrode, such as the following reactions:



Otherwise if it is a oxidation reaction then it is an anodic process, where the stable species is oxidised by the loss of electrons to the electrode.



For these reactions to occur they must be conducted within a cell containing an anode and a cathode; as per the law of conservation of charge, reduction at the cathode and oxidation at the anode must be equal. The total chemical change can be calculated by combining the individual electrode reactions; in water the chemical change is seen by adding reactions C.13 and C.14 i.e.



The total reversible cell voltage is calculated using the cell potentials of the two half-reactions. The convention is that the half- reactions on the left and right are oxidation and reduction respectively:

$$E_{\text{Rev}} = E_{\text{Right}} - E_{\text{Left}} = E_{\text{Cathode}} - E_{\text{Anode}} \quad (\text{C.16})$$

It can therefore be seen that for both conditions, $E_{\text{Rev}} = -1.23 \text{ V}$.

Electrical Conductivity

The electrical conductivity of a solution of an electrolyte is measured by determining the resistance of the solution between two electrodes separated by a fixed distance. To do this the resistance is first determined by using:

$$R = \rho \frac{L}{A} \quad (\text{C.17})$$

Where: R is the electrical resistance, L is the length between the electrodes and A is the cross-sectional area.

Conductivity (σ), ρ , is the reciprocal of the resistivity:

$$\sigma = \frac{1}{\rho} \quad (\text{C.18})$$

Combining Equations C.17 and C.18 resistance can then be converted to conductivity using:

$$\sigma = \frac{L}{RA} \quad (\text{C.19})$$

In a conducting liquid medium, at a defined temperature, the electrolytic conductivity κ , is defined as the ratio of the current density (j) to the applied electrical field strength, which is the driving force of charge transport. In practice, κ is evaluated from the resistance R , measured for an isotropic sample in a measuring cell, when the geometric cell constant K_{Cell} , is known as [192]:

$$\kappa = \frac{K_{Cell}}{R} \quad (\text{C.20})$$

For a cell with parallel electrodes, K_{cell} is determined through the cross sectional area A , and the electrode separation L . However, the result of the electrical measurement for R contains contributions from several other effects, in addition to the desired electric charge transport of ions. These effects include the ion-ion

interactions, the electrode-sample interface or electrical double-layer, and the influences of the connecting cables. In addition, under an AC, the reactance contribution X , to the total impedance Z , must be accounted for:

$$Z = R + jX(j = \sqrt{-1}) \quad (\text{C.21})$$

C.2.1 Carbon Dioxide Reduction Reaction

Potassium bicarbonate (KHCO_3) dissolves in water with a solubility of 23% by weight, at 20 °C [193] The exact process by which CO_2 is reduced to more useful product is not fully understood. The best known works are that by Johnson *et al.* [164] who compiled several of the possible mechanistic pathways of CO_2 reduction to C_1 and C_2 products on copper electrodes (via carbonate formation through aqueous solution) that had been reported [87, 131, 194–203] and produced Figure C.1.

In this diagram, the horizontal axis shows the number of carbons in the molecule with the vertical axis as the number of electrons transferred required to form the intermediate or product. Copper's ability to bind with both CO^* and H^* is the key to C_2 product production, as can be seen in the figure with all products, other than formate, requiring the CO^* species to bond to the electrode surface. The reason copper is unique in its ability to form C_2 products is discussed in section 2.2.

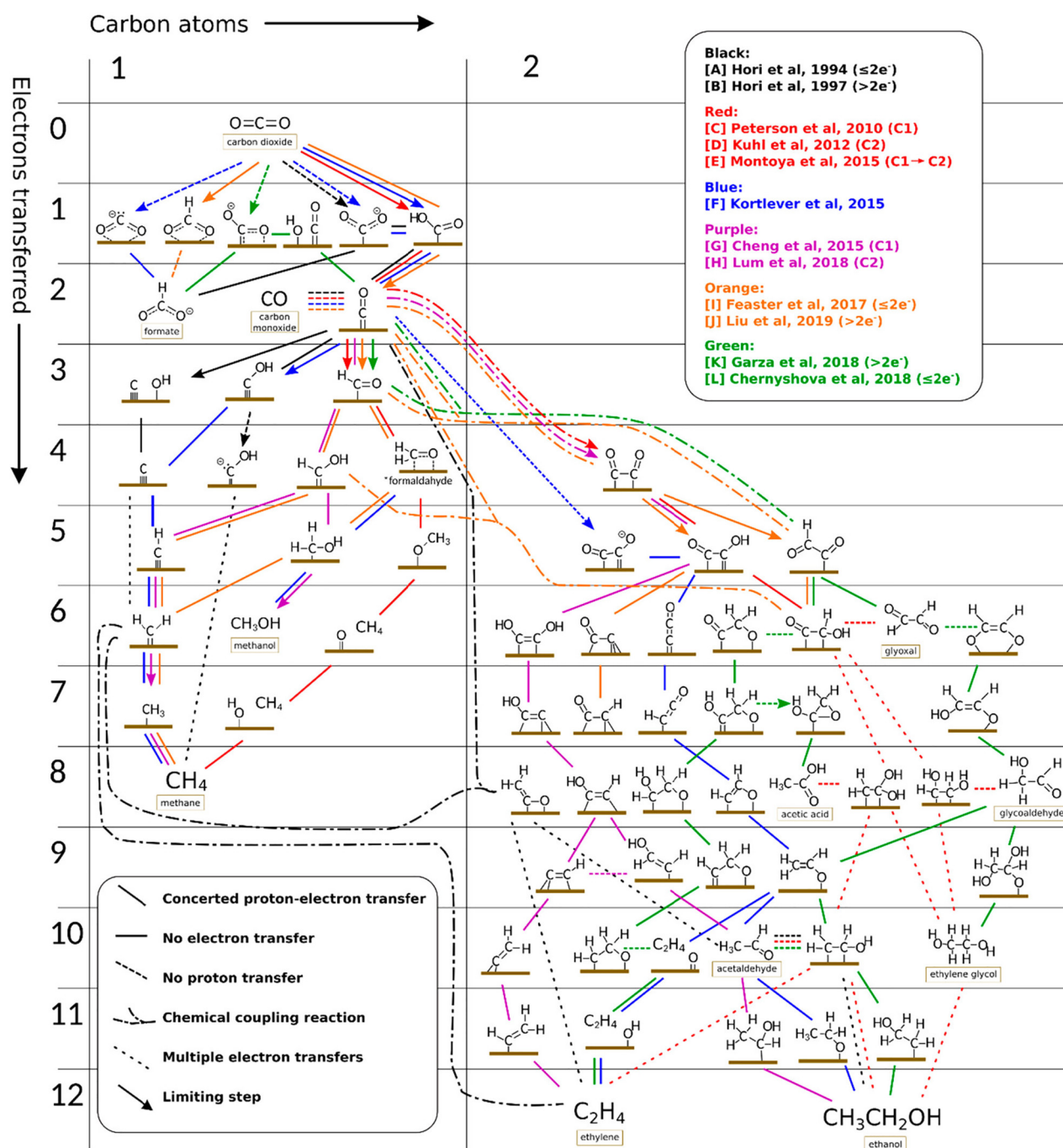


FIGURE C.1: Reproduced with permission from Johnson *et al.* [164]: The possible mechanistic pathways of CO_2 reduction to C_1 and C_2 products on polycrystalline copper, grouped into different coloured reaction schemes taken from the works in the top-right legend: [A] Hori *et al.* [194]; [B] Hori *et al.* [131]; [C] Peterson *et al.* [195]; [D] Kuhl *et al.* [87]; [E] Montoya *et al.* [196]; [F] Kortlever *et al.* [197]; [G] Cheng *et al.* [198]; [H] Lum *et al.* [199]; [I] Feaster *et al.* [200]; [J] Liu *et al.* [201]; [K] Garza *et al.* [202]; [L] Chernyshova *et al.* [203]. The bottom-left legend states the meaning of the texture of the lines connecting intermediates.

Kortlever *et al.* [197] reported that the transition from C_1 to C_2 products is optimum on a copper (100) surface at -0.4 V vs Standard hydrogen electrode.

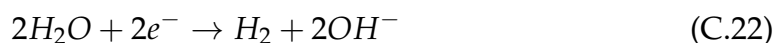
The reduction potentials for each product are listed in Table C.1.

Reactions	E° (V) Versus SHE (at pH 7)
$2H^+ + 2e^- \rightarrow H_2$	-0.41
$CO_2 + e^- \rightarrow CO_2^-$	-1.89
$CO_2 + 2e^- + 2H^+ \rightarrow HCOOH$	-0.60
$CO_2 + 2e^- + 2H^+ \rightarrow CO + H_2O$	-0.52
$CO_2 + 4e^- + 4H^+ \rightarrow C + H_2O$	-0.19
$CO_2 + 4e^- + 4H^+ \rightarrow HCHO + H_2O$	-0.45
$CO_2 + 6e^- + 6H^+ \rightarrow CH_3OH + H_2O$	-0.38
$CO_2 + 8e^- + 8H^+ \rightarrow CH_4 + H_2O$	-0.23
$CO_2 + 12e^- + 12H^+ \rightarrow C_2H_4 + H_2O$	-0.34
$2CO_2 + 8e^- + 8H^+ \rightarrow CH_3COOH + 2H_2$	-0.31
$2CO_2 + 12e^- + 12H^+ \rightarrow C_2H_5OH + 2H_2$	-0.32

TABLE C.1: Reproduced with permission from Marepally *et al.* [204]: CO_2 reduction potentials for various CO_2 reduction reactions products.

C.2.2 Hydrogen Evolution Reaction

A key obstacle to overcome in the development is the suppression of the competing Hydrogen Evolution Reaction (HER). HER has been the subject of multiple studies due to its technological and fundamental importance. The overall reaction at the cathode is stated as:

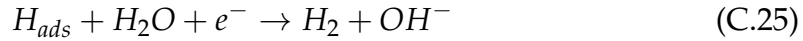


The process of hydrogen evolution is accepted to be via the Volmer-Tafel and Volmer Heyrovsky mechanisms [205]. The hydrogen is adsorbed via the Volmer

reaction:



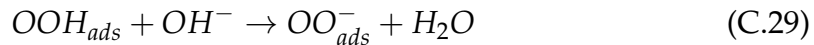
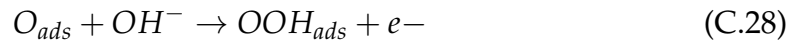
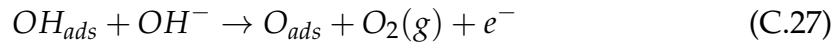
Which is followed by either the chemical Tafel reaction or the electrochemical Heyrovsky desorption step:



There are several way in which researchers are trying to suppress this reaction. One direction or research is Electrode design: geometry, facial orientation and composition [Kim2019, 206] with another approach increasing the availability of CO₂ at the electrode surface, such as the use of Gas Diffusion electrodes [101] and supersaturate electrolyte [207] as well as under high pressure conditions [208]

C.2.3 Oxygen Evolution Reaction

At the anode in the cells being examined oxygen is produced through the oxygen evolution reaction. Although there is no confirmed scheme, the proposed reaction pathways are notably similar; one such reaction pathway is:



There are four different types of adsorbed species (O , OH , OOH and OO^-) and

four of the pathways involve electron transfer, where the potential of the electrode is used to drive the reaction.

C.2.4 Efficiencies

Energy efficiency is used for the comparison of systems, it is generally defined as the ratio of useful energy output to the total energy input. An energy efficiency (η) is defined by:

$$\eta = \frac{\text{Charge used in forming product}}{\text{Total charge Passed}} * 100 \quad (\text{C.31})$$

The energy efficiency is a key factor in determining the economic feasibility of CO₂ electrocatalysis. The energy efficiency for a given product can be calculated using Equation C.32 [102, 168] where the apparent standard cell potential, E_{st} , can be calculated using the Nernst Equation:

$$\text{Energy Efficiency} = \frac{E_{st} \times \text{Faradaic Efficiency}}{\text{Applied Cell Potential}} \quad (\text{C.32})$$

However, there are a number of different ways of expressing the efficiency in an electrocatalytic reaction, as discussed below.

Current Efficiency

Current efficiency is the ratio of the actual mass of a substance liberated from an electrolyte by the passage of current to the theoretical mass liberated according to Faraday's law. Current efficiency can be used in measuring electro-deposition thickness on materials in electrolysis. The current efficiency ϕ is defined by:

$$\phi = \frac{M \times I \times t}{N \times F} \quad (\text{C.33})$$

Where: ϕ is the theoretical yield (current efficiency), M is the Molar mass, I is the electric current in Amperes, t is the time in seconds, N is the Oxidation state, F is Faraday's constant.

Cell Efficiencies

For CO₂ electrochemical cells their performance and selectivity for certain reduction products is usually reported in terms of Faradaic Efficiency (FE), with energy efficiency and current density (j) also being used. The FE represents the percentage of electrons that end up in the desired product and can be defined as the ratio of the measured amount of produced product compared to the theoretical amount of produced product according to Faraday's Law, as shown in Equation C.34, adapted from Garcia [58].

$$FE(\%) = \frac{Q_{Experimental}}{Q_{Theoretical}} \times 100 = \frac{z \times n \times F}{Q} \times 100 \quad (C.34)$$

Where: Q is the charge passed during electrolysis, z is the number of electrons required to form the gas product, n is the number of moles of products, F is Faraday's constant.

EE is the amount of energy stored in the products divided by the amount of electrical energy put into the system [209], as defined by Equation C.35:

$$EE = \sum_k \frac{E_k^0 \cdot FE_k}{E_k^0 + \eta_{(dimensionless)}} \quad (C.35)$$

Where: E_k^0 is the equilibrium cell potential for a specific product k (V), FE_k is the FE of product k , and η is the cell over-potential (V) [210].

Current density relates to the conversion rate of the electrochemical reaction in mA/cm^2 .

An efficient CO₂ electrocatalysis cell should achieve high EEs for desired products with high rates of CO₂ conversion, in other words high FEs and low overpotentials on the cathode and anode.

Ideal Gas Law

The ideal gas law shows the volume that 1 mole of gas will occupy at a given temperature and pressure:

$$pV = nRT = nk_B N_A T \quad (\text{C.36})$$

Where: ' n ' is the number of moles, ' R ' is the ideal gas constant, ' N ' is the number of molecules, ' k_B ' is the Boltzmann constant, ' R ' is the ideal gas constant, ' N_A ' is Avogadro's number, ' T ' is the absolute temperature of the gas, and ' N ' is the number of molecules or atoms of the gas. From this it can be determined that at standard temperature and pressure, 1 mole of any gas will occupy a volume of 22.4 L, i.e. the molar volume.

C.2.5 Over-potential

Bard [211] discussed how the extent of electrode polarization is measured by the over-potential η :

$$\eta = E - E_{eq} \quad (\text{C.37})$$

Where: E_{eq} is the equilibrium potential of an electrode and E is the potential of an electrode versus a reference.

Phillips [98] showed that the overall cell voltage, E_{Cell} , can be broken down into its constituent parts, as shown in Equation C.38

$$E_{Cell} = E_{Rev} + \eta_{Anode} + \eta_{Cathode} + I \cdot R_{Cell} + \eta_{MT} \quad (\text{C.38})$$

Where: E_{Rev} is the total reversible cell voltage, η_{Anode} is the overpotential at the anode, $\eta_{Cathode}$ the overpotential at the cathode, I is the current, R_{Cell} is the resistance of the cell and η_{MT} is the voltage inefficiency caused by mass transport limitations at the electrodes.

Energy efficiency as discussed in Equation C.31 is the percentage of the energy applied that is stored in the creation of desired products compared to the total cell voltage with high value being important as it reduces the cost of electricity required required to operate an electrochemical cell.

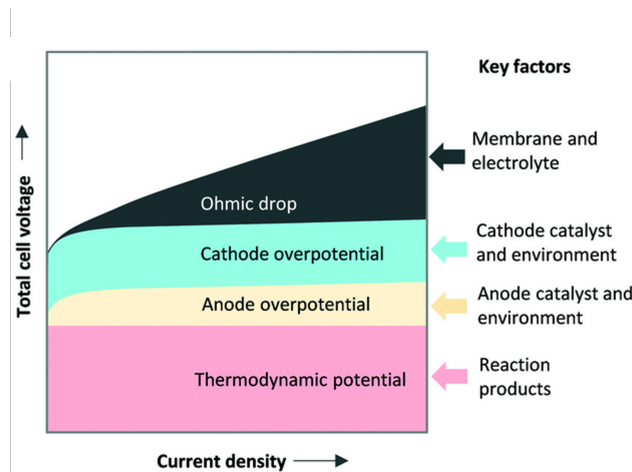


FIGURE C.2: Reproduced with permission from Nguyen *et al.* [212]: Breakdown of overall cell voltage as a function of current density showing the affects of key components.

Nguyen *et al.* [212] showed, in Figure C.2, that increasing energy efficiency requires decreasing total cell voltage.

In order to obtain the optimum cell performance, it is important to understand the interaction between the electrode and the electrolyte. The basic electrode reaction can be considered as $Red \rightarrow Ox + ne$, and using Faraday's 1st law of electrolysis, the number of moles altered at the electrode is directly proportional to the charge applied to the electrode:

$$N = \frac{Q}{nF} = \frac{It}{nF} \quad (C.39)$$

Where: Q is the amount of charge transferred, n is the number of electrons exchanged in each half reaction and F is Faraday's constant.

The number of moles of each reactant electrolysed per unit time is the rate of reaction, v . As reactions occurring at the interface of the electrode and electrolyte are considered heterogeneous, the reaction rate is dependent on the surface area of the electrode, A , for a current density j :

$$v = \frac{1}{A} \cdot \frac{dN}{dt} = \frac{I}{nFA} = \frac{j}{nF} \quad (\text{C.40})$$

From a chemical kinetics approach, the rate of oxidation is expressed as $v_a = k_a c_{Red}$ and the rate of reduction as $v_c = k_c c_{Ox}$ where k_a and k_c are the rate constants of the reactions, and c_{Ox} and c_{Red} the concentrations of the reacting substances.

Rate constants of electrode reactions can be expressed using the Arrhenius Equation:

$$k_a = P_a \exp\left(-\frac{\Delta H_a}{RT}\right) \quad (\text{C.41})$$

$$k_c = P_c \exp\left(-\frac{\Delta H_c}{RT}\right) \quad (\text{C.42})$$

Where: P_a and P_c are pre-exponential factors independent of electrode potential, and ΔH_a and ΔH_c are the activation enthalpies of the oxidation and reduction reactions.

Bringing together the two derivations of the rate of reaction, and acknowledging that the overall current is a summation of the anodic and cathodic currents $j = j_a + j_c$ (where the currents are vectors across the interface), we see that:

$$j_a = nFk_a c_{Red} \quad (\text{C.43})$$

$$j_c = nFk_c c_{Ox} \quad (\text{C.44})$$

and hence:

$$j = nF(k_a c_{Red} - k_c c_{Ox}) \quad (C.45)$$

When there is no net current, the rate of oxidation and reduction must be equal, and the electrode will be at the equilibrium electrode potential E_{eq} , which can be expressed using the Nernst Equation:

$$E_{eq} = E^0 + \frac{RT}{nF} \ln\left(\frac{c_o}{c_R}\right) \quad (C.46)$$

The relationship between the current on an electrode (I) and the applied potential (E) is best described by the Butler-Volmer Equation. This particular form of the equation is correct when the rate of reaction is determined by the transfer of electrical charge at the surface of the electrode, and not by the mass transfer from the bulk electrolyte to the electrode surface.

$$j = j_0[e^{-\alpha f \eta} - e^{(1-\alpha) f \eta}] \quad (C.47)$$

Where: the over-potential $\eta = E - E_0$.

C.3 Carbon Dioxide - Water System

Whilst in the atmosphere, CO₂ is extremely stable as it is the most oxidised form of carbon. It is naturally removed from the atmosphere through photosynthesis by plants and bodies of water, often described as 'carbon sinks'. CO₂ dissolves in water through a simple equilibrium reaction (Equation C.48) with the solubility of CO₂ being 0.1449 grams per 100 ml H₂O under standard conditions [213].



Water, in its pure form, is expected to have a pH of 7. It forms a natural dissociation to hydronium and hydroxide ions.

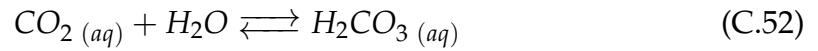


$$K_w = [H^+][OH^-] = 10^{-14} \quad (C.50)$$

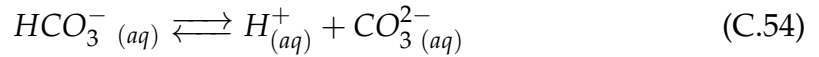
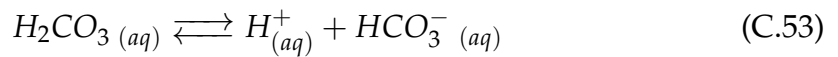
From which the pH can be calculated:

$$pH = -\log_{10}[H^+] = -(-7) = 7 \quad (C.51)$$

However, under standard conditions, H_2O is often slightly acidic, which can be attributed to an equilibrium reaction between dissolved CO_2 and the water, which forms carbonic acid:



With carbonic acid now present, acid-base equilibrium reactions remove protons to form carbonate and bicarbonate ions:



Henry's Law can be used to calculate the amount of CO_2 dissolved in the water; it states that the concentration of dissolved CO_2 is proportional to its partial pressure in the gas phase:

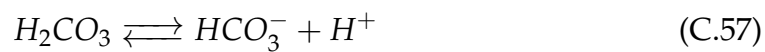
$$[CO_2]_{(aq)} = K_{CO_2} P_{CO_2} \quad (C.55)$$

Therefore, increasing carbon dioxide concentrations in the atmosphere also results in more CO_2 dissolved in water bodies around the world. For the world's oceans, this means the pH will drop as CO_2 levels increase in causing 'ocean acidification'.

C.3.1 Buffers

The buffer capacity of a solution quantifies its ability to resist changes in pH, either by absorbing or desorbing H^+ and OH^- ions. When an acid or base is added to a buffer, the effect on pH change depends on both the initial pH and the capacity of the buffer to resist change in pH. Buffer capacity (β) is defined as the moles of an acid or base necessary to change the pH of a solution by 1, divided by the pH change and the volume of buffer in litres. A buffer resists changes in pH due to the addition of an acid or base through consumption of the buffer. As long as the buffer has not been completely reacted, the pH will not change drastically. The pH change will increase more drastically as the buffer is depleted as it becomes less resistant to change.

Various equilibrium reactions in the $\text{CO}_2 - \text{KHCO}_3$ electrolyte system are (with the equilibrium constants at 25°C from Sullivan *et al.*[214]):



Combining Equations C.56 and C.57 gives:



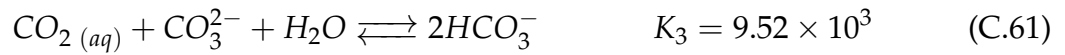
Or in basic solutions where $\text{pH} > 7$ it is written as:



Bicarbonate ions are neutralised by OH^- ions that are generated on the cathode surface by:



Combining C.59 and C.60 gives:



In this study, $\text{CO}_{2(gas)}$ is in equilibrium within the liquid, therefore $\text{CO}_{2(aq)}$ concentration is a constant at a given pressure and temperature. So, for the electrolyte in equilibrium with CO_2 gas at a partial pressure of 101.3 kPa and a temperature of 25°C, $\text{CO}_2(aq)$ is 1.5034 g/L (not considering the effect of ionic strength).

Initial concentrations of the other species; HCO_3^- and CO_3^{2-} and pH, may be determined by considering Equation C.61 to be in equilibrium. While reaction C.57 is fast, carbonic acid (H_2CO_3) never constitutes more than 1 % of the total $\text{CO}_2(aq)$ in solution, and so above a pH of 7.4, reaction C.59 dominates and reactions C.56 and C.57 can be ignored in the pH calculations [214].

Also, the kinetics of both the forward and reverse reactions of Equation C.60 are very fast, so that it can be assumed that HCO_3^- is in equilibrium with CO_3^{2-} at all times.

The charge balance can be described as:

$$[\text{H}^+] + [\text{K}^+] = [\text{HCO}_3^-] + 2[\text{CO}_3^{2-}] + [\text{OH}^-] \quad (\text{C.62})$$

In this example of KOH and CO₂ in water, alkalinity is given by Equation C.62 as the amount of strong base: if $[K^+] = A$

$$A = [HCO_3^-] + 2[CO_3^{2-}] + [OH^-] - [H^+] \quad (C.63)$$

These calculations can be used to produce a graph, as seen in Figure C.3, which shows how the bicarbonate buffer is affected by pH.

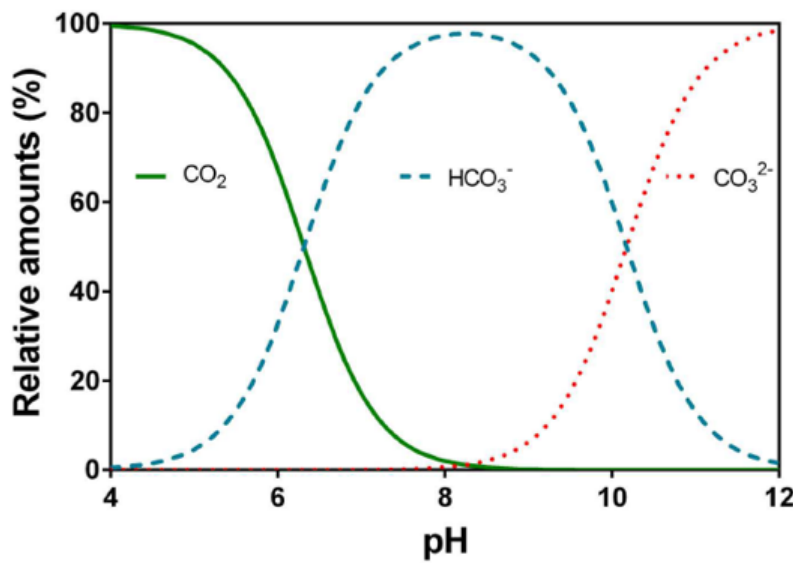


FIGURE C.3: Reproduced from Pedersen *et al.* [215]: Relative percentage of carbon dioxide, bicarbonate and carbonate in water as a function of pH.

C.3.2 Henry's Law

Henry's law describes the relationship between the solubility of a gas in a liquid and the partial pressure of that gas above the liquid. Formulated by the English chemist William Henry in 1803, it states that:

$$C = K_H \cdot P \quad (C.64)$$

Where; C is the concentration of the gas in the liquid, k_H is the Henry's law constant (which varies depending on the gas and the solvent), and P is the partial

pressure of the gas above the liquid. In summary, Henry's law tells us that the amount of gas that dissolves in a liquid is directly proportional to the pressure of the gas above the liquid, provided the temperature remains constant

C.3.3 Diffusion

Fick's laws of diffusion describe the net movement of a given species from a region of higher concentration to a region of lower concentration diffusion. They can be used to solve the diffusion coefficient 'D'. Fick's first law can be used to derive his second law which in turn is identical to the diffusion equation.

Fick's 1st law

Fick's first law relates the diffusive flux (Flow) to the gradient of the concentration. It postulates that the flux goes from regions of high concentration to regions of low concentration, with a magnitude that is proportional to the concentration gradient (spatial derivative). In one dimension, the law can be written in various forms, the most common form is in a molar basis:

$$J = -D \frac{\delta \phi}{\delta x} \quad (\text{C.65})$$

Where: 'J' is the diffusion flux ($\text{mol m}^{-2} \text{s}^{-1}$), 'D' is the diffusion coefficient or diffusivity (m^2/s), ' ϕ ' (for ideal mixtures) is the concentration (mol), 'x' is distance (m). 'D' is proportional to the squared velocity of the diffusing particles which depends on the temperature, viscosity and particles size, according to the Stokes–Einstein relation. In dilute aqueous solutions the diffusion coefficients of most ions are in the range of $(0.6 - 2) \times 10^{-9} \text{ m}^2/\text{s}$ at room temperature.

If diffusion is in 2 or more dimensions then the ∇ , the gradient operator, should be used, generalising the previous equation to:

$$J = -D\nabla\phi \quad (\text{C.66})$$

Where 'J' is the diffusion flux vector.

C.3.4 Flow Characterisation

Laminar flow is the movement of fluid along easily definable paths, where all particles flow parallelly in the same direction. Hence, the particles move in a laminar way (layers gliding over each other) [216]. Conversely, turbulent flow is where the fluid particles move in an inconsistent, indirect way, where eddy current can form leading to high energy loss in the fluids velocity. The speed of the fluid at a point continuously changes in both magnitude and direction [216].

The main method of flow analysis is Computational Fluid Dynamics (CFD). The Navier-Stokes equation or simplified Reynolds-averaged Navier-Stokes equations are the basis for almost all CFD codes [216]. Flow conditions can be visualised practically by using ink, which is injected into the middle of a tube through which water flows. If the ink does not appear to mix with water and the streamlines are parallel, the flow is deemed to be laminar. However, if the flow completely disrupts the ink and the water turns homogenous as the streamlines are chaotic and not linear, the flow is deemed to be turbulent, Figure C.4 illustrates these differences.

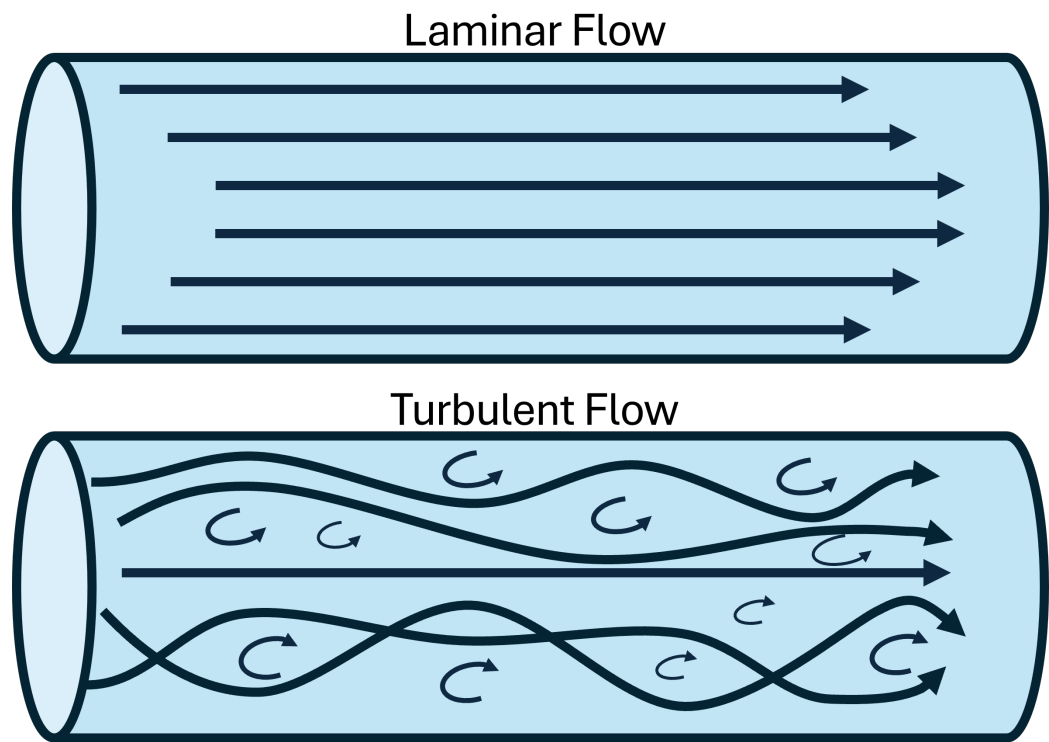


FIGURE C.4: Illustration of the differences between Laminar and Turbulent flow.

The type of flow is determined by a non-dimensional number called the Reynolds number for a pipe flow. If the Reynolds number is less than 2000, then the flow is called laminar flow, between 2000 and 4000 the flow may be laminar or turbulent. If the Reynolds number is over 4000, then the flow is called turbulent.

In practice, matching the Reynolds number is not on its own sufficient to guarantee similitude. Fluid flow is generally chaotic, and very small changes to shape and surface roughness of bounding surfaces can result in very different flows. Nevertheless, Reynolds numbers are a very important guide and are widely used.

Higher turbulence in the flows enhances gas-liquid mass transfer in aqueous solutions [217], this is discussed further in Chapter 4